Synthesis of Aluminum-Titanium Carbide Nanocomposites by the Rotating Impeller Gas-Liquid In-situ Method

by

Inigo Anza

WORCESTER POLYTECHNIC INSTITUTE

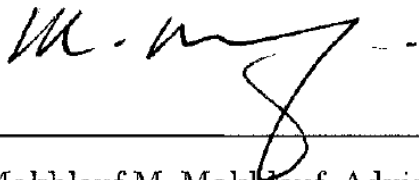*in partial fulfillment of the requirements for the*
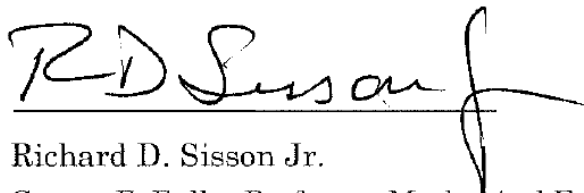
Degree of Doctor of Philosophy

in

Material Science and Engineering

October 2016

APPROVED:

Makhlouf M. Makhlouf, Advisor
Professor, Mechanical Engineering

Richard D. Sisson Jr.
George F. Fuller Professor, Mechanical Engineering
Director, Manufacturing and Materials Engineering

Abstract

The next generation of aluminum alloys will have to operate at temperatures approaching 300°C. Traditional aluminum alloys cannot perform at these temperatures, but aluminum alloys reinforced with fine ceramic particles can. The objective of this research is to develop a process to synthesize Al-TiC composites by the Rotating Impeller Gas-Liquid In-situ method. This method relies on injecting methane into molten aluminum that has been pre-alloyed with titanium. The gas is introduced by means of a rotating impeller into the molten alloy, and under the correct conditions of temperature, gas flow, and rotation speed, it reacts preferentially with titanium to form titanium carbide particles. The design of the apparatus, the multi-physics phenomena underlying the mechanism responsible for particle formation and size control, and the operation window for the process are first elucidated. Then a parametric study that leads to the synthesis of aluminum reinforced with TiC microparticles and nanoparticles is described. Finally, potential technical obstacles that may stand in the way of commercializing the process are discussed and ways to overcome them are proposed.

Acknowledgments

This PhD thesis has been an extraordinary journey that would have not ended well without the collaborative effort of many others. Here in these lines I would like to express them my gratitude.

First of all, I would like to thank my advisor Professor Makhlouf. His clear initial description of the objectives, technical obstacles to overcome and resources needed to achieve a happy end has been instrumental for my success. During the PhD his advice has been always available when I required guidance. I would also like to thank Professor Apelian. He was my initial contact with WPI. He encouraged me to come, provided the funding and made my transition from my original homeland to Worcester very welcoming. Professor Sisson, head of the MTE department, always knew the right person to approach in topics outside of my expertise. Professor Mishra's broad knowledge in chemical metallurgy has been also very meaningful anytime he had the opportunity to contribute.

My colleagues of the ACRC group, Carl, Theo, Shaymus, Yang Yang, Eunkyung and Libo, have been extremely helpful in the labs. They gave me support to assemble my plant and to optimize my sample preparation and characterization. We had endless discussions on my empirical results and theoretical approach.

Special thanks also to Dr. Jim Bredt and Will Shambley from Viridis 3D and Professor Hansen's team from UMass Lowell. They have used their 3D printing capabilities anytime I required new 3D printed ceramic impellers for my process. Also I would like to thank David Weiss from Eck Industries. His industrial perspective has been extremely rich so our technology can be eventually transferred to the industry.

I would also like to thank the MTE and MPI staff. Carol, Renee, Rita and Maureen have been an outstanding support with accommodation search, office amenities, purchases for the project, funding and budget allocation or trips organization.

My time here has not only been work but also cultural exchange, new friends, experiences and fun time. Friends like, among others, Yuwei, Haize, Aaron, Behnam, Selim, Farhad, Christian, Lorenzo and my girlfriend Liz have made my stay also very pleasant. Barbecues, hiking, biking, squash matches, sailing, Boston and NYC weekend trips, all them contributed to have a better and balanced life.

A special thanks to my family and friends from Spain. They all supported my decision to come to the USA to do my PhD from the very beginning. My parents' visits during the summer and my visits back to Spain during Christmas time to catch up with friends, cousins and my sister were refreshing, recharging and always a motivation to excel in my return to the USA.

I express my apology to anyone I didn't mention here.

Table of Contents

Executive Summary

The objective of this research is to develop a process to synthesize Al-TiC composites by the Rotating Impeller Gas-Liquid In-situ (RIGLI) method. The Rotating Impeller Gas-Liquid In-situ method, which was developed by Borgonovo and Makhlouf to synthesize Al-AlN nanocomposites [1-7], relies on dispersing a nitriding gas into liquid aluminum by means of a rotating impeller. The nitriding gas (nitrogen, ammonia, or a mixture of nitrogen and ammonia) is in the form of very small bubbles that react with the melt to produce the AlN nanoparticles. The resulting product is a solid aluminum alloy ingot that contains 30-60nm AlN particles. This ingot may be used as a master alloy to be added to commercial aluminum alloys in order to enhance their strength and stiffness. The RIGLI method satisfactorily circumvents most, if not all, of the limitations associated with other methods for making nanocomposites; i.e., clustering of the nanoparticles, lack of wetting between the nanoparticles and the aluminum matrix, and the high cost associated with all other methods of synthesizing nanoparticles. When as little as 0.5 volume pct. of the nano-size aluminum nitride particles are added to commercial A356 aluminum alloy, the cast tensile specimens show 25% improvement in yield strength when measured at 573K (300°C).

This thesis builds on the Borgonovo and Makhlouf effort and uses it as a technological platform on the basis of which composite materials with different compositions may be synthesized. Specifically, this work aims to adapt the Rotating Impeller Gas-Liquid In-situ method to synthesizing Al-TiC composites. The thesis is divided into 3 Chapters as follows:

Chapter 1 presents a narrative that describes the evolution of the Gas-Liquid In-situ method starting with the first generation concept, followed by the rationale that led to the second and third generation concepts. Also discussed in Chapter 1 are advantages and limitations of each of these incremental progressions of the process, and a detailed description of the design of the third generation apparatus.

Chapter 2 is a comprehensive theoretical framework that describes the complex physicochemical phenomena associated with the production of Al-TiC composites by the Rotating Impeller Gas-Liquid In-situ method. The model developed and presented in this Chapter fulfills the dimensional analysis conditions, and decreases the uncertainty associated with scaling-up the process for commercial production of Al-TiC composites. The fundamental ideas underlying the thermodynamics and kinetics of synthesizing TiC microcomposites are based on previous works made in the context of TiC grain refiners for aluminum [8, 9], Al-TiC, Al-SiC and Al-AlN micro-composites made by gas-liquid [10-23] and solid-liquid [24-28] methods, and on the work of Borgonovo and Makhlouf on Al-AlN nanocomposites [1-7]. Sections 4 and 5 of this Chapter, which discuss particle size control and gas-liquid dispersion, as well as fluid dynamics analyses, are an

original effort on this thesis. The Growth Interruption Mechanism (GIM), as a mechanism to control TiC particle size is introduced for the first time in this work. Recognizing the dramatic viscosity increase associated with metal nanofluids as a problem that must be overcome in order to achieve high nanoparticle loading, and the limitations imposed by the impeller gas dispersion technique are also important contributions of this work. The section on soot formation and control, which is critical to enabling production of TiC nanoparticles, has been based – to a large extent – on standard chemical engineering modeling and simulation of gas tube reactors.

Chapter 3 presents an empirical parametric study that is designed with the aid of conclusions arrived at in Chapter 2. The Crumbling Cascade mechanism, which opens the door to TiC microparticle size control under 2µm, is elucidated. The right parameters are found to prevent soot formation, and some of the open questions regarding the kinetics of TiC nanoparticle formation (i.e., the limiting step and chemisorption dynamics) are answered. The processing parameters are optimized leading to the production of an Al-TiC nanocomposite with less than 1 volume pct. TiC particles that are on average smaller than 30nm. Chapter 3 concludes by calling attention to the fact that further investigation of the evolution of the melt's rheology is needed in order to allow increased TiC particle loading. Actions to achieve this goal are proposed, and potential applications for Al-TiC nano- and micro-composites are discussed.

Finally, it remains to be said that due to limits on funding, measurement of the strengthening and stiffening effect of the TiC particles in both casting and wrought aluminum alloys remains a pending activity that should be undertaken by future researchers.

Nomenclature

Geometric Variables

x	Longitudinal cylindrical coordinate	[L]
r	Radial cylindrical coordinate	[L]
L_i	Length of object 'i'	[L]
S_{trans}	Tube cross section	[L^2]
D_{tube}	Gas tube diameter	[L]
R_{tube}	Gas tube radius	[L]
V	Gas volume inside the gas tube	[L^3]
w	Impeller blade width	[L]
L	Impeller blade length	[L]
A	Tank diameter	[L]
D	Impeller diameter	[L]
c	Impeller bottom clearance	[L]
H	Stirred liquid height	[L]

Thermodynamics Variables

(d)	Diluted/dissolved state of component in a reaction	[-]
(l)	Liquid pure state of component in a reaction	[-]
(s)	Solid pure state of component in a reaction	[-]
(g)	Gas pure state of component in a reaction	[-]
ΔG_{Ri}	Free energy of reaction 'i'	$[F \cdot L \cdot M^{-1}]$
ΔG_{Ri}^0	Free energy of reaction 'i' in its standard state	$[F \cdot L \cdot M^{-1}]$
$\Delta G_{f,i}$	Free energy of formation of compound 'i'	$[F \cdot L \cdot M^{-1}]$
$\Delta G_{f,i}^0$	Free energy of formation of compound 'i' in its standard state	$[F \cdot L \cdot M^{-1}]$
a_i	Activity of compound 'i'	[dimensionless]
K_i	Equilibrium constant of reaction 'i'	[dimensionless]
X_i	Molar fraction of component 'i'	$[^0/_1]$
γ_i	Activity coefficient of component 'i'	[dimensionless]
γ_i^H	Activity coefficient of component 'i' in Henryan state	[dimensionless]
k_B	Boltzmann constant = 1.3806 × 10^{-23}	$[M \cdot L^2 \cdot T^{-2} \cdot \theta^{-1}]$
R	Universal gas constant = 8.314	$[F \cdot L \cdot M^{-1} \cdot \theta^{-1}]$

T	Temperature	$[\theta]$
$\%wt_i$	Weight percentage of component 'i'	$[\%]$
MW_i	Molecular weight of component 'i'	[dimensionless]
$\%wt_{i\_sat}$	Saturated state for dissolved component 'i'	$[-]$
$\%wt_{i\_eq}$	Equilibrium state for dissolved component 'i' in reacting system	$[-]$

Kinetics Variables

c_i	Concentration of component 'i'	$[M \cdot L^{-3}]$
P_i	Partial pressure of component 'i'	$[F \cdot L^{-2}]$
X_i	Volume fraction of component 'i'	$[^0/_1]$
n_i	Number of moles of specie 'i'	$[M]$
R_i	Reaction rate of specie 'i'	$[M \cdot L^{-3} \cdot T^{-1}]$
E_{ai}	Activation energy of process 'i'	$[F \cdot L \cdot M^{-1}]$
K_L	Overall mass transfer coefficient in the liquid	$[L^{-2}]$
J_i	Specific mass flow of specie 'i'	$[M \cdot L^{-2} \cdot T^{-1})]$
t	Time	$[T]$

Gas-Liquid Dispersion and Fluid Dynamics Variables

a	Specific volume interface	$[L^{-2}]$
V_i	Volume of body 'i'	$[L^3]$
R_p	Particle radius	$[L^3]$
v_{growth}	Particle growth rate	$[L \cdot T^{-1}]$
ρ	Density	$[M \cdot L^{-3}]$
ρ_g	Gas density	$[M \cdot L^{-3}]$
μ	Viscosity	$[M \cdot L^{-1} \cdot T^{-1}]$
μ_o	Zero shear viscosity	$[F \cdot L^{-2} \cdot T]$
μ_{ap}	Apparent viscosity	$[F \cdot L^{-2} \cdot T]$
μ_g	Gas viscosity	$[F \cdot L^{-2} \cdot T]$
v_g	Kinematic viscosity	$[L^2 \cdot T^{-1}]$
τ	Fluid shear stress	$[M \cdot L^{-1} \cdot T^{-2}]$
τ_0	Fluid yield stress	$[M \cdot L^{-1} \cdot T^{-2}]$
$\dot{\gamma}$	Shear rate	$[T^{-1}]$
n	Shear thinning index	$[-]$
K	Material consistency index in rheology equation	$[M \cdot L^{-1} \cdot T^{-2+n}]$

d_c	Diameter of agitated nucleus in stagnant tank	[L]
b	Empirical parameter in threshold mixing equation	[-]
k_{MO}	Metzner and Otto constant in threshold mixing equation	[-]
d_b	Bubble size	[L]
d_{av}	Volume average bubble size	[L]
d_p	Nanoparticle size	[L]
d_h	Impeller noozle diameter	[L]
D_o	Nanoparticles diffusion coefficient	$[L^2 \cdot T^{-1}]$
q	Volumetric flow	$[L^3 \cdot T^{-1}]$
q_F	Flooding flow	$[L^3 \cdot T^{-1}]$
q_{CD}	Complete dispersion flow	$[L^3 \cdot T^{-1}]$
q_R	Complete recirculation flow	$[L^3 \cdot T^{-1}]$
N	Impeller speed	$[T^{-1}]$
N_F	Impeller flooding speed	$[T^{-1}]$
N_{CD}	Impeller complete dispersion speed	$[T^{-1}]$
N_R	Impeller complete recirculation speed	$[T^{-1}]$
P	Stirring power	$[M \cdot L^2 \cdot T^{-3}]$
ω	Angular impeller speed	$[T^{-1}]$
V	Voltage	$[M \cdot L^2 \cdot T^{-3} \cdot I^{-1}]$
I	Intensity	$[I]$
a	Gas-liquid interfacial surface	$[L^{-1}]$
f_d	Coalescence intensity factor	[-]
λ_{min}	Kolmogorov scale	[L]
ϕ	Gas hold up (gas volume fraction in liquid)	[%]
ε	Energy dissipation rate	$[L^2 \cdot T^{-3}]$
v_g	Gas speed at impeller nozzle	$[L \cdot T^{-1}]$
σ	Surface tension	$[M \cdot T^{-2}]$

Gas Phase Fluid Dynamics Variables

v_{flow}	Volumetric flow in gas tube	$[L \cdot T^{-1}]$
ρ_i	Density of gaseous specie 'i'	$[M \cdot L^{-3}]$
μ_i	Dynamic viscosity of gaseous specie 'i'	$[F \cdot L^{-2} \cdot T]$
$u_{flow}(x,r)$	Gas flow velocity profile	$[L \cdot T^{-1}]$

u_{flow_av}	Average gas flow velocity	$[\mathrm{L \cdot T^{-1}}]$
u_{max}	Maximum velocity parabolic profile inside gas tube	$[\mathrm{L \cdot T^{-1}}]$
ΔP	Pressure drop along the gas tube	$[\mathrm{F \cdot L^{-2}}]$
λ	Pipe friction coefficient	$[\text{-}]$
T_{wall}	Gas tube wall temperature	$[\theta]$
T	Gas temperature	$[\theta]$
Q	Transferred heat	$[\mathrm{F \cdot L \cdot \theta^{-1})}]$
C_{pi}	Specific heat gas	$[\mathrm{F \cdot L \cdot \theta^{-1} \cdot M^{-1})}]$
U	Tube wall overall mass transfer coefficient	$[\mathrm{F \cdot L^{-1} \cdot \theta^{-1} \cdot T^{-1})}]$
k_i	Gas/solid Specie 'i' conductivity	$[\mathrm{F \cdot \theta^{-1} \cdot T^{-1})}]$
D_i	Binary diffusivity argon-gaseous compound 'i'	$[\mathrm{L^2 \cdot T^{-1}}]$
σ_{ij}	Chapman-Enskog parameter	$[\mathrm{L}]$
Ω	Chapman-Enskog parameter	$[\text{-}]$
ε_{ij}	Chapman-Enskog parameter	$[\text{-}]$
v_{ij}	Stechiometric coefficient of compound 'i' in reaction 'j'	$[\text{-}]$
LFL_T	Lower flammability limit at a given temperature	$[\%]$
UFL_T	Upper flammability limit at a given temperature	$[\%]$
$\gamma_i^{U,inert}$	Upper dilution coefficient in inert gas of compound 'i'	$[\text{-}]$
$\gamma_i^{L,inert}$	Lower dilution coefficient in inert gas of compound 'i'	$[\text{-}]$
MIC	Minimum inert concentration	$[\%]$

Dimensionless Numbers

Re	Reynolds number
Ne	Newton number
We	Weber number
Fr	Froude number
Q	Flow number
Pe	Peclet number
Ha	Hatta number
E	Enhancement coefficient
Pr	Prandtl number
Z	Reactants diffusive flows ratio

CHAPTER 1

Motivation and Design of Apparatus

1.1. Motivation

One of the main strengthening mechanisms operative in aluminum alloys is precipitation strengthening. However, the high diffusivity of the typical alloying elements that constitute the precipitate particles; i.e., magnesium, silicon, zinc, copper, lithium, and manganese, causes the particles to coarsen when they are exposed to temperatures exceeding 250°C so the alloys' mechanical properties suffer. Other elements, which have much lower diffusivity in aluminum, such as scandium and zirconium, are not extensively used due to their high cost. The addition to the alloy of *ex-situ* produced ceramic particles (e.g., AlN, TiN, SiC, and TiC) that are properly wetted by the melt and become well dispersed in the matrix alloy appears as a very promising alternative to precipitated particles [5]. After the melt solidifies, these particles stiffen the alloy and remain stable at temperatures higher than 250°C. Several *ex-situ* processes for making particle reinforced aluminum matrix composites have been developed over the past few years. These include arc-plasma, mechanical alloying, and ultrasonic assisted cavitation, but some of them lack good particles/melt wetting and some cannot be easily replicated under industrial conditions [5]. The *in-situ* method has the potential to overcome these two issues. Among the many *in-situ* methods that exist today (i.e., gas-liquid reactions, solid-solid preform sintering, solid-liquid reactions, and combustion synthesis), gas-liquid reactions stands alone as the most promising process [5, 13]. It can be performed in a similar way as melt degassing, and by varying the operation and design parameters (impeller type, gas flow rate, and rotation speed) the particle size can be controlled [5, 29]. In this research a process to synthesize Al-TiC composites by an in-situ gas-liquid method is investigated.

The gas-liquid in-situ method attracted first attention after the introduction of a patent to produce net shaped microcomposite castings for applications that required abrasion resistance and thermal stability [30] by the Lanxide company in 1987. In the new process, aluminum oxidation or nitridation is effected by contacting a static atmosphere of air or pure nitrogen with the molten metal under the correct conditions of temperature, pressure and composition [31, 32]. The reaction is enhanced with magnesium and slowed down with silicon as alloying elements to proceed over the whole molten body producing a continuous 3D composite with over 50 volume pct. Al_2O_3 or AlN in aluminum [21]. When lithium is used instead of magnesium, the reaction rate becomes uncontrollable and a 100 pct. AlN crust is produced as a

precursor to AlN powder for semiconductor industry [20]. Lanxide industrialized the process and signed a contract in 1995 with Lotus Sport Cars for the production of breaking discs that eventually turned to be uneconomic, shutting down the process.

In 1989, an evolution of the process was developed by Koczak's at Drexel University for the production of TiC microcomposites [11, 14]. The proposed system consisted of a static hollow tube with a bubbler in its bottom immersed in the molten metal. Metal carbide based composites were not possible to be synthesized by the Lanxide process and the Koczack process did overcome this obstacle. The main reason, as explained by Koczack, was formation of soot from the carbonaceous gas, the entrapment of the soot particles by the liquid and the consequent formation of TiC particles by a solid-liquid reaction. The static tube process produced discontinuous microcomposites with particle size <10µm and loading up to 20-30vol pct. As an important advantage, the process is not oxygen sensitive and there is no need to introduce an oxygen getter (Li, Mg) to allow the reaction to proceed. Wu and Reddy [16] explored a decade later (2002) the synthesis of SiC-Al based composites and both Hou and Koczack [10] and Zheng and Reddy [18, 19] explored the synthesis of AlN-Al based microcomposites by this method with nitrogen and ammonia. Two patents resulted from the TiC [12]and SiC [15] composites development but no commercial application arose.
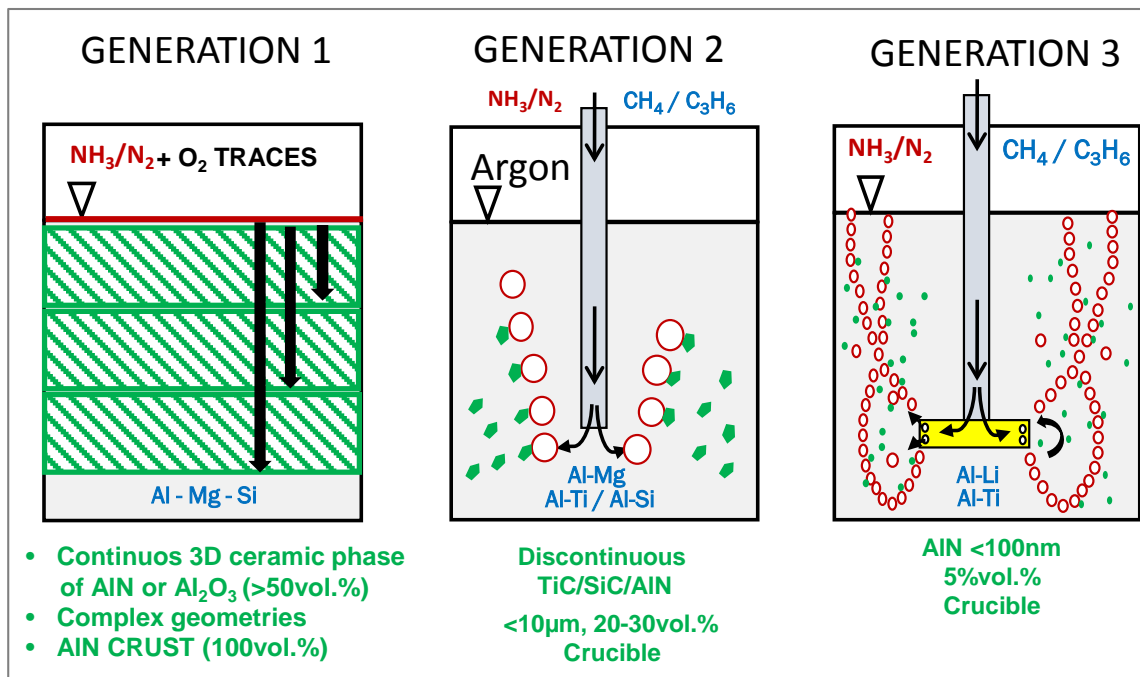

Figure 1. Schematic representation of the different process generations of gas - liquid *in-situ* process.

Finally, Borgonovo and Makhlouf developed an apparatus in which the gas is bubbled into the melt through a hollow shaft-impeller assembly [5]. The impeller has nozzles

in the blade tips through which the nitriding gas is introduced in an Al-2.5 Li[1] melt and efficiently dispersed in the form of small bubbles. Particle size can be within the nano-scale limit (< 100nm) by increasing the rotation speed and reducing the gas flow rate. Al-AlN 4 volume pct. nanocomposites with particle size in the 30-60nm range were satisfactorily produced. The nanocomposite was incorporated as a master alloy into an Al-Si-Mg melt. Both yield strength and ultimate tensile strength at room temperature and 300°C were improved by 40-75 pct. and 25-50 pct., respectively in comparison with typical values, with negligible change in elongation [1]. With this improvement in mind, this research focuses on leveraging the existing laboratory scale apparatus as an initial platform for expanding the production of Al-based nanocomposites into the carbides family of materials. Figure 1 is a schematic representation of the different generations of gas-liquid in-situ processes for making composites.

1.2. Design of Apparatus

A schematically representation of the apparatus is shown in Figure 2. It is divided into 4 subsystems:

(1) The gas abatement subsystem, in which moisture and oxygen are removed from the gas.

(2) The rotating subsystem, which is composed of a rotary swivel, a motor, a rotary feed through, and the rotating shaft. It has been designed to go up to 600rpm with acceptable vibration level.

(3) The heating and protective atmosphere subsystem, which includes the furnace and the retort. The retort is sealed from the outside and operated with a slight argon overpressure. A thermocouple measures the temperature in the melt and the oxygen inside the furnace is continuously monitored to reveal operational anomalies and to protect the furnace against explosion.

(4) The crucible and impeller subsystem that contain the molten metal. The crucible capacity is about 2.5-3lbs of aluminum. The impeller is 3D printed in mullite and it has a diameter of 2" long.

An isometric view of the ceramic retort interior is shown in Figure 3.

Whereas the gas abatement subsystem and the furnace and protective atmosphere subsystems are built based on standard engineering calculations with components available from industry suppliers, the impeller-crucible subsystem has been designed to meet key specifications including gas-dispersion efficiency and ability to handle viscous fluids. Two main turbine candidates (Figure 4), the pitch blade turbine (PBT)

---

[1] All compositions are in weight percent unless otherwise stated.

and the Rushton turbine, have been theoretically reviewed. The design rationale will be described in detail in the Fluid Dynamics section.
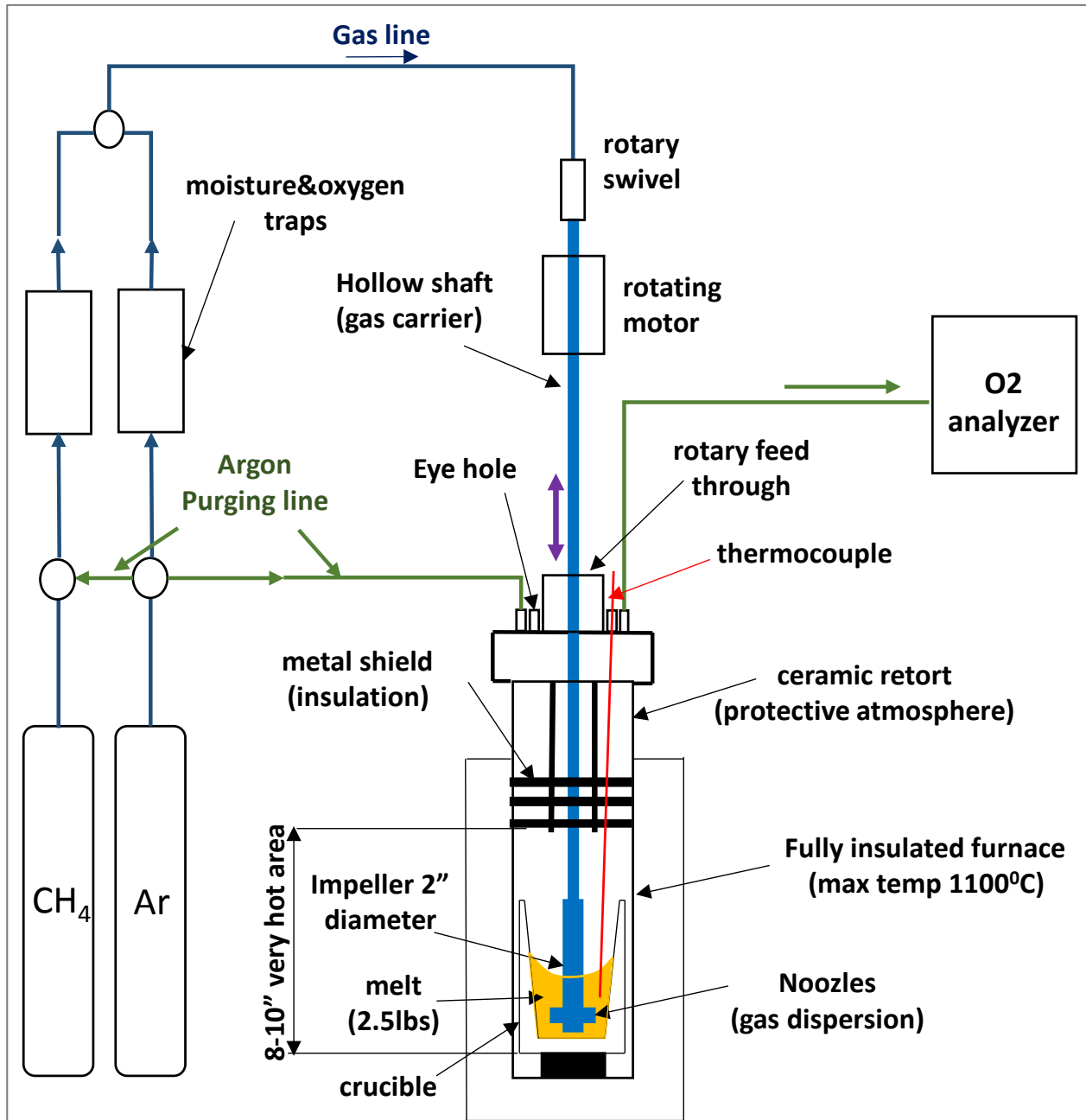

Figure 2. Schematic representation of the apparatus with a 3lbs maximum capacity.
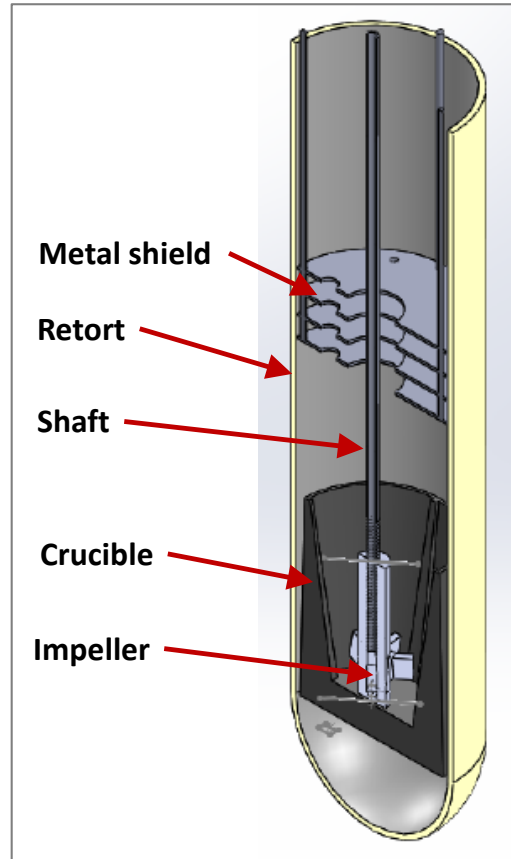
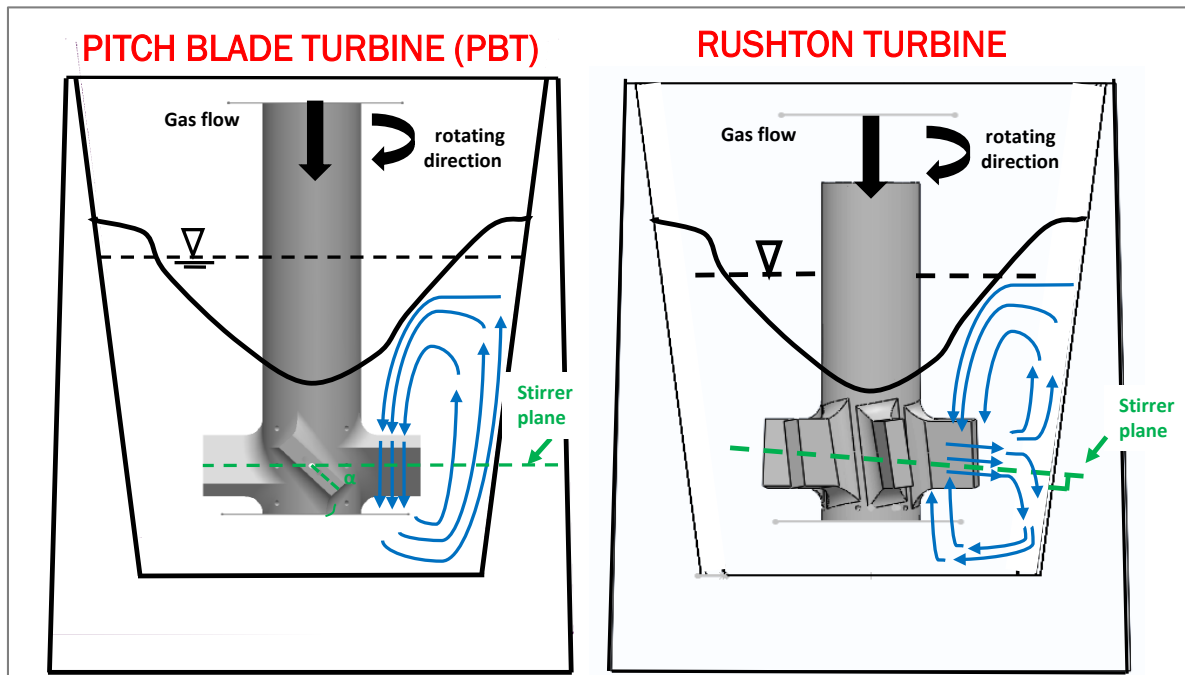Figure 3. Isometric view of the retort interior

Figure 4. Schematic representation of the two turbine models.

1.2.1. Gas abatement system for oxygen removal

Main goal of the gas abatement system is to reduce as much as possible the molten metal oxidation. The Ellingham diagram (Figure 5) shows the free energy of oxide formation per mol of oxygen gas, i.e. the tendency of metals to oxidize, dependent on the temperature. The oxygen partial pressure in equilibrium with a given metal at a set temperature can be calculated by drawing a straight line from the vertical axis origin that crosses the intersection between a vertical line located at the set temperature and the function of the free energy of formation of the metal of interest. Following this procedure, the oxygen partial pressure in equilibrium with molten aluminum at 1000^0C has been calculated to be approximately $P_{O2}=10^{-36}$atm in Figure 5. Any P_{O2} above the equilibrium pressure will oxidize the metal. It is concluded that the aluminum oxidation cannot be avoided but only mitigated. Commercial natural gas typically has about 10^{-2}-10^{-5}vol pct. of oxygen impurities. Assuming ideal gas:

$$P_{O2}V_T = n_{O2}RT$$

$$P_TV_T = n_TRT$$

Dividing the equations and considering the pressure in the furnace is 1atm, it results that:

$$P_{O2}[atm] = \frac{n_{O2}}{n_T}P_T = X_{O2}P_T = X_{O2}[ppm, ppb, ppt] \cdot 1atm \tag{1}$$

So *volume fraction* or *atm* will indifferently be used as the pressure units. The design of the gas abatement system is illustrated in (Figure 6). A moisture removal with drierite and activated alumina is first installed followed by an oxygen removal system composed of three different oxygen removal traps are included in series:

(1) A Vici trap is installed in first place. It operates at RT and contains a proprietary mixture of Si, Al, Cu, Zn and Na powders that reduces the oxygen concentration up to 1ppm.

(2) A second trap of activated carbon operating at RT further reduces the oxygen level up to 100ppb. In the methane line a SAES trap with proprietary Zr modified powder reduces the oxygen up to 10^{-9}-10^{-12} [33].

(3) Finally a tube furnace with metal powder operating at high temperature to enhance the oxidation kinetics further reduces the oxygen content. The operating temperature must be limited to the range 400-600^{0}C to avoid the possible pyrolysis of the carbonaceous gas.
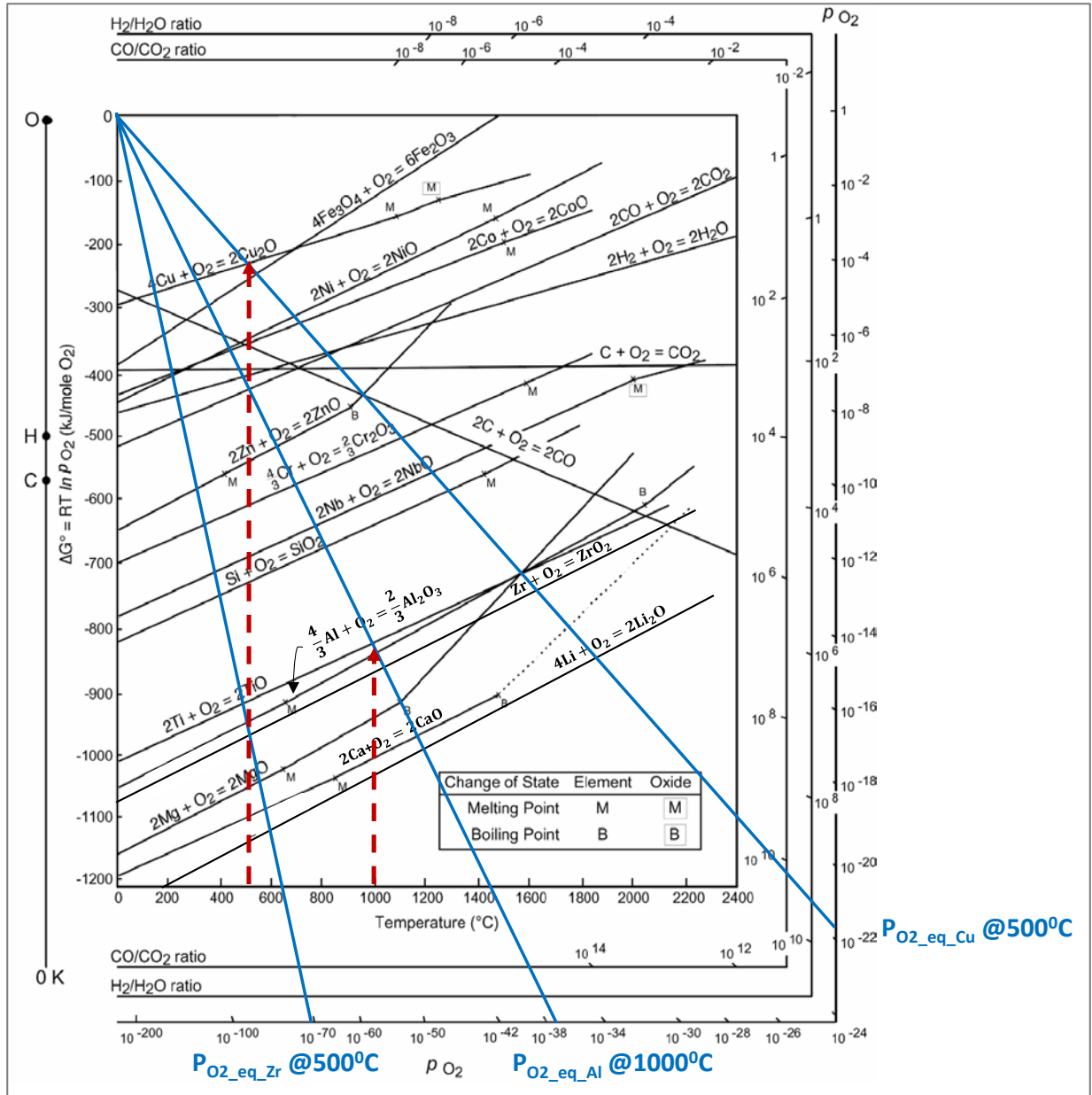
Figure 5. Ellingham diagram for metal oxidation.

The metal candidates for the tube furnace need to show (1) a strong tendency to be oxidized, (2) high melting point to avoid melting or premature sintering inactivation and (3) no option to form carbides. Metals under aluminum in the Ellingham diagram are Li, Mg, Ca and Ti and Zr. The first three are low melting metals and Ti or Zr, that are widely used by the industry, have an equilibrium oxygen pressure in the range of 10^{-60}-10^{-70}atm but they are prompt to produce TiC and ZrC. Cu is one of the few high melting point metals that doesn't combine with methane to produce carbides and will be initially used. Its equilibrium oxygen pressure at 500⁰C is 10^{-20}–10^{-22}atm.
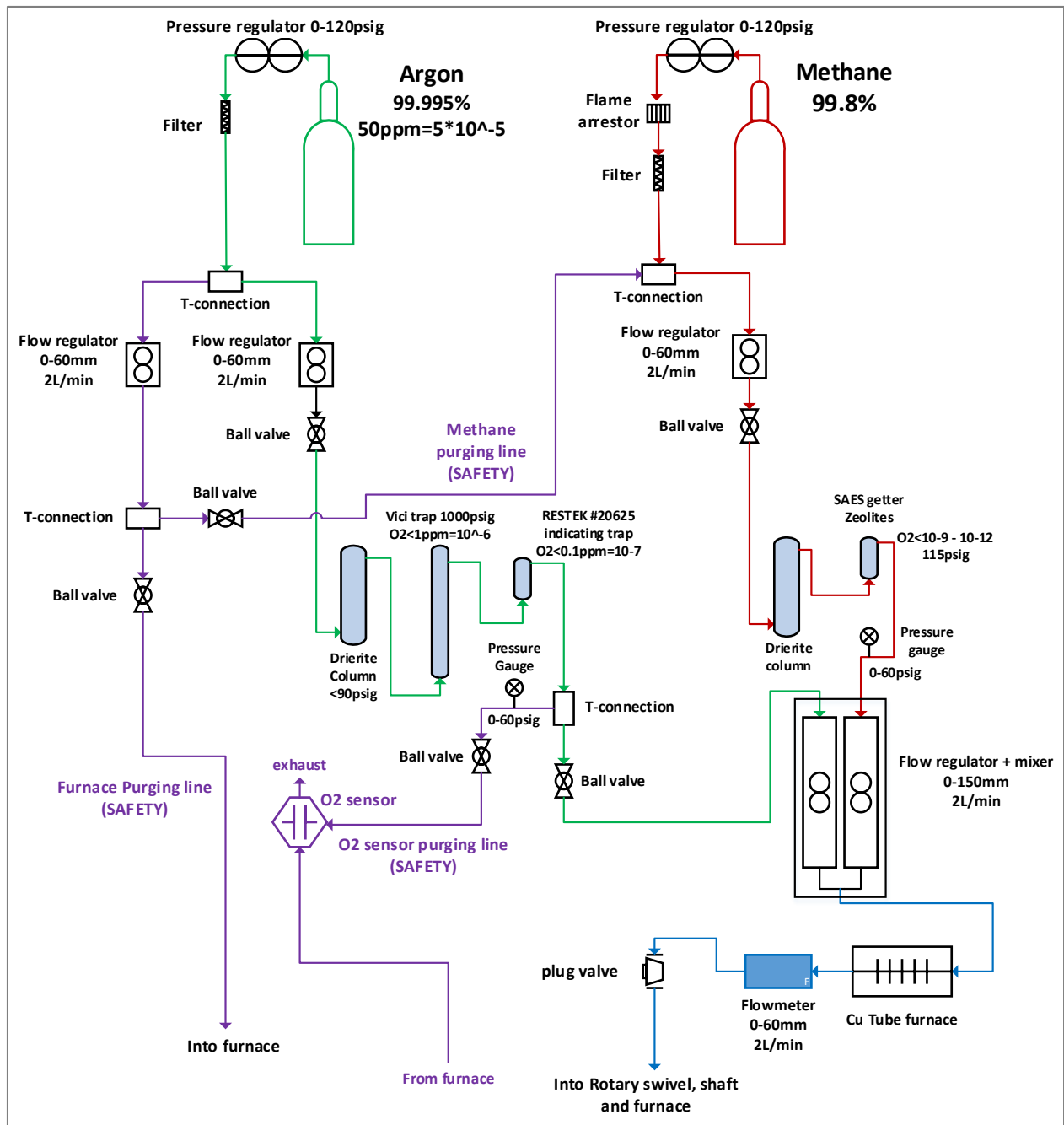
Figure 6. Flow chart of the gas-abatement system with 2L/min gas flow maximum capacity.

An apparatus has been designed that:

(1) Operates at maximum values of 1050^0C, 450rpm, gas flow of 2L/min and 3lbs of melt capacity.

(2) The protective oxygen atmosphere has a purity of 0.1vol pct.O_2 and the bubbling gas purity goes up to 10^{-9}atm with trap purification and up to 10^{-25} atm. with Cu furnace purification.

<div align="center">

CHAPTER **2**

Theoretical Perspective

</div>

2.1. Introduction and Overall Perspective

This chapter develops, for the first time to the best of our knowledge, a comprehensive theoretical framework for the production of TiC nanoparticles by the third generation of the gas-liquid in-situ method. It explores an answer to the next three questions;

(1) Which is the thermodynamic process operation window for TiC formation?

(2) How much TiC is produced at a given time under given process and melt design parameters?

(3) Which is the particle size distribution at a given time under given process and melt design parameters?

The present system intends a melt in which a constant supply of carbon takes place across the gas liquid interface. In this way it keeps the melt saturated and away from its equilibrium. The gas is introduced into the liquid through the nozzles located at the blades tip in form of small bubbles that are intensely dispersed into the liquid that continuously coalesce and break up due to the high turbulence. The titanium content decreases and the continuous production of solid TiC particles converts the melt into a slurry with varying rheology [34-36] affecting the gas dispersion. Figure 7 shows the region of the Al-Ti phase diagram in which the process occurs and the path it follows. Figure 8 shows the qualitative expected evolution during an experiment of the main experiment magnitudes at the macro scale.

The first question listed above will be answered in the thermodynamic analysis in section 2. For the second and third questions the overall TiC mass production equation is applied [37, 38]:

$$\frac{\partial}{\partial t}(wt\%TiC_{macro}) = \frac{\partial}{\partial t}(wt\%TiC_{micro}) \cdot a \cdot V_{melt} \qquad (2)$$

Given that $R_{TiC} = \frac{\partial}{\partial t}(wt\%TiC_{micro})$, in equation 2:

$$\frac{\partial}{\partial t}(wt\%TiC_{macro}(x,y,z)) = R_{TiC\_micro}(x,t) \cdot a(x,y,z,t) \cdot V_{melt} \qquad (3)$$

being (4) a partial differential equation that must be solved. The overall production rate is coupled to the micro-scale production rate that takes place in the bubble-liquid interface ($'R_{TiC\_micro}'$) multiplied by the gas-liquid interface ('a'). Both the specific volume interface 'a' (gas liquid dispersion dynamics) and the TiC reaction rate $R_{TiC_{micro}}$ (interfacial TiC kinetics) must be analyzed.
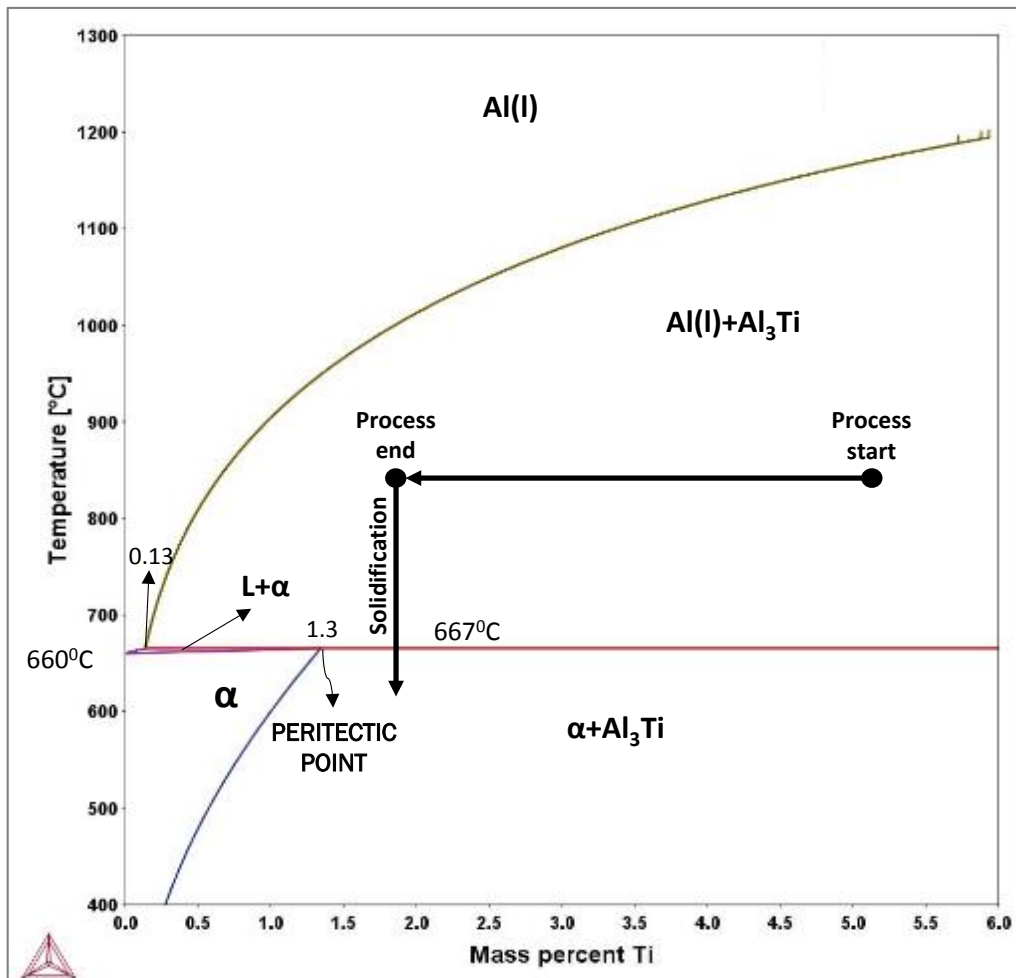

Figure 7. Al-Ti phase diagram in the Al rich corner and path followed by the melt during a experiment.
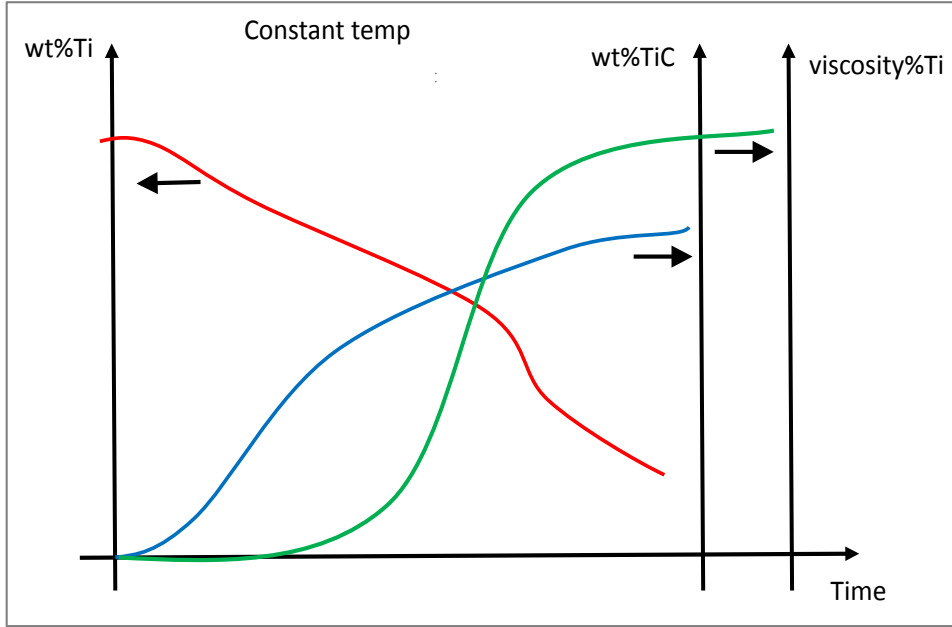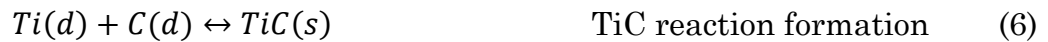
Figure 8. Qualitative macromodel at constant temperature and saturated in carbon.

2.1.1. Thermodynamic considerations

A complete thermodynamic analysis takes into account the set of linearly independent reactions. From [11, 14] the compounds *Al(l), Al₃Ti(s), Ti(d), C(d), Al₄C₃* and *TiC* are identified. For the melt to follow the path indicated in Figure 7 the Al₃Ti intermetallics must dissolve in a continuous manner so titanium transforms into TiC. Three independent reactions will be analyzed:

$$Ti(d) + \frac{1}{3}Al_4C_3(s) \leftrightarrow TiC(s) + \frac{4}{3}Al(l) \qquad \text{Al}_4\text{C}_3 \text{ displacement reaction} \quad (4)$$

$$TiAl_3(s) + C(d) \leftrightarrow TiC(s) + 3Al(l) \qquad \text{Al}_3\text{Ti displacement reaction} \quad (5)$$

$$Ti(d) + C(d) \leftrightarrow TiC(s) \qquad \text{TiC reaction formation} \quad (6)$$

Aluminum carbide is an unwanted product because it is soft and tends to react with water. The questions that this section must answer are:

(1) Which is the process operation window for TiC formation instead of Al₄C₃?

(2) Will the Al₃Ti intermetallics dissolve so their titanium content is used for TiC formation?

2.1.2. Energetics considerations

Given the small size of the crucible the temperature field is considered constant throughout the melt and no heat balance is included.

2.1.3. Kinetics considerations

The interfacial gas-liquid reactions at the bubble-melt interface are usually disclosed in several serial reactions, in which the slowest step the rate limiting step. References [11, 14] describe two possible parallel mechanisms for the decomposition of carbon atoms (step 1) and further adsorption (steps 2 and 3) at the gas-liquid interface, that affect the particle size, as shown schematically in Figure 9.

(1)   The soot formation route involves the pyrolysis of carbon in the gas phase and the release of amorphous graphite nanoparticles (step 1). These amorphous graphite nanoparticles are dragged by the liquid (steps 2-3) becoming nucleating sites for the TiC phase (step 4). TiC forms upon them and coats them, initially at a fast rate – until a TiC layer of $\cong$ 100nm thickness forms – and then at a relatively slower rate by a diffusion limited growth mechanism. Titanium atoms flow through the TiC layer by a vacancy diffusion mechanism until they reach the graphite particle, which is gradually consumed to contribute to the formation of a TiC particle [11, 14, 24-26].

(2)   The chemisorption route involves transfer of non-decomposed methane into the boundary layer (step 1), carbon atoms chemisorption at the liquid surface (step 2) and diffusion across the melt (step 3) and reaction with titanium to form TiC nuclei. The nuclei grow (step 4) until they exit the liquid boundary layer and their growth is interrupted (step 5). We will refer to the mechanism to control the particle size as 'the growth interruption mechanism' (GIM).
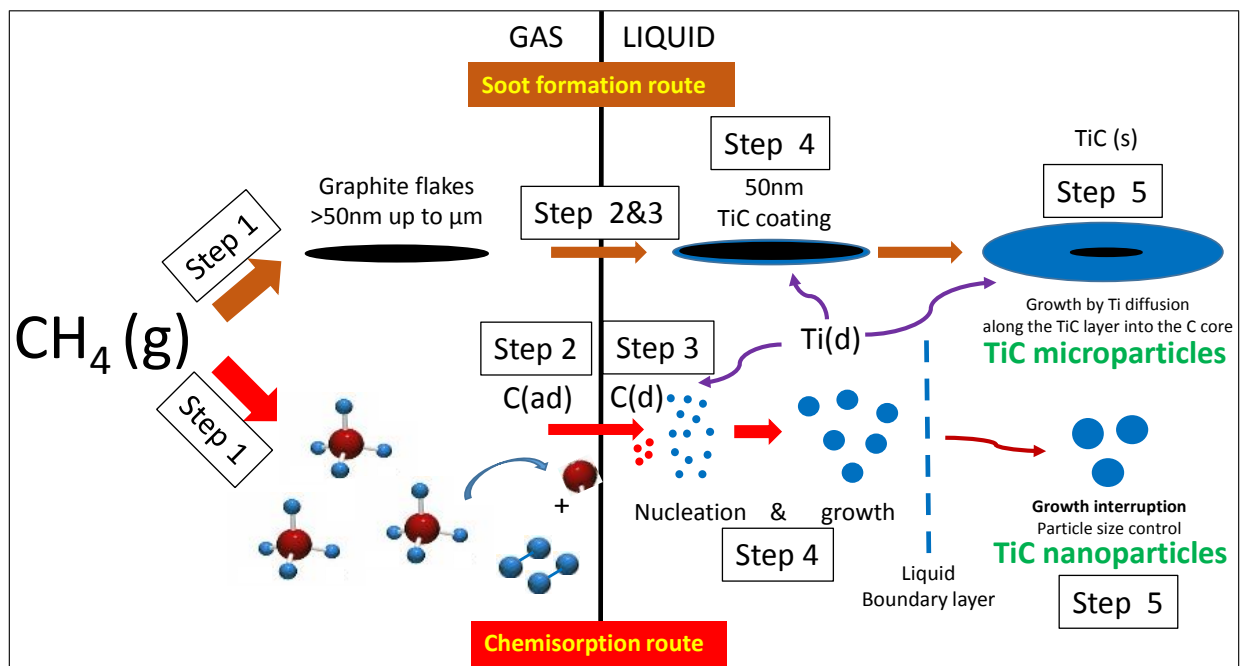

Figure 9. Possible routes for the decomposition and consumption of methane for TiC formation.

The soot formation route must be depressed and it is the focus occupies our efforts in section 6. For what follows it assumed that its depression is successful and the chemisorption route is the only mechanism that occurs:

$$\frac{\partial}{\partial t}(wt\%TiC_{micro}) = R_{TiC\_micro} = \begin{cases} K_L \cdot \Delta wt\%(Ti) = K_L \cdot \{wt\%(Ti)_{bulk} - wt\%(Ti)_{int}\} \\ K_L \cdot \Delta wt\%(C) = K_L \cdot \{wt\%(C)_{int} - wt\%(C)_{bulk}\} \end{cases} \quad (7)$$

The determination of the reactant that limits the reaction rate (carbon or titanium) and the calculation of the global mass transfer liquid coefficient (K_L) are required to propose a kinetic expression in (4). It is reasonable to believe the reaction is happening in the liquid boundary layer and not in the gas because the evaporation of both aluminum and titanium is negligible (melting points of 2327°C and 3260°C respectively). The chemisorption route has been initially proposed as a hypothesis. Questions to answer are:

(1) Is the chemisorption route feasible?

(2) What is the limiting step in the chemisorption route?

(3) What is the kinetic expression for the TiC formation?

2.1.4. Particle size control and gas-liquid dispersion

The proposed mechanism suggests that the TiC nuclei grow in size until they eventually exit the boundary layer. Outside of the boundary layer, the particles stop growing because the liquid bulk concentration of dissolved carbon is lower than its equilibrium value. We call the exact event that describes the particle detachment from the liquid boundary layer the *growth interruption mechanism* (GIM). The particle size produced by this mechanism in the liquid boundary layer is given by next expression:

$$R_{pF} = R_{pnuclei} + \int_0^{t_F} v_{growth} dt \quad (8)$$

Based on the above, it is concluded that the particle size can be controlled by monitoring its growth time, nucleus size and growth rate in the boundary layer. The questions to answer in this section are:

(1) How does the particle nucleation happen?

(2) How does the particle growth happen?

(3) How short is the particle growth time so nanoparticles are produced?

(4) How does the particle detach from the bubble interrupting its growth?

(5) What processing parameters need to be controlled and how are they calculated?

(6) Can the nanoparticles be produced with the 2nd generation of the gas-liquid in-situ method (static tube)? Or only the 3rd generation is suitable (stirred tank)?

(7) How does the mean bubble particle size, the gas volume fraction in the melt and the specific gas-liquid interface change with the processing parameters?

2.1.5. Fluid dynamics considerations

A good gas-liquid dispersion (high 'a') can be achieved only under a high turbulent mixing regime [39, 40]. An effective gas-liquid dispersion promotes the decrease of the bubble size, the increase of the gas-liquid reaction interface and enhances the mass transfer coefficient for the production of TiC. The high shear stresses of the turbulent flow on the bubble interface promote the GIM and control the TiC particle size below 100nm. High contents of dissolved titanium, Al₃Ti particles and the synthesized TiC nanoparticles may increase the melt viscosity promoting pseudo plastic thinning behavior[40, 41], creating liquid stagnant areas and low turbulence. Whereas the viscosity of pure aluminum is $10^{-4} Pa \cdot s$ at 1100ºC (see Figure 10), measured viscosities for Al-Ti melts go up to $0.1\ Pa \cdot s$[41]. A380 alloy with 20wt pct. of 15μm SiC particles[42] has a viscosity even in the range 1-6 $Pa \cdot s$.
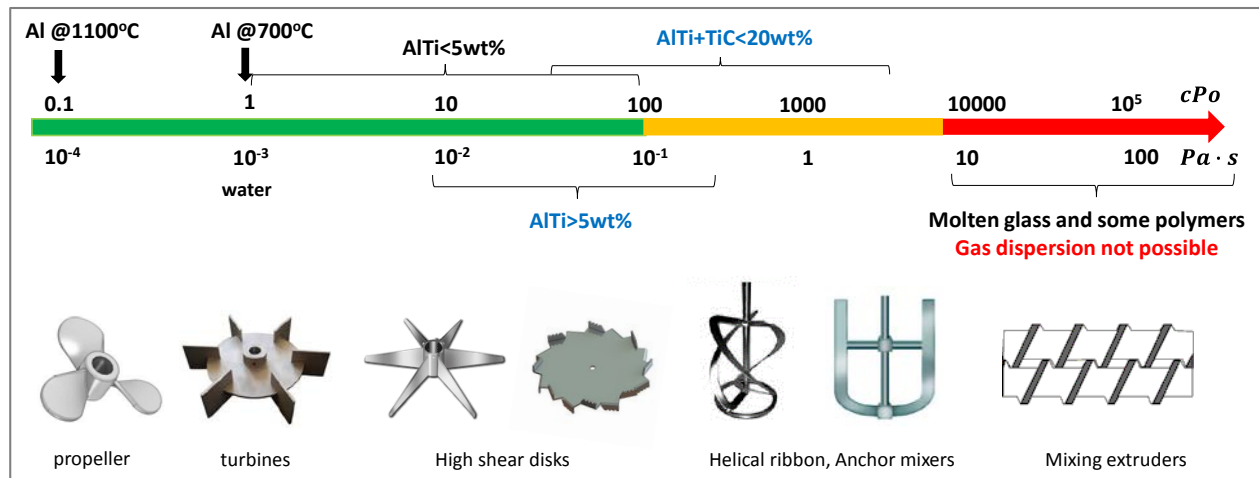

Figure 10. Allocation of fluids and mixing-shearing techniques in the viscosity spectrum [37, 39, 43].

In this section we develop the necessary understanding in order to answer the following questions:

(1) What is the impeller-crucible geometry that will maintain a fully mixed crucible under a high turbulent regime for a very viscous liquid?

(2) What is the impeller rotation speed that will maintain a fully mixed crucible under a high turbulent regime for a very viscous liquid?

2.1.6. Gas kinetics and control of Soot formation

As indicated in Figure 9, it is imperative to understand the dynamics of soot formation and apply mechanisms to suppress it. The gas flows along the hollow shaft before being bubbled into the melt by means of the rotating impeller. The shaft has a hot interval inside the furnace and it could potentially pirolyze producing soot. Figure 11 shows a schematic of the system and a picture detail of the tube.
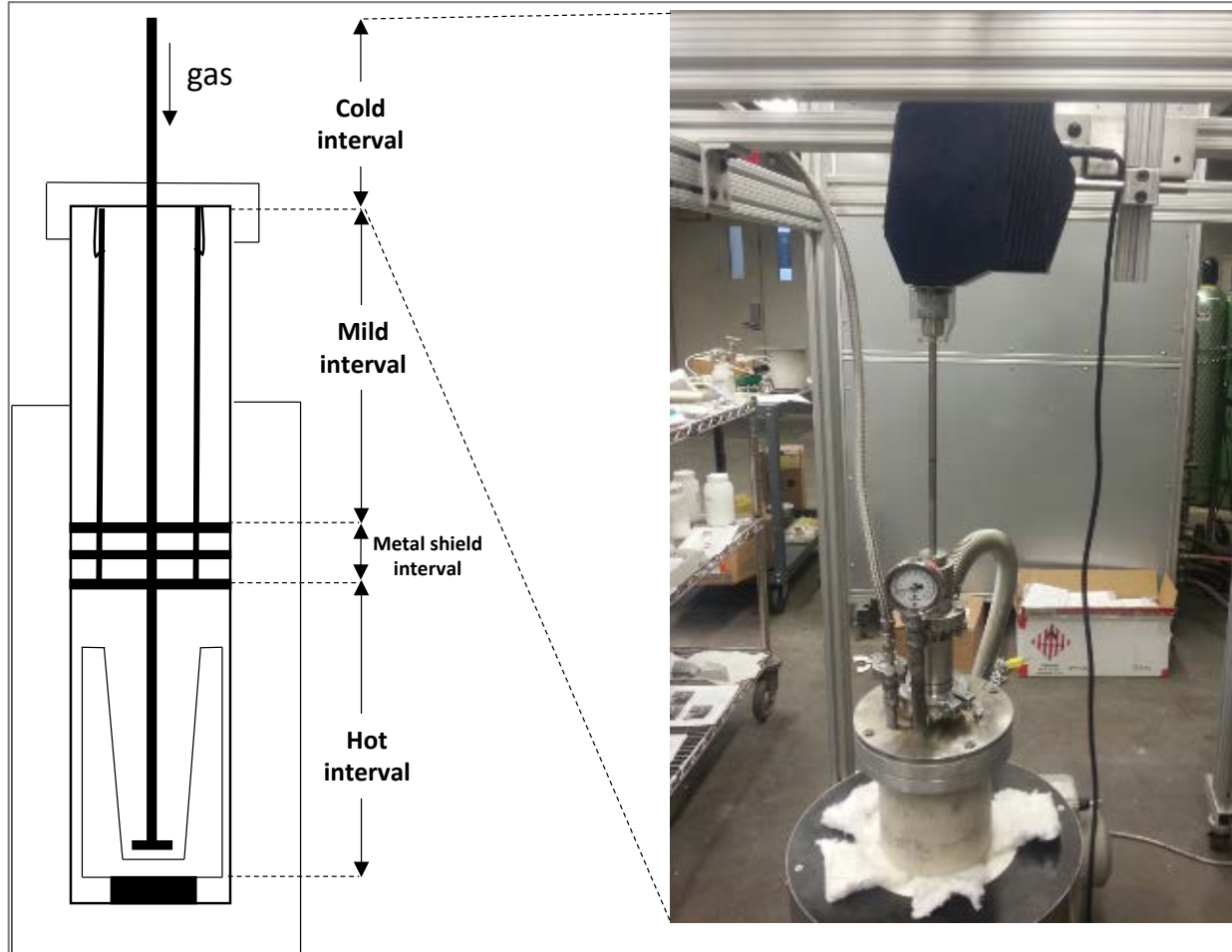

Figure 11. Schematic and picture of the tube cold interval to be modelled and simulated.

The homogeneous pyrolysis of methane is

$$CH_4(g) \leftrightarrow C(s) + 2H_2(g) \qquad\qquad \Delta G(\frac{J}{mol}) = 91863 - 111.2T \qquad (9)$$

The evolution of the methane decomposition in equilibrium, dependent on temperature and dilution percentage in argon, is illustrated in Figure 12.
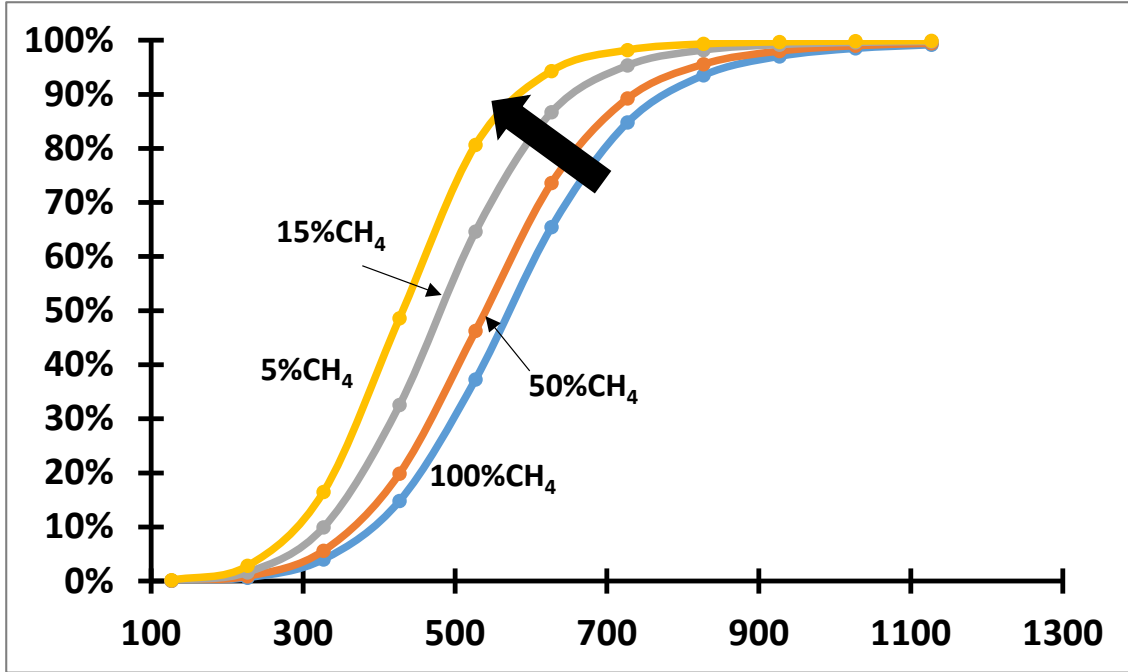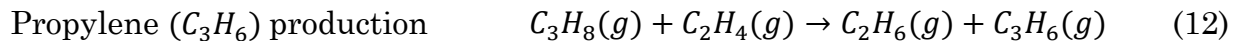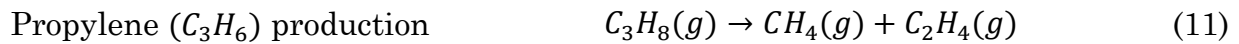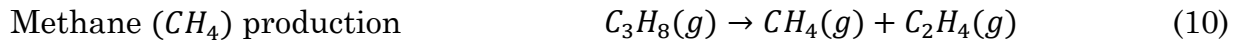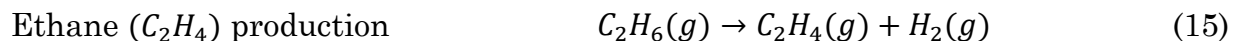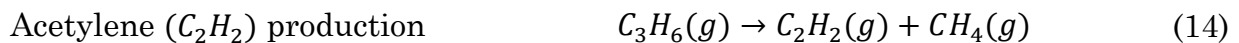
15

Figure 12. Evolution of the methane decomposition in equilibrium.

At 900-1000⁰C the methane is fully decomposed in equilibrium, what perhaps leads to the wrong conclusion that soot cannot be avoided However, the gas will spend a limited amount of time at high temperature (less than 1s). We will study the kinetics of decomposition to find a gas kinetic window in which the decomposition is suppressed. The homogeneous pyrolysis of methane follows a complex endothermic mechanism [44, 45] as it is shown below:
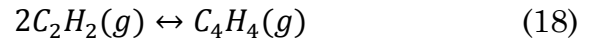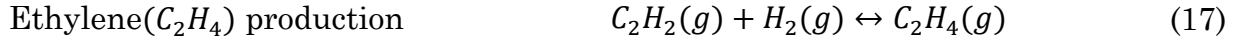
Propane pyrolysis

Methane (CH_4) production	$C_3H_8(g) \rightarrow CH_4(g) + C_2H_4(g)$	(10)
Propylene (C_3H_6) production	$C_3H_8(g) \rightarrow CH_4(g) + C_2H_4(g)$	(11)
Propylene (C_3H_6) production	$C_3H_8(g) + C_2H_4(g) \rightarrow C_2H_6(g) + C_3H_6(g)$	(12)

Propylene pyrolysis

Ethylene production(C_2H_4)	$2C_3H_6(g) \rightarrow 3C_2H_4(g)$	(13)
Acetylene (C_2H_2) production	$C_3H_6(g) \rightarrow C_2H_2(g) + CH_4(g)$	(14)
Ethane (C_2H_4) production	$C_2H_6(g) \rightarrow C_2H_4(g) + H_2(g)$	(15)

Methane and/or acetylene pyrolysis

Acetylene (C_2H_2)production	$CH_4(g) \leftrightarrow C_2H_2(g) + 3H_2(g)$	(16)

16

| Ethylene(C_2H_4) production | $C_2H_2(g) + H_2(g) \leftrightarrow C_2H_4(g)$ | (17) |
| | $2C_2H_2(g) \leftrightarrow C_4H_4(g)$ | (18) |

Aromatics and solid carbon formation (soot)

Benzene (C₆H₆) production	$C_4H_4(g) + C_2H_2(g) \rightarrow C_6H_6(g)$	(19)
Solid carbon formation	$C_2H_2(g) \rightarrow 2C(s) + H_2(g)$	(20)
Solid carbon formation	$C_6H_6(g) \rightarrow 6C(s) + 3H_2(g)$	(21)
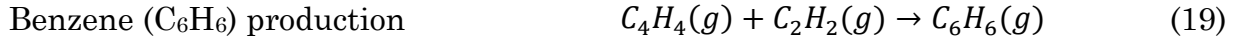
As reactions (16) through (21) suggest, methane polymerizes into heavier species, such as acetylene(C_2H_2) and benzene(C_6H_6), and these further pyrolyze to produce solid carbon ((20) and (21)). The formation of first soot and/or tar nuclei takes place in a few miliseconds when the right conditions exist [46]. Further growth occurs via nuclei agglomeration rather than single particle growth [47]. The left side in Figure 13 [48] shows several initial soot submicron particles and the right side [49] shows char particles heavily agglomerated in the 100μm range.
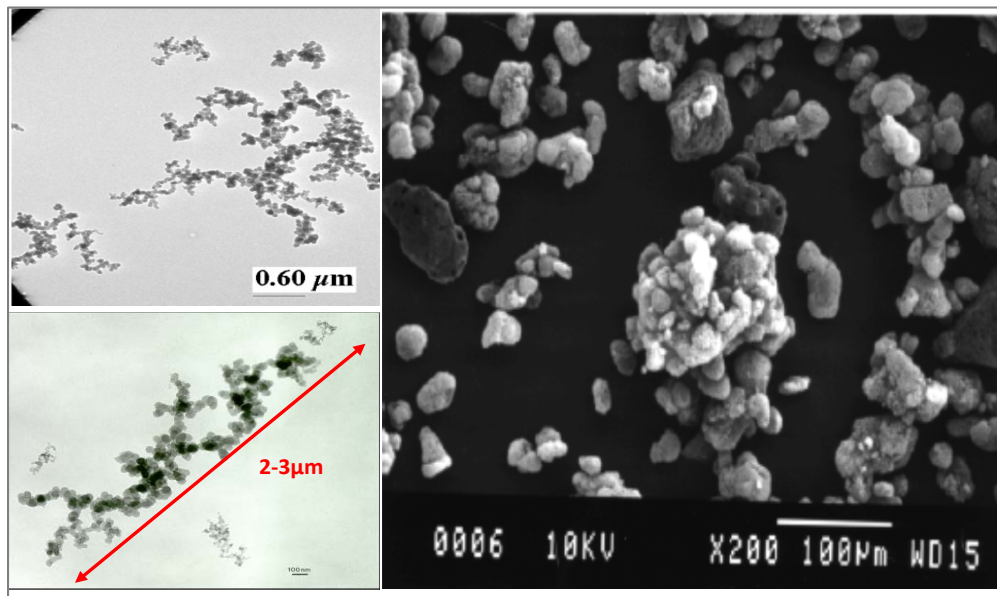

Figure 13. Few microns soot particles [48] (left) and char particles [49](right).

An optimization analysis will be performed in order to

(1) Demonstrate why methane(CH_4) has been selected among some other common different carburizing gases as propane(C_3H_8) or acetylene(C_2H_2).

(2) Calculate the appropriate argon/carburizing gas ratio

(3) Determine whether or not a gas preheating furnace is required

(4) Determine the impact of the hollow shaft thickness on controlling the soot formation

(5) Calculate the explosion safety requirements inside the furnace

2.1.7. Length and time scales

The different length and time scales at which the complex multi-physics phenomena occurs, are represented in Figure 14 and Figure 15. Whereas the experiment time can go up to 8 hours of time, each bubble released by the impeller nozzles doesn't last longer than 1 second. The bubbles break up frequency is several times per tenth of a second and the particles nucleation and growth might be happening in the milliseconds time frame. Also, the analysis of the process at the macro scale is modeled as a transient system whereas the mass transfer with reaction occurring inside the boundary layer during the bubble lifetime is considered to be in pseudo-stationary state. The reaction by itself, nucleation and growth, happens in the nanoscale. The different scales must be coupled in the final model.
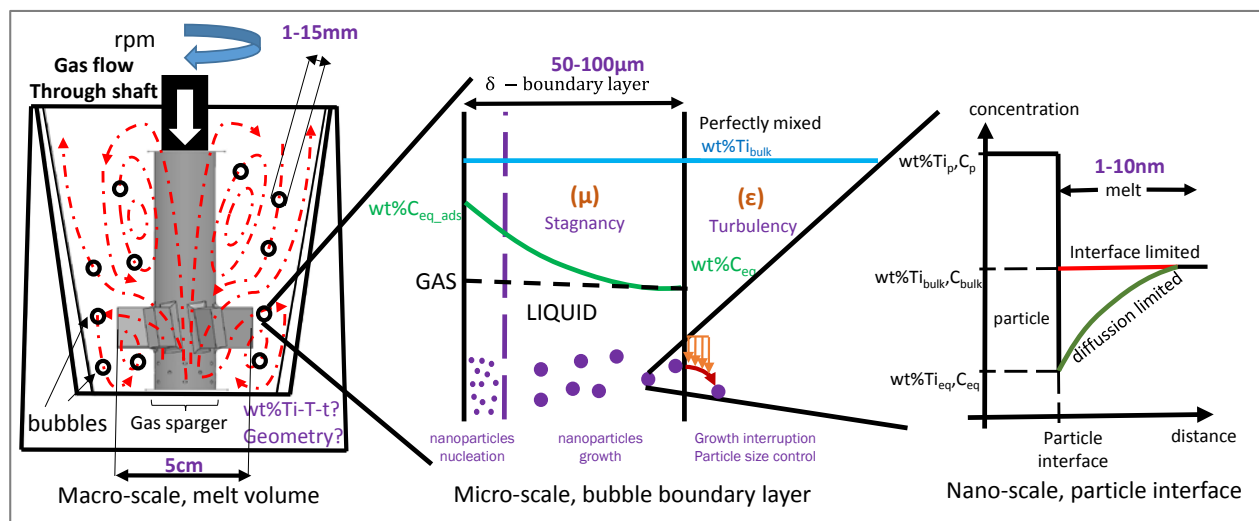

Figure 14. Multiphysics phenomena description happening at the different length scales.
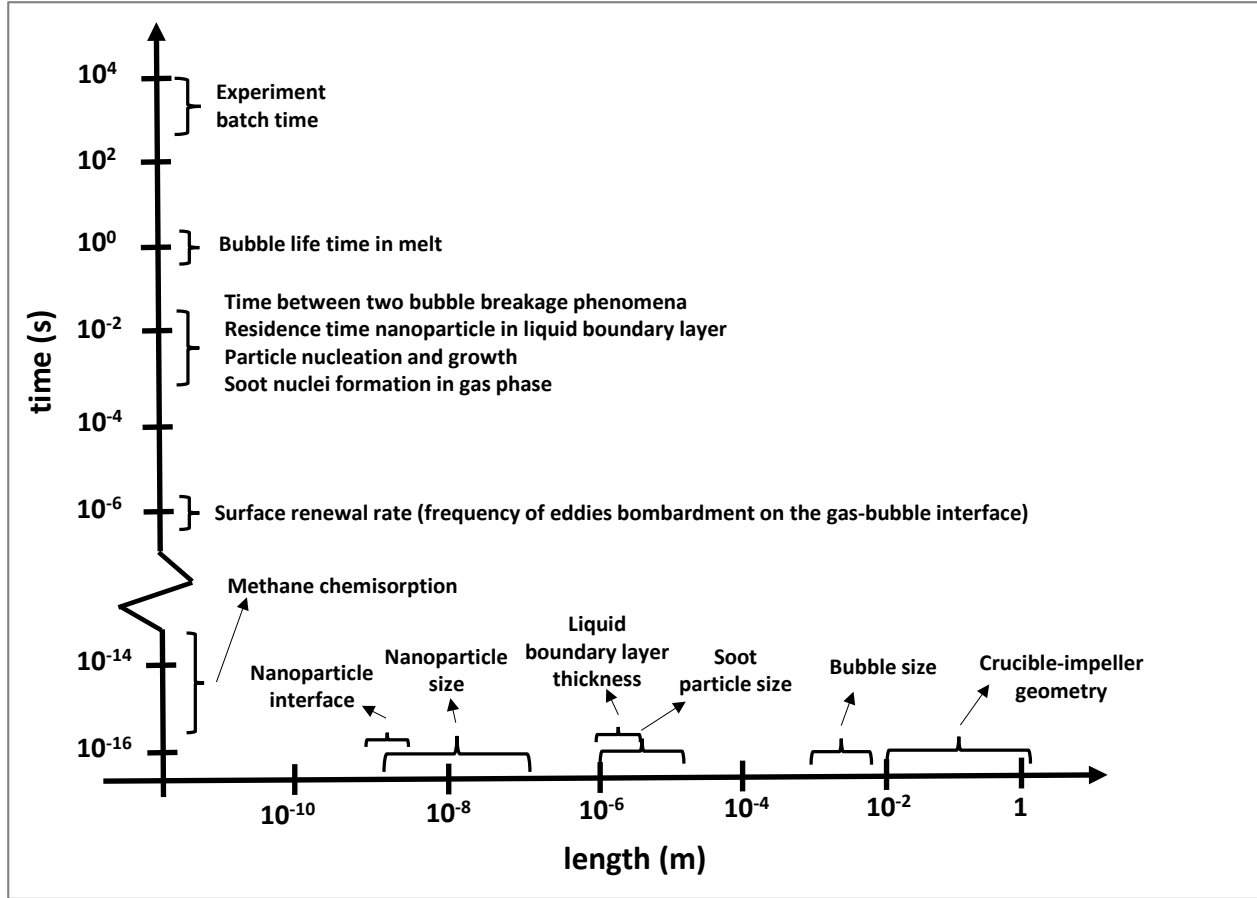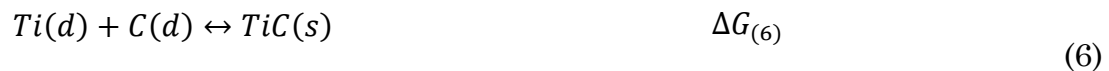
Figure 15.Length and time scales of the generation 3 gas-liquid in-situ method.

2.2. Thermodynamic Considerations

2.2.1. Thermodynamic operation window for TiC formation

In what follows the standard state of the metal will be pure liquid. The thermodynamic operation window (i.e., alloy composition vs. temperature) in which the metal carbides will form and be stable is of major importance. It can be determined by studying the metal carbide displacement reaction. The reactions to be compared are:

$$Ti(d) + C(d) \leftrightarrow TiC(s) \qquad\qquad \Delta G_{(6)} \qquad\qquad (6)$$

$$\frac{4}{3}Al(l) + C(d) \leftrightarrow \frac{1}{3}Al_4C_3(s) \qquad\qquad \frac{1}{3}\Delta G_{(22)} \qquad\qquad (22)$$

19

$$Ti(d) + \frac{1}{3}Al_4C_3(s) \leftrightarrow TiC(s) + \frac{4}{3}Al(l) \qquad \Delta G_{(4)} = \Delta G_{(6)} - \frac{1}{3}\Delta G_{(22)} \qquad (4)$$

In reactions 4, 6 and 22 the titanium in diluted state *(Ti(d))* competes against pure liquid aluminum *(Al(l))* to capture the carbon atoms and form the metal carbide. It is easily concluded from the Ellingham diagram applied to carbides formation in Figure 16 that TiC is thermodynamically more stable than aluminum carbide. Data in Figure 16 has been taken from [16, 50, 51]. However, Ellingham diagram shows stability of metal carbides produced from the pure elements Ti and C and both Ti and C are diluted in the molten aluminum. The the TiC stability will depend on the Ti and C activity in the melt, i.e. the melt composition. The carbon is canceled in (4) by substracting (22) from (6) so its activity does not play a role in the displacement reaction. The Van't Hoff equation [52] for the displacement reaction dictates that at equilibrium:

$$\Delta G_4 = \Delta G_4^0 + RTlnK_a = 0$$

$$\Delta G_4^0 = -RTlnK_a = -RTln\left(\frac{a_{TiC} \cdot a_{Al}^{4/3}}{a_{Ti} \cdot a_{Al4C3}^{1/3}}\right)$$

$$as\ a_{TiC} = a_{Al4C3} = 1$$

$$\Delta G_4^0 = -RTln\left(\frac{a_{Al}^{4/3}}{a_{Ti}^{a/b}}\right) where\ a_i = \gamma_i(T, X_i) \cdot X_i$$

$$-\frac{\Delta G_4^0}{RT} = lnK_a = ln\frac{[\gamma_{Al}(X_{Al}, T) \cdot X_{Al}]^{4/3}}{[\gamma_{Ti}(X_{Ti}, T) \cdot X_{Ti}]}$$

$$and\ solving\ for\ lnX_{Ti}$$

$$lnX_{Ti} = \frac{b}{a}\left(\frac{\Delta G_4^0}{RT} + \frac{4}{3}ln\gamma_{Al} + \frac{4}{3}lnX_{Al} - \frac{a}{b}ln\gamma_{Ti}\right)$$
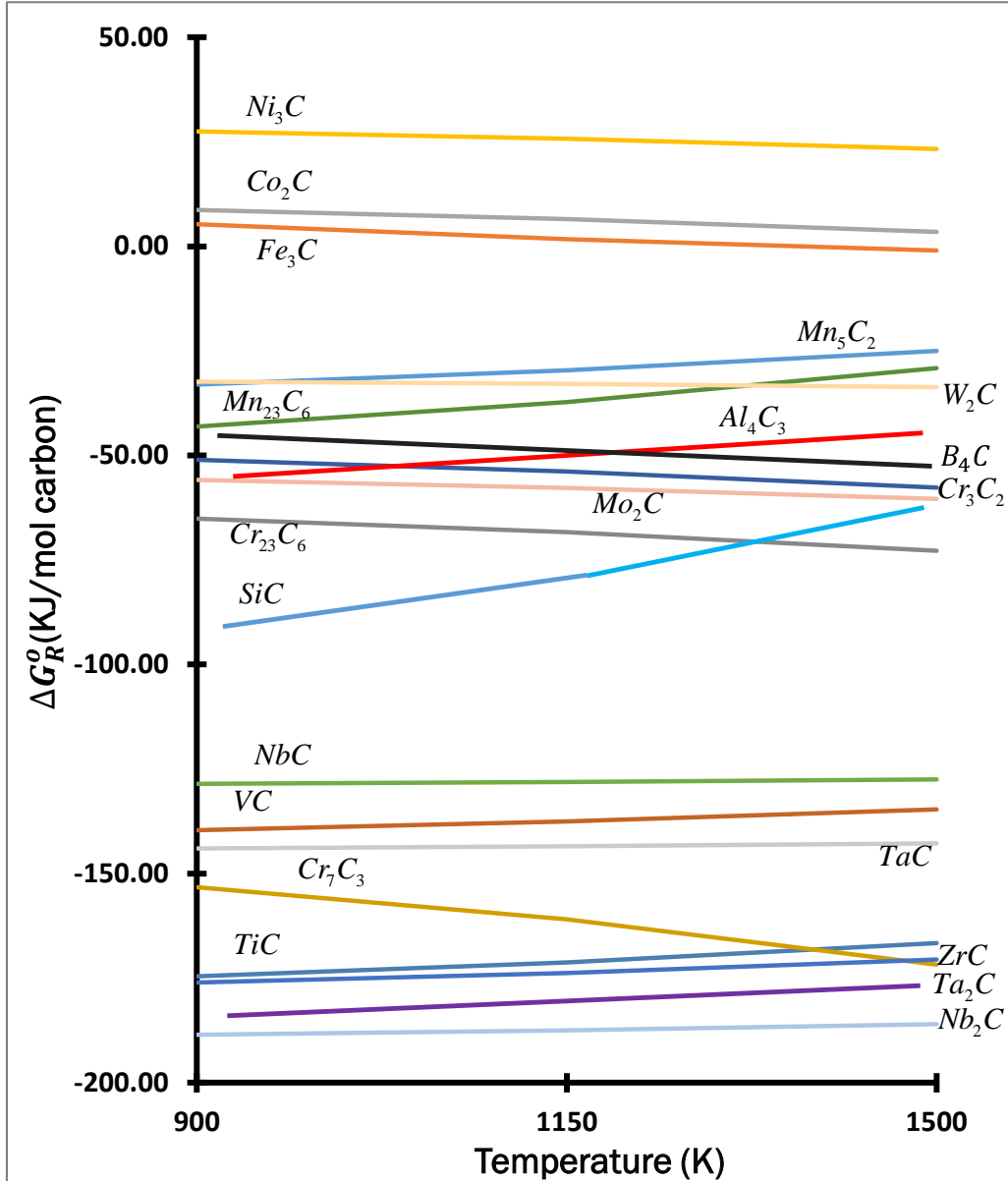
Figure 16. Ellingham diagram for carbide formation.

For a two-component mixture $X_{Al} = 1 - X_{Ti}$, and

$$ln\frac{X_{Ti}}{(1 - X_{Ti})^{4/3}} = \left(\frac{\Delta G_4^0}{RT} + \frac{4}{3}ln\gamma_{Al} - ln\gamma_{Ti}\right) \tag{23}$$

In order to plot this equation, the activity coefficients of aluminum and titanium in a dilute aluminum-titanium alloy are required. The activity coefficients of aluminum is calculated assuming Raoultian solutions and the activity coefficients of titanium is calculated assuming Henryan diluted solutions. For $ln\gamma_{Ti}$:

$$\frac{X_{Ti}}{(1 - X_{Ti})^{\frac{4}{3}}} \approx X_{Ti}$$

$$X_{Ti} = \frac{\frac{wt\%Ti}{MW_{Ti}}}{\frac{wt\%Ti}{MW_{Ti}} + \frac{(100 - wt\%Ti)}{MW_{Al}}} = \frac{wt\%Ti \cdot MW_{Al}}{100 \cdot MW_{Ti}} \qquad \Bigg| \quad for\ X_{Ti} \to (Henryan\ assumption))$$

$$ln\gamma_{Ti} = ln\gamma_{Ti}^{H}$$

And assuming the Raoultian state for aluminum, $ln\gamma_{Al} = 0$, and equation (22) results in:

$$wt\%Ti = \frac{100 MW_{Ti}}{MW_{Al}} exp\left(\frac{\Delta G_4^0}{RT} - ln\gamma_{Ti}^{H}\right) \qquad (24)$$

In which [9] $ln\gamma_{Ti}^{H} = \frac{-13639}{T} + 4.55$

ΔG_4^0 is calculated taking into account the enthalpies of reactions 6 and 22 (see [9])

$$\Delta G_6^0 = 4.184\left(-45200 - 0.23 lnT + 0.11 \cdot 10^{-3}T^2 + 0.74 \cdot \frac{10^5}{T} + 4.96T\right) - 16234 + 8.368T$$

$$\Delta G_{22}^0 = -89611 + 32841T$$

The expressions for ΔG_4^0 and $ln\gamma_{Ti}^{H}$ are introduced in equation 24 resulting in a constant value of wt%.Ti=0.5 independent on temperature. It can therefore be stated that:

TiC stable in molten Al if wt pct.Ti(d) > 0.5

A vertical line, referred as "Line 1", is plotted at wt pct.Ti=0.5 delimiting the TiC and Al$_4$C$_3$ stability regions in the Al-Ti phase diagram in Figure 17. A horizontal line, referred as "Line 2", is introduced delimiting the maximum furnace temperature at T=1050⁰C. Finally attention is given to the fact that in the binary phase domain (Al(l) + Al$_3$Ti(s)) the total wt pct.Ti given by the horizontal axis is the sum of wt pct.Ti (d) + wt%.Ti$_{Al3Ti}$. A third line ("Line 3") needs to be drawn delimiting the region in which wt%.Ti (d) >0.5. For the plot of Line 3 next mass balance is calculated:

$$wt\%.Ti(d) \geq 0.5 = \frac{Ti\ dissolved\ in\ liquid}{liquid} = \frac{wt.\%Ti_{tot} - wt\%.Al_3Ti \cdot wt.\%Ti_{Al3Ti}}{1 - wt\%.Al_3Ti} \qquad (25)$$

Being:

$$wt\%.\,Ti_{Al3Ti} = \frac{MW_{Ti}}{3MW_{Al} + MW_{Ti}} 100 = 37\% \tag{26}$$

$$wt\%.\,Al_3Ti = \frac{wt\%Ti_{tot} - wt\%Ti_{liquidus}(T)}{37 - wt\%Ti_{liquidus}(T)} \quad \text{(Lever rule)} \tag{27}$$

The variable $wt\,pct.\,Ti_{tot}$ is solved in equation 25 as a function dependent on the temperature and plot in Figure 17 as "Line 3".
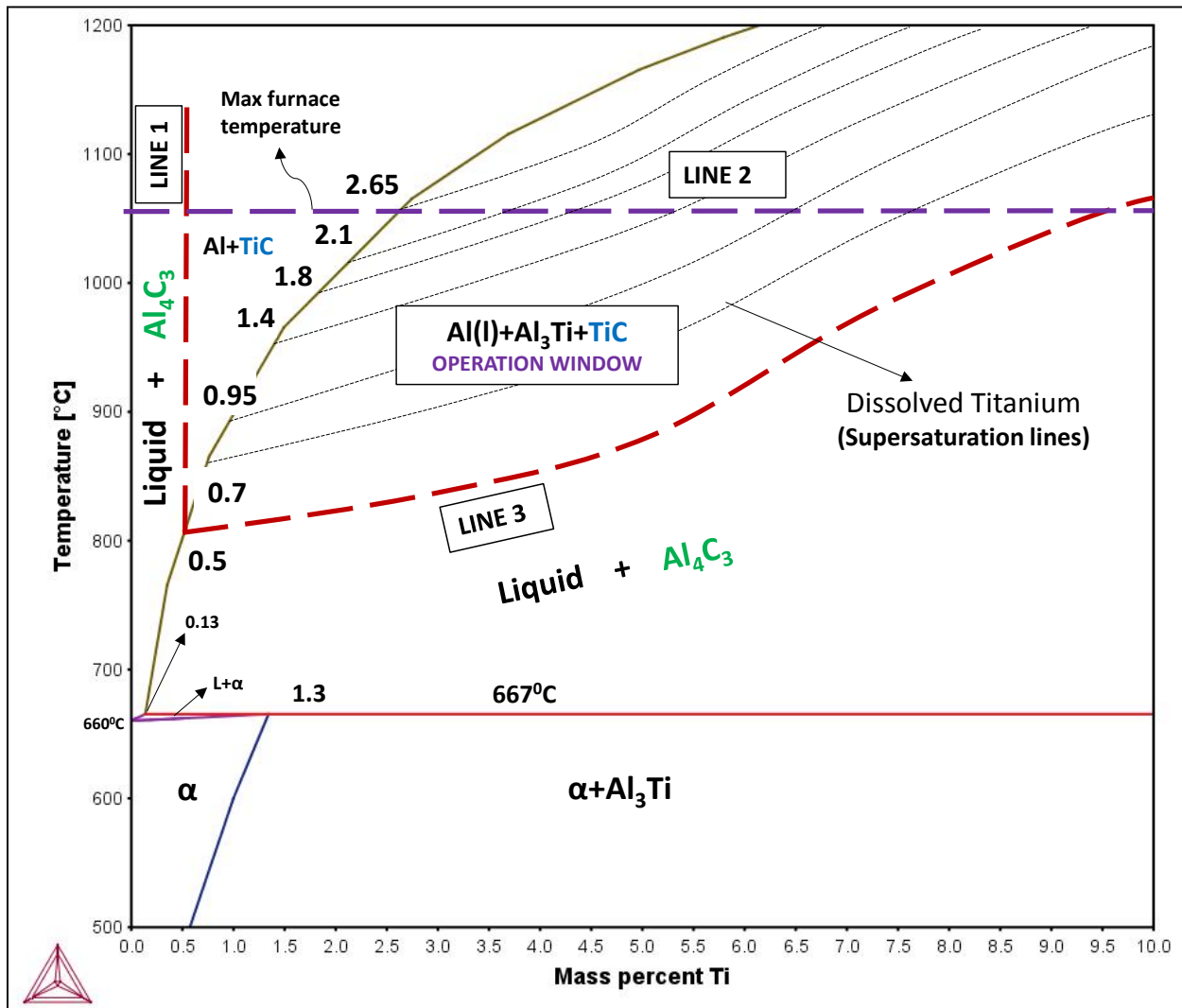

Figure 17. TiC stability window in the Al-Ti phase diagram.

If equation 25 is equated to $wt\%.\,Ti(d)$ values from 0.7 to 2.65, the different dissolved titanium supersaturation lines can be plot indicating the chemical potential of the melt for the TiC synthesis reaction to occur.

2.2.2. Al₃Ti intermetallics stability

From Figure 17 it is noted that most of the titanium is in form of Al₃Ti intermetallics for high wt pct.Ti values. An extreme example is point (9.5 pct.Ti, 1050⁰C) for which 9wt pct.Ti is contained in the Al₃Ti intermetallics. For the TiC to form in this region the Al₃Ti intermetallics have to continuously dissolve so the melt progresses along the path in Figure 7. Displacement reaction (5) is analyzed.

$$TiAl_3(s) + C(d) \leftrightarrow TiC(s) + 3Al(l) \tag{5}$$
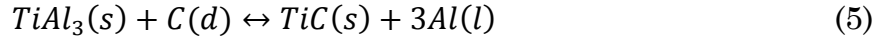
The standard states for this section are Raoultian for the aluminum and Henryan 1wt pct. for the titanium and the carbon. Van't Hoff equation [52] states that at equilibrium:

$$\Delta G_5^0 = -RTlnK_{a5} = -RTlna_c^{-1} = RTlna_c \tag{28}$$

From [9]

$$\Delta G_5^0 = 224279 - 53.608T - 0.460 \cdot 10^{-3}T^2 - 3.096 \cdot \frac{10^5}{T} + 0.962TlnT$$

It is clear from (28) that the competition between TiC and TiAl₃ depends only on the activity of carbon in the melt and it is independent of the activity of titanium.

For the one percentage standard state, a_c = wt pct.C [52], and so equation 28 yields

$$RTlna_c = RTlnwt\%C$$

$$RTlnwt\%C = 224279 - 53.608T - 0.460 \cdot 10^{-3}T^2 - 3.096 \cdot 10^5/T + 0.962TlnT$$

$$\text{wt\%C} = \exp\left(\frac{224279 - 53.608T - 0.460 \cdot 10^{-3}T^2 - 3.096 \cdot 10^5/T + 0.962TlnT}{RT}\right) \tag{29}$$

Equation 29 calculates the carbon concentration dissolved in the aluminum melt for which equation 28 is in equilibrium. If the real wt pct.C(d) is lower than the value calculated by equation (29), then TiAl₃ is stable and TiC doesn't form but if it is higher, then TiAl₃ is unstable and TiC forms. The carbon content in solution is difficult to determine accurately, but its maximum value in saturated state and its minimum value in equilibrium state can be calculated.

Saturated carbon content

From [53], the carbon solubility (assuming Henryan solution) in the melt is

$$X_{C(d)} = 294\exp\left(-\frac{19370}{T}\right)$$

and keeping in mind that for a Henryan solution

$$X_c = \frac{wt\%C \cdot MW_{Al}}{100 \cdot MW_C}$$

The carbon solubility is rewritten as follows

$$wt\%C_{sat} = \frac{100 \cdot MW_C}{MW_{Al}} 294\exp(-\frac{19370}{T}) \tag{30}$$

Dissolved carbon in equilibrium

The minimum value at the equilibrium state is given by equation 6:

$$Ti(d) + C(d) \leftrightarrow TiC(s) \qquad K_{eq} \approx 10^{22} \tag{31}$$

Van't Hoff equation [52] gives, in equilibrium,

$$\Delta G_{29}^0 = -RTlnK_{a10} = -RTln\frac{1}{wt\%Ti \cdot wt\%C}$$

From [9]

$$\Delta G_{29}^0 = -163382 + 80.347T + 0.460 \cdot 10^{-3}T^2 + 3.096 \cdot \frac{10^5}{T} - 0.962TlnT$$

being finally
$$wt\%C_{eq} = \frac{1}{wt\%Ti}\exp\left[\frac{\Delta G_{R10}^0}{-RT}\right]$$

$$wt\%C_{eq} = \frac{1}{wt\%Ti}\exp(9.664 + 5.533 \cdot 10^{-5}T - 1.965 \cdot \frac{10^4}{T} + 3.724 \cdot \frac{10^4}{T^2} - 0.116lnT) \tag{32}$$

If Eqs. (29), (30) and (32) are plotted vs. temperature for wt%.Ti(d)=0.5 and wt%.Ti(d)=10 in Figure 18. TiAl₃ is unstable and TiC will form as long as a continuous surplus

2.2.3. Conclusions

A thermodynamic operation window for synthesizing titanium carbide in aluminum (i.e., wt pct.Ti vs. temperature) has been quantitatively calculated.

A quantitative thermodynamic analysis of the stability of titanium carbide relative to the stability of TiAl₃ has been performed. It is concluded that TiAl₃ continuosly dissolves releasing titanium into the melt that transforms into TiC in the bubble boundary layer of carbon is provided to the bubble melt vicinity.
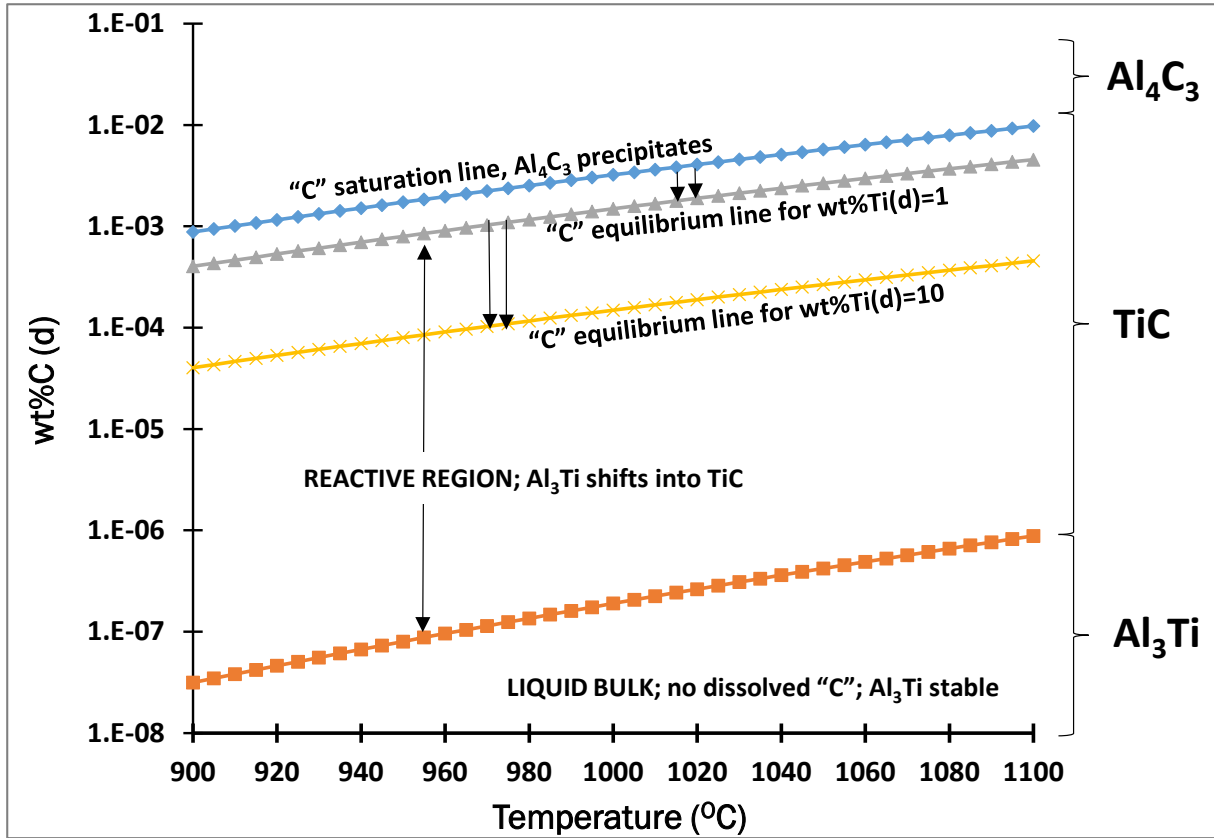
Figure 18. Thermodynamic phase stability chart for the TiAl₃-TiC displacement reaction.

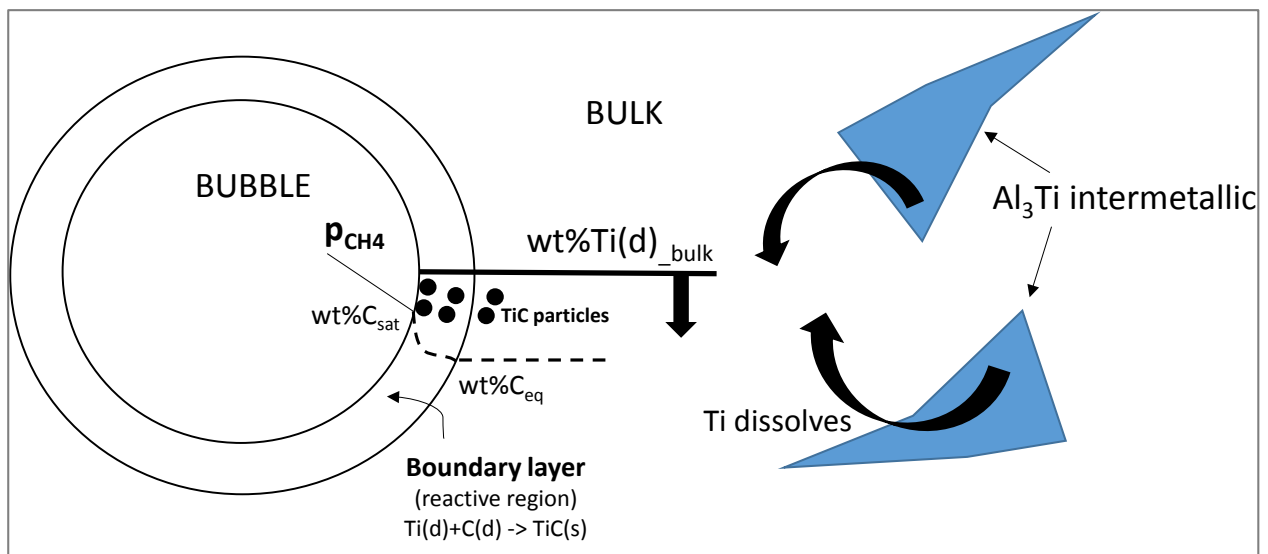Figure 19 presents the melt mass transfer dynamics during the path followed by the melt in Figure 7.

Figure 19. Dynamics for melt Ti content decrease after Figure 17 and Figure 18

2.3. Kinetic Considerations

Figure 20 sketches the different reaction steps, assumed the two films model is valid, that consecutively take place during the gas-liquid-solid reaction at the bubble-melt interface. It is considered that the steady state is instantaneously reached in both films. The boundary layer thicknesses are set by the external melt and gas fluid conditions. These are: (1) soot formation, (2) methane diffusion across the gas boundary layer, (3) methane chemisorption at the gas-liquid interface, (4) carbon and titanium atoms diffusion across the liquid boundary layer and (5) TiC reaction of formation.
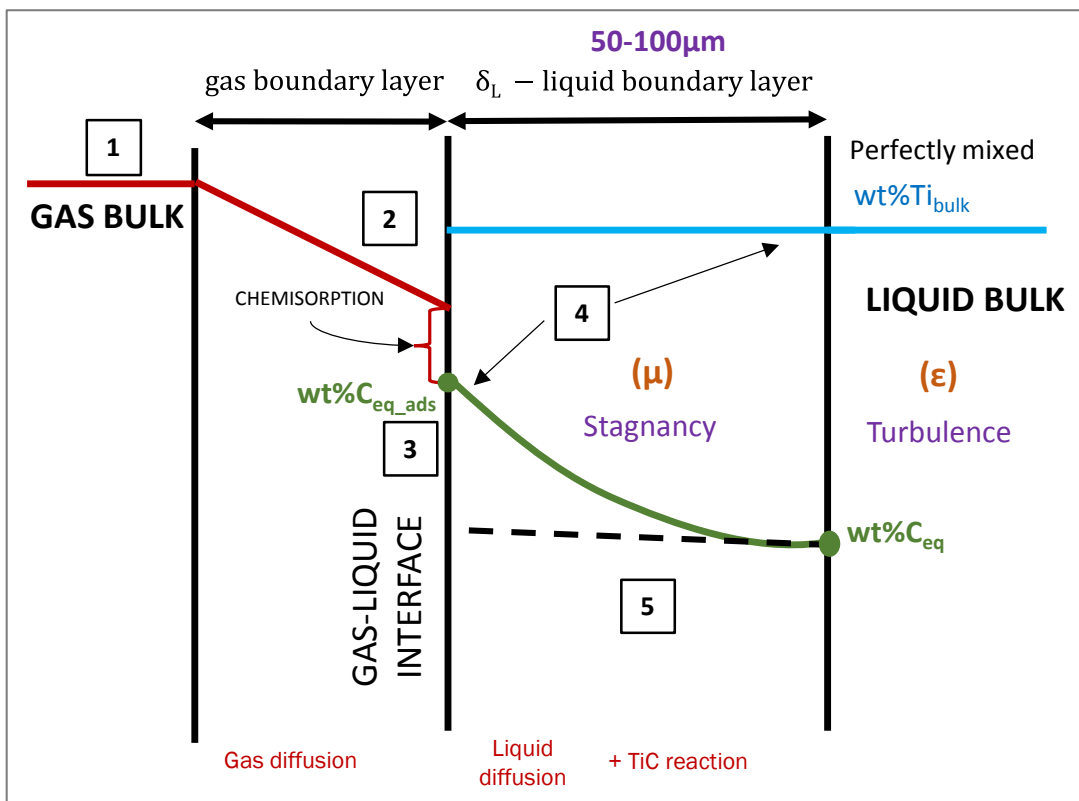

Figure 20.Two film model for the bubble-melt interfacial gas-liquid TiC reaction

2.3.1. Analysis of reaction steps and limiting step

Soot formation (step 1, to be avoided) is treated separately in section 6. Methane molecules diffusion across the gas boundary layer **(step 2)** is driven by 1st Fick's law:

$$J_{CH4} = -D_{CH4-Ar}(x,t)\frac{\partial X_{CH4}(x,t)}{\partial x}; being\ D_{CH4-Ar}[m^2 \cdot s^{-1}] \approx 2.5 \cdot 10^{-4} \qquad (33)$$

Chemisorption of methane (step 3) on the molten aluminum surface is a complex unexplored process that is next treated in depth. The most general adsorption process englobes the physisorption and chemisorption (see Figure 21). The physisorption consists of Van der Walls weak reversible bonds created between the gas molecule and the catalytic surface. The molecule can be desorbed applying heat. The chemisorption is a type of adsorption in which the adsorbed molecule chemically reacts with the catalytic surface producing intermediates that can dissolved into the catalyzer for further reaction (liquid catalyzers) or can react in the surface with others intermediates leading into a product that finally desorbs (solid catalyzers).
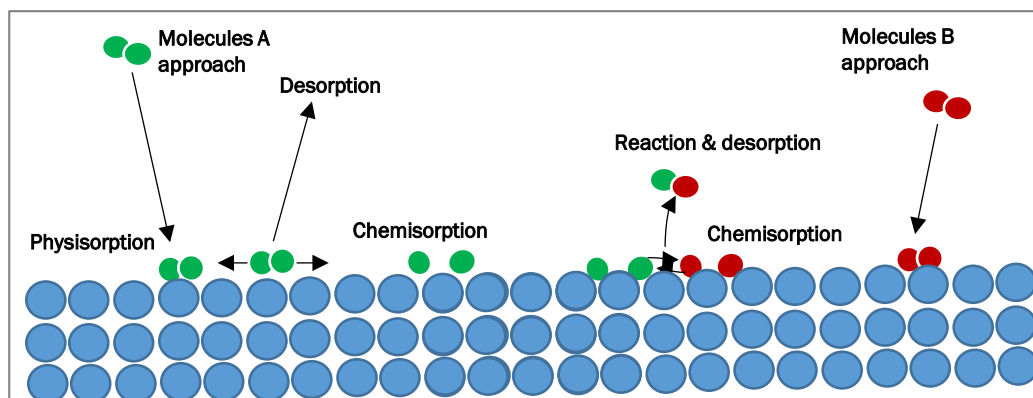

Figure 21. Physisorption (left) vs. Chemisorption (right) in a solid catalyzer

The typical energy profile for two different molecules 1 and 2 along its distance to the reactive surface is sketched in Figure 22, assumed attractive Van der Walls force (IVWF<0). It has three domains (1) Brownian motion domain (d>10nm), (2) Van der Walls forces domain (0.4<d<10nm) and (3) chemisorption domain (d<0.4nm). Those molecules with not enough energy get captured in the secondary minimum and physisorption occurs. With applied heat, the thermal energy of the molecule ($-k_B T/2$ for a 2D model) is high enough to liberate the molecule from the secondary minimum and desorbes. For chemisorption to occur, the activation energy must be overcome and only molecules with enough energy will be chemisorbed. The sticking probability concept is by this way introduced. It increases with the partial pressure, temperature[54] and decreasing activation energy. Therefore chemisorption rate of molecule 1 in Figure 22 will be very small in comparison with molecule 2 chemisorption rate. The activation energy of a molecule – surface pair depends on the affinity of both components of the pair and it is best modeled by molecule quantum dynamics, what it is out of the scope of this project. In the case of methane-aluminum chemisorption, the process implies the intermediates CH^{3+} and H^+ [54, 55] that follows next reactions:

$$CH_4(g) \leftrightarrow C(ad) + 4H(ad) \tag{34}$$

The chemisorption rate can be hence expressed as [19]:

$$R_{chemisorp} = c \cdot (2\pi MRT)^{-1/2} \left(P_{CH4,int} - \frac{wt.\%C_{int} \cdot (wt.\%H_{int})^4}{K_{34}} \right) exp\left(\frac{-E_a}{RT} \right) \tag{35}$$

In equation 35 'c' accounts for a constant related to the nature and activity of the chemisorption surface. The surface activity is related to specific surface area of chemisorption and the concentration of active sites.
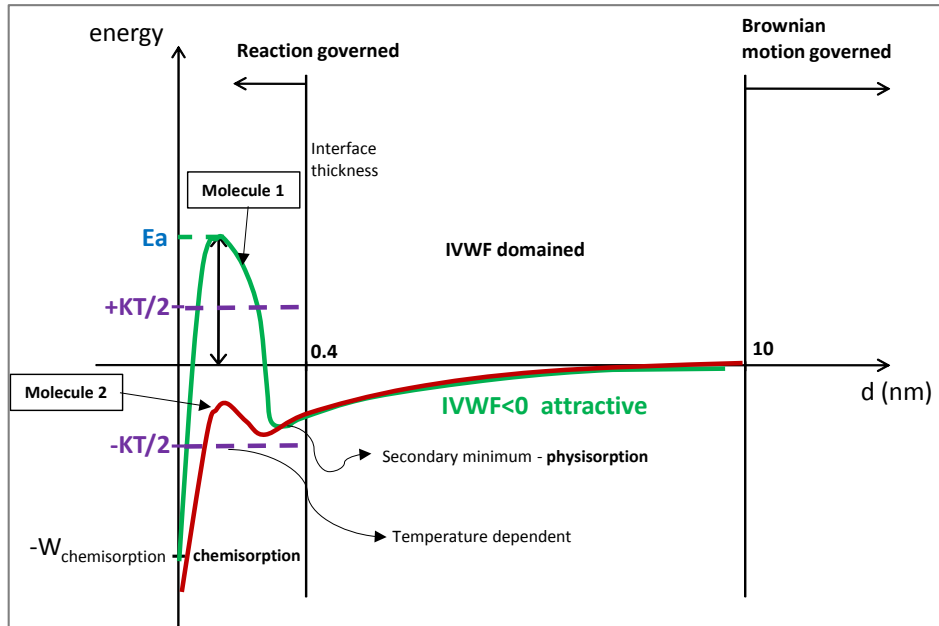

Figure 22. Atom energy evolution vs. interface distance.

The time scale for the molecules to impact the surface and react with it is in the order of 200fs [56].
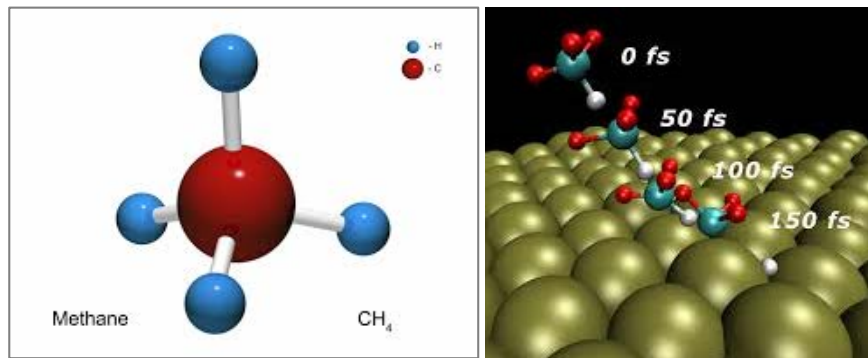

Figure 23. The methane molecule (left), time scale for chemisorption (right) [56]

Step 4 in the reaction process is the reactants diffusion across the melt for encountering and reaction. Given the orders of magnitude of the carbon and titanium concentrations in liquid solution (10^{-3} vs. 10^1 respectively) as well as the diffusion coefficients ratio.

$$\frac{D_{C-Ar}}{D_{Ti-Ar}} = \frac{R_{Ti^{4+}}}{R_{C^{4-}}} = \frac{0.76 \cdot 10^{-8}m}{0.26 \cdot 10^{-7}m} = 0.29$$

A constant titanium profile and a parabolic convex carbon profile are considered in Figure 20. 2nd Fick Law with reaction and no mass accumulation dictates the carbon concentration profile.

$$0 = D_{C-Al}(T)\frac{\partial^2 c_C(x,t)}{\partial x^2} + R_C \tag{36}$$

With $R_C = -R_{TiC}$ and in [14], $D_{C-Ar}(1000°C) = \frac{k_B T}{4\pi R_C \eta} = \frac{1.38 \cdot 10^{-36}}{4\pi \cdot 0.76 \cdot 10^{-8} \cdot 0.01} = 2.5 \cdot 10^{-8}\ m^2 s^{-1}$

Finally TiC is produced in step 5. The reaction affect also step 4 so it is included in equation 36 (term $R_C = -R_{TiC}$). It is considered a fast reaction so it is not the limiting step. Such statement can be based on the experimental work of Schweighofer and Kudela [57] based on the Al-AlN composites for the first generation of the gas-liquid in-situ method (Figure 1). We assumed AlN and TiC reactions are comparable in nature. They did an analysis of the influence of both temperature (reaction strength) and pressure (gas solubility, reactant availability) on the AlN synthesis rate. They detected two main reaction regimes:

(1) Surface reaction regime takes place for low pressure and high temperature. A dense AlN layer is produced on the gas-liquid interface.

(2) Volume reaction regime occurs for high pressure and low temperature conditions. A 3D network of ceramic phase progresses along the melt.

The existence of the surface reaction regime implies that the AlN reaction is very fast. In this case, the chemisorption step is limiting. Its kinetics follow equation 35 and it is removed from the present analysis. Also, the first generation of the gas-liquid in-situ method has no turbulence and thus no boundary layer. A third reaction regime, including the boundary layer effect for the third generation of the gas-liquid in-situ method, is included:

(1) Boundary layer reaction regime at low pressure and high temperature. Dispersed coarse particles are produced in the melt.

(2) Bulk reaction regime in the melt at high pressure and low temperature. Dispersed fine particles are produced in the melt.

We are working under normal atmosphere, so other than chemisorption (surface) limited regime, the reaction will be contained in the liquid boundary layer and the

bulk reaction regime is unlikely. In summary, two options will be examined: (1) the chemisorption limiting case, and (2) the carbon diffusion limiting case.

2.3.2. Chemisorption as limiting step

The chemisorption will be the limiting step if (1) the activation energy is very high or (2) the surface activity (constant 'c' in equation 35) is very low. The activation energy of methane chemisorption in molten aluminum is initially unknown. In solid catalyzers, a typical activation energy value for methane chemisorption in nickel and platinum is in the interval 0.5-1eV. This range value make it to be the limiting step in many chemical processes as the steam reforming or the Haber-Bosch process [55]. The possibility of using liquid metals instead of solid metals has been acknowledged by Steacie and Elkin [58] already in 1933 for molten zinc and methane and by several other authors more recently [58-61] with tin or lead as molten metals also with methane. Among the advantages of using liquid catalizers stand (1) the possibility of operating at low temperature (>300^{0}C) so soot does not form, (2) a higher specific surface area and thus higher activity of liquid surfaces, (3) continuous liquid surface renewal and no catalyzer deactivation, and finally (4) no use of precious metals like gold or platinum as the catalyzers. The second and third advantages imply a higher concentration of active sites and a rather smaller activation energy of chemisorption in a gas-liquid metal system in comparison with a gas-solid metal. The chemisorption may thus not likely be the limiting step in a gas-liquid metal system.

Oxygen poisoning of chemisorption

The oxygen impurity content in the bubbling gas can have a critical effect on the chemisorption rate. Its influence has been studied in detail by several authors for the case of Al-AlN composites and nitrogen atmosphere [19-21, 62] but there are no studies for the Al-TiC system and methane atmosphere. Competition between the N_2 and O_2 atoms at the molten metal surface occurs so a thin layer of a single row of oxygen atoms is adsorbed in the melt surface. This oxygen atoms layer occupies most of the surface active sites hindering the nitrogen chemisorption (Figure 24 left and 'c' constant in equation 35). This phenomena happens even at oxygen concentration values as low as parts per trillion. Main reason is the most favorable energy profile [19] of the oxygen molecule chemisorption (Figure 24 right) that has no activation energy. In summary, liquid surfaces have high adsorption activity and in systems containing water or organic liquids the chemisorption rate is high and not limiting. However, non-noble liquid metals like aluminum are prompt to suffer poisoning by oxygen chemisorption.
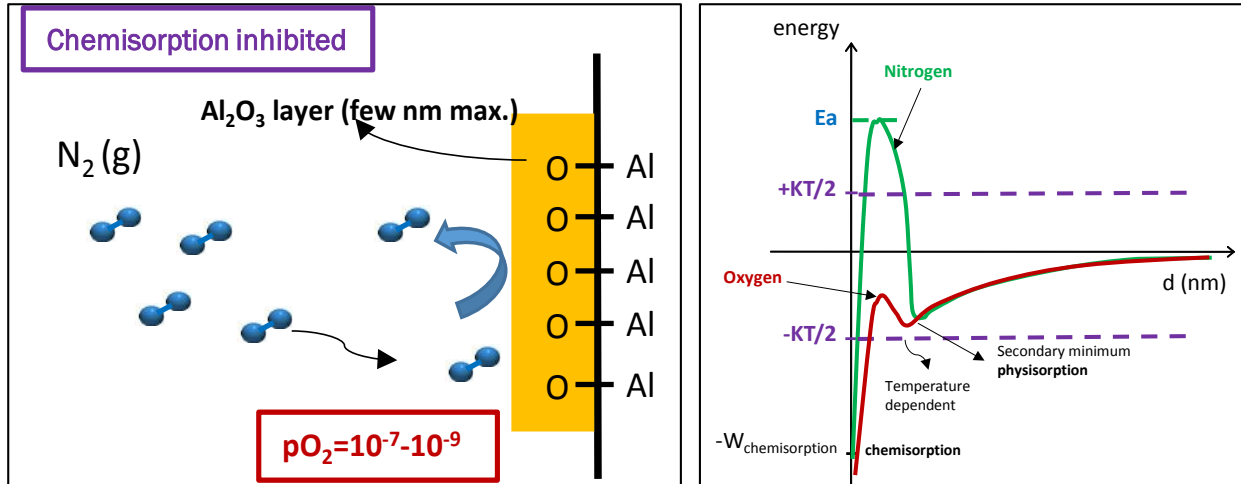
Figure 24. O_2 poisoning of N_2 adsorption (left) and chemisorption energy profile of N_2 and O_2 (right).

Volatile alloying elements

Daniel and Murthy [31, 32], mostly based on the work of Scholz and Greil [20, 21] for the first generation of the gas-liquid in-situ method, did an extraordinary review of the different existing reaction regimes for the Al-AlN composite. They include the use of volatile alloying elements to overcome the oxygen poisoning obstacle. Three process variables are identified:

  (1) Oxygen impurities in the atmosphere

  (2) Volatile alloying elements as Li, Mg, Na or Zn

  (3) Static or flowing atmosphere

Two different mechanisms were proposed for nitrogen chemisorption to occur in the presence of oxygen:

(1) First mechanism is called the direct nitridation [19-21, 63]. It describes the alloying element as an oxygen getter. It volatilizes in the gas boundary layer and combines with the oxygen cleaning the aluminum surface and hence enabling the direct contact between the methane molecules and molten metal surface.

(2) Second mechanism is the indirect nitridation mechanism [10, 57, 64, 65]. It defines the alloying element **as a catalyzer** that produces an intermediate compound between the alloying element and the nitrogen. It is Li_3N in the case of the lithium or Mg_3N_2 in the case of magnesium. This intermediate is produced in the cloud of volatilized alloying element, it gets grabbed by the liquid and once in the molten metal it evolves into AlN by solid-liquid reaction.

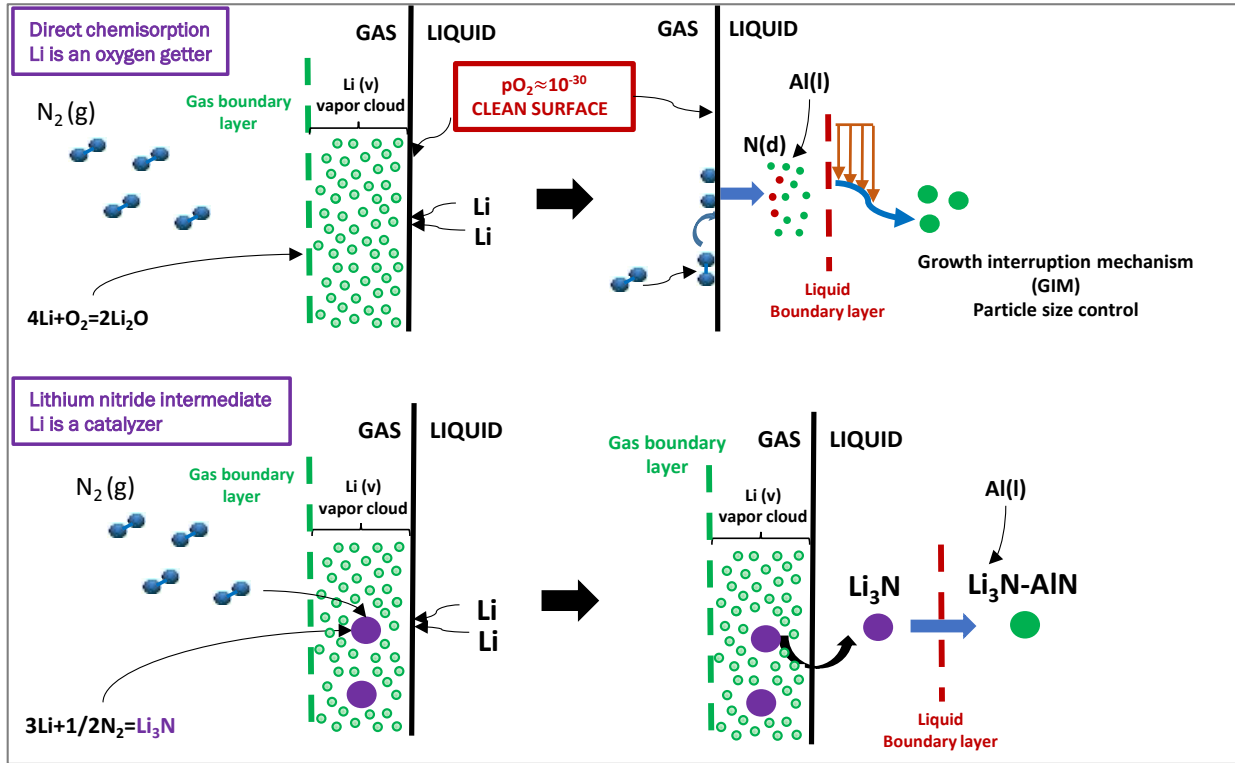 Figure 25 shows the two chemisorption mechanisms with lithium as an example.

Figure 25. Direct and indirect nitridation mechanisms with lithium as the oxygen getter.

Which mechanism occurs is uncertain. Li_3N is a strong stable component and its existence should be considered. For the case of Al-CH_4 chemisorption, Li_2C_2 is the most stable lithium carbide and possible intermediate. It dissociates at T>800^0C [66]so the catalyzing mechanism is not considered. **The incubation period** is another important concept included in the work of Scholz and Greil[20, 21] for generation 1 gas-liquid in-situ method. For a given value of oxygen impurities and a content of oxygen getter, the reaction rate (or the isothermal system weight change along the reaction time) is monitored. A typical set of curves is shown in Figure 26. An incubation period is necessary to consume the existing oxygen in the atmosphere so the chemisorption occurs and the reaction accelerates. It can get eventually out of control leading to the production of an AlN crust and total consumption of aluminum, what is called breakaway reaction. Both the incubation period and the breakaway point can be controlled by choosing the type of oxygen getter, its concentration and oxygen impurity in the gas as illustrated in Figure 26. Scholz and Greil [20] reduce the incubation period by a ratio of 6X for an aluminum melt at 1000^0C, 1atm and a nitrogen gas with 0.0003wt pct.O_2 and 0.0005wt pct.H_2O as impurities by including 2.3wt pct.Li as the oxygen getter instead of 2.5wt pct.Mg. The curves obtained in this way for the generation 1 gas-liquid in-situ method can only be used in geometrically similar systems, i.e., the ratios gas-liquid interface to gas volume and gas volume to

liquid volume must be constant. The involve ratios can be extended to generation 2 and 3 of the gas-liquid in-situ method by using the terms specific surface area 'a' and gas volumetric fraction (vol pct.).
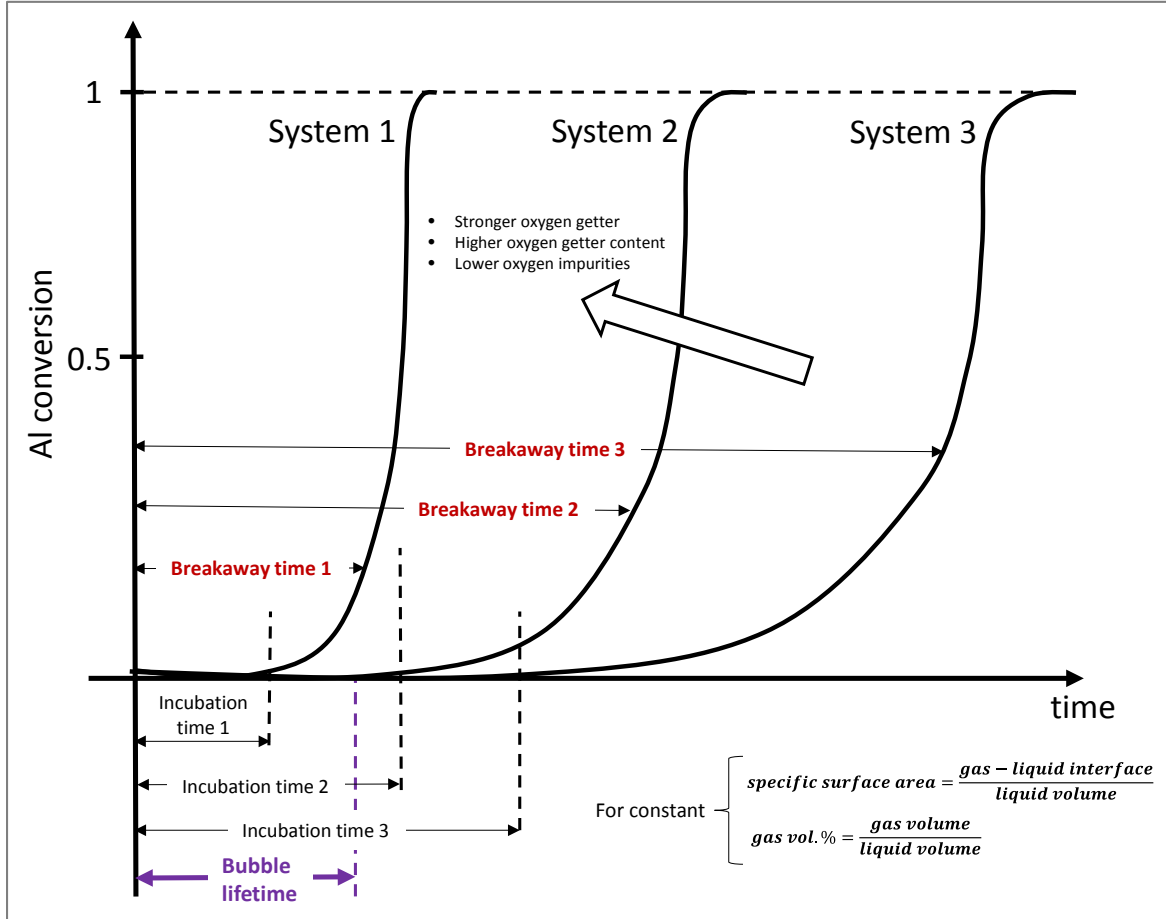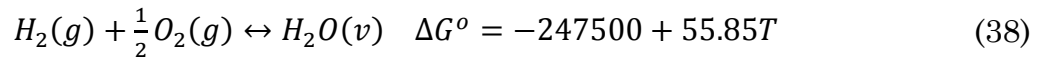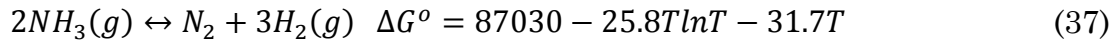

Figure 26. Qualitative nitridation curves for the 1st generation of the gas-liquid in-situ method.

Finally, a flowing atmosphere will keep the reaction under control as the atmosphere is continuously renewed and the reaction rate does not reach the breakaway point. In our case, each bubble represents a single volume of atmosphere that is being continuously renewed. As a qualitative example, a gas-liquid system with the bubble lifetime of Figure 26 will only be active for system 1. The lifetime of a bubble inside our melt is around 1s [37] and no reaction will happen for a longer incubation period. Shortest incubation period obtained by Scholz and Greil in the above example was 40minutes. It seems reasonable to think that extra-purified argon-methane mixtures will be required for the second and 3rd generations of the gas-liquid in-situ method. Borgonovo and Makhlouf [4] and Zhang and Rheddy [19] satisfactorily produced Al-AlN microcomposites with the 2nd generation of the gas-liquid in-situ method with

Mg and Li below 15wt pct. as oxygen getters and nitrogen gas of high purity (ppb impurities). **In summary**, for an oxygen sensitive generation 3 gas dispersed aluminum based in-situ manufacturing method working at a given temperature and pressure and having a given size, geometry, bubble size and gas volumetric fraction, a minimum amount of a selected oxygen getter is required for a gas with a given oxygen impurity level.

Oxygen poisoning of methane chemisorption

It is uncertain if the oxygen poisoning will occur also when methane instead of nitrogen is used as a gas. Information on the quantum dynamics of the methane chemisorption on molten aluminum surface are scarce and its activation energy unknown (Figure 22 and Figure 24). The production of Al-TiC [11, 14, 22, 23] and Al-SiC [16] microcomposites is not sensitive to oxygen impurities but both Khatri, Sahoo and Koczak [11, 14] and Wu and Reddy [16] acknowledge the existence of solid carbon particles that evolve into TiC via the soot formation route (Figure 9). Both Zheng and Reddy [18, 19] and also Borgonovo and Makhlouf [4] recognize the effect of the hydrogen released during ammonia decomposition as an oxygen getter. When ammonia decomposes next reactions occur [52]:

$$2NH_3(g) \leftrightarrow N_2 + 3H_2(g) \quad \Delta G^o = 87030 - 25.8TlnT - 31.7T \quad (37)$$

$$H_2(g) + \frac{1}{2}O_2(g) \leftrightarrow H_2O(v) \quad \Delta G^o = -247500 + 55.85T \quad (38)$$

Consequently, the P_{O2} decreases to the point that even lithium or magnesium can be unnecessary or at least reduced and commercial gas can be used. Zheng [18, 19] identifies the nitrogen chemisorption as the limiting step when nitrogen gas is used whereas the nitrogen atoms diffusion across the liquid is identified as the limiting step when ammonia gas is used. It could be argued that same principle applies to CH_4 and its decomposition. However, ammonia breaks down in the interval 200-500⁰C whereas methane decomposes in the interval 400-900⁰C so the produced H_2 and its oxygen getter yield will be smaller. Moreover, methane decomposition into soot and hydrogen must be avoided so nanoparticles instead of microparticles are synthesized (Figure 9). A possible gas flow combination is the introduction of CH_4+H_2 diluted in argon. The H_2 will combine with the O_2 traces whereas at the same time methane does not decompose into soot. The effect of H_2 on soot control is illustrated in section 6. The experimental work in chapter 3 will elucidate how important is the oxygen poisoning in the methane-aluminum chemisorption. Experiments without oxygen getter and with oxygen getter will be done.

2.3.3. Carbon diffusion in liquid as limiting step

The carbon diffusion along the liquid boundary layer is the limiting step. The existence of the TiC chemical reaction is enhancing the carbon flux across the

boundary layer by pushing the carbon concentration profile into the bubble interface maximizing the profile gradient. For the extreme case of very slow reaction and high gas solubility the concentration profile follows a straight line as indicated in Figure 27.
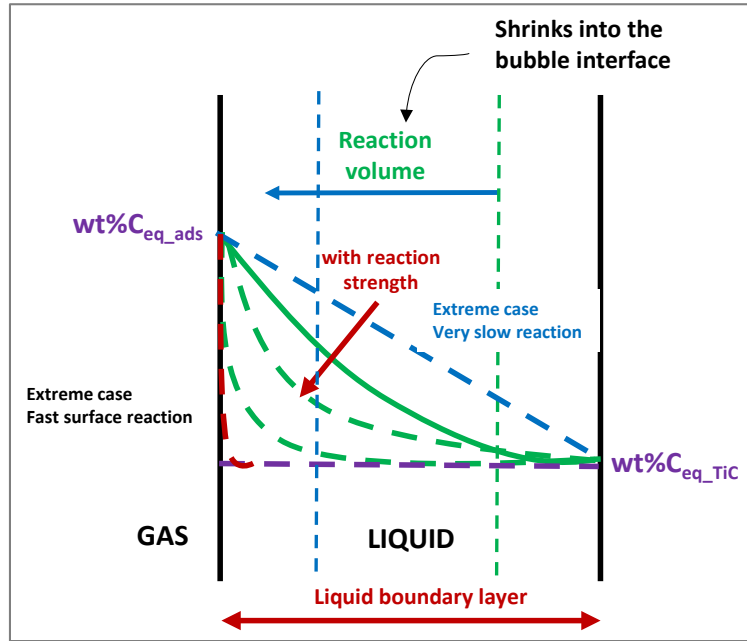

Figure 27. Carbon concentration profile dependent on the TiC reaction strength.

In this case the reaction happens inside the melt bulk. With increasing reaction strength the reaction volume moves inside the boundary layer and the carbon concentration profile adopts a convex parabolic profile that has its bottom value at the equilibrium carbon concentration calculated in Figure 18. For further stronger chemical reaction the carbon profile gets closer to the gas-liquid interface until it becomes a surface reaction (red profile in Figure 27). The extreme fast reaction is therefore analogous to the chemisorption limited rate case. The reaction volume shrinks and gets thinner than the boundary layer, which is set by the external fluid dynamics conditions. The described dynamics are illustrated in Figure 27 and included in equation 36. The chemical reaction enhances the mass transfer along the liquid boundary layer. An enhancement coefficient (E) is defined [37, 67]:

$$E = \frac{mass\ transfer\ with\ chemical\ reaction}{mass\ transfer\ without\ chemical\ reaction} = \frac{K_{L\_chem}}{K_L}$$

$$R_{TiC\_micro} = K_L \cdot E \cdot (\Delta wt\%Ti_{micro})$$

Both the mass transfer coefficient (K_L) and the enhancement factor (E) must be calculated.

Overall liquid mass transfer coefficient (K_L) calculation

The overall liquid mass transfer coefficient (K_L) for the two film theory is [11, 39, 67, 68]:

$$K_L \left[\frac{grTiC}{cm^2 bubble \cdot s} \right] = \rho_{melt} \frac{D_i}{\delta_L}; \tag{39}$$

The boundary layer thickness (δ_L) around a bubble at high turbulence is within the range of 50-100μm [69].

Enhancement factor calculation

From the dimensionless form of the Fick's law with chemical reaction introduced in equation 36, a pi-set of the form is demonstrated [37, 67].

$$\Pi \equiv \{E, Ha, Z\}$$

There are two numbers besides the enhancement factor "E". The Hatta number 'Ha' and 'Z' ratio. The Hatta number allocates the reactive system into a reaction regime, analogous to the Reynolds number and fluid mechanics regimes. It accounts for:

$$Ha^2 = \frac{kinetic\ rate\ in\ absence\ of\ transport\ effects}{maximum\ diffussional\ rate} = \frac{R_{TiC}}{K_L \cdot (\Delta wt\% Ti_{micro})} \tag{40}$$

So the Hatta number is a measure of how fast the reaction is in comparison with the diffusional rate. The Z ratio is the ratio of the reactants mass transfer and it follows next expression:

$$Z = \frac{mass\ transfer\ titanium}{mass\ transfer\ carbon} = \frac{D_{Ti,l} \cdot C_{Ti,bulk}}{D_{C,l} \cdot C_{C,sat}}$$

An analytical expression of the next type is expected:

$$E = \varphi(Ha, Z) \tag{41}$$

The Hatta number results from the dimensionless form of the 2nd Fick law with chemical reaction, equation 36, and it depends on the TiC reaction kinetics. Homogeneous reaction in the liquid boundary layer in chemical engineering has the kinetic expression listed below:

$$A(d) + B(d) \leftrightarrow C(d) \tag{42}$$
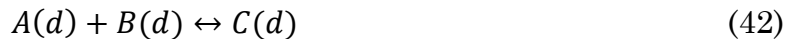
$$R_C = k(T)C_A \qquad\qquad 1\text{st oder kinetics}$$

$$R_C = k(T)C_A C_B \qquad\qquad 2\text{nd order kinetics}$$

$$R_C = k(T)C_A^n C_B^m \qquad\qquad m\text{th, n}\text{th order kinetics}$$

Unfortunately, only the first and second order kinetics have analytical solutions of the type of equation 41. Higher order kinetics are solved by numerical simulation [70, 71]. The order of our TiC reaction is initially unknown. It is a precipitation heterogeneous liquid-solid reaction driven by both wt pct.Ti and wt pct.C local supersaturation in the boundary layer. The precipitation reaction is composed of two parallel steps, nucleation and grow. The kinetic expression is:

$$R_{TiC} = R_{TiC\_nuc} + R_{TiC\_growth}$$

The nucleation and growth kinetics will be analyzed in the next section with the objective of controlling the particle size. The determination of the reaction order is however out of the scope for the present thesis. Both the enhancement coefficient and the Hatta number are foreign concepts for the aluminum metallurgist. The reason is that no gas-liquid systems with chemical reaction have been of interest up to date. The gas-liquid in-situ method is, to the best of our knowledge, the first gas-liquid system with chemical reaction studied in the field. The closest studied system is aluminum degassing. It involves hydrogen mass transfer via chemisorption but no chemical reaction in the gas or liquid boundary layer.

2.3.4. Conclusions

(1) Two different kinetic regimes have been identified: chemisorption limited regime and carbon liquid diffusion limited regime. The concentration profiles have been sketched and the boundary conditions set. A summary is illustrated in Figure 28.

(2) A kinetic expression is proposed for the CH_4 chemisorption rate in molten aluminum. Both its activation energy is unknown and the impact of the oxygen poisoning in the surface related constant 'c' is unknown. It will be experimentally evaluated.

(3) Two ways are proposed to alleviate the possible oxygen chemisorption: (1) a volatile alloying element as Mg, Li or Na, can act as an oxygen getter or catalyzer, (2) the addition of small fraction of H_2 in the gas mixture can also act as an oxygen getter. A smart use of this methods may shift the reaction regime into the carbon liquid diffusion limited regime.

(4) A kinetic expression for the carbon liquid diffusion limited regime requires an expression for the enhancement coefficient E. Analytical expressions are available in literature for 1st and 2nd order kinetics but not for mth and nth order kinetics. The kinetics order of our gas-liquid-solid precipitation kinetics must be first established. It is unfortunately out of the scope of the present thesis.

(5) A qualitative model of the kinetics is proposed in Figure 29 . This model does not predict the amount of TiC produced under a set of conditions but it enables the

interpretation of experimental results so guidelines can be set for further experiments.

(6) The knowledge limitations for a quantitative model have been listed so future lines of research can be designed to address them.
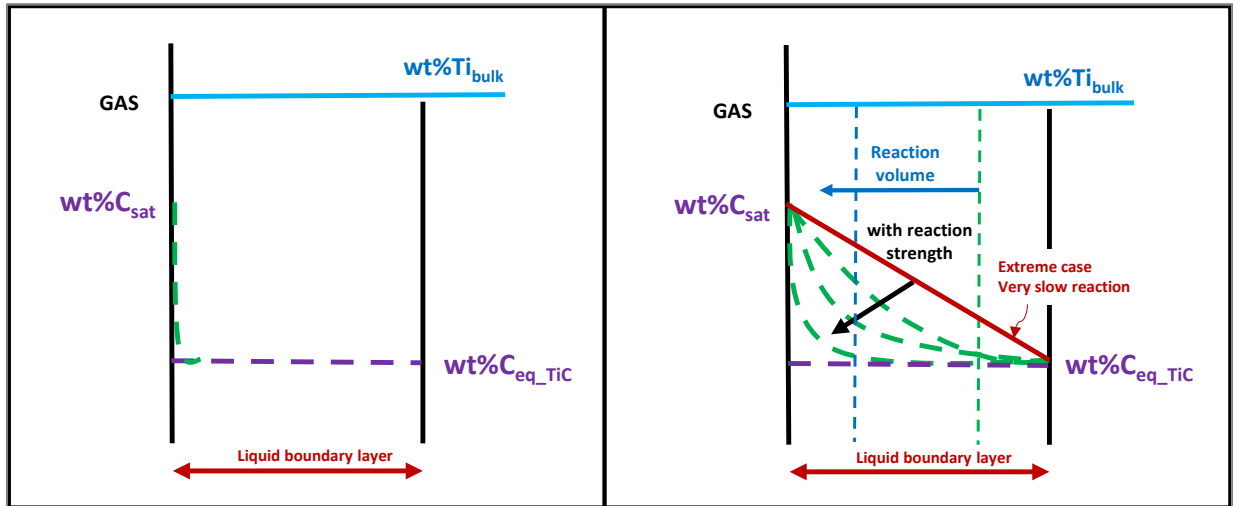

Figure 28. Carbon profile for chemisorption limited reaction (left) and liquid reaction limited kinetics (right).
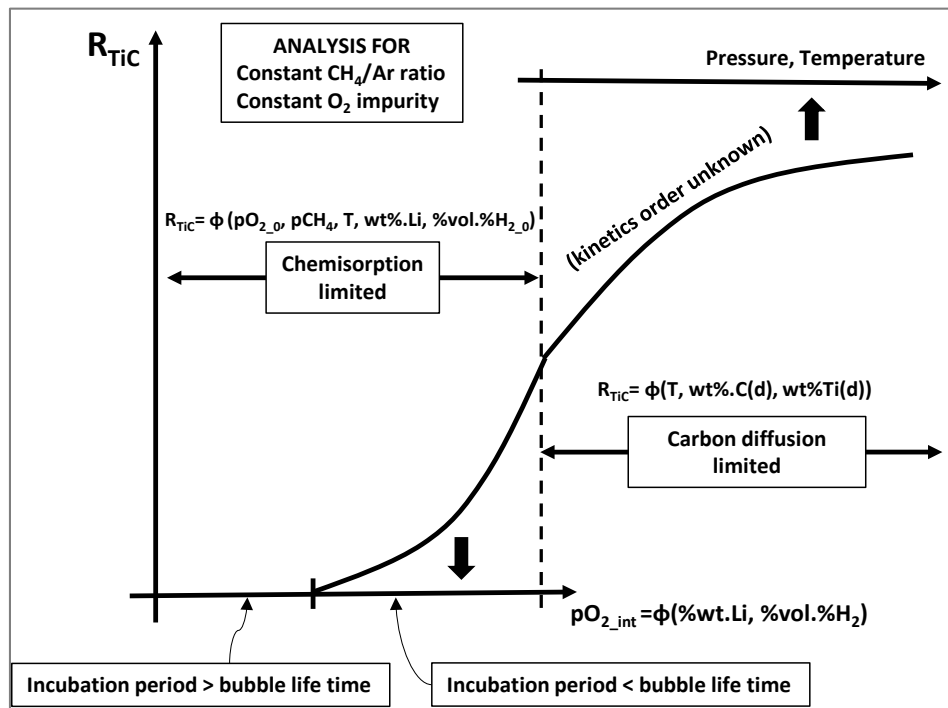

Figure 29. Qualitative kinetics model for TiC production in Al-TiC chemistry with the 3rd generation of the gas-liquid in-situ method.

2.4. Particle Size Control and Gas-Liquid Dispersion

The objective of this section is to theoretically prove that the particles can be produced and controlled in the nanoscale range. Next requirements must be fulfilled:

(1) Nucleation and growth of the particles must be feasible and allocated into the nanoscale

(2) The mechanism of TiC particles evacuation into the melt bulk via the growth interruption mechanism (GIM) must be theoretically supported by the gas-liquid dispersion dynamics.

TiC reaction of formation (step 5) was included in Figure 20. However, the step can be subdivided in 3 steps that are: (5.1) TiC nucleation, (5.2) TiC particles growth and finally (5.3) growth interruption and evacuation to the melt bulk. Figure 30 illustrates the mentioned steps. It includes the possibility of oxygen getter need for the chemisorption limiting case and the change on the parabolic carbon profile dependent on the reaction strength for the carbon diffusion limiting case.
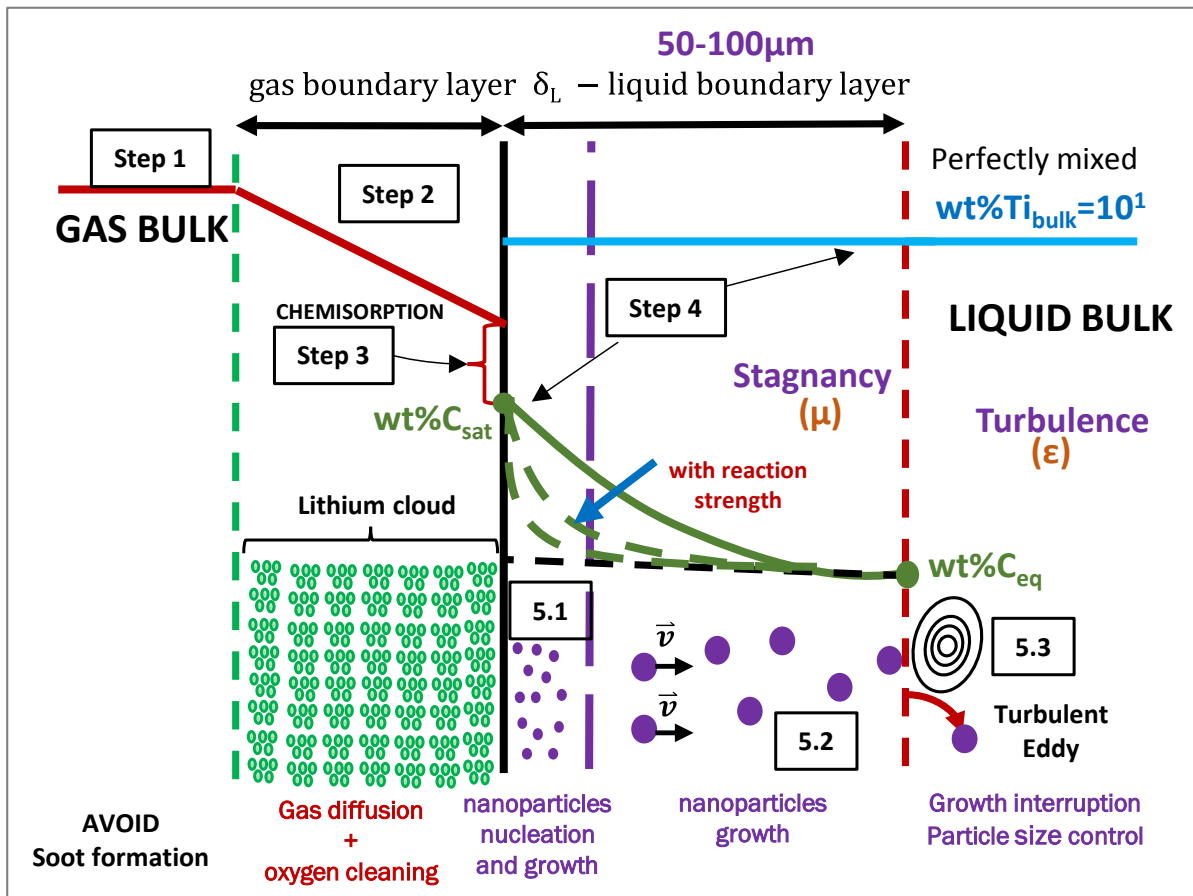
Figure 30. Complete kinetics model that includes all phenomena in Section 3.

From classical precipitation kinetics we know that:

$$R_{TiC} = R_{nuc} + R_{growth}$$

For a typical supersaturated system with solute depletion (transient system), Figure 31 shows the solute concentration evolution along the crystallization time and both the nucleation and growth rate along the solute concentration axis (in our case the wt pct.C). The figure shows four points of solute concentration and bottom values that are: (1) saturation limit, (2) precipitation equilibrium limit, (3) homogeneous nucleation threshold and (4) heterogeneous nucleation threshold. The first two points were already included in our analysis of the 3rd generation of the gas-liquid in-situ method. The other two points, the nucleation thresholds, are included in Figure 32. Note that in our case there is no solute depletion. Both carbon and titanium are continuously supplied by methane and Al₃Ti intermetallics and the system is considered pseudostationary. In the case of chemisorption limited kinetics (left side Figure 32), the carbon does not accumulate inside the boundary layer so all the reaction volume is restricted to the bubble interface and probably the nucleation is mostly heterogeneous. In the case of carbon liquid diffusion limited kinetics (right side Figure 32) a carbon profile develops inside the melt and the homogeneous nucleation is also an option.
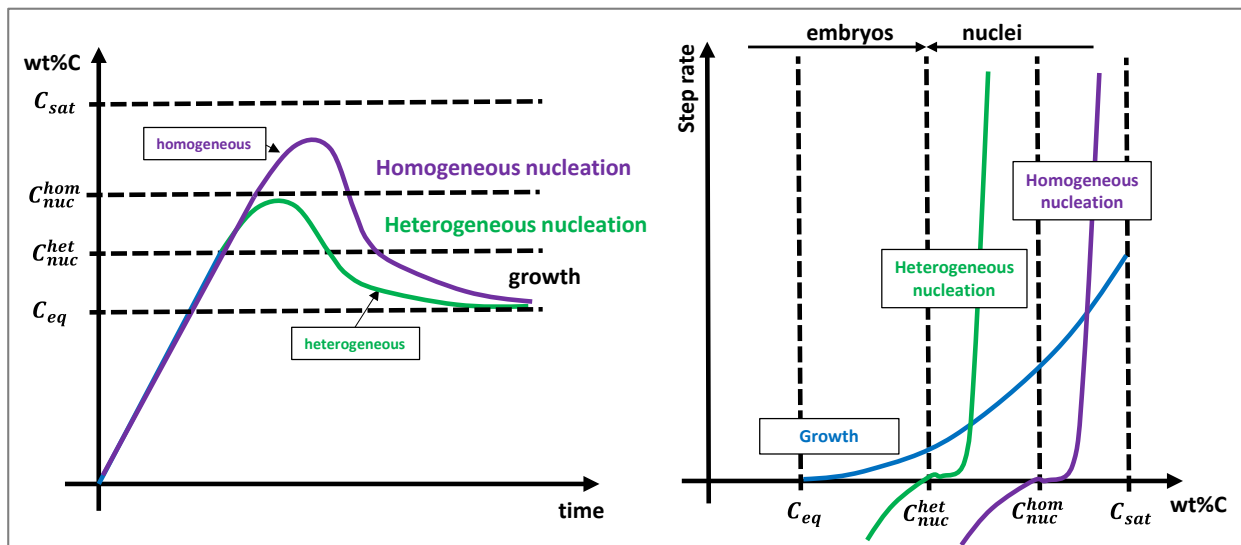

Figure 31. Supersaturated system with solute depletion (transient): Solute concentration evolution along the crystallization time (left) and both the nucleation and growth rate along the solute concentration axis (right).
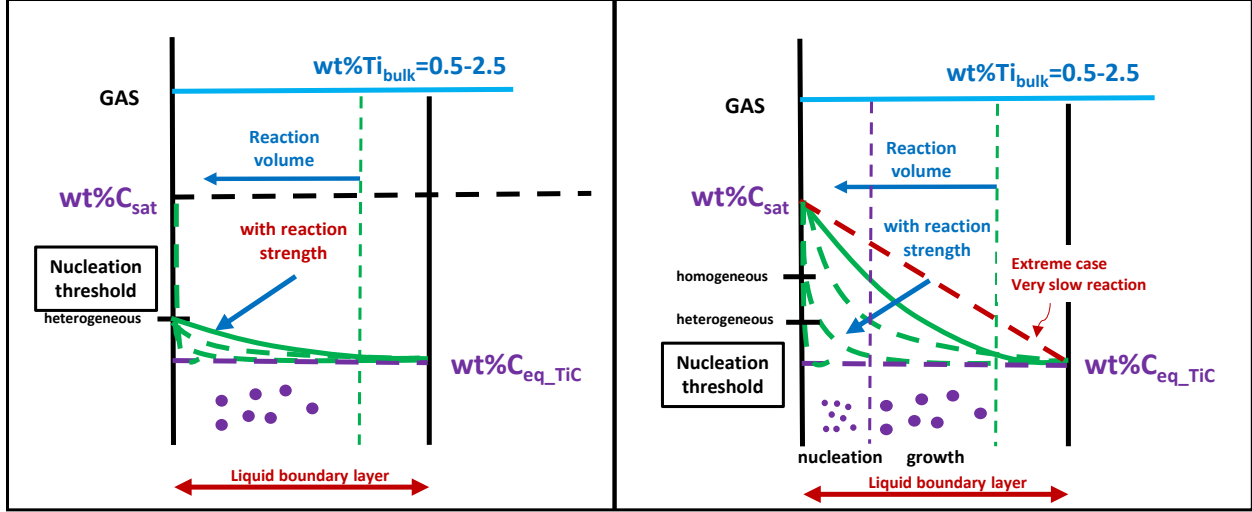
41

Figure 32. 3rd generation of the gas-liquid in-situ method (pseudostationary): Carbon concentration and nucleation thresholds for chemisorption limited (left) and carbon diffusion limited case (right).

2.4.1. Particles nucleation

In this section the nuclei size and the nucleation rate vs. the dissolved carbon will be studied so the nucleation threshold can be calculated. The nucleation rate and critical radius have next expressions [72] :

$$R_{nucl}\left[\frac{gr\ TiC}{cm^3\ melt \cdot s}\right] = \left[f_0 C_0 exp\left(\frac{-\Delta G_v^* \cdot S(\theta)}{kT}\right)\right]\left[\frac{nuclei}{cm^3 melt \cdot s}\right] \cdot \frac{4}{3}\pi(r^*)^3 \left[\frac{cm^3\ TiC}{nuclei}\right] \cdot \rho_{TiC}\left[\frac{gr\ TiC}{cm^3\ TiC}\right] \quad (43)$$

$$(r^*)\ [nm] = -\frac{2\sigma_{TiC-Al}}{\Delta G_{v\_TiC}} \quad (44)$$

Being:

(1) Critical energy (ΔG_v^*) $[Jul/cluster] = \Delta G_v^* = \frac{16\pi\sigma_{TiC-Al}^3}{3(\Delta G_{v\_TiC})^2}$

(2) Heterogeneous geometry factor $S(\theta) = (2 + cos\theta)(1 - cos\theta)^2/4$

(3) Successful jumps frecuency growth of atoms (f_0) $\left[\frac{nuclei}{cluster}s^{-1}\right] = \frac{kT}{3\pi\lambda^3\mu_{melt}}$

(4) Concentration of growth species, (C_0) $[atoms/cm^3] = 2wt\%C * \rho_{melt} \cdot MW_C^{-1} \cdot N_{Av}$

Equation 43 is interpreted by blocks as it follows.

(1) $C_0 exp\left(\frac{-\Delta G_v^* \cdot S(\theta)}{kT}\right)$ $[clusters/cm^3]$ represents the number of clusters from the initial concentration of species C_0 that have the critical energy at a given time.

(2) $f_0 C_0 exp\left(\frac{-\Delta G_v^* \cdot S(\theta)}{kT}\right)$ $[nuclei/cm^3 \cdot s]$ represents the number of critical clusters that manage to gain one more atom and convert into stable nuclei.

The properties σ_{TiC-Al}, ΔG_{v_TiC}, η, μ_{melt} and λ_{TiC} must be calculated for equation 43. For the calculation of σ_{TiC-Al} Young equation is used:

$$\sigma_{TiC-Al} = \sigma_{TiC-v} - \sigma_{Al-v}cos\theta \tag{45}$$

Being:

σ_{Al-v}(N/m) = $(948 - 0.202T)/1000$ [73]

$\theta_{TiC-AlTi1\%} = 16 - 0.027 \cdot (T(K) - 933)$ $(for\ T = 850 - 1050°C)$ [74]

σ_{TiC-v}(N/m) =0.725 [75, 76]

For the calculation of ΔG_{v_TiC}, that is composition dependent, the 1wt pct. Henryan standard state is assumed. From [14]

$$\Delta G_{v\_TiC}\left[\frac{J}{m^3}\right] = \left(\Delta G_{TiC}^0 + RTln\frac{1}{wt\%C \cdot wt\%Ti}\right)\left[\frac{Jul}{mol}\right] \cdot MW_{TiC}^{-1} \cdot \rho_{TiC} \tag{46}$$

being $\Delta G_{TiC}^0 = -163382 + 80.347T + 0.460 \cdot 10^{-3}T^2 + 3.096 \cdot \frac{10^5}{T} - 0.962TlnT$

For the calculation of the viscosity, the melt is approximated as pure aluminum

$\mu_{melt\_Al} = 1.49 \cdot 10^{-4}exp\left(\frac{1984.5}{T}\right) Pa \cdot s$ [18]

For the calculation of λ_{TiC} in f_0, a Ti_1C_1 stoichiometry is assumed

$\lambda_{TiC} = \frac{(R_{Ti^{+4}}+R_{C^{-4}})}{2} = 16.5\mathring{A}$

Equations 43 is calculated and plotted in Figure 33 for four different conditions inside the thermodynamic operation window in Figure 17 in the range wt pct.Ti(d)=0.7-2 and 900-1050°C. It is observed that the nucleation rate at 1050°C, compared with the nucleation rate at 900°C, increases by several orders of magnitude.
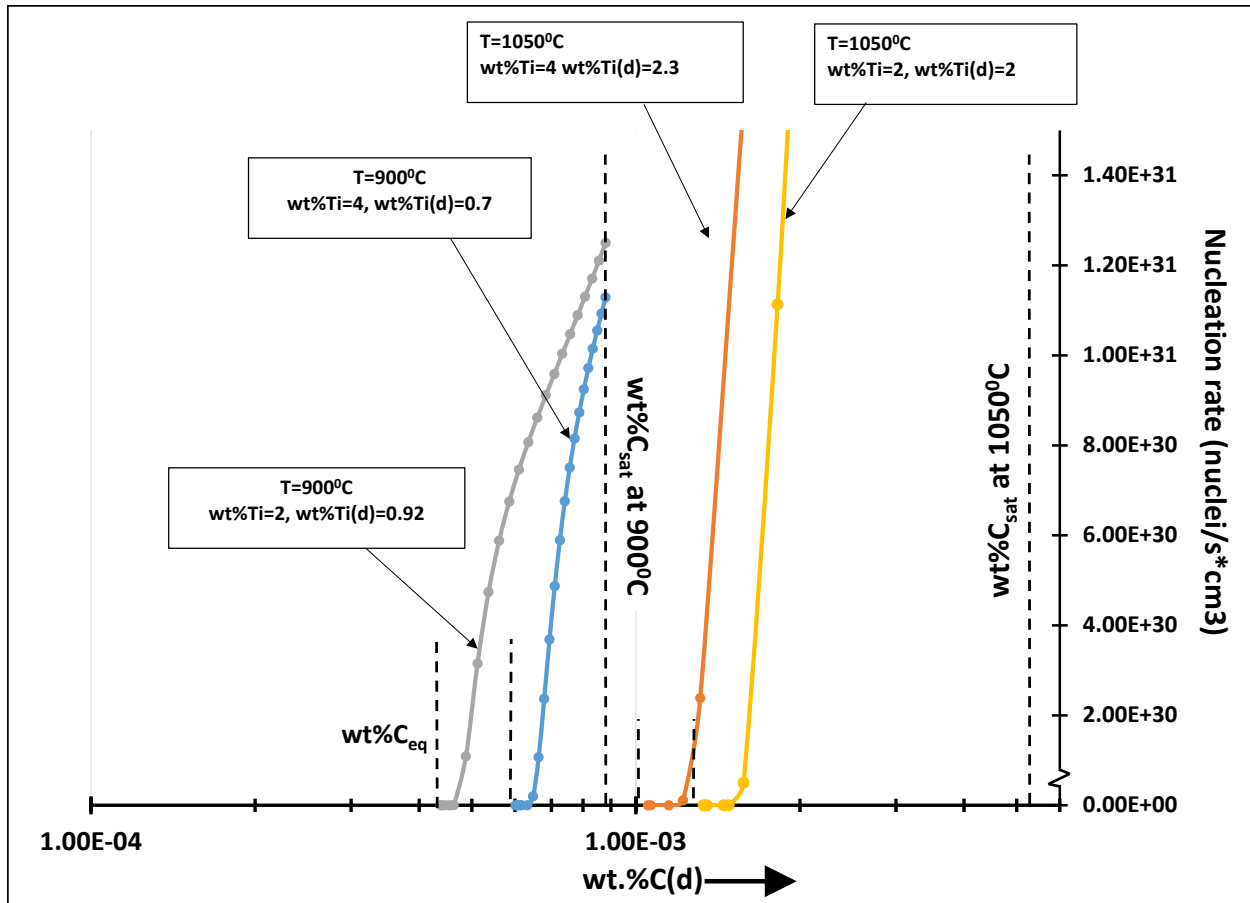
Figure 33. Nucleation rate for different points in Figure 17.

Homogeneous and heterogeneous nucleation

The geometry factor (S(θ)) included in equation 43 establishes the nature of the nucleation. It has next expression:

$$S(\theta) = (2 + cos\theta)(1 - cos\theta)^2/4 \tag{47}$$

θ is traditionally referred to be the wetting angle between a solid substrate (the TiC) and a molten metal (the melt) in the sessile drop experiment in Figure 34, left side. Its value is available in bibliography. However, in the gas-liquid in-situ method, it is hypothesized that TiC particles nucleates on the gas-liquid bubble interface as illustrated in Figure 34, right side. A different angle θ' forms.
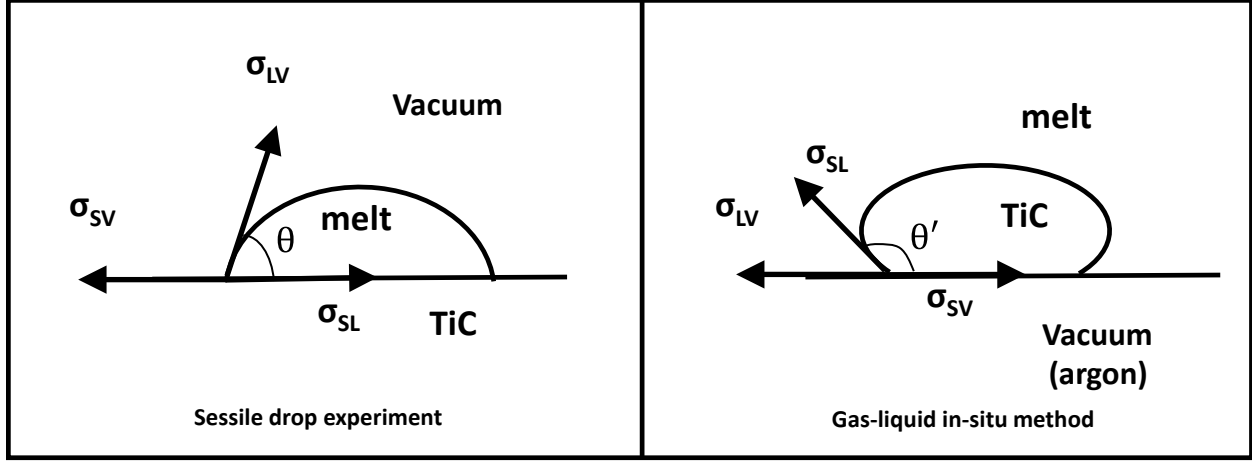
Figure 34. Wetting angle geometry for the sessile drop experiment and the gas-liquid in-situ method.

For the calculation of θ', the force balance (Young equation) is next written for both cases:

$\sigma_{TiC-v} = \sigma_{TiC-Al} + \sigma_{Al-v}cos\theta$ sessile drop experiment case

$\sigma_{Al-v} = \sigma_{TiC-v} + \sigma_{TiC-Al}cos\theta'$ gas-liquid in-situ method

$$cos\theta' = \frac{\sigma_{Al-v} - \sigma_{TiC-v}}{\sigma_{TiC-Al}} = \frac{\sigma_{Al-v} - \sigma_{TiC-Al} - \sigma_{Al-v}cos\theta}{\sigma_{TiC-Al}} = \frac{\sigma_{Al-v}(1 - cos\theta)}{\sigma_{TiC-Al}} - 1 \quad (48)$$

Equation 48 is introduced in the geometry factor expression in equation 47, resulting in:

(1) At 900⁰C, $S(\theta') = 0.88$. The wetting angle of AlTi1 on TiC has a value of $\theta \approx 10^0$ and the wetting angle of TiC in argon is $\theta' \approx 126^0$.

(2) At 1050⁰C, $S(\theta') = 0.99$. the wetting values are $\approx 5.5^0$,$\theta' \approx 158^0$.

The homogeneous nucleation of TiC in molten metal is strong enough to occur be itself with no surface assistance as long as enough carbon is accumulated in the interface. Both heterogeneous and homogeneous nucleation are equivalent and a single nucleation threshold will be calculated.

Nucleation threshold calculation

The critical radius in equation 44 is plotted along with the nucleation rate for wt%.Ti(d)=0.95 and T=900⁰C in Figure 35. A nucleation threshold for $wt.\%Ti = 4.9 \cdot 10^{-5}$ is selected at which $r^* \approx 1nm$ and $R_{nucl} = 10^{30} \frac{nuclei}{cm^3 melt \cdot s}$. Figure 36 shows the carbon profiles for chemisorption limited and carbon diffusion limited cases including the quantitative values of the saturation and equilibrium values of dissolved carbon as well as the nucleation threshold. The nucleation threshold is so close to the

equilibrium value that the growth interval is restricted to a very narrow range of the carbon concentration.
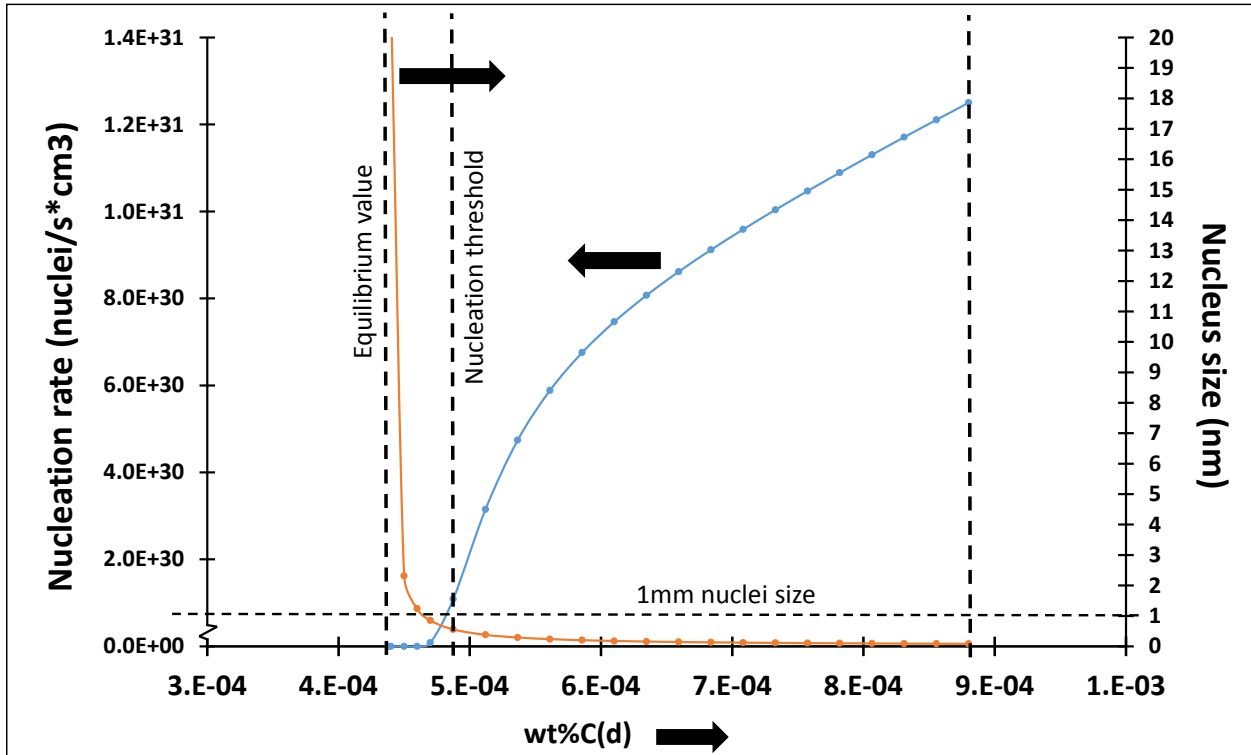

Figure 35. Nuclei size, nucleation rate, and nucleation threshold for wt. Ti(d) = 0.95 (900°C).
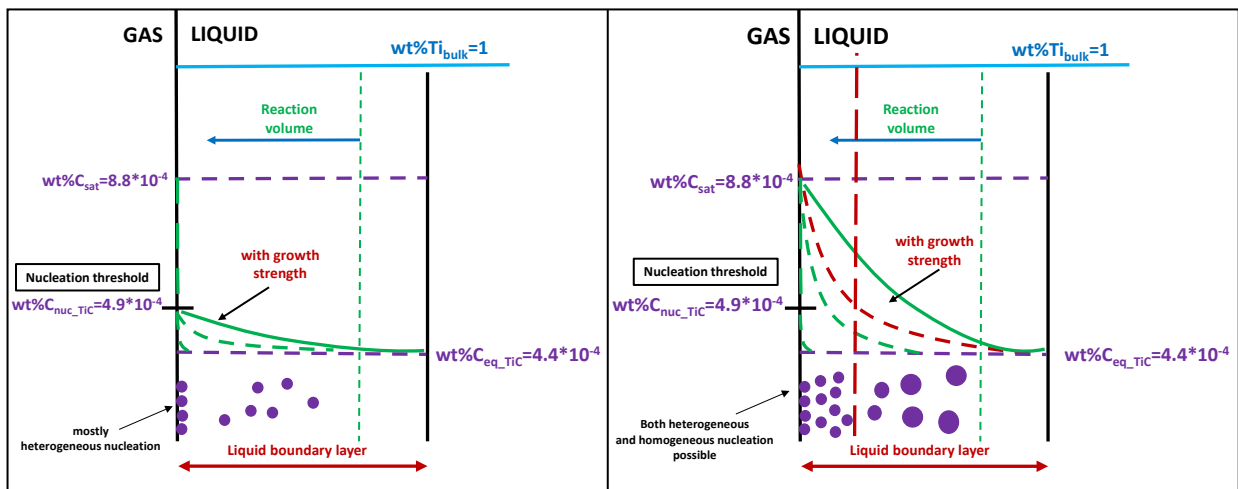

Figure 36. Carbon profile for the case wt.%Ti(d)=2 and T=900⁰C and chemisorption as limiting step (left) and TiC chemical reaction as limiting step (right).

46

2.4.2. Particles growth

The general growth rate expression is next given:

$$R_{growth}\left[\frac{gr\ TiC}{cm^3\ melt \cdot s}\right] = \frac{\#particles}{cm^3\ melt} \cdot \rho_{TiC} \cdot 4\pi R_p^2 \cdot \frac{dR_p}{dt} = f_0 C_0 exp\left(\frac{-\Delta G_v^*}{kT}\right)\rho_{TiC} \cdot 4\pi R_p^2 \frac{dR_p}{dt} \quad (49)$$

Being

(1) $\frac{\#particles}{cm^3\ melt} = f_0 C_0 exp\left(\frac{-\Delta G_v^*}{kT}\right)$ with $f_0 \equiv \left[\frac{nuclei}{cluster}\right]$, i.e. the liquid boundary layer is assumed to be in pseudostationary state and there is no accumulation of particles. For each new nucleated particle another particle leaves the boundary layer.

(2) $\frac{dR_p}{dt}$ is the particle-interface growth rate and the only term that changes in the growth rate expresion.

The growth can be limited by the reactants bulk mass transfer diffussion or by the interface reaction. As the particle-interface growth is a serial process (atoms diffusion into the interface and jump plus reaction into the interface), the slowest calculated growth rate will be limiting. The two steps model and the concentration profile resulting from them is illustrated in Figure 37. For the interface limited growth the concentration profile is flat, and the only gradient is given at the interface by the difference (wt%i_p - wt%i_{bulk})for the reactant "i". For the diffussion limited case, the solute concentration follows a concave profile into the particle interface ending at the reactants equilibrium values for the TiC formation reaction.
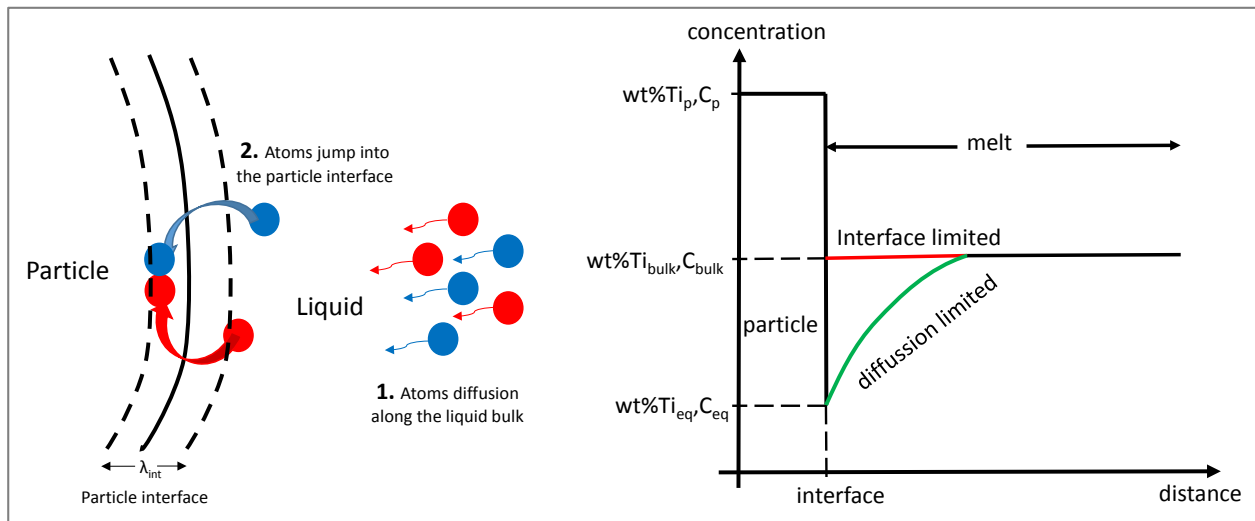

Figure 37. Serial steps difussion and interface jump (left) and species concentration profile (right).

Diffusion limited growth

From [72] the diffusion limited growth rate follows next formula, for spherical coordinates

$$\frac{dR_{p\_diff}}{dt}\left[\frac{nm}{s}\right] = v_{i\_diff} = \frac{C_{i,bulk} - C_{i,eq}}{C_{i,p} - C_{i,eq}} \cdot \frac{D_{i,Al}}{R_p} \tag{50}$$

Recall that the developed concentration profile occurs at the nanoscale. Therefore, in equation 50 the bulk concentration does not refer to the melt bulk but to the coordinate 'x' at which the particle is located inside the liquid boundary layer. In conclusion, $C_{i,bulk} = C_i(x,t)$. The diffussion coefficients ratio is next calculated, taking into account references [11, 14, 18]

$$\left.\begin{array}{l} D_{Ti}\left[\frac{cm^2}{s}\right] = \frac{k \cdot T}{4\pi R_{Ti}\eta_{melt}} \\ D_C\left[\frac{cm^2}{s}\right] = \frac{k \cdot T}{4\pi R_C\eta_{melt}} \end{array}\right\} \rightarrow \frac{D_{Ti}+4}{D_{C^{-4}}} = \frac{R_C}{R_{Ti}} = \frac{0.26nm}{0.07nm} = 3.71 \quad \text{and assumed that the titanium}$$

concentration change due to the reaction can be considered negligible (see Figure 20), the carbon mass transfer is considered limiting. The expressions of the different terms in equation 50 are shown below:

$$C_c(x,t)\left[\frac{mol}{cm^3}\right] = wt\%C(x,t) \cdot \rho_{melt} \cdot MW_c^{-1}$$

$$C_{c,p}\left[\frac{mol}{cm^3}\right] = wt\%C_p \cdot \rho_{TiC} \cdot MW_c^{-1} \text{ being } wt\%C_p = \frac{12}{48+12} = 20$$

$$C_{c,eq}\left[\frac{mol}{cm^3}\right] = wt\%C_{eq} \cdot \rho_{melt} \cdot MW_c^{-1}$$

Interface limited growth

From [72], the interface limited growth rate follows next formula

$$v_{interf}\left[\frac{nm}{s}\right] = \frac{dR_{p\_int}}{dt} = A\lambda v \cdot exp\left(\frac{-E_{a\,TiC}}{kT}\right) \cdot \left[ln(X_C(x,t)) - ln(X_{C,eq})\right] \tag{51}$$

with

(1) $X_C = \frac{wt\%i \cdot MW_{Al}}{100MW_i}$

(2) $E_{a\,TiC}$ the activation energy of the 'C' atoms to jump into the particle.

(3) A = accomodation factor. Probability of jumping atom to accommodate at the interface

(4) $\lambda = 1nm \equiv$ TiC-Al interface. It is approximated to be 5 rows of Ti-C atoms

(5) $v[s^{-1}] = 10^{13} \equiv$ atom vibration frecuency. It is a quantum mechanic property for any atom.

The activation energy is not considered in literature to be a limiting factor[25, 77] . We assume it is small enough so $E_{a\,TiC} \approx kT$ and $exp\left(\frac{-E_{a\,TiC}}{kT}\right) = 0.1 - 1$. The value of the accomodation factor 'A' depends on the nature of the surface. After the Jackson criterium:

$if\ \frac{\Delta G}{T} < 4R$ rough surface, A=1

$if\ \frac{\Delta G}{T} > 4R$ smooth surface, A<<1

For our case, $\frac{\Delta G}{T} < 0.17 J/mol$ for the carbon and titanium profile in the boundary layer at 900^0C. The surface is rough and equation 53 results:

$$v_{interf}\left[\frac{nm}{s}\right] = \lambda v \cdot \left[ln\big(X_C\,(x,t)\big) - ln\big(X_{C,eq}\big)\right]$$

The calculation of both v_{interf} and v_{c_diff} is plotted along the carbon concentration profile for wt.%Ti(d)=0.95 and T=900^{0}C in Figure 38. The diffussion limited growth is inversely proportional to the particle size so its variation is also included.
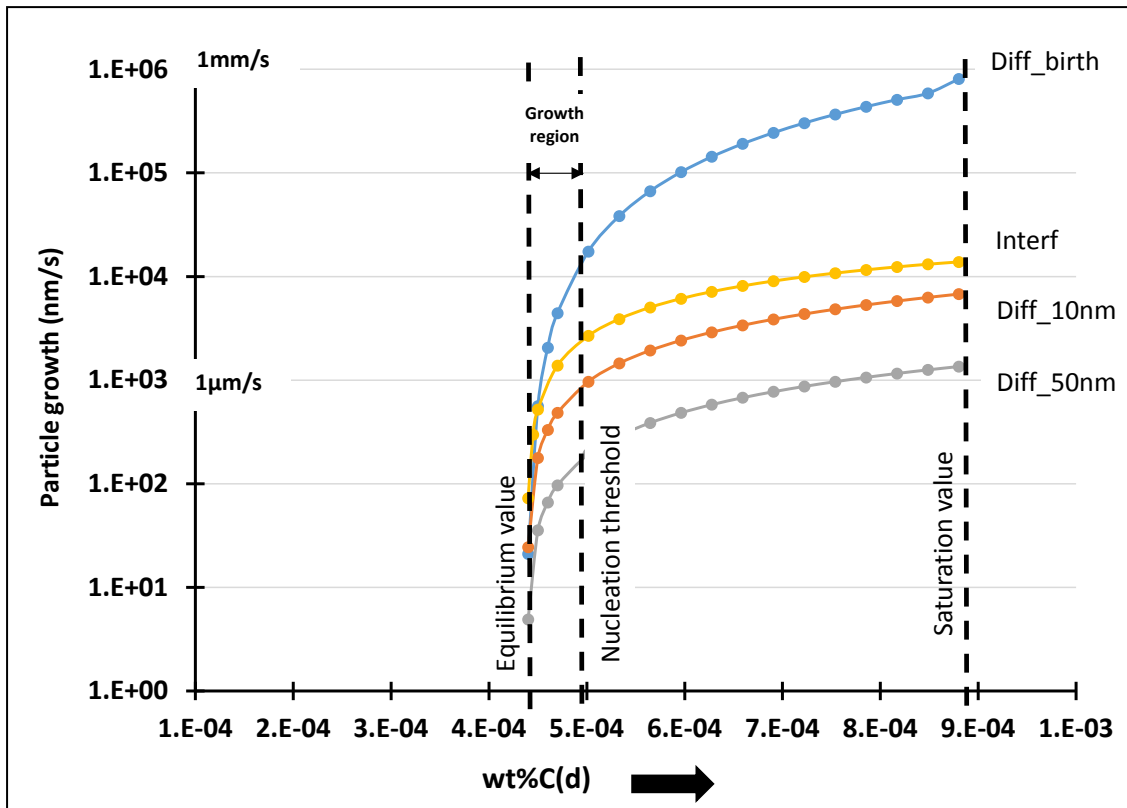
Figure 38. Interface vs. diffusion limited growth analysis plot.

The growth is mixed controlled in the region under 50nm and diffusion limited controlled above 50nm. In the region below the nucleation threshold the growth rate is below 1μm/s.

2.4.3. Bubbles break-up

The bubbles are first produced at the nozzle and a continuous break-up and coalescence process occurs. This section analyzes the interaction between the turbulent flow and the gas bubbles leading to bubble breakage. The nature of the turbulent flow is first introduced and then its interaction with the gas bubbles studied.

<u>**Turbulent flow description**</u>

Kolmogorov[78] stated in 1941 the structure of a turbulent flow. Local chaotic circulating fluid elements of different length scale called eddies are continuosly formed and destroyed. Anisotropic large eddies of characteristic length L, responsible of the macrofluids, transmit its kinetic energy into smaller local isotropic eddies of length λ which present a large amount of mass specific kinetic energy. This energy release is called **the energy cascade** and its flow of energy is called the energy dissipation rate (ε). At a given eddie size λ_{min} the Reynolds number of the eddy approaches 1 and the internal eddy flow transitions into laminar fluid regime in which its kinetic energy dissipates in form of heat. This eddie size is the smallest eddie size possible, called the Kolmogorov scale λ_{min} and it follows next expression.

$$\lambda_{min} = \left(\frac{\mu^3}{\rho^3 \cdot \varepsilon} \right)^{1/4} \tag{52}$$

The turbulent flow is hence multiscale in nature and presents global anisotropy and local scale isotropy. The distribution of eddy sizes dependent on its energy is called the **energy spectrum.** The energy spectrum characterizes a turbulent flow. In continuum mechanics, the energy dissipation rate relates to the fluid shear stress and shear rate with the expression:

$$\varepsilon \cdot \rho = \tau \cdot \dot{\gamma} = \mu \cdot \dot{\gamma}^2 \tag{53}$$

<u>**Bubble-turbulent flow interaction**</u>

Kolmogorov[79] in 1949 and Hinze[80] in 1955, stated that in gas-liquid systems isotropic eddy-bubble interactions continuosly take place due to the local velocity and pressure difference in the form of fluid shear. The eddies, within a size or wavelength range, hit the bubble and (1) break down into smaller eddies or (2) transmit their kinetic energy into the bubble in the form of surface deformation (Figure 39)[81].
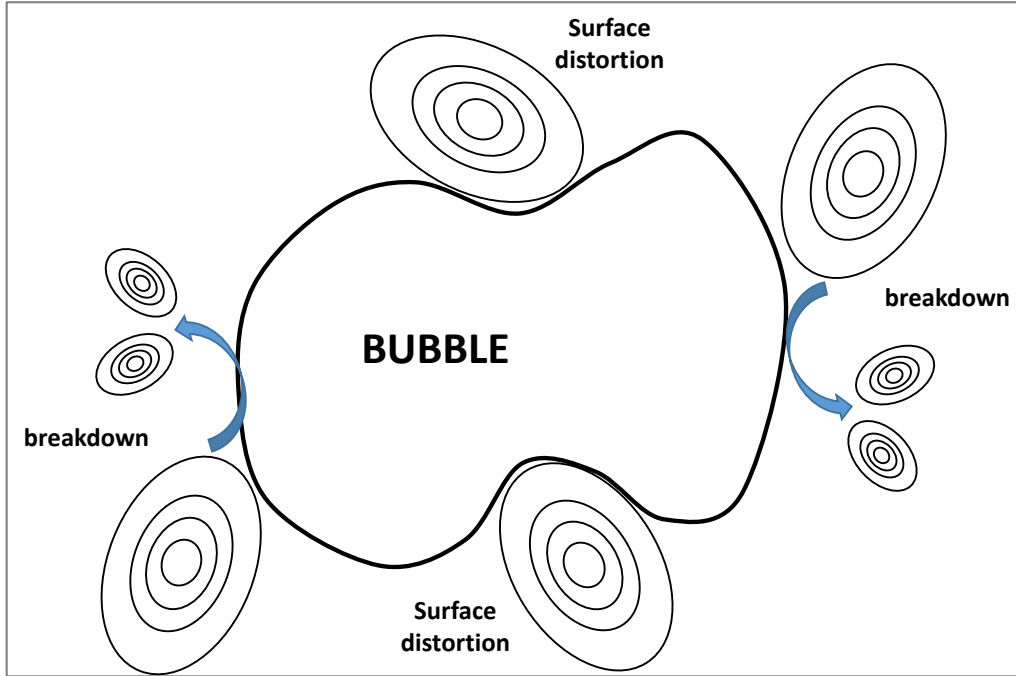
Figure 39.Bubble-fluid eddies interaction [81].

A surface stress balance at the bubble surface between the fluid shear stress ($\propto \tau$) and the bubble surface tension stress is established ($\propto \frac{\sigma}{d_b}$) [82, 83]. The ratio between the different surface stresses is called the Weber number:

$$We = \frac{\tau d_b}{\sigma_{Al-Ar}} = \frac{\mu \dot{\gamma} d_b}{\sigma_{Al-Ar}} \equiv \frac{shear\ stresses}{surface\ tension\ stresses} \tag{54}$$

There is a critical shear stress the fluid exerts on a bubble of a given size so the bubble breaks, i.e. there is a critical Weber number associated with a bubble size. The critical We number depends on the system characteristics and it is determined empirically. Its value for a bubble in a turbulent fluid is $We_{cr} = 1.2$ [80] Only eddies and bubbles of similar scales interact with each other. As a consecuence, bubbles smaller than the Kolmogorov scale λ_{min} are not possible. The critical shear stress is plot in Figure 40 vs. the bubble size for an aluminum melt at 700-1100⁰C.
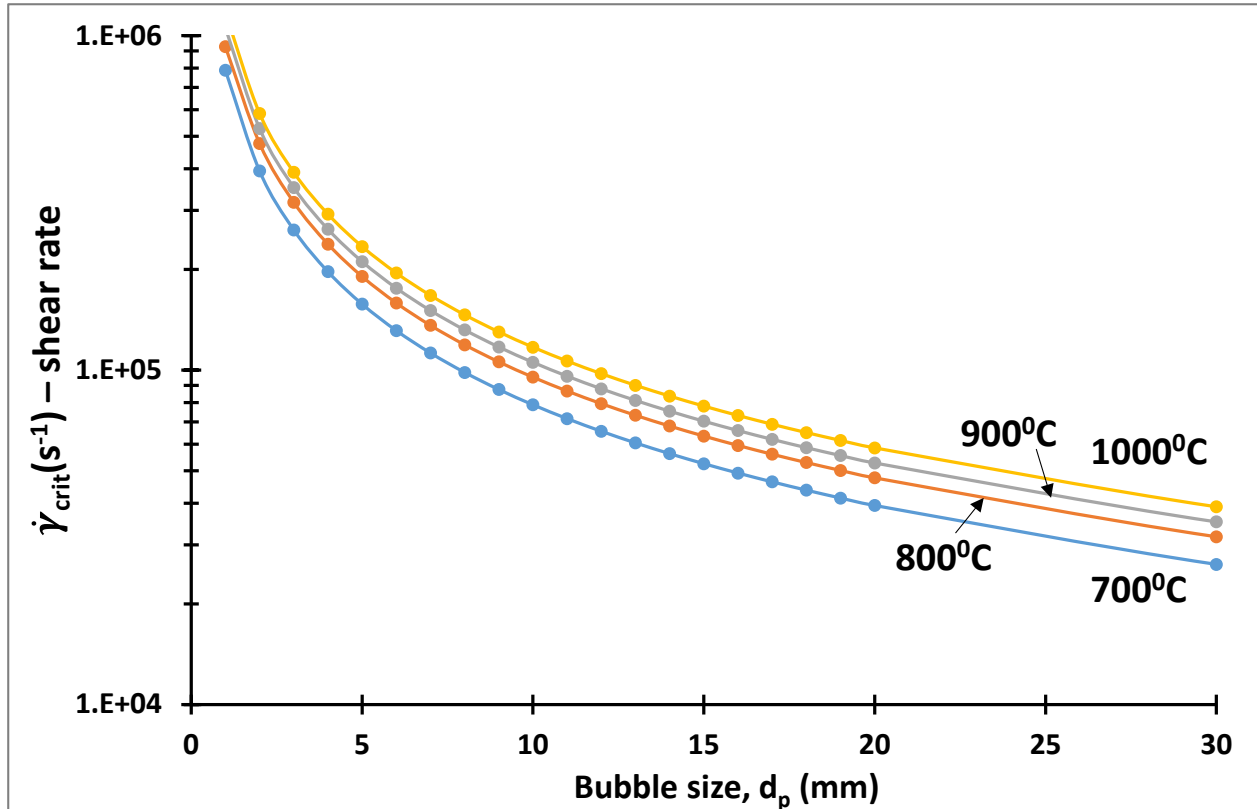
Figure 40. Critical shear rate in an aluminum melt.

Stirred tanks show shear rates at least one order of magnitude above bubble columns for same specific power input in W/Kg [84]. A typical air-water bubble column in chemical engineering has maximum shear rates surrounding the bubbles under 10,000s^{-1}[85]. An air-water stirred tank reaches shear rates up to at least 100,000s^{-1}. Molten metals have a surface tension around 10X bigger than water ($\sigma_{H2O-air} = 0.07 N/m$), a viscosity 5X smaller for molten aluminum at 1000^{0}C and a density 2.5X bigger. Hence, three observations are made:

(1) The critical shear rate for a bubble to break is for metal-argon is 10-50X bigger than for water-air systems.

(2) For a similar energy dissipation rate, the shear rate in a metal-argon system is up to 5X above the shear rate in a water-air system. Hence, a metal-argon bubble column may have at 1000^{0}C shear rates up to 50.000s^{-1} and a metal-argon stirred tank may have shear rates up to 500.000s^{-1}.

(3) The bubble column is considered analogous to the 2nd generation of the gas-liquid in-situ method whereas the stirred tank is analogous to the 3rd generation of the method.

(4) From Figure 40, a bubble size below 5mm is unlikely.

2.4.4. The growth interruption mechanism (GIM)

Nucleation, growth and bubble breakage phenomena have been analyzed in the previous subsections. The time for a particle to grow up to a radius is calculated based on next equation:

$$R_{pF} = R_{p\_nuc} + \int_0^{t_F} v_{growth} dt \tag{55}$$

Diffusion controlled growth applies along the whole size range of interest and its expression will be used. 'v_{growth}' is inversely proportional to R_p and next arrangement in equation 55 is done.

$$R_{pF} - R_{p\_nuc} = \int_{Rp_{nuclei}}^{Rp_F} dR_p = \int_0^{t_F} v_{growth} dt = \int_0^{t_F} \frac{C_c(x,t) - C_{c,eq}}{C_{c,p} - C_{c,eq}} \cdot \frac{D_{c,Al}}{R_p} dt$$

$$\int_{Rp_{nuclei}}^{Rp_F} R_p dR_p = \int_0^{t_F} \frac{C_c(x,t) - C_{c,eq}}{C_{c,p} - C_{ceq}} \cdot D_{c,Al} \cdot dt \tag{56}$$

The term $C_c(x,t)$ in equation 56 is the solution of 2nd Fick law in equation 36. Equation 36 contains the precipitation kinetics term R_{TiC} and the boundary conditions change depending on the limiting step (see Figure 36). The solution is not trivial and it is out of the scope of this thesis. However, a first insight is taken for the chemisorption limited case. In Figure 36 it is reasonable to approximate $C_c(x,t)=C_{c,nucl}$ as the whole nucleation ad growth happens in the bubble melt interface contour. For this specific case:

$$\frac{1}{2}\left(R_{pF}^2 - R_{p\_nuc}^2\right) = \frac{C_{c,nuc} - C_{c,eq}}{C_{c,p} - C_{ceq}} \cdot D_{c,Al} \cdot (t_F - t_0)$$

And solving for the time needed by a particle to grow up to a given radius, we have:

$$\Delta t = (t_F - t_0) \cong \frac{\frac{1}{2}\left(R_{pF}^2 - R_{p\_nuc}^2\right)}{\frac{C_{c,nuc} - C_{c,eq}}{C_{c,p} - C_{c,eq}} \cdot D_{c,Al}} \tag{57}$$

Equation 57 is plot in Figure 41 for wt%.Ti=2 and 900ºC and 1050ºC. From Figure 41 it is concluded that some sort of particle-bubble detachment event needs to happen at very high frequency (once every 100mS at least) so particle growth interrupts and particle size is controlled in the nanoscale.
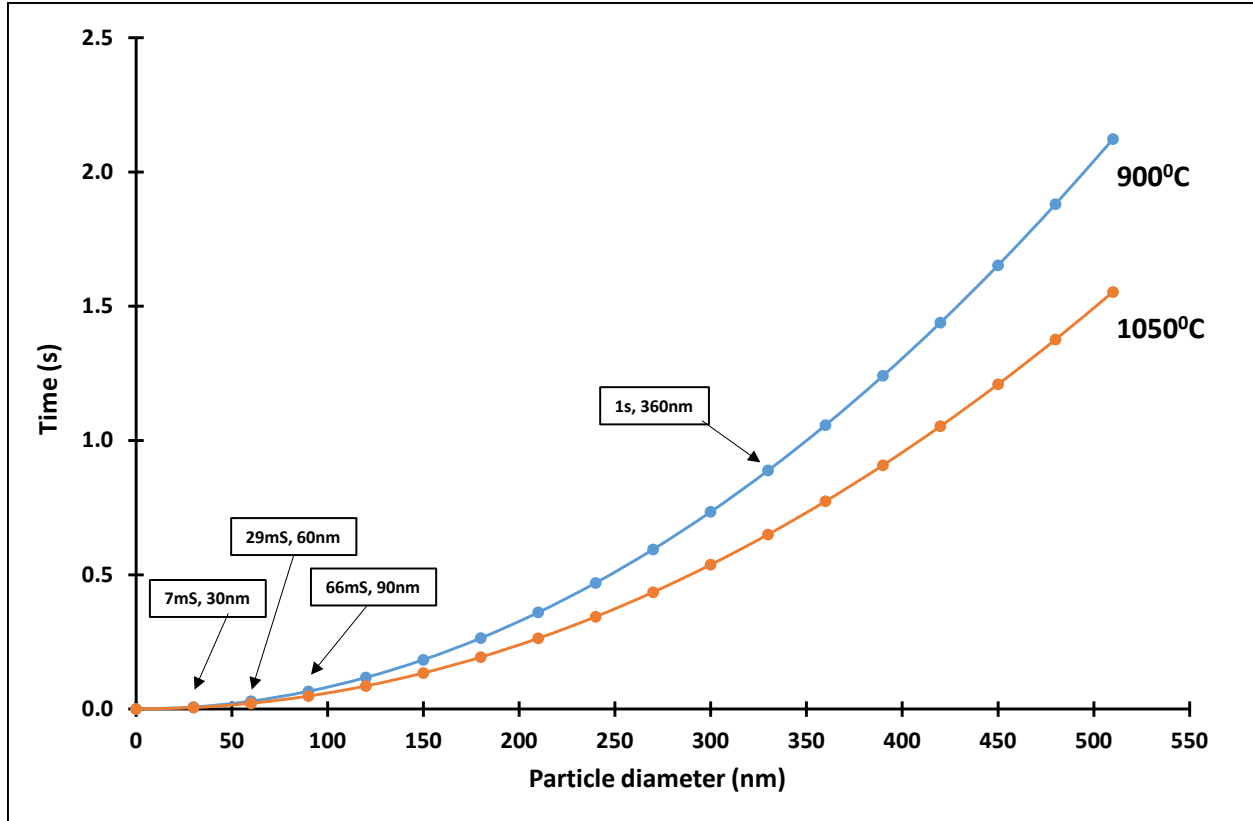
Figure 41. Time for particle to grow up to a size, for wt.%Ti = 2, chemisorption limited case.

Two possible events are proposed as a hypothesis to explain the growth interruption mechanism (GIM): (1) nanoparticle migration into the melt bulk and (2) bubble breakage. The events can work separately or in combination.

GIM by nanoparticle migration into the melt bulk

A model for the nanoparticle migration along the boundary layer is explored in Figure 43. Two concepts are first introduced: (1) The diffusive/Brownian character of the nanoparticle and (2) the boundary layer nature dependency on the external turbulence. Nanoparticles are small enough to experiment thermal diffusion motion. The Peclet number is used to calculate the particle size limit above which diffusive assumption is not valid [86].

$$Pe = \frac{convective\ particle\ flow}{diffussive\ particle\ flow} = \frac{6\pi R_p^{\ 3}\mu}{k_B \cdot T \cdot \rho}\dot{\gamma} = \frac{R_p^2}{D}\dot{\gamma} \qquad (58)$$

With $D = D_0 = \frac{k_B T}{6\pi v_0 R_p} \equiv$ diffusion coefficient from Stokes-Einstein theory for particles vol pct.$\rightarrow 0$. Pe>>1 implies dominant convective flow and Pe<<1 indicates self-diffusive/Brownian particle flow when a external shear is applied. The brownian character of a particle and its diffusion coefficient depend on the particle size and the

shear rate. Figure 42 illustrates the Peclet number in molten aluminum versus particle size at 900^0C and shear rate up to $\dot{\gamma}=1000,000s^{-1}$.
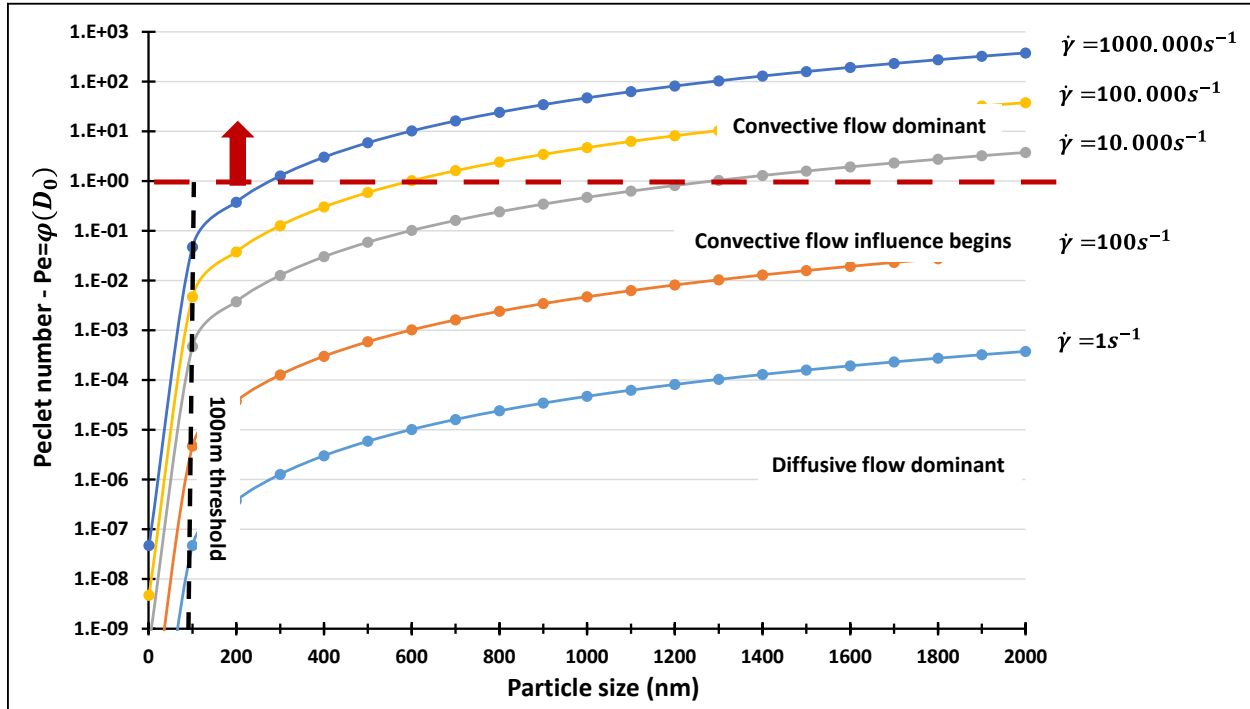

Figure 42. Peclet number evolution versus particle size and shear rate at 900^0C.

The nature of the boundary layer and the associated stresses may also be important. For $Re < 2 \cdot 10^5$ the boundary layer is laminar. The energy dissipation inside the boundary layer occurs only by viscous mechanism and the existing shear stress is mostly parallel to the interface. For $Re > 2 \cdot 10^5$ the boundary layer is turbulent. Energy dissipation for turbulent layer is a mixed mode between the viscous mode close to the gas interface and the turbulent eddies dissipation mode of the fluid bulk. The existing shear stress is both parallel and transversal to the interface. Some of the characteristics the model may have are next listed:

(1) A typical boundary layer thickness for a 5mm bubble will be around 50-100µm [69]. The shear rate profile inside the boundary layer follows a parabolic function from $\dot{\gamma} = 0$ at δ=0 to $\dot{\gamma} = \dot{\gamma}_{bulk}$ at δ=δ$_L$ (see Figure 43). It is reasonable to say that the nanoparticles inside the boundary layer are mostly diffusive in character and obey Fick's law.

(2) The thickness of reaction volume is much smaller than the boundary layer thickness. It is close to zero for the chemisorption limited case. For the carbon diffusion limited case, it is given by the coordinate at which the concentration

profile equals the carbon equilibrium concentration (see Figure 43). A reasonable order of magnitude might be 1-5µm.

(3) TiC nuclei form at x=0 with a production rate given by the nucleation rate (Figure 35). The synthesized nuclei detach from the bubble-melt interface at δ=0, and progress and grow towards the boundary layer limit. Nuclei detaching must be quick.

(4) Nuclei detaching should not be extremely difficult taking into account the poor existing wetting (Figure 34). The wetting surface tension needs to be overcome. The shear stress at $\delta_L \to 0$ may be important. Its value will depend on the nature of the boundary layer (viscous or turbulent), that depends on the melt bulk Reynolds number and the associated shear stress.

(5) The particle will stop growing as soon as it leaves the reaction volume. Taking the general x-t relationship for diffusive motion:

$$D = \frac{x^2}{2t} \to x = \sqrt{2D} \cdot \sqrt{t}$$

$$v = \frac{\partial x}{\partial t} = \frac{1}{2}\sqrt{\frac{2D}{t}} \equiv migration\ speed$$

(59)

with $D = D_0(900^0C, Rp = 50nm) = \frac{k_B T}{6\pi\eta R_p} = 5.5 \cdot 10^{-7} \frac{cm^2}{s}$ and applying equation 59, a 100nm particle will cover a distance of 3.3.µm in 100ms, the time for a particle to grow over 100nm calculated in Figure 41. In this way nanoparticles <100nm are evacuated from the reaction volume fast enough and nanoparticles are synthesized.

(6) For high enough shear rate in the melt bulk, a next flux of nanoparticles is washed away from the liquid boundary layer into the melt by the turbulent eddies bombarding the interface at x=δ_L. **If the washing rate is infinitely high there is no accumulation of particles in the boundary layer** and the 1st Fick Law applies with next boundary conditions:

$$x = 0, \qquad\qquad J_{nanopart_{x=0}} = R_{TiC\_nuc}\left[\frac{nuclei}{m^2 \cdot s}\right]$$

$$x = \delta_L, \qquad\qquad C_{nanopart} = 0 \quad if\ particles\ washed\ away$$

Note in Figure 42 the shear rate must be $\dot\gamma > 10^5 s^{-1}$ so particles with d_p<100nm in diluted media (for $D = D_0$) are affected by the turbulence. For particles with d_p>1µm the shear rate must be only $\dot\gamma > 10^3 - 10^4 s^{-1}$. **If the turbulence is low the nanoparticles washing rate is zero** and they

accumulate inside the boundary layer given that $R_{TiC\_nuc} > D_{nanopatr}\frac{\partial C_{nanopart}}{\partial x}$ and 2nd Fick law with next boundary conditions is proposed:

$$t = 0, \qquad\qquad C_{nanopart}(x, 0) = 0$$

$$x = 0, \qquad\qquad J_{nanopart_{x=0}} = R_{TiC\_nuc}\left[\frac{nuclei}{m^2 \cdot s}\right]$$

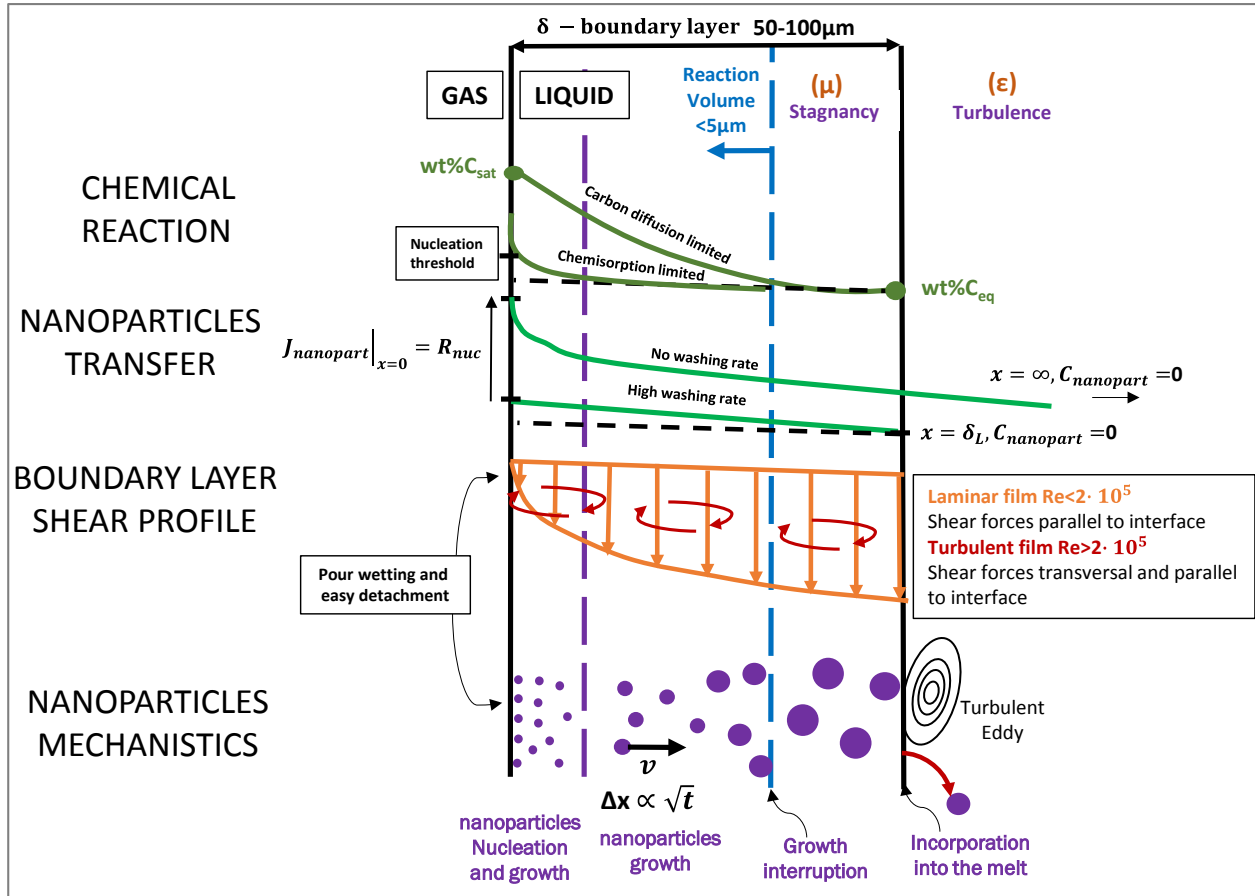$$x = \infty, \qquad C_{nanopart} = 0 \quad if\ particles\ not\ washed\ away$$

Figure 43. Complete model including the carbon profile, nanoparticles profile and shear profile.

For the case of no accumulation, the nanoparticles are in diluted state and $D=D_0$ (equation 58). If the particles accumulate, the concentration increases, particles interaction occur and the diffusion coefficient (D) decreases. The kinematic viscosity, associated to the diffusion coefficient, follows next expression [86] :

$$v = v_0\left(1 - \frac{vol\ pct.}{vol\ pct._{max}}\right)^{-2} \tag{60}$$

The term $vol\,pct._{max}$ equals 64, the value associated with random close packing. For $vol\,pct. \approx 30 - 50$ the kinematic viscosity increases 5-20 times and so it decreases the diffusion coefficient in equation 58. For a diffusion coefficient 5-20 times smaller, application of equation 59 results into a covered distance by the nanoparticle of 0.04-0.1μm in 100ms, i.e., microparticles will be likely synthesized. **In summary, a shear rate above $\dot{\gamma} > 10^5 s^{-1}$ at $x = \delta_L$ is critical to efficiently evacuate the nanoparticles into the melt before they grow up to 100nm (time scale in the range of 100ms) so particle size control is achieved.**

GIM by bubble breakage

The evolution of the boundary layer during bubble break up is uncertain. However, the evolution of the boundary layer during **coalescence** is well understood in 3 steps [87]. When two bubbles approach, (1) the liquid in between the bubbles drains with a given thinning rate (dδ/dt in Figure 44), (2) the layer between the two bubbles thins up to δ<100nm [88] and (3) the bubbles join and an instantaneous bubble geometry rearrangement, driven by the surface energy minimization, occurs. The boundary layer thinning is the limiting step. A backwards analogy is done for the bubble break up. In this case the process is happening under high turbulence: (1) the bubble surface is strangulated due to fluid shear forces overcoming the surface tension, (2) a critical bubble neck thickness is reached and (3) the bubble breaks up. The bubble strangulation is the limiting step. **We hypothesize** that, when the bubble strangulation occurs, analogous to the coalescence the boundary layer also thins up to δ<100nm. A massive amount of nanoparticles located in the strangulation region are released to the melt in this way. The bubble breakage, that needs shear rate above 100.000 s⁻¹ for bubbles with d_b<10mm (see Figure 40), occurs within a few tenths of a millisecond.

In summary, whichever is the right GIM event or combination of them, high turbulence and shear rate close or above 100,000s⁻¹ on the bubble interface is needed so the particle size is controlled in the nanoscale. **The threshold 100,000s⁻¹ is not intended to be an accurate frontier but an indicative order of magnitude.** The 2nd generation of the gas-liquid in-situ method (static tube) cannot offer such a high shear rate and turbulence whereas the 3rd generation (rotating impeller) does.
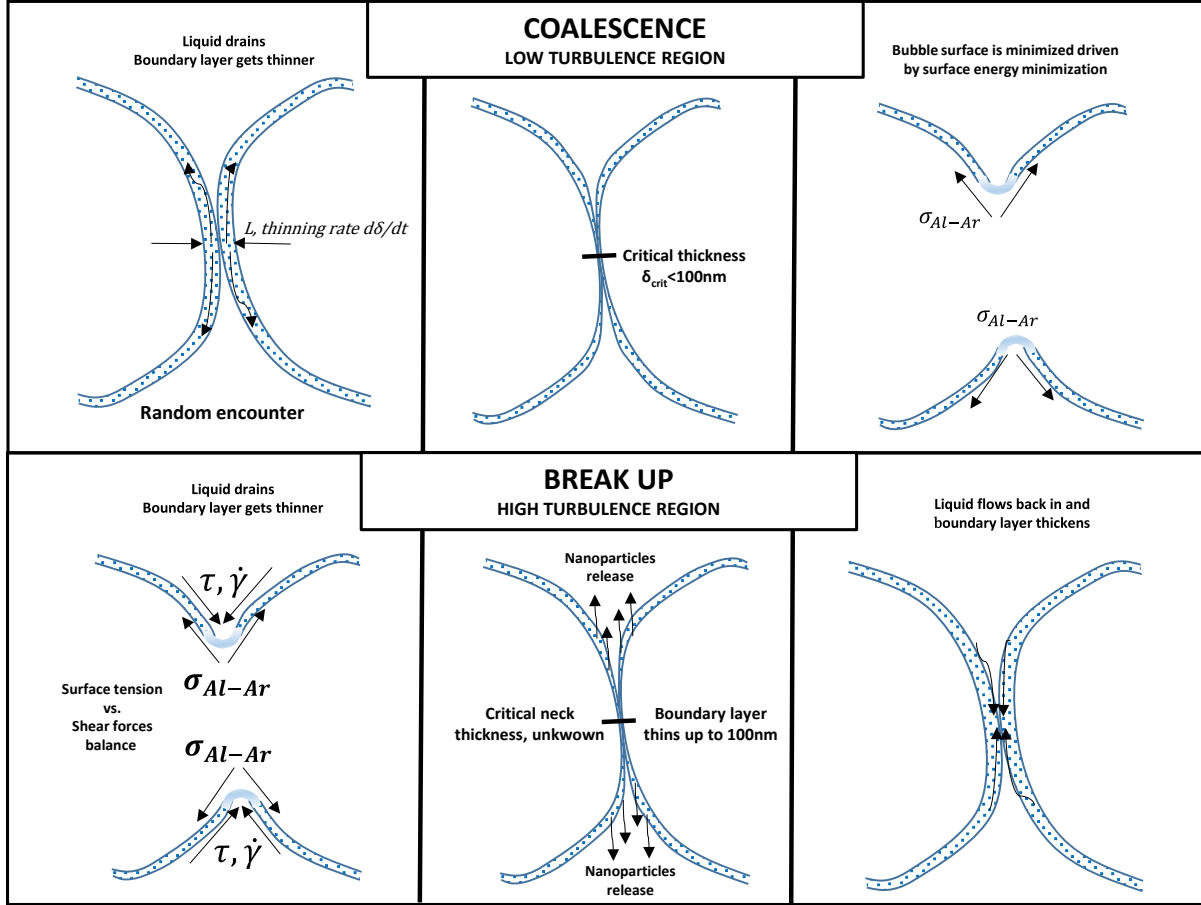
Figure 44. Coalescence and break up processes. Participating forces and boundary layer evolution.

2.4.5. Gas dispersion dynamics in a stirred crucible

In the previous subsection the interaction bubble-turbulent flow has been analyzed from a fundamental phenomenological point of view. The engineering part of it, which impeller is selected, how to calculate the processing parameters or which impeller-crucible geometry is used is next approached. In general, the tank-impeller geometry is fully defined by the dimensions of Figure 45. The π-set of the system is next introduced for a given impeller design (Rushton or PBT turbine in Figure 4). See [68] for a better understanding of dimensional analysis. After Zlokarnik [37]

$$\Pi \equiv \left\{ Ne, Q, Fr, Re, We, \frac{c}{D}, \frac{D}{A}, \frac{H}{A} \right\} \tag{61}$$
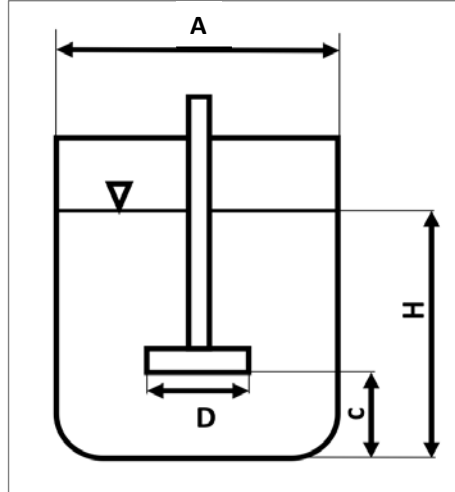
Figure 45. Main dimensions tank-impeller geometry.

The dimensionless number characteristics of the π-set are listed in Table 1.

Table 1. List of dimensionless numbers.

Number	Interpretation	Formula
Newton number (Ne)	Ratio of drag resistance force to inertia force	$\dfrac{P}{N^3 \cdot D^5 \cdot \rho_{melt}}$
Flow number (Q)	----------	$\dfrac{q}{N \cdot D^3}$
Froude number (Fr)	Ratio of inertia and gravity/buoyancy forces	$\dfrac{N^2 \cdot D}{g}$
Reynolds number (Re)	Ratio of inertia to viscous forces	$\dfrac{\rho N D^2}{\mu_{ap}}$
Weber number (We)	Ratio of shear forces to surface tension	$\dfrac{\tau D}{\sigma}$
$\dfrac{c}{D}, \dfrac{D}{A}, \dfrac{H}{A}$	Geometry ratios	----------

In this section it is assumed turbulent flow regime ($Re > 10^4$) and a constant set of geometry numbers. The geometry numbers will be optimized in the next section so flow turbulence is maximum. Also, for $Re > 10^4$, Ne is constant for small Q [37]. The remaining π-set is:

$$\prod \equiv \{Fr, Q, We\}$$

The mechanistic explanation of the gas dispersion takes place in the impeller boundary area and it is next given in Figure 46.
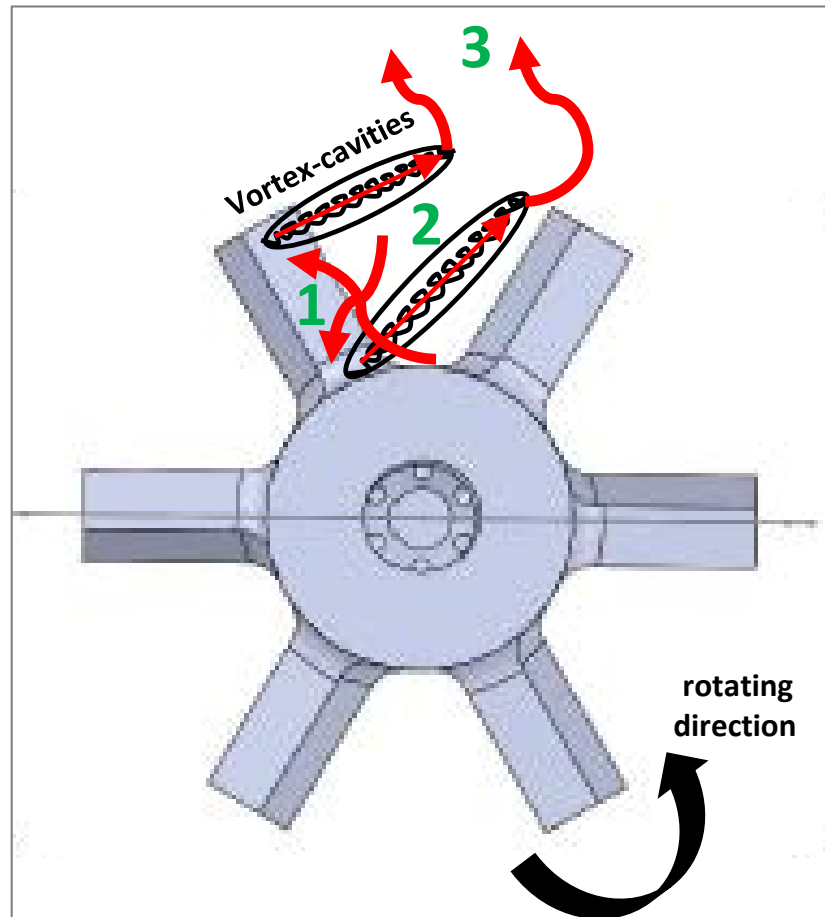
Figure 46. Mechanistic explanation of gas dispersion in a Ruhston turbine.

Behind the blade tips low pressure areas appear called trailing vortexes (see Figure 46) in which shear rate and energy dissipation rate are maximum. First (step 1 in Figure 46), the gas bubbles, attending to the ratio buoyancy forces/liquid centrifugal forces (given by the Froude number) are sucked by the trailing vortex or escape to the liquid free surface. Second (step 2 in Figure 46), the bubbles break up by the bubble-eddy interaction inside the blade vortex and third (step 3 in Figure 46) the bubbles are finally evacuated with the pumped flow. The liquid trailing vortex is called cavity when mixed with gas. Depending on the gas flow and impeller speed there are five main flow regimes associated with five types of cavity systems in the impeller region (Figure 47)[39].
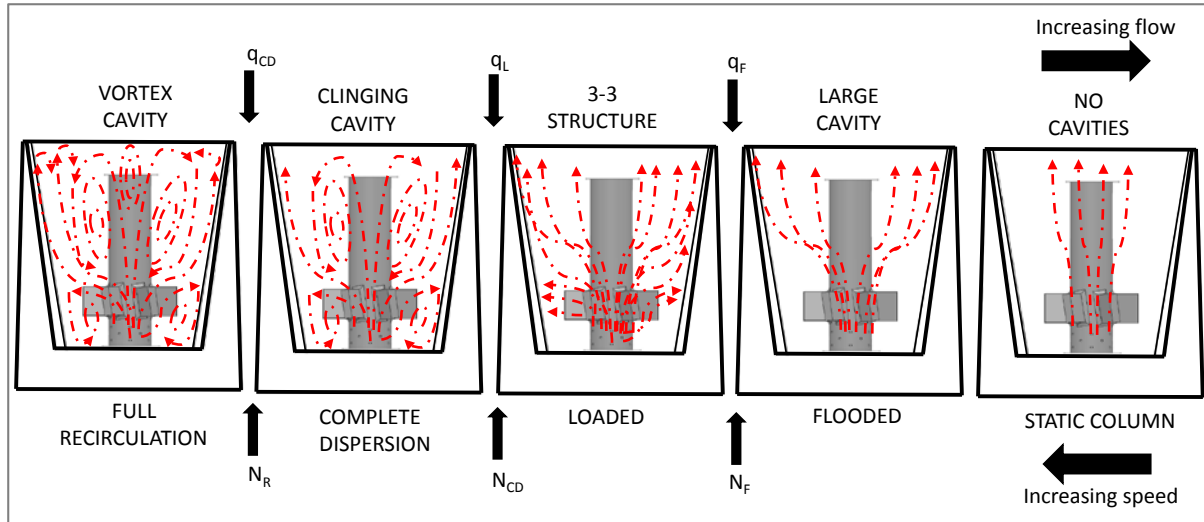
Figure 47. Schematic representation of the different gas-liquid flow regimes.

Figure 47 is analyzed for a constant rotation speed and increasing gas flow (upper part from left to right direction). An initial minimum gas flow is sucked by the impeller cavity (vortex cavity) and fully recirculated in the tank (full recirculation regime). Continuous increase of the gas flow (q_{CD}) loads the gas cavities (clinging type cavities) which still disperse the gas in the full tank volume (complete dispersion regime) but only partially recirculate the gas. Further increase of gas flow (q_L) loads the cavities and some get partially flooded (3 large cavities appear in a 3-3 clinging-large cavities structure) not being the impeller able to spread the bubbles along the full tank volume (loaded regime). Finally, the flooding gas flow (q_F) is reached, in which the gas is not dispersed, the cavities are all large cavities and the tank behaves as a static gas-liquid column. The static gas-liquid column is analogue to our 2nd generation of the gas-liquid ins-itu method. Industrial chemical tanks normally work at the loaded regime as a compromise between a good dispersion and mass transfer, which it might not be the solution to produce nanoparticles of a given size.
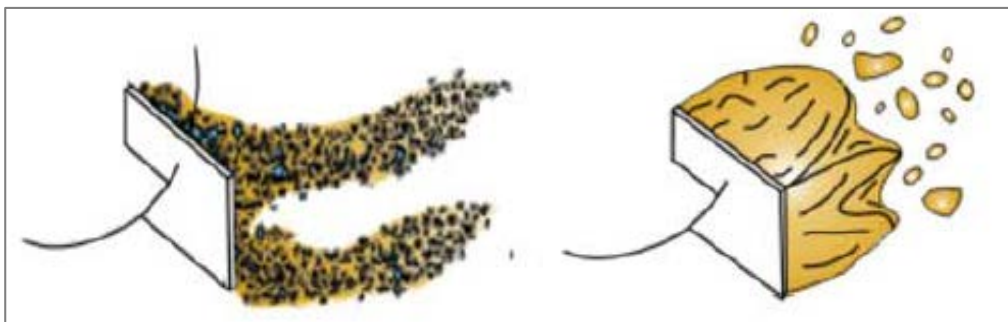
Figure 48. Vortex cavity (left) and large cavity (right). They are set by the gas dispersion regime.

Gas-flow regime quantitative allocation

The surface tension is demonstrated to have no influence on the allocation of the different gas dispersion regimes [37] so the *We* number is also removed from the pi-set. After Niewnow [39], next correlations are proposed, for a six blades Rushton turbine, to allocate the different gas-liquid flow regimes (Figure 47) for the pi-set $\prod \equiv \{Fr, Q\}$ and Re>10^4 (turbulent conditions).

Gas Flow number intervals	Cavity type/gas-liquid flow regime	
$Q < 13Fr^2 \cdot \left(\dfrac{D}{A}\right)^5$	Vortex cavity/full recirculation	(62)
$13Fr^2 \cdot \left(\dfrac{D}{A}\right)^5 < Q < 0.2 \cdot \left(\dfrac{D}{A}\right)^{0.5} \cdot Fr^{0.5}$	Clinging cavity/full dispersion	(63)
$0.2 \cdot \left(\dfrac{D}{A}\right)^{0.5} \cdot Fr^{0.5} < Q < 30Fr\left(\dfrac{D}{A}\right)^{3.5}$	3-3 cavity structure/Loaded	(64)
$Q > 30Fr\left(\dfrac{D}{A}\right)^{3.5}$	Large cavity/Flooded regime	(65)
$Fr < 0.045$	Static bubble column alike	(66)

For a four blades PBT turbine, for the pi-set $\prod \equiv \{Fr, Q\}$ and Re>10^4 (turbulent conditions):

Gas Flow number intervals	Cavity type/gas-liquid flow regime	
$Q < 0.08Fr^{0.75}$	Clinging cavity/full dispersion	(67)
$Q > 0.08Fr^{0.75}$	Large cavity/Flooding regime	(68)

Because of the instabilities in torque and power draw which can occur with PBT turbines [89], there is no practical operating regime between flooding regime and complete recirculation regime and only one correlation and two gas dispersion regimes are identified. Solving the correlations for both turbines Figure 49 and Figure 50 result, for a Rushton turbine with diameter 2" and a PBT turbine with diameter 2", respectively. These figures are called the gas-liquid dispersion maps and they allocate the different dispersion regimes dependent on the gas flow – rotation speed pair of variables. For scaling up purposes, a more powerful analysis chart independent on the size plots the *Fr* and *Q* variables in the X and Y axis respectively. It is observed in Figure 49 that a small gas flow under 10L/min is the key factor to maintain the gas dispersion intensity (shear stress and energy dissipation on bubbles) at its highest value. **Any of the two previously proposed** events for the

GIM to happen may be explained in a system allocated in the full recirculation regime region. In this region both the external turbulence, the shear rate at the bubble interface and the bubble breakage frequency inside the blade cavity are maximized.
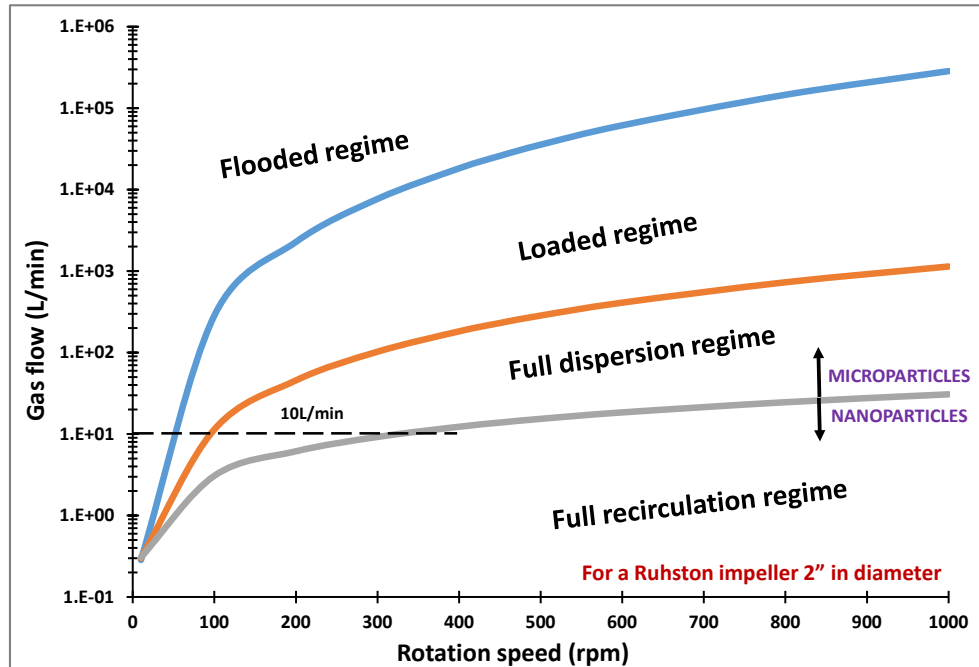

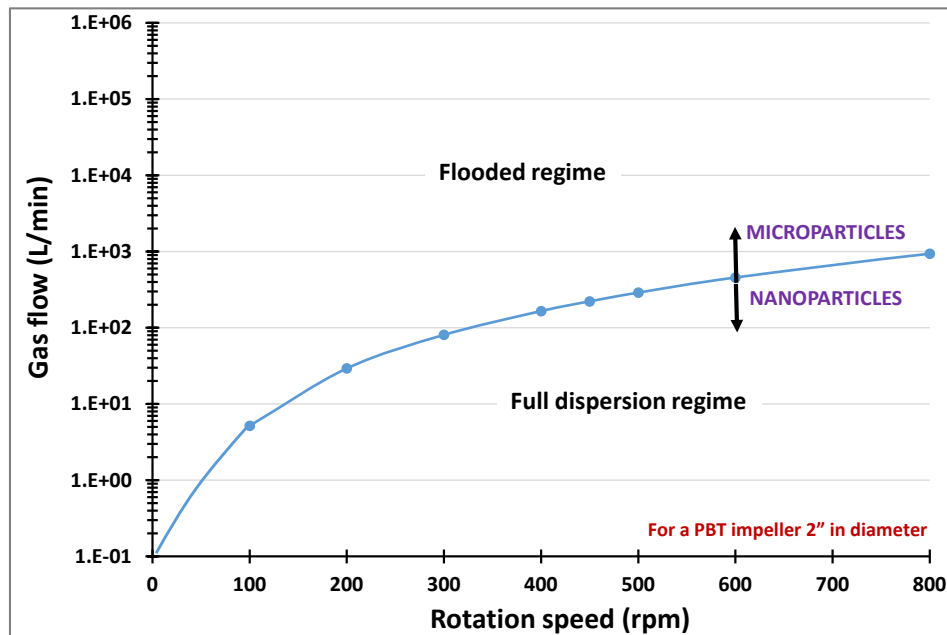Figure 49. Gas-liquid flow regime map for a Rushton turbine 2" in diameter and Re>10^4.

Figure 50. Gas-liquid flow regime map for a PBT turbine 2" in diameter and Re>10^4.

Impeller selection

We have selected a Rushton turbine with 6 blades for the experimental part. This is the traditional Rushton turbine, with higher gas flow capacity for gas dispersion than the PBT [37, 39, 82]. The blades angle to the vertical line is 8^0 to guarantee perpendicular fluid into the wall and equal flow upwards and downwards (see Figure 51). The blades surface (width and length) is big enough to enable a good pumping capacity (step 3 dispersion in Figure 46). The design of the gas sparger is based on [90, 91]. The sparger has been placed right below the blades. It has 6 nozzles with a diameter of 0.05"(1.25mm). The nozzles number and nozzles diameter has been selected based on the criterion of minimum Reynolds [90]. This criterion stablishes that all nozzles are equally effective so gas flow is equally dispersed, if $Re_{nozzle}>2100$. For a 1.5L/min gas flow at the tube inlet, i.e. $F_g \cdot \frac{T_{noozle}}{T_{flowmeter}} = 1.5\frac{L}{min}\frac{1273K}{298K} = 4.25\frac{L}{min}$, $\rho_g = 1.5kg \cdot m^{-3}$, $\mu_g = 2.1 \cdot 10^{-5}Pa \cdot s$ and $\frac{T_{noozle}}{T_{flowmeter}} = \frac{1273K}{298K}$

$$Re = \frac{d_{nozzle} \cdot v_g \cdot \rho_g}{\mu_g} = \frac{d_h \cdot F_g \frac{T_{noozle}}{T_{flowmeter} \cdot nozzles \#} \cdot \rho_g}{\mu_g} = 2083 \text{ for 4 nozzles.}$$

Two extra nozzles up to 6 nozzles are included in case any nozzles gets clogged with soot.
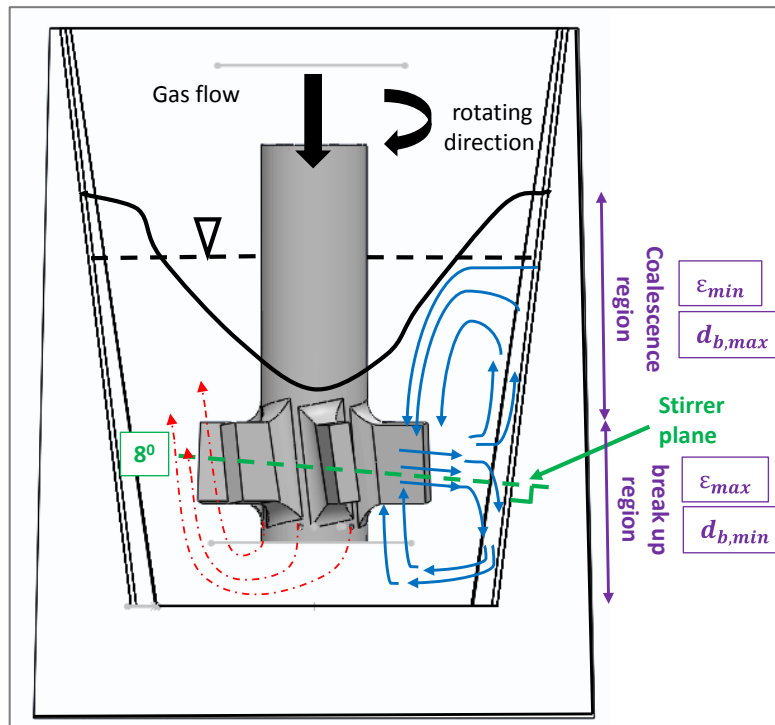
Figure 51. Impeller design and main regions of bubble break-up and coalescence.

Calculation of the volumetric energy dissipation 'ε' and shear rate $\dot{\gamma}$

The allocation of the system in the fully recirculated gas flow regime in Figure 49 and Figure 50 is a neccesary condition but probably not enough. We stated in the previous subsection that a shear rate in the range of 100,000s⁻¹ is neccesary so the GIM occurs. The shear rate in the fluid can be calculated with equation 53, once the volumetric energy dissipation 'ε' is known. Okamoto et al.[92] also reported two different levels of energy dissipation, one near the impeller and another in the liquid bulk. For a six-blade disk style turbine impeller with w=0.2D, 0.05<w/A<0.3 and 0.25<D/A<0.70:

$$\varepsilon_{imp} = 7.8 \cdot \left(\frac{P}{\rho V_{melt}}\right)\left(\frac{D}{A}\right)^{-1.38} exp\left(\frac{-2.46D}{A}\right) \tag{69}$$

$$\varepsilon_{bulk} = 0.90 \cdot \left(\frac{P}{\rho V_{melt}}\right)\left(\frac{D}{A}\right)^{1.10} \tag{70}$$

The impeller power 'P' can be calculated from the Newton number in next correlation of the type $Ne = \varphi(Re, Fr, Q)$, for a six flat blade turbine with $D/A=0.2$ and for a $Q<0.2$ and $Fr>0.15$ is used [37]:

$$Ne = 1.5 + (0.5Q^{0.075} + 1600Q^{2.6})^{-1} \tag{71}$$

The energy dissipation rate and the shear rate (calculated from equation 53) are plot in Figure 52 at 900⁰C. The averaged volume energy dissipation is calculated from:

$$\varepsilon_{av} = \frac{1}{3}\varepsilon_{imp} + \frac{2}{3}\varepsilon_{bulk} \tag{72}$$

At least 400-450rpm (maximum rotation speed of our apparatus in Figure 2) are required to get shear rates in the range of 100,000s⁻¹, inside the complete recirculated regime in Figure 49.
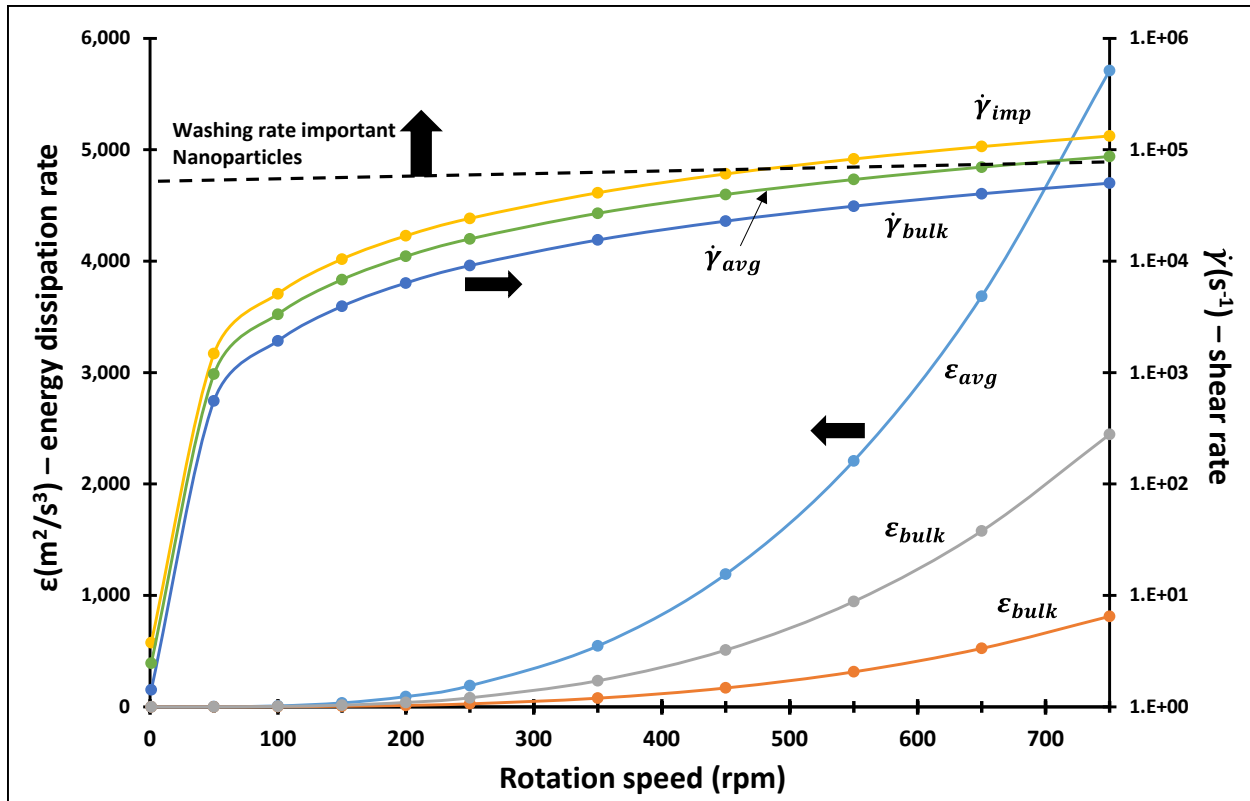
Figure 52. Energy dissipation and shear rate vs. rotation speed for a 2" Rushton turbine at 900°C.

Calculation of the volumetric gas-liquid interface 'a'

The volume specific bubble interfacial area a inside the melt is next calculated based on the topics previously covered. It is a neccesary magnitude as it is related to the overall TiC production by equation (4). It is a complex spatial dependent magnitude [37, 82]. Two distinct bubble sizes are usually analyzed: (1) the minimum bubble size $(d_{b,min})$ obtained at the impeller cavitites and (2) a maximum bubble size $(d_{b,max})$ above the impeller where the coalescence dominates (Figure 51). An average volumetric bubble size (d_{av}), also called Sauter diameter, is assumed for the calculation of $d_b = d_{b,av}$. The Sauter diameter approach implicitly assumes that: (1)the bubbles are spherical, (2) the rate of break-up and coalescence is infinite and (3) the variation of the liquid mass transfer coefficient (K_L) in equation 41 is dependent on the turbulent flow characteristics and not on the bubble size [83]. This last assumption is the least accurate and to overcome it more sophisticated approaches introduce population balances which are out of the scope here [83]. The volumetric gas liquid interface is related to the gas volumetric fraction (ϕ) and bubble diameter $(d_{b,av})$ with next expression, assumed monodispersed size distribution and spherical bubbles [82, 83]:

67

$$a = \frac{\phi}{6d_{b,av}} \tag{73}$$

The calculation of the minimum bubble size $(d_{b,min})$ has been correlated experimentally by dimensional analysis [37, 82] for a specific gas-flow dispersion regime under turbulent conditions. Under this conditions, the pi-set in equation is (see [37]):

$$\Pi \equiv \left\{ \frac{d_{b,min}}{D}, We \right\} \tag{74}$$

For the target number $d_{b,min}/D$, correlations of the form below are published in bibliography [83]:

$$\frac{d_{b,min}}{D} = \varphi(We) \tag{75}$$

$$\text{with } We = \frac{\tau_{av} \cdot D}{\sigma_{AlTi-Ar}} = \frac{\mu \cdot \dot{\gamma}_{av} \cdot D}{\sigma_{AlTi-Ar}}$$

Note the characteristic length included on the dimensionless numbers is the impeller diameter (D) and not the bubble size $(d_{p,min})$, which is the target. The volume averaged diameter d_{av} is correlated taking into account the gas volumetric fraction (ϕ). Next correlation [82] is valid for an unbaffled gassed tank with a Rushton turbine, $H/D=1$, $D/A=0.66$ and $Re>10^4$.

$$d_{av} = f_d \cdot Ne^{-2/5} \cdot We^{-3/5} \cdot D^{3/5} \cdot H^{2/5} \cdot \phi^{1/2} + \lambda_{min} \tag{76}$$

With $f_d = 3.76$ and λ_{min} calculated from equation 52 and 72. For the calculation of the Newton number correlation71 is used. For the calculation of the gas hold up (ϕ), Smith [93] calculated next correlation for the loaded dispersion regime:

$$\phi = 0.85 \cdot (Re \cdot Fr \cdot Q)^{0.35} \left(\frac{D}{A} \right)^{1.25} \tag{77}$$

Eventhough the dispersion regime of the current system operation window is the fully dispersion/recirculation regime, the previous correlation is still accurate enough [93]. A variability analysis of the average bubble size, gas hold up and specific interface area is done in Figure 53, Figure 54, Figure 55 for a gas flow of 1L/min (or 3-5L/min at 800-1100⁰C) using equations 73-77. For the calculation of the Weber number, the bubble surface tension is calculated from [75].

$$\sigma_{AlTi-Ar}[N/m] = (948 - 0.202 \cdot T)/1000$$

f_d is experimentally calculated, indicates the coalescence intensity and it is specific of the gas-liquid system, in this case the air-water system. The aluminum-argon system has a surface tension ten times bigger and a viscosity 5 times times smaller

for a temperature above 1000^0C that the air-gas system. The results here obtained should be taken cautiously given the inaccuracy derived from f_d in equation 76.
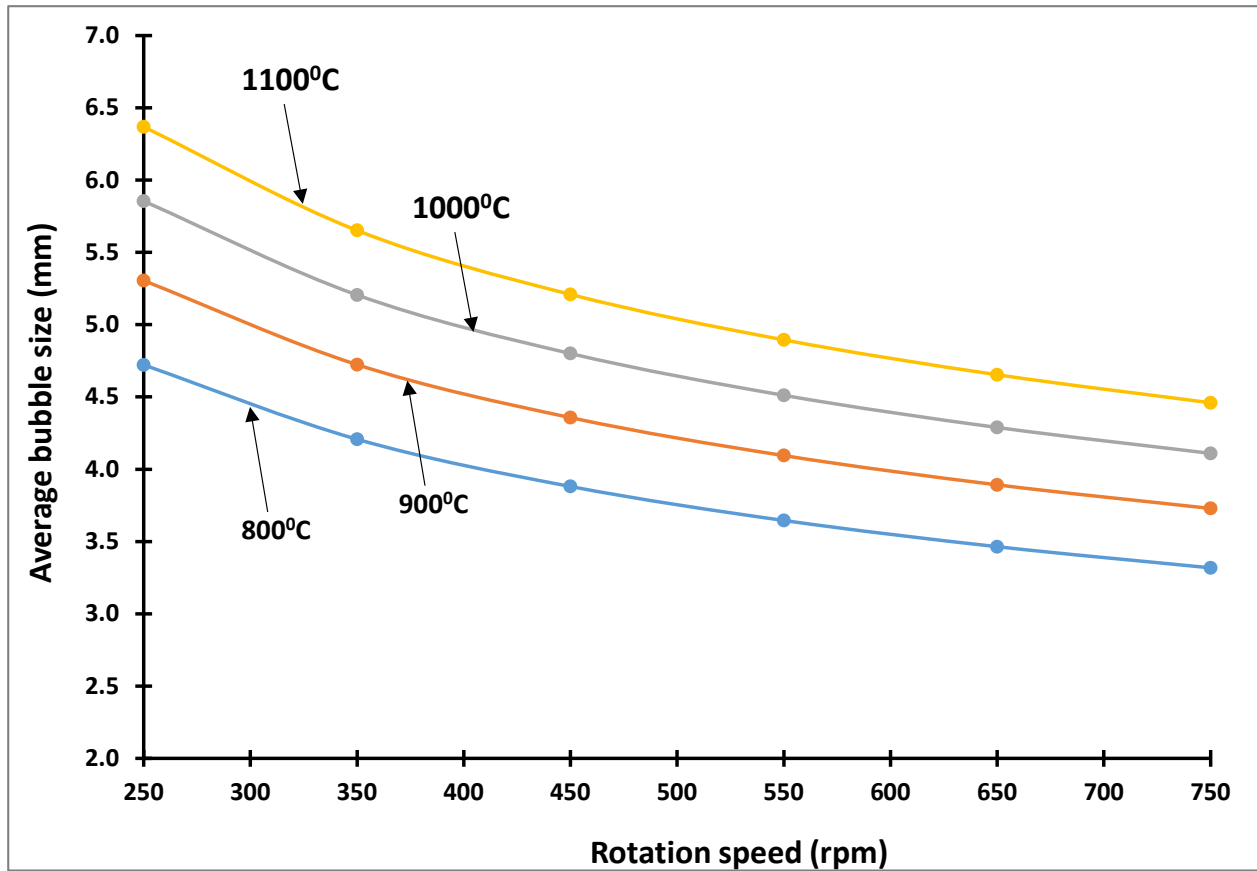

Figure 53. Bubble size variation vs. rotation speed and temperature.
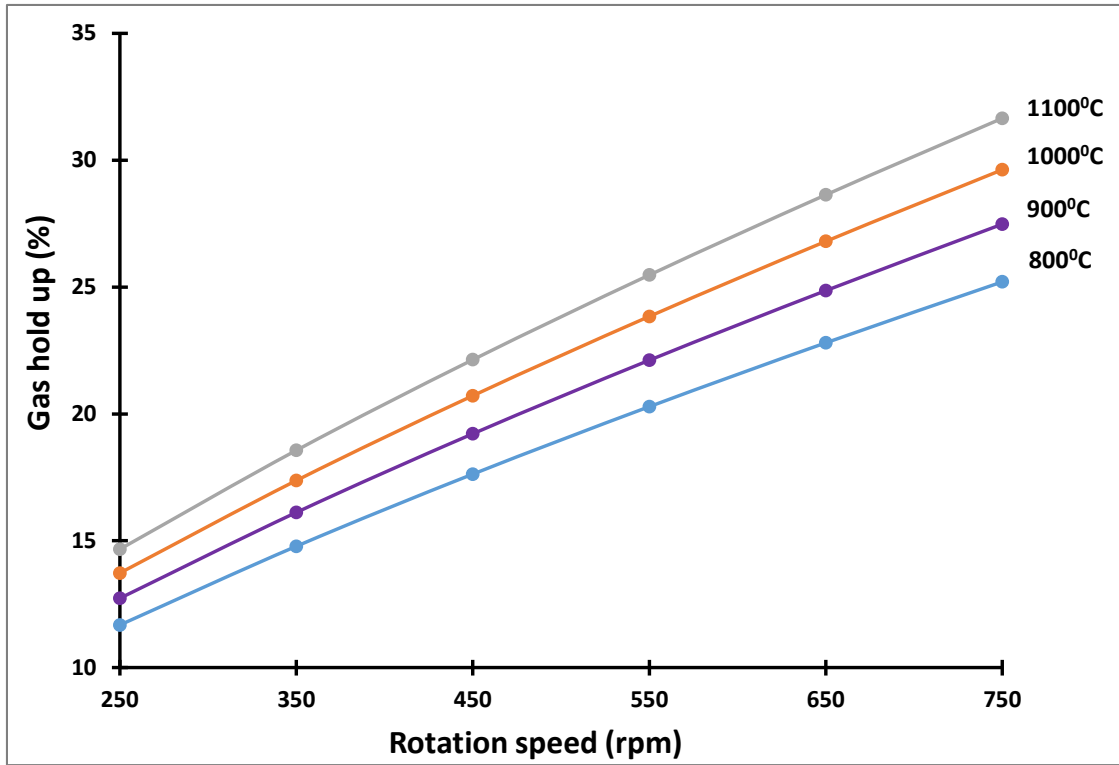
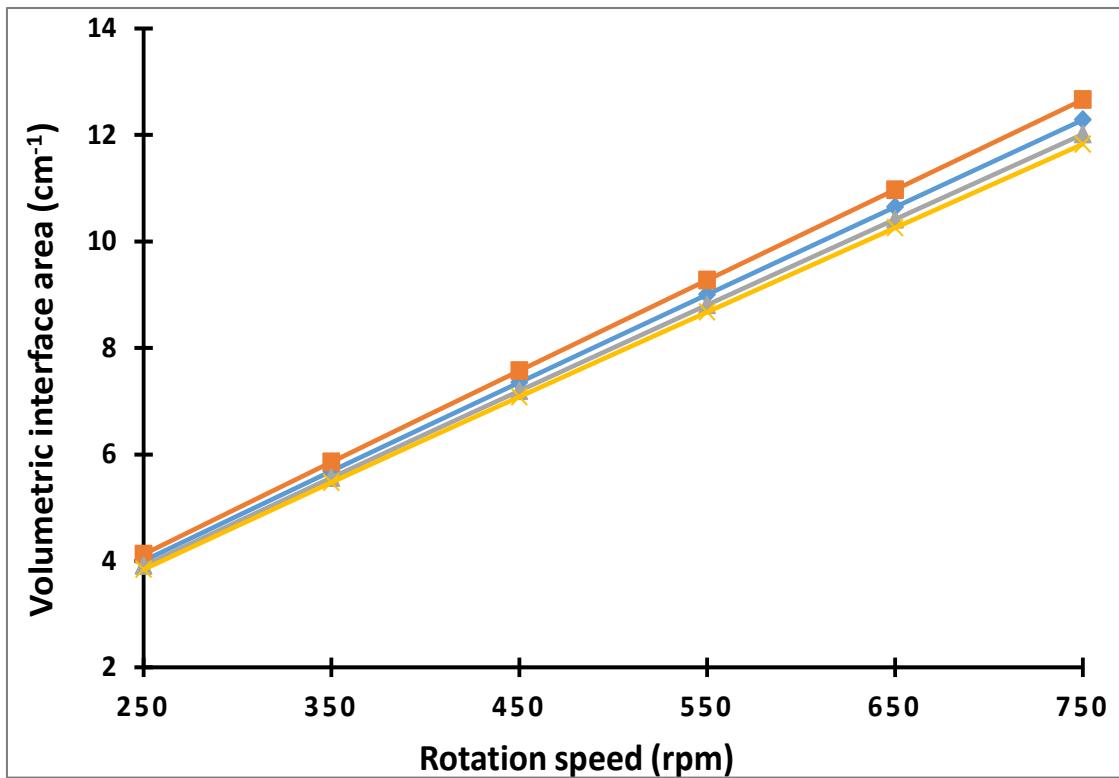Figure 54. Gas hold up variation vs. rotation speed and temperature.

Figure 55. Gas hold up variation vs. rotation speed and temperature.

The rotation speed does not have a big impact on the average bubble size but it clearly impacts the gas volume fraction (or gas hold up) and the volumetric interface area. The bubble size becomes asymptotic because the smallest eddy size (given by the Kolmogorov scale in equation 52 behaves asymptotically. However, the gas hold up increases because a higher rotation speed implies higher capability of the impeller cavities to suck the bubbles several times and for longer time so the residence time of the bubble in the melt increases. More important, and as a result of the gas hold up increase, the interface area increases by 4X , from $3cm^{-1}$ up to $12cm^{-1}$,for a rotation speed increase from 250rpm to 750rpm and constant gas flow. The nanoparticles production rate increases by 4X (see equation (4)). Temperature effect is negligible.

2.4.6. Conclusions

A particle size control model has been proposed in which:

(1) Nucleation can happen in both heterogeneous and homogeneous conditions. Chemisorption limited kinetics will favor the heterogeneous nucleation whereas diffusion limited kinetics will account for both.

(2) A single nucleation threshold is calculated. Both nucleation and growth domains are included in the boundary layer model.

(3) The growth is both interface and diffusion dependent (mixed control) for particle size below 10nm and diffusion dependent for particle size above 10nm.

(4) For the particle size to be controlled under 100nm some sort of particle bubble detachment event must occur every 100mS or less

(5) Two events are proposed to explain the growth interruption mechanism (GIM), the nanoparticle migration into the melt bulk and the bubble breakage mechanism. They can occur individually or in combined occurrence.

(6) Both are strongly linked to a very intense gas- dispersion regime with shear rate above $100,000s^{-1}$. Such a high shear rate is only achievable by the 3rd generation of the gas-liquid in-situ method and not the 2nd one. Only the third generation can produce nanoparticles.

(7) The gas dispersion dynamics are described at the engineering level. A method for the calculation of the gas flow and impeller rotation speed, independent on the scale, is proposed so high dispersion intensity (high energy dissipation 'ε' and shear rate '$\dot{\gamma}$') is assured. At least 350-450rpm are required for a1L/min gas flow.

(8) A 6 blades Rushton turbine has been selected so both gas dispersion and mixing flow are maximum.

(9) The impact of the impeller rotation speed on the volumetric bubble melt interface 'a' has been quantitatively analyzed.

2.5. Fluid Dynamic Considerations for Viscous Liquids

5.1. Empirical observations

Borgonovo and Makhlouf [1] did a parametric analysis with 14 experiments for the production of Al-AlN nanocomposites with the third generation of the gas-liquid in-situ method and a PBT turbine. The 14 experiments are allocated in the PBT turbine gas-flow map in Figure 56.
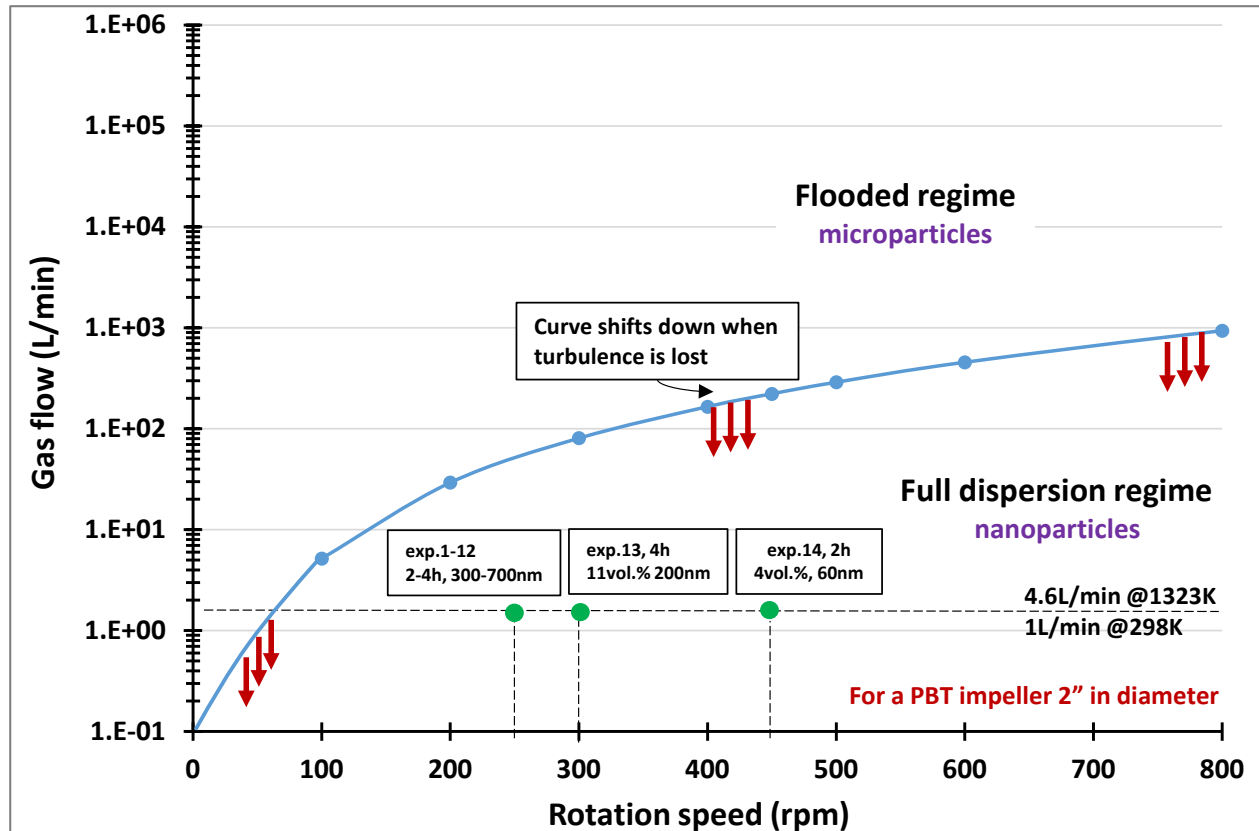

Figure 56. Allocation in the PBT turbine gas-flow map of the experiments performed in [1].

Only experiment 14 resulted in narrow particle size distribution with particle size of 30-60nm. However, experiments 1-13 seem to be well positioned in the diagram in Figure 56 based on the GIM mechanism introduced in the previous section. A turbulent regime is expected at the beginning of the run in which the GIM is valid. The nanoparticles concentration increases along the time so a gradual increase in rheology and a decrease of turbulence occurs simultaneously (see Figure 8). The melt eventually transitions into the laminar regime, gas dispersion is not possible and microparticles are produced. It is expected that, an initial narrow nanoparticles distributions widens and coarsens along the experiment time until it eventually

becomes a microparticle distribution. Figure 57 shows the qualitative effect of experiment time in the particle size distribution.
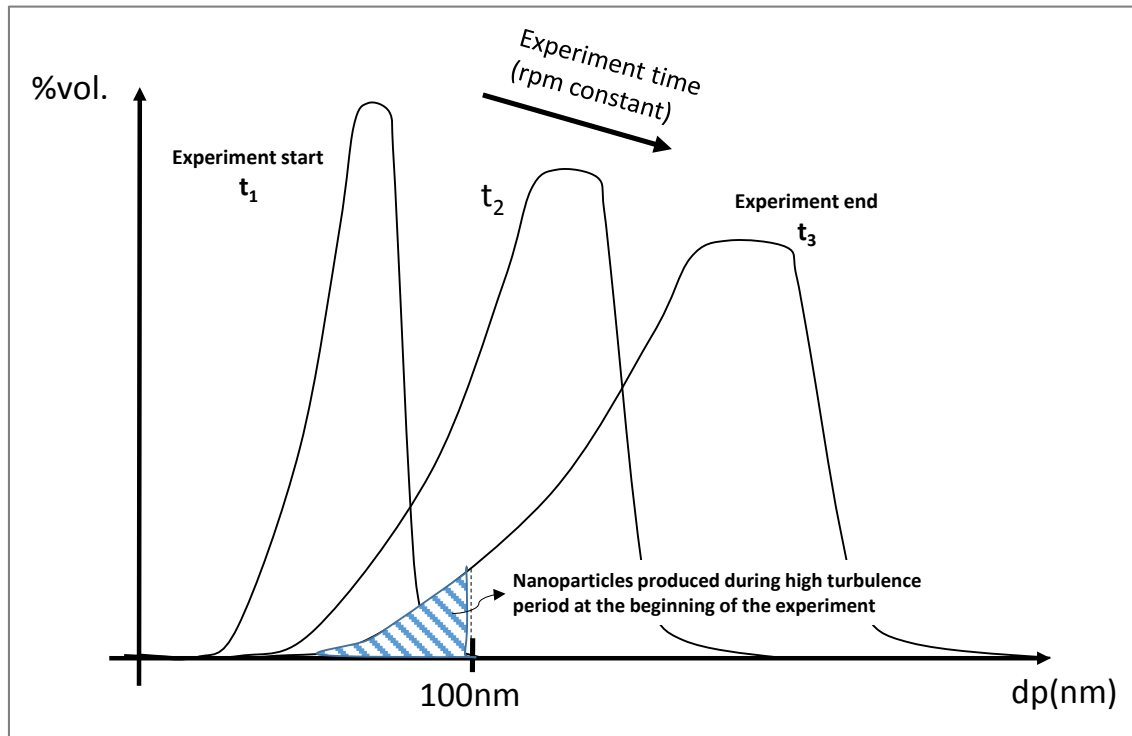
Figure 57. Particle size evolution along the experiment time for a constant rotation speed.

It is hence hypothesized that Experiment 13 in [1] will lead to a narrow particle size distribution when the experiment time (4h) is reduced to 1 or 2 hours. A new experiment was done by us in order to confirm the previous hypothesis. Experiment 14 was reproduced following the procedure in [1], but for a longer experiment time up to 3h so the nanoparticles concentration raised from 4vol pct. up to 7vol pct. The new ingot, that we call Experiment 15, has been analyzed at different height locations. Figure 58 shows: (1) nascent stagnancy on the ingot top peripheral region, (2) dramatic loading segregation up to 14vol pct. in the top of the ingot and (3) particle coarsening with average size increase up to 60-90nm in the top of the ingot. Figure 59 shows another picture of the top of the ingot with two microparticles over 1μm surrodunded by nanoparticles.
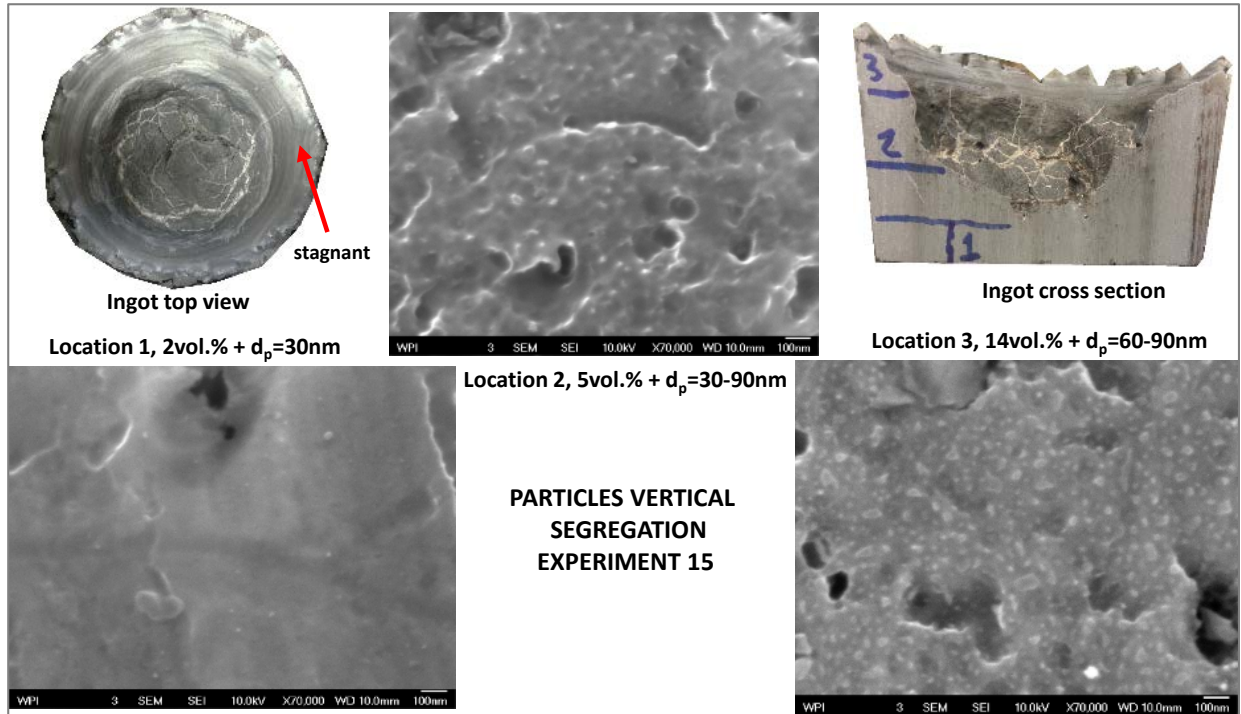
Figure 58. Loading segregation in the ingot vertical direction in experiment 15.
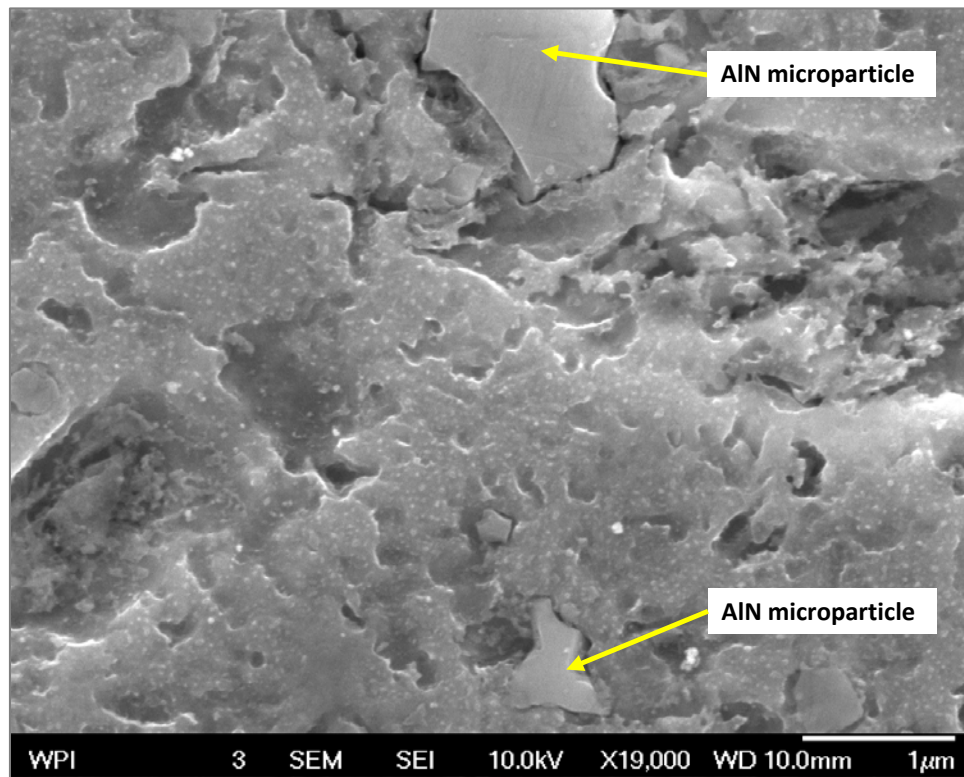
Figure 59. Nanodispersion with isolated AlN microparticles in the ingot top for a 7 vol pct. AlN.

The vertical segregation pattern is explained as follows: the peripheral top side of the ingot is the furthest region from the impeller and the region in which turbulence rheology problems appear first. Two events occur there: (1) thicker particles are produced and (2) nanoparticles from the ingot bottom flowing across the top, helped by the gas bubbles and liquid flow, are trapped by the viscous liquid. Eventually stagnancy appears and progresses downwards and inwards. Figure 60 illustrates the above explanation. Kadic et. al[94], for example, describe exactly the same stagnancy phenomena in the melt bulk when non Newtonian liquids with increasing viscosity along the time are mixed.
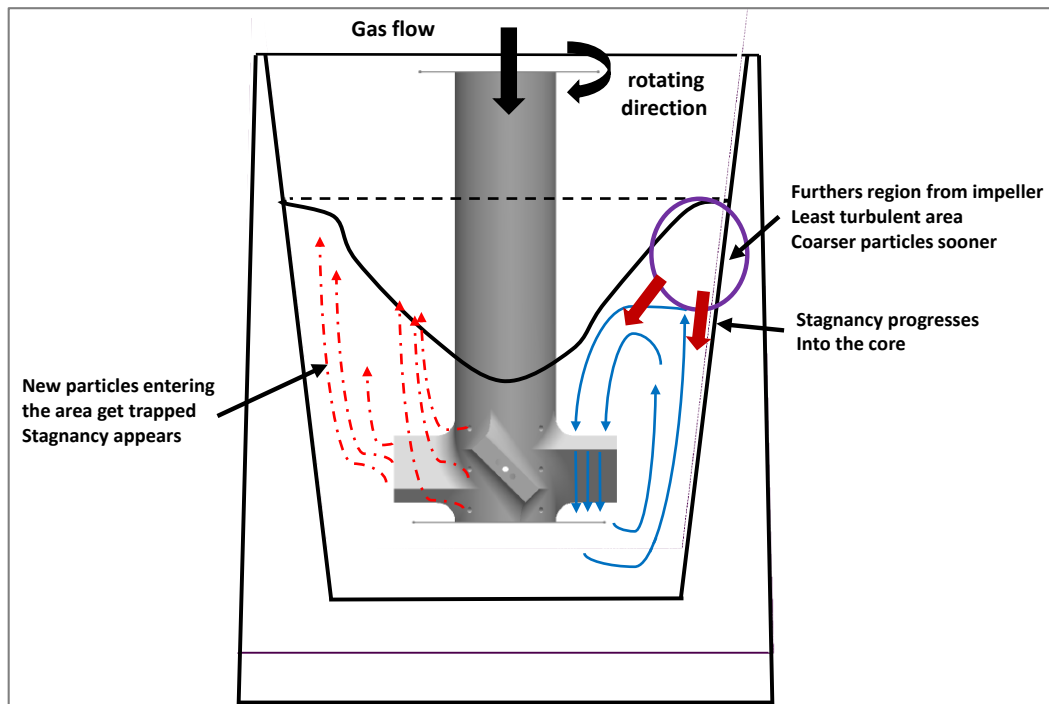
Figure 60. Spatial pattern for turbulence lost along the melt in an un-baffled-PBT system.

In summary, the whole description of particle size control and gas-liquid dynamics included in the previous section is valid for *Re>10⁴*. A theoretical quantitative understanding of the role of the impeller-crucible geometry and rotation speed on how to handle the rheology increase is further developed in this section. The melt rheology equations are first introduced. Second, the impeller-tank geometry is optimized so laminar regime and stagnancy are delayed as much as possible. Third, a quantitative effort is done to understand how rotation speed and crucible baffling help to avoid laminar regime and stagnancy. Finally, the critical rotation speed for Al_3Ti intermetallics floating, that form in the solid-liquid zone of the operation window (Figure 17) is calculated. This will assure melt homogeneity and properties control.

2.5.2. Melt rheology

The melt, due to the nanoparticles effect on rheology, is considered to be a pseudo plastic shear thinning liquid [40], i.e. its viscosity decreases with increased shear rate following equation 78.

$$\tau = \tau_0 + K \cdot \dot{\gamma}^n \tag{78}$$

In which 'n' is the shear thinning coefficient (dimensionless) and K is the material consistency index (dimension dependent on 'n'). The apparent viscosity (μ_{ap}) is

$$\mu_{ap} = \frac{\tau}{\dot{\gamma}} = \frac{\tau_o}{\dot{\gamma}} + K \cdot \dot{\gamma}^{n-1} = \mu_o + K \cdot \dot{\gamma}^{n-1} \tag{79}$$

$$\text{where} \quad \tau = \mu_{ap} \cdot \dot{\gamma}$$
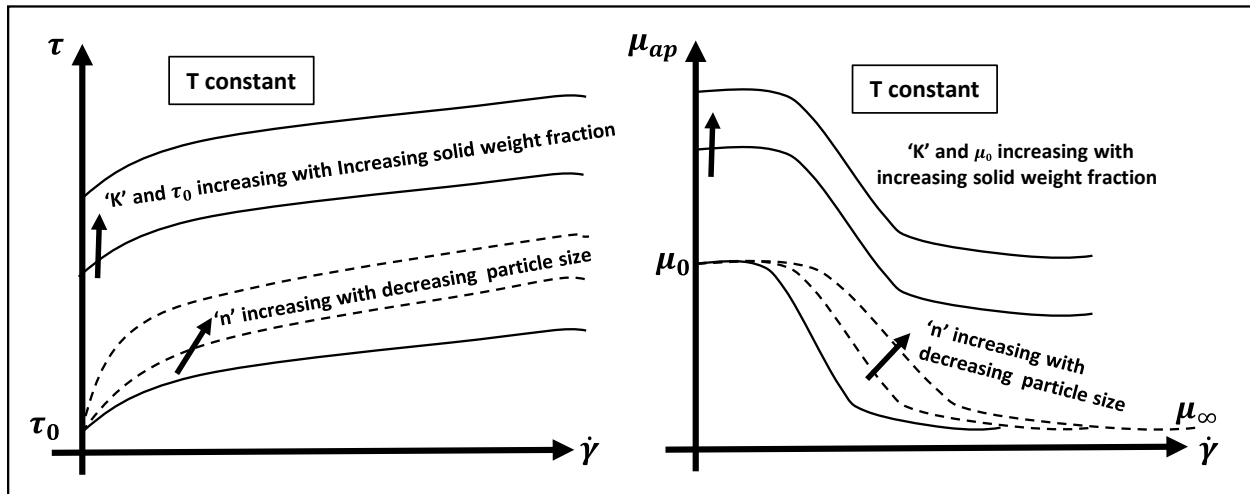
Figure 61. Shear stress and apparent viscosity evolution in nanoparticle suspensions along the shear rate axis for varying solid fraction and particle size [95].

Figure 61 shows the melt rheology behavior. 'τ_0' is the yield stress below which there is no deformation and stagnant areas occurs. The K index is strictly dependent on the solid weight fraction and temperature whereas the n coefficient refers to the ability of the particles to self-orient and ease the strain driven by the flow. n values range from 0 to 1 and a small n value means high shear thinning ability whereas high n value means no shear thinning ability and no shear rate transmission into the liquid. From the Peclet number in equation 58:

Microparticles	$n = 0.1\text{-}0.5$	High shear thinning ability
Nanoparticles <10nm	$n = 0.5\text{-}1$	No shear thinning ability

2.5.3. Impeller-crucible geometry

The Newton number can be correlated to the Reynolds number resulting into the so called characteristic curve of a mixing tank (see Figure 62). It is analogous to the drag friction factor vs. Reynolds number plot in a fluid pipe and it is independent on Fr and on Q for small Q values [37].
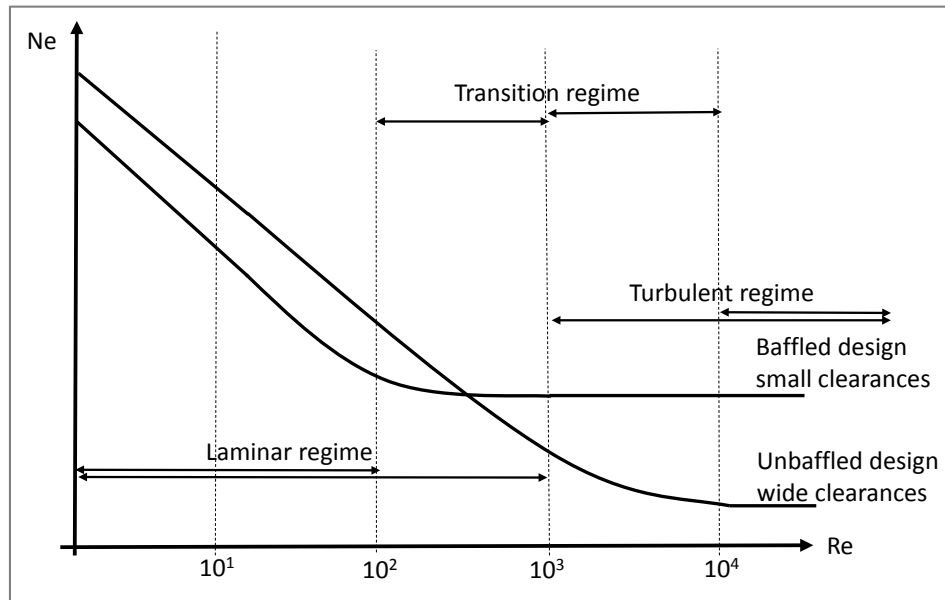

Figure 62. Ne-Re characteristic curves to allocate the different flow regimes (right).

The geometry numbers strongly affect the Reynolds interval as Figure 62 right shows. The Reynolds flow regime thresholds are listed in Table 2.

Table 2. Reynolds threshold values between the different flow regimes and geometries

Geometry	Laminar	Transient	Turbulent
Baffled design, small clearances	$Re<10^2$	$Re=10^2$-10^3	$Re>10^3$
Unbaffled design, big clearances	$Re<10^3$	$Re=10^3$-10^4	$Re>10^4$

Two observations are made from Table 2 and Figure 62: (1) Adding baffles to the tank and (2) decreasing the clearances between the impeller and the tank enables turbulence for longer time when working with high viscous liquids. Figure 63 shows the real impeller-crucible design for the current project. Table 3 shows the typical

geometry relationships between the impeller and the tank found in bibliography for close and wise clearance respectively and the relations selected for the current project. All the gas-liquid dispersion correlations introduced in the previous section may not fulfill Table 3 geometry ratios but the related inaccuracy can be neglected.

Table 3. Present design geometrical relationships and typical values found for gas-liquid impeller-tank systems from low to high viscous fluids [96].

Geometry numbers	D/A	H/A	c/D	w/D	L/D
for high viscous liquids	0.5-0.75	0.8-1	<0.6		
for low viscous liquids	0.2-0.6	0.8-1	>0.6	0.35	0.29
Present design	0.6	0.85	0.5		

For the projected liquid height (H=3') and assuming a typical gas volume fraction of 10vol pct. [97] an amount of 3lbs of produced aluminum per batch is calculated. The tank is initially an unbaffled graphite crucible with 8^0 of demoulding angle. Baffling with 8^0 wall angles (see Figure 63) might be considered as well. Off bottom distance (*c* in Figure 63) is 1" and c/D=0.5.
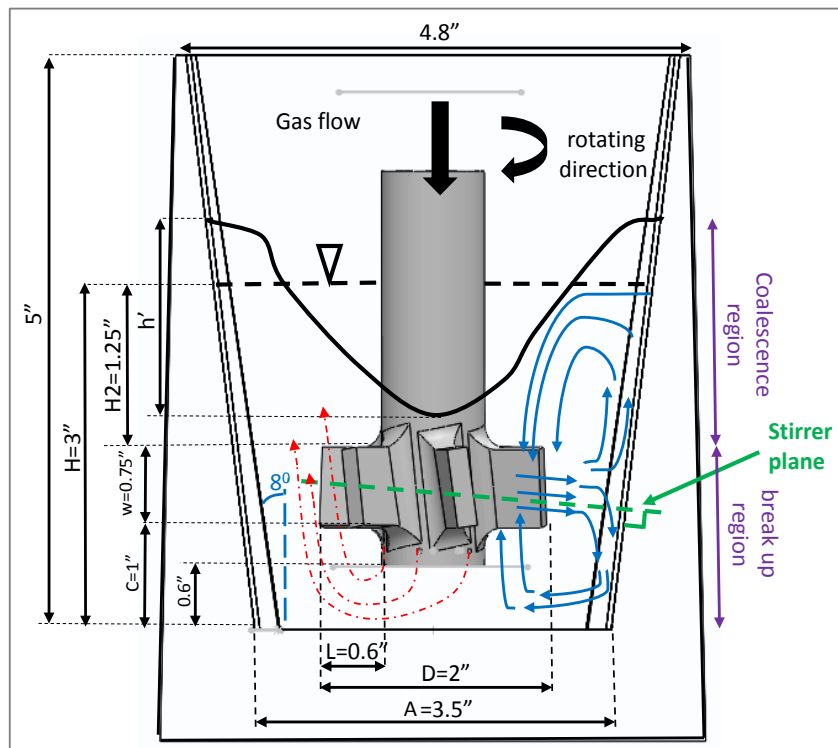
Figure 63. Front view of tank-impeller design and liquid flow pattern.
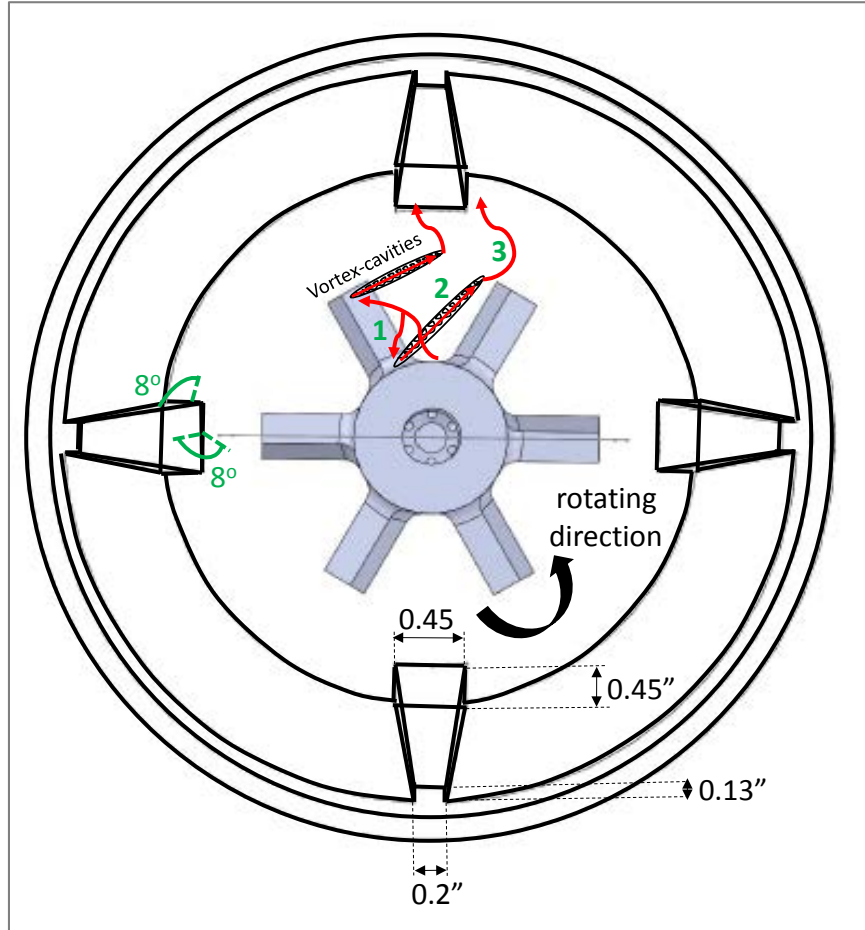
Figure 64. Top view of real tank-impeller design and gas flow pattern. The numbers refer to the three gas-liquid dispersion steps taking place in the impeller blades.

2.5.4. Impeller rotation speed influence on fluid regime

After the impeller and crucible geometry has been selected the processing parameters (rotation speed and gas flow) must be calculated to guarante that non-stagnancy condition is fulfilled.

Stagnancy threshold

The stagnant areas appear in shear thinning liquids when zero shear viscosities (μ_o) values are very high (see Figure 65). Wichterle and Wein work [98] for pseudoplastic fluids defines the full tank mixing threshold as the Reynolds number for which the diameter of the agitated nucleus (d_c) and the tank diameter (A) coincide, i.e. no stagnant areas exist (Figure 65). They conclude that Ruhston turbines are twice more efficient than PBT turbines for a given crucible geometry (A/D and H/A ratios).
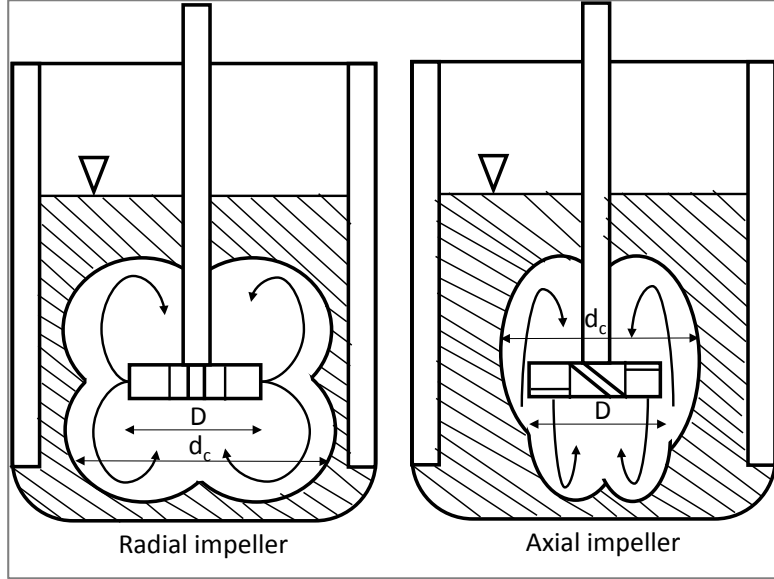
Figure 65. Shape of agitated nucleus and bulk-flow pattern under non full mixed tank conditions.

In [98] next empirical equation is proposed for turbine and radial impellers for $\frac{c}{H} = 1/3$ and $\frac{H}{A} = 1$.

$$\frac{d_c}{D} = b \cdot \sqrt{Re_{ap}} \tag{80}$$

$$\text{in which} \begin{cases} b = \begin{cases} 0.3 \; for \; propellers \\ 0.6 \; for \; radial \; turbines \end{cases} \\ d_c = diameter \; of \; the \; mixed \; nucleus \\ Re_{ap} = \frac{D^2 \cdot N \cdot \rho}{\mu_{ap}} = \frac{D^2 \cdot N \cdot \rho}{K \cdot \dot{\gamma}^{n-1}} \end{cases}$$

From Mettzer and Otto [98, 99] the strain rate is approximated by the volume averaged strain rate, given by next expression $\dot{\gamma}_{av} = k_{MO} \cdot N$, where k_{MO} is the Metzner-Otto constant. It is dependent on the tank-impeller geometry and its value is 11.5 for a Rushton turbine in an unbaffled crucible [96]. Finally:

$$Re_{ap} = \frac{N^{2-n} \cdot D^2 \cdot \rho}{K \cdot k_{MO}^{n-1}} \tag{81}$$

The condition for fully mixed tank (no stagnant areas) is in equation (80) $d_c = A$ being the required Reynolds:

$$Re_{ap} = \left(\frac{A}{0.6 \cdot D}\right)^2 \simeq 10 \tag{82}$$

which only depends on the crucible-impeller geometry.

Turbulence threshold

From Table 2, Re=10^3 and Re=10^4 are the laminar-transient regime and the transient-turbulent regime threshold values respectively for unbaffled tank. For a baffled tank the thresholds become an order of magnitude smaller Re=10^2 and Re=10^3 so viscous liquids can be maintained under turbulent regime for longer time. Unfortunately both the consistency index K and the shear thinning coefficient 'n' are melt properties, dependent on the particles size, concentration and temperature (Figure 61). For a nanoparticles melt they are unknown and time changing. Moon [100] characterized the rheology behaviour of molten AlSi6.5 with externally immersed SiC particles of 8.5μm. Material consistency index values between 5 and 50 were measured at 700^0C for weight fractions from 10vol pct.SiC to 30vol pct.SiC and a relatively constant 'n' index of 0.4. In our case, nanoparticles melt with vol pct.<10, the apparent Reynolds number is next plot vs. the rotation speed for:

(1) Microparticles melt→ n value 0.4 and K index values of 1 and 50Pa· s.

(2) Nanoparticles melt → n value 0.9 and K index values of 1 and 5Pa· s.
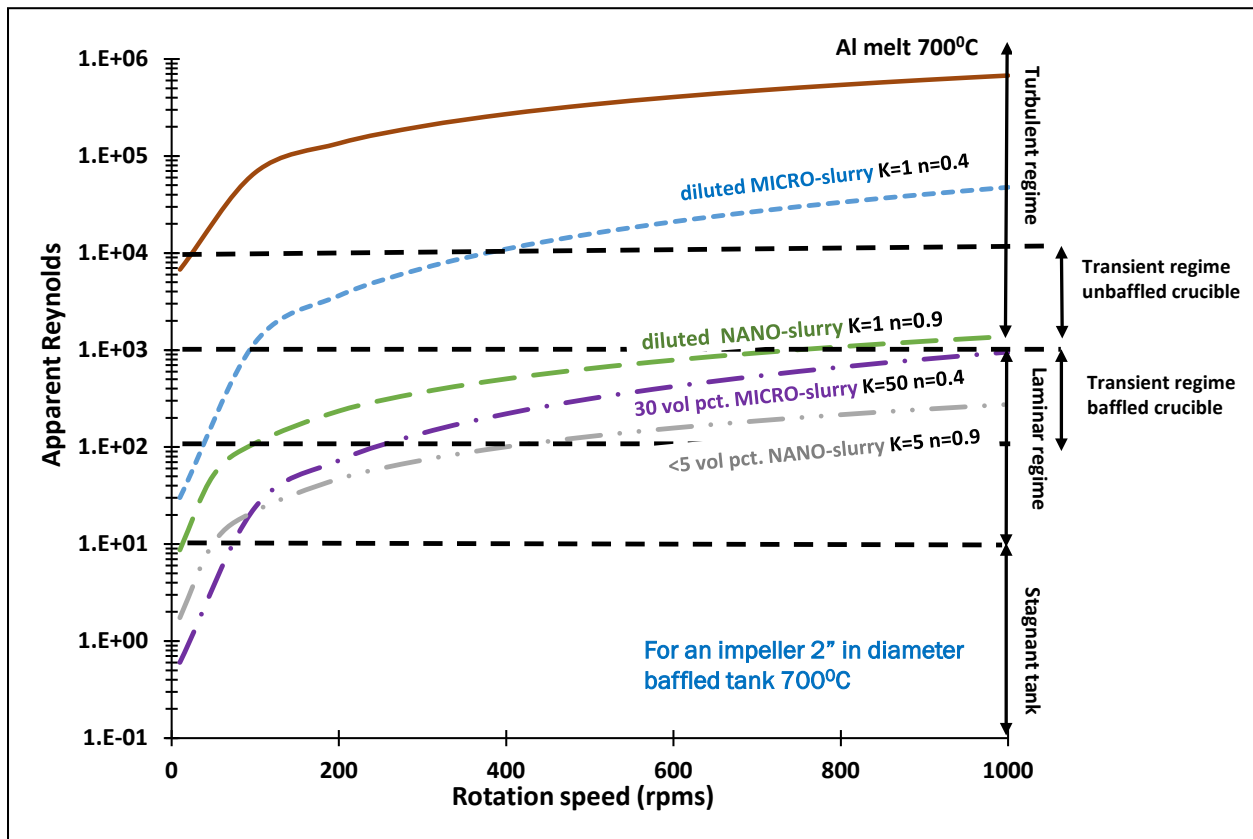
Figure 66. Reynolds vs. velocity parametric study for an impeller with 2" diameter and consistency indexes K in the range 1-50 and n = 0.4 - 0.9.

Three observations are made:

(1) The stagnant tank conditions are apparently not an issue. However, the shear rate introduced in equation 81 is the volume averaged shear rate. For the furthest region of the impeller the shear rate will be smaller and the stagnacy of experiment 15 is likely to appear if the nanoparticles melt is loaded.

(2) A diluted nanoparticles melt has a comparable impact on the mixing regime with K = 1-5 and $n = 0.9$ to the impact of a highly loaded microparticles melt with K = 50 and $n = 0.4$

(3) The minimum rotation speed to guarantee turbulence regime in a diluted nanoparticles melt is 450-500rpm. Higher rotation speeds up to 600-1000rpm might be needed to keep a good gas dispersion at very high loadings. There are equipment references going up to 1500rpm [101].

2.5.5. Intermetallics flotation

Finally, the Al₃Ti intermetallics are wished to be floating during the experiment so they do not sediment. Zwietering [43] propose next correlation for a Ruhston turbine with A/D = 1.75 and turbulent regime:

$$N_{crit} = 3 \frac{v^{0.1} d_p^{0.2}}{D^{0.85}} \left(\frac{g \Delta \rho}{\rho_L}\right)^{0.45} \times \left(\frac{wt.\% Al_3 Ti}{100}\right)^{0.13} \cdot 60 \tag{83}$$

And Nienow [43] calculated the increment of the rotation speed required from the impeller pumping capacity decrease when gas is being dispersed to be:

$$N_{crit\_gas} = N_{crit} + 0.94 \frac{q}{V_{melt}} \; with \; q \left[\frac{L}{min}\right]$$

N_{crit_gas} is plot in Figure 67 for intermetallic size dp=0.5mm and dp=1mm and q=0.5L/min and q=1L/min in 3lbs of melt. From Figure 17 the maximum values of total titanium inside the operation window at 900⁰C and 1050⁰C are respectively $wt.\% Ti_{tot}=5$ and $wt.\% Ti_{tot}=10$. From equations 26 and 27 $wt.\% Al_3 Ti$ are 10 and 25 for the previous values. They have been included in Figure 67 for reference. It is observed that the critical velocity for intermetallics flotation is specially sensitive to the gas flow increase and not so sensitive to the particle size.
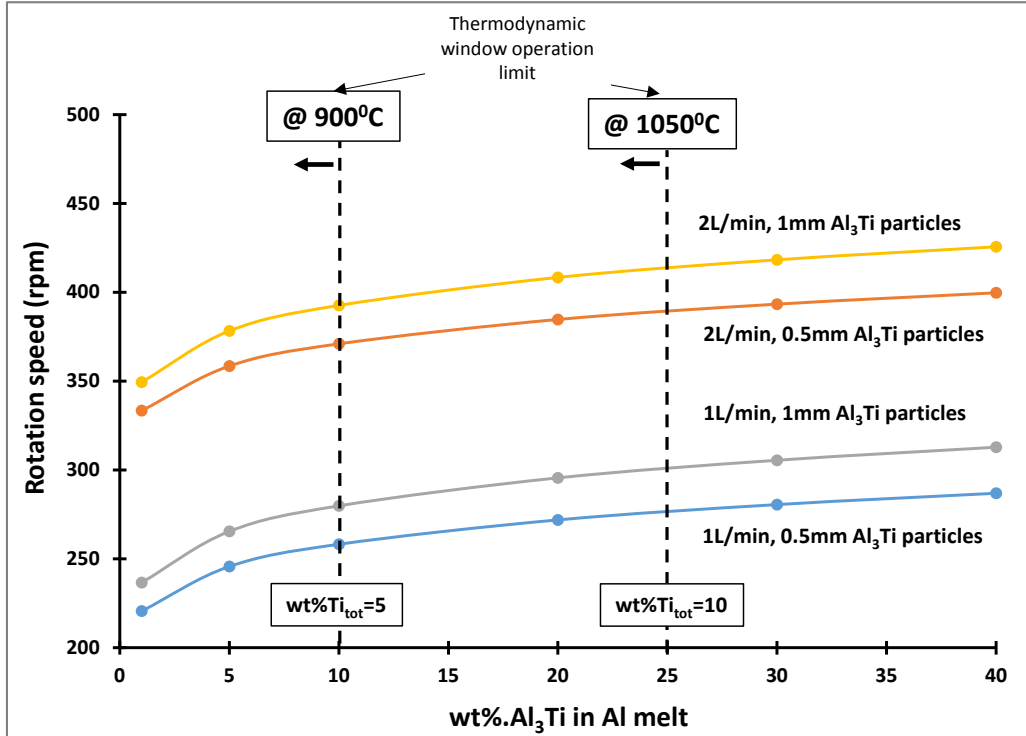
Figure 67.Critical rotation speed for particles flotation for our crucible-impeller geometry.

2.5.6. Conclusions

Main conclusions in this section are:

(1) It has been empirically stated that the rheology of the melt increases along the experiment time with increasing particle concentration. This event coarsens the particle average size, widens the size distribution into the microscale and provokes particle concentration segregation along the vertical direction.

(2) The melt is classified as a shear thinning melt. Diluted nanoparticles melts (K = 1, $n = 50$, $n = 0.4$)

(3) The impeller-crucible geometry has been optimized so experiment time and concentration can be maximized without losing turbulence.

(4) The impact of crucible baffling, impeller rotation speed and liquid rheology on the fluid mixing regime has been quantitatively studied.

(5) It is confirmed that, a very high rotation speed is required for maintaining a turbulent liquid during nanoparticles loading of at least 400rpm.

(6) A critical rotation speed for suspension of Al₃Ti intermetallics has been calculated to be at least 350rpm.

2.6. Gas Kinetics and Control of Soot Formation

The restrictions of the model and simulation are

(1) A combination of the different gas candidates will not be considered.

(2) The inlet flow, is kept in the range 1-2L/min. 2L/min is the maximum capacity of thr gas line in Figure 6.

(3) Avoid impeller nozzles clogging due to solid carbon deposition along the tube

2.6.1. Model definition

The pipe is made with Inconel 600. Main dimensions are length 55cm, OD 10mm and ID 7mm. The internal cross section is $0.385cm^2$. It is assumed cylindrical symmetry along the longitudinal axis and stationary regime. The system behaves as an ideal gases mixture and it is composed of different species diluted in argon. As the gas is compressible, the continuity equation applies for any two spatial points:

$$\rho_1 u_1 = \rho_2 u_2 = \rho u = constant \tag{84}$$

The type of flow (laminar, turbulent) along the tube must be first identified. The Reynolds number is:

$$Re_{flow\_0} = \frac{\rho_{Ar} \cdot u_{flow\_av\_0} \cdot D_{tube}}{\mu_{Ar}}$$

It is calculated at the tube entrance (25⁰C), assuming argon as the solvent (major component), with the next data

$$P = 1atm, v_{flow} = \frac{1L}{min}, \rho_{Ar} = \frac{1.5kg}{m^3}, \quad \mu_{Ar} = 0.021cPo\frac{1Pa \cdot s}{1000cPo} = 2.1 \cdot 10^{-5}Pa \cdot s$$

$$\text{being } u_{flow\_av\_0} = \frac{v_{flow}}{S_{trans}} = \frac{v_{tube}}{\pi\frac{D_{tube}^2}{4}} = 1\frac{L}{min} \cdot \frac{1m^3}{1000L} \cdot \frac{1min}{60s} \cdot \frac{4}{\pi \cdot 0.007^2}m^{-2} = 0.43\frac{m}{s}$$

It results in a Reynolds number $Re_{flow} = 216.5$, i.e. the flow regime at the entrance is laminar. Taking into account the continuity equation the Reynolds number can be expressed as

$$Re_{flow} = \frac{\rho_{Ar} \cdot u_{flow} \cdot D_{tube}}{\mu_{Ar}} = \frac{cnst \cdot D_{tube}}{\mu_{Ar}} \tag{85}$$

Since the cross section of the tube is constant and the viscosity of the gases increases for temperature increments (in opposition to liquids behavior [102]), the Reynolds number (85) steadily decreases along the tube axis and the flow can be considered fully laminar along the full tube axis. The flow is assumed to be unidirectional and fully developed laminar flow (FDLF) for the whole tube length. The parabolic velocity profile follows next expression [103].

$$u_{flow}(x,r) = u_{max}(x)(1 - (r/R_{tube})^2) \text{ being } u_{max} = 2u_{flow\_av} = 2 \cdot \frac{v_{flow}}{S_{trans}}$$

The temperature at different distances from the retort cover has been measured. A wall temperature profile to be included in the model has been calculated, and it is given in Figure 68 and Table 4. The temperatures in the internal metal shield have been measured with thermocouple.
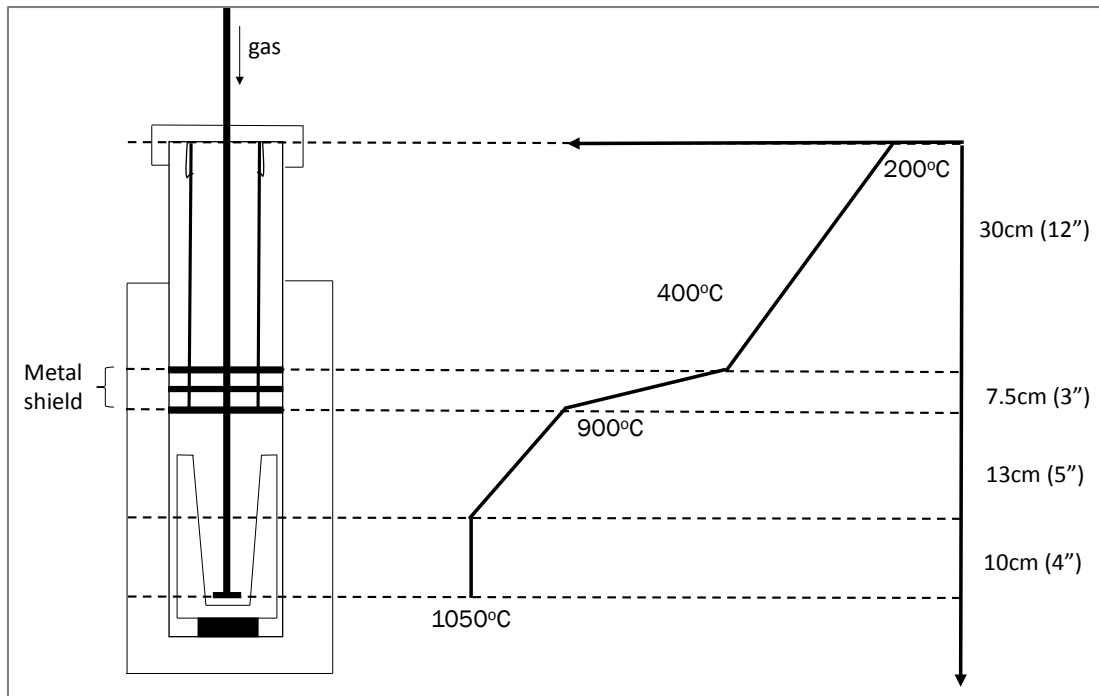

Figure 68. Schematic of temperature profile along the gas tube for a 24" retort.

The temperature functions of each interval are given in Table 4.

Table 4. Temperature functions of each interval (in K).

$T_1(x)$	$\frac{400-200}{0.3} \cdot x + 473$
$T_2(x)$	$\frac{900-400}{0.075} \cdot x + 673$
$T_3(x)$	$\frac{1050-900}{0.13} \cdot x + 1173$
$T_4(x)$	1050

Three balances must be initially included; momentum, energy and mass balance.

2.6.2. Energy balance

An energy balance is applied to a differential volume of the pipeline in which FDLF, argon as dilutant and a negligible heat of reaction are assumed. FDLF is treated with an average front velocity (u_{flow_av}) what converts the balance into a plug-flow energy balance.
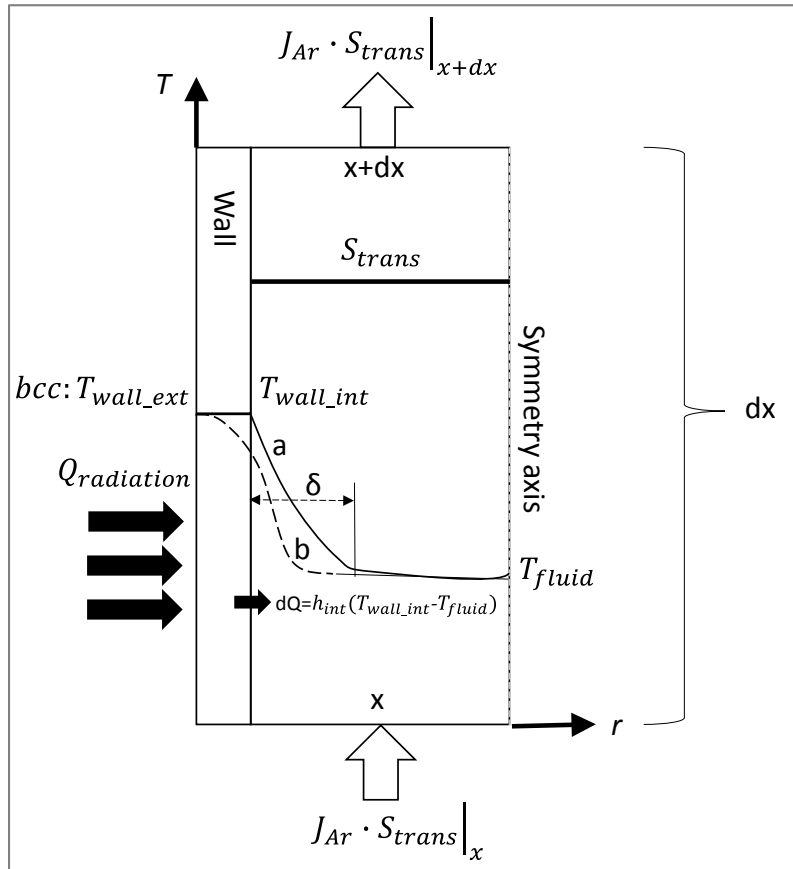
Figure 69. Energy balance in shaft and temperature profile for (a) flat and (b) unflatten profile at wall.

The heat balance equation is (see [38])

$$J_{Ar} \cdot S_{trans} \cdot C_{pAr} \frac{dT}{dV} = \frac{dQ}{dV}$$
$$\text{and } dV = S_{trans} dx$$
$$\left. \frac{dQ}{dV} = \frac{U}{S_{trans} dx} \left(T_{wall} - T_{fluid} \right) 2\pi \frac{D}{2} dx = \frac{U}{S_{trans}} \left(T_{wall} - T_{fluid} \right) \pi D_{tube} \right\} \rightarrow$$

$$\rightarrow J_{Ar} \cdot C_{pAr} \frac{dT}{dx} = \frac{U}{S_{trans}} \left(T_{wall} - T_{fluid} \right) \pi D_{tube}$$

in which 'U' is the tube wall overall heat transfer coefficient. In a typical heat exchanger $\frac{1}{U}\left[\frac{m^2 \cdot K}{W}\right] = \frac{1}{h_{ext}} + \frac{\delta_{wall}}{\lambda_{Inconel}} + \frac{1}{h_{int}}$, but in the present case the wall temperature is supplied by the furnace radiation system (not by an external gas), which along with the tube conductivity are powerful enough to keep both the internal and external sides of the tube at the same temperature (profile 'a' in Figure 69). The wall is hence modeled as a wall with no thickness and constant temperature in each dx interval, being $\frac{1}{U}\left[\frac{m^2 \cdot K}{W}\right] = \frac{1}{h_{int}}$ or $U\left[\frac{W}{m^2 \cdot K}\right] = h_{int}$.

Equation is normalized in non-dimensional form by substituting $dx = Ld\varepsilon$ and rearranging by variables separation next equation results

$$\frac{dT}{(T_{wall} - T)} = \frac{h_{int} \cdot \pi D_{tube}}{J_{Ar} \cdot S_{trans} \cdot C_p} L \cdot d\varepsilon$$

Integrating 'ε' from 0 to 'ε' and 'T' from T_o to T,

$$-ln(T_{wall} - T) + ln(T_{wall} - T_o) = \frac{h_{int} \cdot \pi \cdot D}{J_{Ar} \cdot S_{trans} \cdot C_p} L \cdot \varepsilon$$

$$T = T_{wall} - (T_{wall} - T_o) \cdot exp\left(-\frac{h_{int} \cdot \pi \cdot D}{J_{Ar} \cdot S_{trans} \cdot C_p} L \cdot \varepsilon\right)$$

$$T = T_{wall} - (T_{wall} - T_o) \cdot exp\left(-\frac{h_{int} \cdot \pi \cdot D}{J_{Ar} \cdot \pi \frac{D^2}{4} \cdot C_p} L \cdot \varepsilon\right)$$

$$T = T_{wall} - (T_{wall} - T_o) \cdot exp\left(-4 \frac{h_{int}}{J_{Ar} \cdot D \cdot C_p} L \cdot \varepsilon\right)$$

$$T = T_{wall} - (T_{wall} - T_o) \cdot exp(-mL \cdot \varepsilon) \quad with \quad m\ [m^{-1}] = \frac{h_{int}}{J_{Ar} \cdot D \cdot C_p} \qquad (86)$$

As $\lambda_{Inconel}$ and T_{wall} change along the tube with the temperature, equation (86) is solved in Figure 70 by finite differences for a given set of arbitrary 'm' values. Next expression is used for any 'i' interval (1cm long).

i-1   i   i+1

$$T_i = T_{wall\_i} - (T_{wall\_i} - T_{i-1}) - exp(-4 \cdot m_i \cdot \Delta L_i \cdot 1)$$
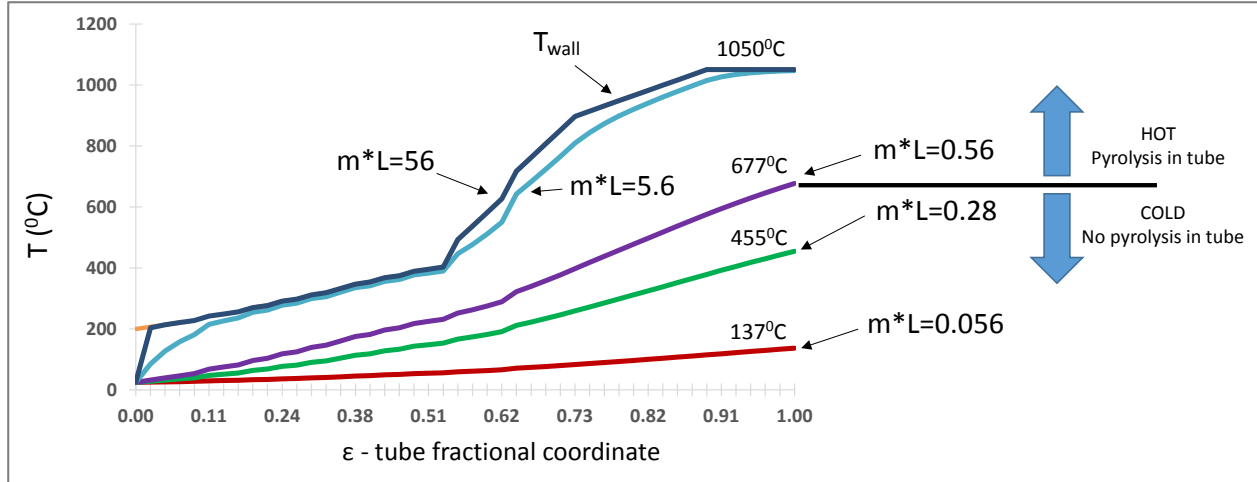
Figure 70. Parametric analysis Tube wall and gas temperatures evolution along the longitudinal axis.

To control the gas pyrolysis along the tube without changing the melt temperature (@1050⁰C) $m \cdot L$ <0.5 should be achieved. For the calculation of '$m \cdot L$' in the present system 'h_{int}' in equation 86 is first calculated, for a gaseous laminar flow. From [104]

$$Ne = \frac{h_{int} \cdot D_{tube}}{k_{Ar}} = 3.66 + \frac{0.065 Re Pr \frac{D_{tube}}{L}}{1 + 0.04 \left(Re Pr \frac{D_{tube}}{L}\right)^{\frac{2}{3}}} = 3.66 + \frac{0.065 \cdot 200 \cdot \frac{20 \cdot 2.1 \cdot 10^{-5}}{0.016} \cdot \frac{7}{560}}{1 + 0.04 \left(200 \cdot \frac{20 \cdot 2.1 \cdot 10^{-5}}{0.016} \cdot \frac{7}{560}\right)^{\frac{2}{3}}} = 3.66;$$

$$\text{being } h_{int} = 8.37 \frac{W}{m \cdot K}$$

Thus, a typical value for '$m \cdot L$' for 1 atm and 1L/min is:

$$m \cdot L = \frac{h_{int}}{J_{Ar} \cdot D \cdot C_p} L = \frac{8.37 \left[\frac{W}{m^2 \cdot K}\right]}{6.81 \cdot 10^{-4} \left[\frac{mol}{m^2 \cdot s}\right] \cdot 7[mm] \cdot \frac{1m}{10^3 mm} \cdot 20 \left[\frac{J}{mol \cdot K}\right]} 0.56[m] = 5 \cdot 10^4 \gg m \cdot L|_{lim} = 0.5$$

Some conclusions are made:

(1) The gas 'catches' the wall temperature in the first centimeter for a tube of 56cm temperature. This has full physical sense for a small gas flow (1L/min) with low specific heat. The flow inside the tube has no thermal inertia and instantly heats up to the wall temperature.

(2) The thickness of the tube has no influence. The furnace radiation and the conductivity of the tube are considered powerful enough to keep the tube temperature constant along its thickness (profile 'a' in Figure 69). A ceramic or insulator tube as well as a fluid with higher heat transfer coefficient (a cold liquid) could unflatten the wall temperature profile (profile 'b' in Figure 69).

(3) A cooling jacket made of a ceramic insulator containing a liquid with high density (up to $10^3 \left[\frac{kg}{m^3}\right]$) and high heat capacity (up to $1\frac{kcal}{kg \cdot K}$) may push the '$m \cdot L$' value up to *0.5* in Figure 70. Oil or water could be good candidates.

In summary, the carbon pyrolysis cannot be controlled by changing the gas flow or tube thickness variation. A heat balance inside the furnace is concluded not to be necessary. The assumption of considering the heat due to the gas chemical reactions inside the tube negligible is valid.

2.6.3. Momentum balance

The momentum balance solution is a pressure field which is meaningful in case of high pressure variations. The number of gaseous mol along the tube can be assumed to be constant ($n_T = n_{T0}$) as the compounds are diluted in argon, a non-reactive gas. The pressure drop for laminar flow in a pipe follows next expression [103]

$$\int_{P_o}^{P_F} -dP = \int_{x=0}^{L} \frac{\lambda}{D_{tube}} \cdot \frac{\rho_{Ar}}{2} \cdot u_{flow\_av}^2 dx = \int_{x=0}^{L} \frac{\lambda}{D_{tube}} \cdot \frac{cnst}{2} \cdot u_{flow\_av} dx \qquad (87)$$

in which $\lambda = \frac{64}{Re} = 0.295$ is the pipe friction coefficient. Also for gases,

$$u_{flow_{av}}(x) = \frac{v_{flow}}{S_{trans}} = \frac{n_T RT}{P\pi \frac{D_{tube}^2}{4}} = \frac{n_{T0} RT}{P\pi \frac{D_{tube}^2}{4}} = \frac{P_0 v_{flow\_0} RT}{RT_0 \cdot P \cdot \pi \frac{D_{tube}^2}{4}} = \frac{P_0 v_{flow_0} T(x)}{T_0 \cdot P \cdot \pi \frac{D_{tube}^2}{4}} \quad \text{being } (87)$$

$$\int_{P_o}^{P_F} -dP = \int_{x=0}^{L} \frac{\lambda}{D_{tube}} \cdot \frac{cnst}{2} \cdot \frac{P_0 v_{flow_0} T(x)}{T_0 \cdot P\pi \frac{D_{tube}^2}{4}} dx$$

From the heat balance it is assumed that the temperature of the flow is the temperature of the pipe wall (Table 4), being:

$$\int_{P_o}^{P_F} -dP = 2\frac{\lambda}{\pi D_{tube}^3} \cdot cnst \cdot \frac{P_0 v_{flow_0}}{P \cdot T_0} \left\{ \int_{x=0}^{L1} T_1(x)dx + \int_{L1}^{L2} T_2(x)dx + \int_{L2}^{L3} T_3(x)dx + \int_{L3}^{L4} T_4(x)dx \right\}$$

By variables separation and integration

$$P_0^2 - P_F^2 = 4\frac{\lambda}{\pi D_{tube}^3} \cdot cnst \cdot \frac{P_0 v_{flow_0}}{T_0} \cdot \sum Int_i$$

For $P_0 = 10^5 Pa$, $v_{flow_0} = 1 L/min$, $T_0 = 298K$, $cnst = 0.42 \cdot 1.5 \frac{kg}{m^2 s}$, $\sum Int_i = 722\ K \cdot m$ and the pressure drop is:

$$P_0^2 - P_F^2 = 11884 Pa \rightarrow P_0 - P_F \approx 110 Pa$$

The pressure drop is 0.1% and the momentum balance is not required.

2.6.4. Mass balance

In summary, only the mass balance will be simulated in the Chemical Engineering Module of Comsol Multiphysics. The model is a system of 'n' mass balance equations for n chemical species. In the present system n=8 (components number, see 10-15). The mass balance is plot in Figure 71 for cylindrical coordinates.
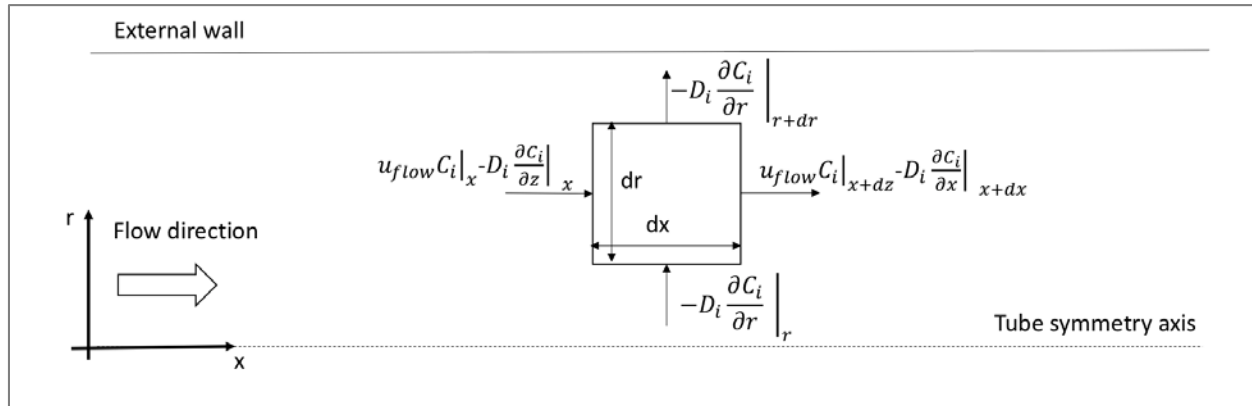

Figure 71. 2D cylindrical coordinates mass balance along the gas tube.

A mass balance in the differential volume results in 2nd Fick's law for a stationary tube in cylindrical coordinates

$$\frac{\partial(u_{flow}C_i)}{\partial x}\bigg|_x - D_i \frac{\partial^2 C_i}{\partial x^2}\bigg|_x - D_i \frac{\partial^2 C_i}{\partial r^2}\bigg|_x = \sum_{j+1}^{6} v_{ij} R_j \ for \ i = 1,2,3 \dots n$$

The binary diffusivity coefficients for each specie 'i' diffusing into argon are considered constant and isotropic.

The boundary conditions are

- inlet mass flow at x=0 known; $J_i|_{x=0^+} = u_{flow}c_i|_{x=0^+} - D_i \frac{\partial C_i}{\partial x}\bigg|_{x=0^+} =$ $u_{flow}c_{i,o}$

- no diffusive flow at x=L, $\frac{\partial c_i}{\partial r}\bigg|_{x=L} = 0$

- no flow at r=0 (symmetric axis) $\frac{\partial c_i}{\partial r}\bigg|_{r=0} = 0$

- no flow at r=R (not permeable wall) $\frac{\partial c_i}{\partial r}\bigg|_{r=R} = 0$

The kinetic laws introduced in the model are taken from [44]. They are valid for atmospheric pressure, high operation temperature and short residence time. All the conditions apply in the present system [44, 45]. The binary diffusivities of each specie

'i' in argon, assuming diluted system, are calculated from the Chapman-Enskog equation [102], theoretic equation with +-8% of relative error:

$$D = \frac{1.86 \cdot 10^{-3} \cdot T^{3/2} \left(\frac{1}{MW_1} + \frac{1}{MW_2} \right)}{P \sigma_{12} \Omega} \; with \; P[atm] \; and \; T[K]$$

$$\sigma_{12} = \frac{1}{2}(\sigma_1 + \sigma_2) \, [\text{Å}] \; and \; \Omega = f(kT/\varepsilon_{12}) \, [dimless] \; being \; \varepsilon_{12} = \sqrt{\varepsilon_1 \varepsilon_2} \; [K]$$

From [105]

Table 5. Binary diffusion coefficients at 1000K for the diluted Ar-component

Comp	σ_{comp} [Å]	$\sigma_{comp-Ar}$ [Å]	$\frac{(\varepsilon_{comp})}{k}$[K]	$\frac{(\varepsilon_{comp-Ar})}{k}$	$\frac{(kT)}{/(\varepsilon_{comp-Ar})}$	$\Omega_{comp-Ar}$ [dimless]	M_{comp} [$g \cdot mol^{-1}$]	$D_{comp-Ar} \cdot 10^4$ [$m^2 \cdot s^{-1}$]
Ar	3.54	-	93.3	-	-	-	40	-
CH$_4$	3.76	3.65	148.6	117.75	10.81	0.75	16	2.5
C$_2$H$_2$	4.03	3.79	231.8	147.06	8.66	0.76	24	2
C$_2$H$_4$	4.16	3.85	224.7	144.79	8.79	0.76	26	1.89
C$_4$H$_4$				Unknown				
C$_6$H$_6$	5.35	4.44	412.3	196.13	6.49	0.8	78	1.04
H$_2$	2.83	3.18	59.7	74.63	17.06	0.7	2	8.62
C$_3$H$_8$	5.12	4.33	237.1	148.73	8.56	0.76	44	1.3
C$_2$H$_6$	4.44	7.98	215.7	167	7.62	0.78	42	1.42
C$_3$H$_6$	4.68	4.11	298.9	141.86	8.97	0.76	30	1.69

For the C$_4$H$_4$ compound, the C$_2$H$_4$ diffusivity will be given. It is reasonable to do the diffusivities calculation for an average temperature of 1000K since at low temperature, the reactions-mass transfer have no strength and in the range 900-1273K an average diffusivity at 1000K introduces an assumable error.

2.6.5. Simulation and parametric analysis

The produced solid carbon at the tube exit is calculated in a parametric study for methane and acetylene. The composition is parametrized for inlet methane volume fraction values 0.1, 0.2 and 0.3 as well as for acetylene inlet volume fraction values

0.05, 0.1, 0.2 and 0.3. Figure 72 shows the behavior of the solid carbon specific flow along the tube length for the longitudinal axis position.
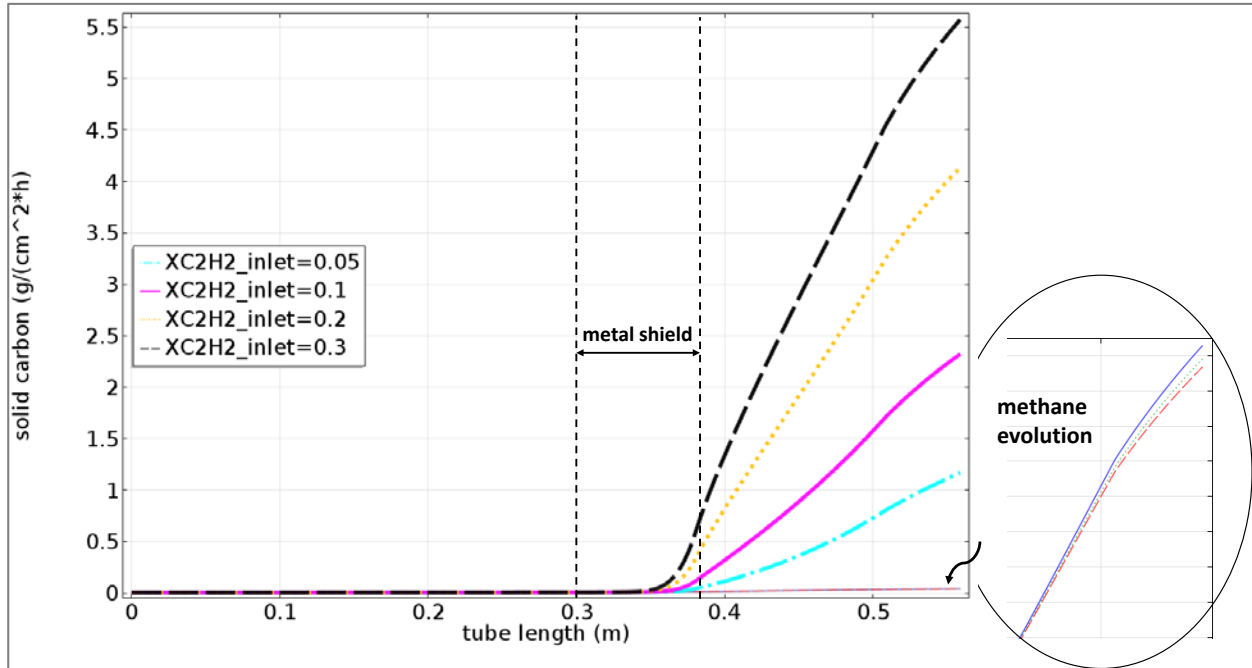

Figure 72. Solid carbon evolution along the tube length for different acetylene and methane inlet compositions.

To calculate the overall solid carbon flow at the end of the tube, next surface integral is applied for the shaft cross section in contact with the melt:

$$\dot{M}_c = 2\pi \int_0^R \dot{m} \cdot r \, dr \tag{88}$$

The total carbon introduced into the tube contained in the gases is calculated following next expression

$$1\frac{L}{min} \cdot \frac{60min}{1h} \cdot \frac{1mol}{22.4L} \cdot X_{CH_4/C_2H_2}$$

The calculated data is shown in Figure 73. Propylene or propane are also included in Figure 73 for qualitative purposes. So far gas selection, the content in argon and gas flow variables have been determined. Another two parameters, hydrogen inlet flow and temperature, also affect the soot decomposition reaction and will be analyzed. For methane, the soot formation reaction is rewritten below:

$$CH_4(g) \leftrightarrow C(s) + 2H_2(g)$$
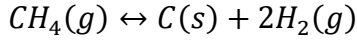
And from Van't Hoff equilibrium equation

$$\Delta G_R = 91863 - 112T = RTlnK = RTln\frac{\%volH_2^2}{\%volCH_4}$$

Reducing the furnace temperature and introducing hydrogen in the bubbling gas mixture shift the reaction to left side decreasing the soot formation. A parametric analysis for hydrogen composition has been done for 10vol pct.CH4 diluted in argon immersed in the melt at 1050⁰C and a gas flow of 1L/min in Figure 74. A set of H_2 compositions has been introduced in the range 0.01-5vol pct. A reduction of 66pct. in soot formation is achieved with 10vol pct.H_2 but only 1vol pct.H_2 is need to get a 50wt pct. soot reduction.
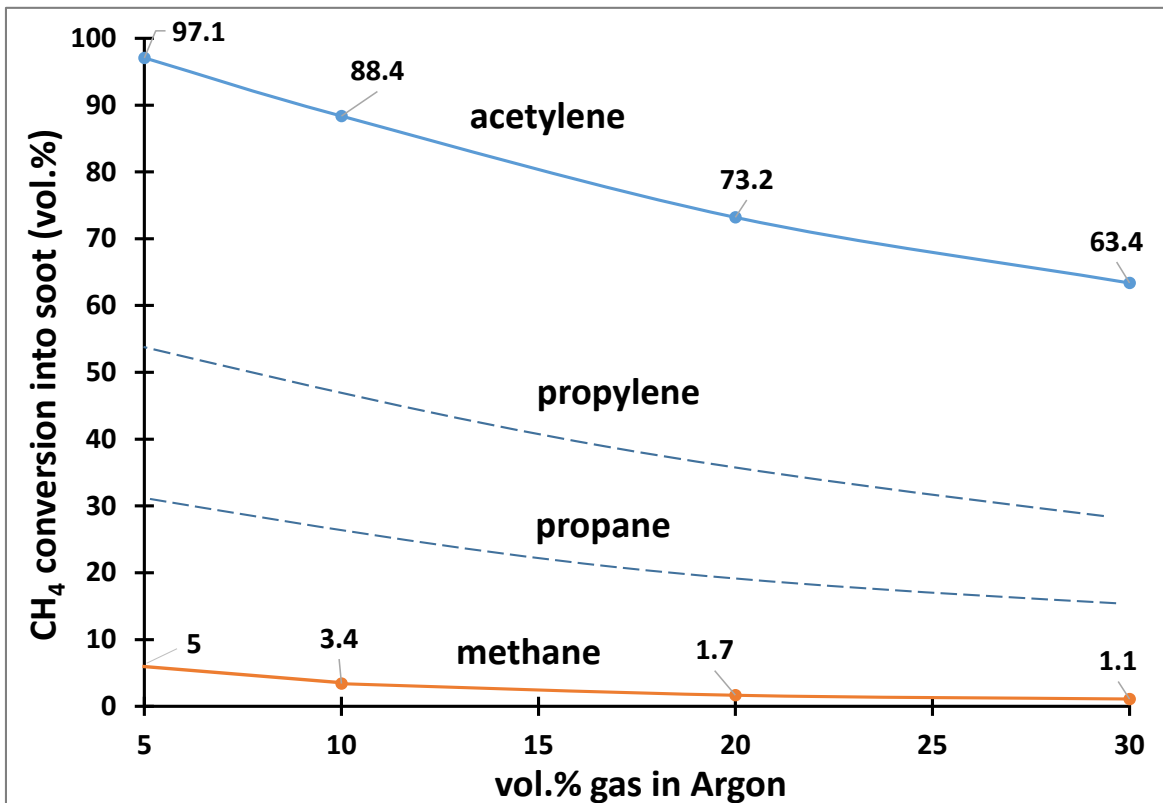
Figure 73. Methane and acetylene soot conversion at the melt at 1050°C, 1L/min. Propane and propylene are qualitative.
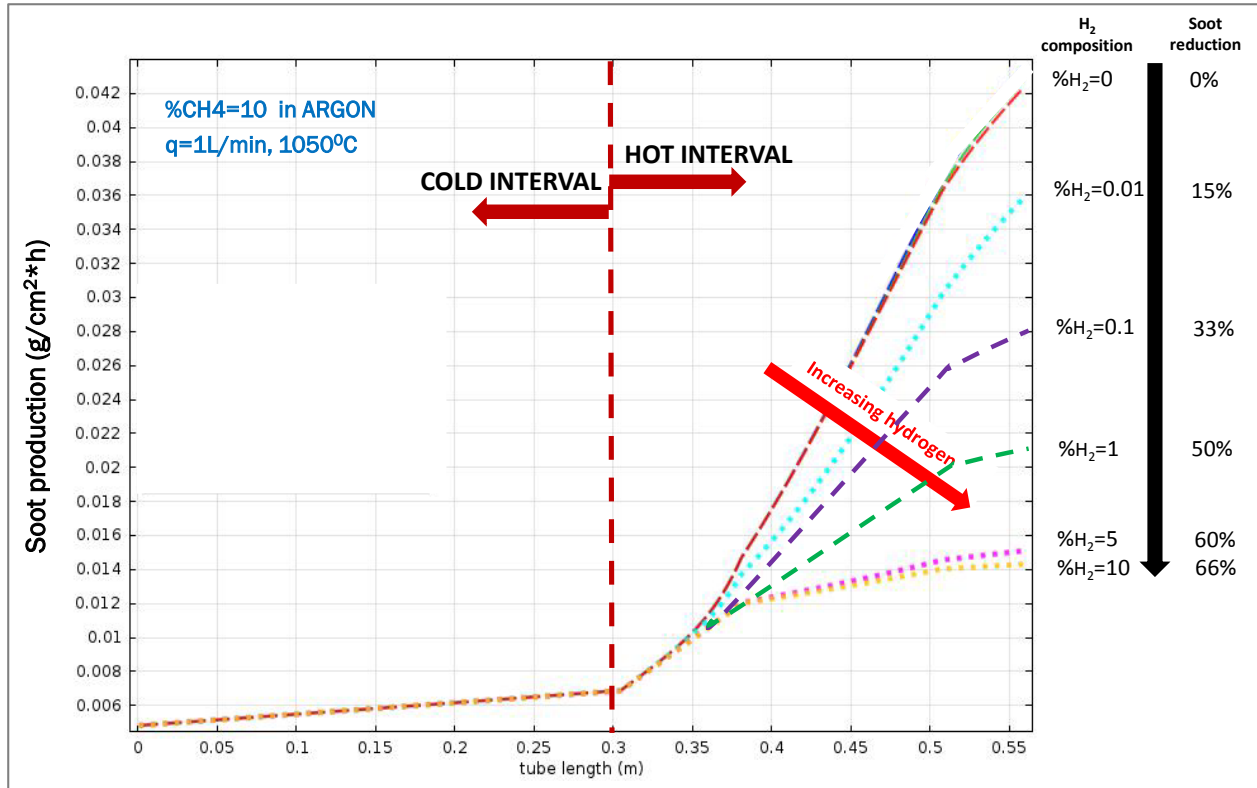
Figure 74. H_2 impact on soot formation for 1L/min methane diluted in argon and furnace at 1050°C.

In summary, for the current shaft-furnace geometry:

(1) Methane decomposition into soot at 1050^0C is below 5vol pct. enhancing the chemisorption route in Figure 9.

(2) Acetylene decomposition into soot is >60vol pct. supporting the soot route in Figure 9.

(3) Other gases as propane or propylene will have an intermediate behaviors.

(4) The pyrolysis begins as soon as the temperature reaches 750^0C at the metal shield location. This in agreement with the time scales of mS for soot precursors [46].

(5) The addition of 1vol pct.H_2 in argon further depresses the soot formation up to 50wt pct.

2.6.6. Explosion safety analysis

A generic flammability diagram is shown in Figure 75 [105, 106]. Characteristic points are, for the flammable gas-oxygen/air mixture, the lower flammability limit (LFL) and the ultimate flammability limit (UFL). This data is in bibliography and it can be extrapolated to higher temperatures with next empirical correlations [106]

$$\frac{LFL_T}{LFL_{25}} = 1 - 0.000784(T - 25) \text{ , T in } ^0\text{C}$$

$$\frac{UFL_T}{UFL_{25}} = 1 + 0.000721(T - 25) \text{ , T in } ^0\text{C}$$

UFL=100 is the maximum value for the UFL limit. The addition of inert gas narrows the interval (UFL-LFL) up to the minimum inert concentration (MIC) at which LFL equals UFL. Below this oxygen value the mixture does not explode.
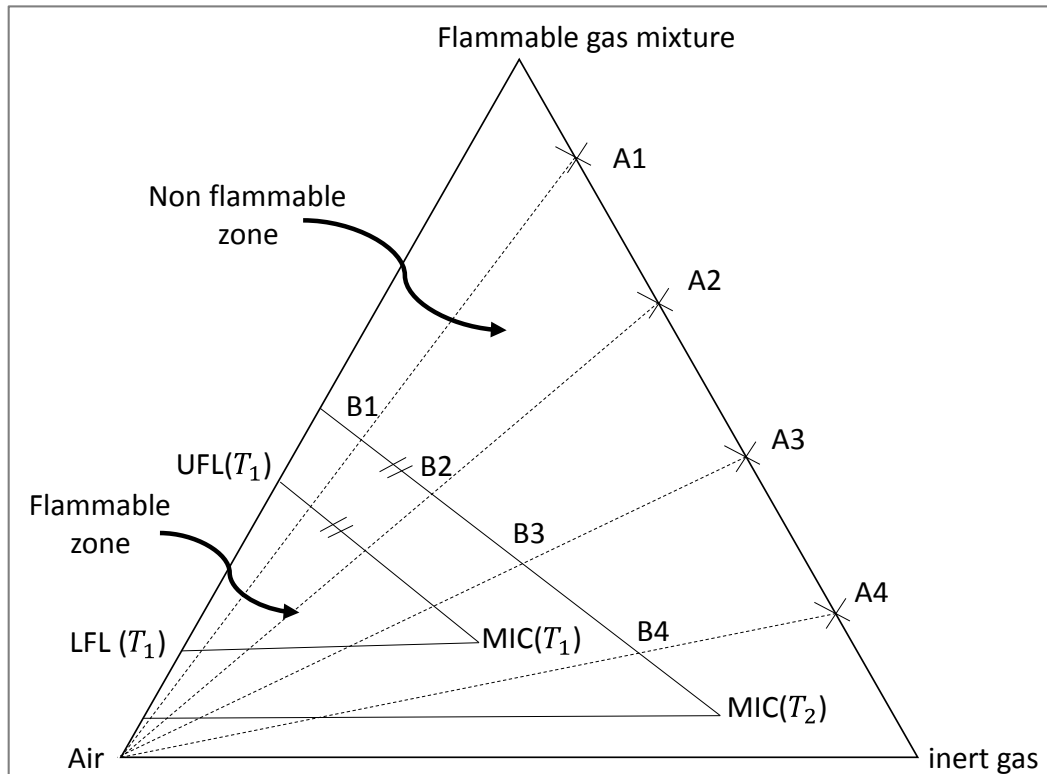
Figure 75. Generic flammability diagram.

The inert gas dilution coefficient is introduced as the ratio of change between the flammable limit and the addition change of inert gas, i.e. the slope of the straight lines UFL-MIC and LFL-MIC. It can be found in literature as well and it has next expression [7]

$$\gamma^{U,inert} = \frac{\Delta UFL}{\Delta inert\%} \qquad \gamma^{L,inert} = \frac{\Delta LFL}{\Delta inert\%}$$

The MIC can be hence calculated equalizing UFL and LFL resulting in the next expression

$$MIC_{inert} = \frac{UFL - LFL}{\gamma^{L,inert} - \gamma^{U,inert}} \tag{89}$$

In an inert furnace atmosphere, any point Ai is considered. Any oxygen contamination moves the mixture along the segments A_i–Air up to any point Bi where the mixture explodes. Likewise, the length of the line A_i-B_i represents the fraction of oxygen that is accepted at the inert-flammable gas atmosphere before explosion. The furnace atmosphere corresponds closely to the composition present at the end of the tube, i.e. for an inlet composition of 20vol pct. of acetylene, the outlet composition is calculated in Table 6 with equation 88 and Figure 76. The flammability data is taken from [105].
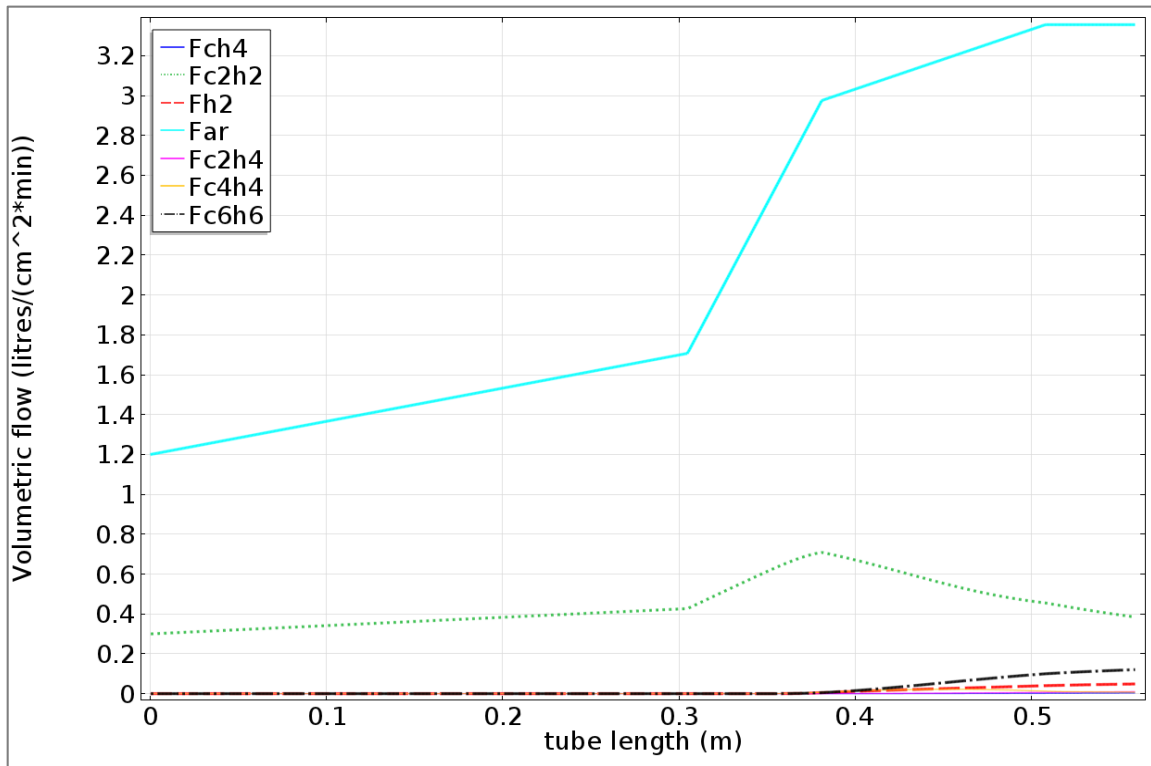
Figure 76. Gaseous compounds evolution along the tube and its value at the end of the tube.

Equation 89 can be applied for any hydrocarbons mixture [106] and it takes next form

$$MIC_{inert} = \frac{UFL_{mix} - LFL_{mix}}{\gamma_{mix}^{L,inert} - \gamma_{mix}^{U,inert}} \tag{90}$$

The different mixture flammability properties can be calculated from Le Chatelier's formula

$$\frac{1}{prop_{mix}} = \sum_i^n \frac{X_i}{prop_i} \tag{91}$$

in which volume fractions are free of argon. Equations 89 and 90 are valid as long as no ethylene (C_2H_4) is present. From equation 90 the MIC results to be 96.01 pct. The interval A_i-B_i in Figure 75, the amount of air that can leak inside the furnace before explosion, is calculated to be 21vol pct., i.e. 4.2vol pct. of oxygen. A continuous oxygen monitoring is scheduled to be purchased and installed as safety measure.

Table 6. Gas composition at end of the tube (inside the furnace) and gas compounds flammability

Gaseous compound	Overall volumetric flow(L/min)	Gas composition (vol%)	LFL/UFL (25^{0}C)	LFL/UFL (1000^{0}C)	$\gamma_{N2}^{U,inert}$ [96]	$\gamma_{N2}^{L,inert}$ [96]
Argon	**1.94**	**89.8**	Inert gas			
CH4	0.21	9.8	**5.3/15**	**1.25/25.5**	**-0.266**	**0.0031**
H2	**0.007**	**0.3**	**4/75**	**0.95/100**	**-0.117**	**0.006**
C2H2	**0.003**	**0.1**	**2.5/80**	**0.56/100**	**-1.2**	**0.043**
C6H6	<10^{-3}	-				
C6H6	<10^{-3}	-				
C2H4	<10^{-3}	-				
C4H4	<10^{-3}	-	Minor components			
Total (L/min)	**2**	**100**				

Table 7. Gaseous mixture flammability properties

Gaseous compound	Gas composition (vol%)	Gas composition (vol%) Ar free	LFL_{mix}/UFL_{mix} (1000^{0}C)	$\gamma_{mix}^{U,inert}$	$\gamma_{mix}^{L,inert}$
CH4	9.8	95.7			
H2	0.3	3	1.22/26.4	-0.259	0.003
C2H2	0.1	1.3			
Total	13.4	100			

2.6.8. Conclusions

Assuming a deviation of the simulation results from reality of 10-20%, next conclusions are still valid:

(1) Methane gas in argon with a volume fraction of 0.1-0.15 at a flow rate of 1L/min will be applied.

(2) No gas preheater is needed. The wall thickness has no effect in keeping the gas cold and the soot under control.

(3) Alternative strategies to keep the soot formation under control are: (1) reduce the furnace temperature, (2) gas introduction at the crucible bottom (typical arrangement in steel ladles) or (3) diluted hydrogen introduction in the mixture Ar-CH$_4$.

(4) The maximum air concentration in the furnace for the above gas bubbling operation window has been calculated to be 21vol pct., i.e. 4.2vol pct. of oxygen, high enough to allow safety operation. Nevertheless, a continuous oxygen monitoring system has been installed.

CHAPTER 3

Experiments

3.1. Parametric analysis design

In Chapter 2, I have reported on my efforts to calculate (1) the thermodynamic operational window of the process, (2) the simultaneous physicochemical phenomena on kinetics and gas dispersion inside the melt that controls particle size and TiC reaction rate, (3) the design of the tank-impeller geometry and its optimization for handling shear thinning viscous fluids and finally (4) the pyrolysis of the carbon gas carrier and soot formation control to enable nanoparticles formation. With the previous accumulated knowledge we design the parametric analysis of Table 8.

Table 8. Conditions employed in the ten experiments.

Experim	Alloy composition	Ingot weight (lb.)	Melt temperature (°C)	Processing time (h)	CH_4 gas in Ar (vol pct.)	CH_4 purity (vol pct.)	Gas flow (L/min)	Rotation speed (rpm)	Crucible design
1	Al-5.65Ti	2.5	1050	0.5	15	99.0	1	450	Unbaffled
2	Al-5.65Ti	2.5	1050	2	15	99.0	1	450	Unbaffled
3	Al-2.65Ti	2.5	1050	0.5	5	99.0	1	450	Unbaffled
4	Al-2.65Ti	2.5	1050	2	5	99.0	1	450	Unbaffled
5	Al-1.7Ti	3	950	2	10	99.0	1	450	Unbaffled
6	Al-1.2Ti	3.2	900	2	5	99.0	1	450	Unbaffled
7	Al-2Ti	3	900	8	10	99.0	1	450	Unbaffled
8	Al-1Li-2Ti	3	900	1	10	99.0	1	450	Unbaffled
9	Al-2.5Li-2Ti	3	900	0.5	10	99.0	1	450	Unbaffled
10	Al-2.5Li-2Ti	3	900	0.5	10	99.999	1	450	Baffled

Figure 17, which contains the thermodynamic operation window is reproduced in Figure 77 including the experiments allocation. The main characteristic of the experiments are as follows:

(1) Exps. 1-4 have wt pct.Ti >2. Exps. 5-10 have wt pct.Ti ≤2, very close to the peritectic point, which is at wt pct.Ti = 1.3 so to study the needles precipitation,

stability and elimination. Experiment 6 has the only hypoperitectic composition.

(2) The temperature varies between 1050 and 900°C in Exps.5-7 to locate the region free of soot in the thermodynamic operation window.

(3) The vol pct. CH$_4$ is varied between 5 and 15 to analyze its influence in the TiC formation. Explosions hazard is avoided if vol pct.CH$_4$<15 as indicated in Chapter 2.

(4) The experiments last from 30 minutes up to 2 hours. Experiment 7 goes up to 8 hours to confirm TiC is not forming at 900°C.

(5) The rotation speed (450 rpm) and gas flow (1L/min) rate have been calculated in Chapter 2 (Figure 49 and Figure 52) so as to maximize turbulence and shear in the melt in order to enhance the formation of nanoparticles.

(6) Experiments 8-10 include lithium in the 1-2.5 pct. range added in order to enhance chemisorption and nanoparticles formation.
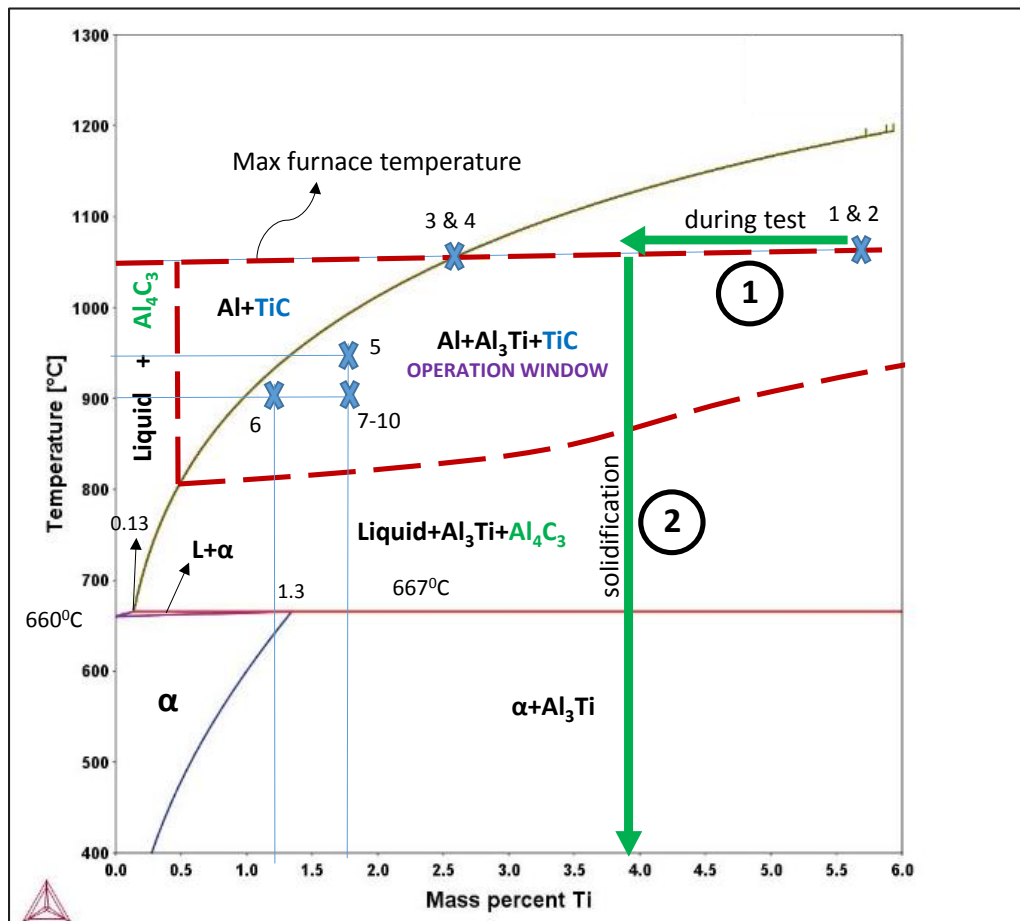
Figure 77. Allocation of experiments in the Al-Ti operation window.

3.2. Materials, Experiments and Characterization Procedures

The composition of materials used in the experiments are shown in Table 9.

Table 9. Materials composition used for producing the Al-TiC composite materials.

	Supplier	%Ti	%Si	%Fe	%Cu	%V	%Al
Al-5.65Ti master alloy	Millward Alloy	5.65	0.11	0.13	0.00	0.03	remainder
Aluminum (99.99% purity)	Millward Alloy	0.0001	0.0008	0.0018	0.0047	0.00	remainder

The master alloy microstructure is shown in Figure 78. Polygonal Al_3Ti particles with size 20-50 micrometers are present.
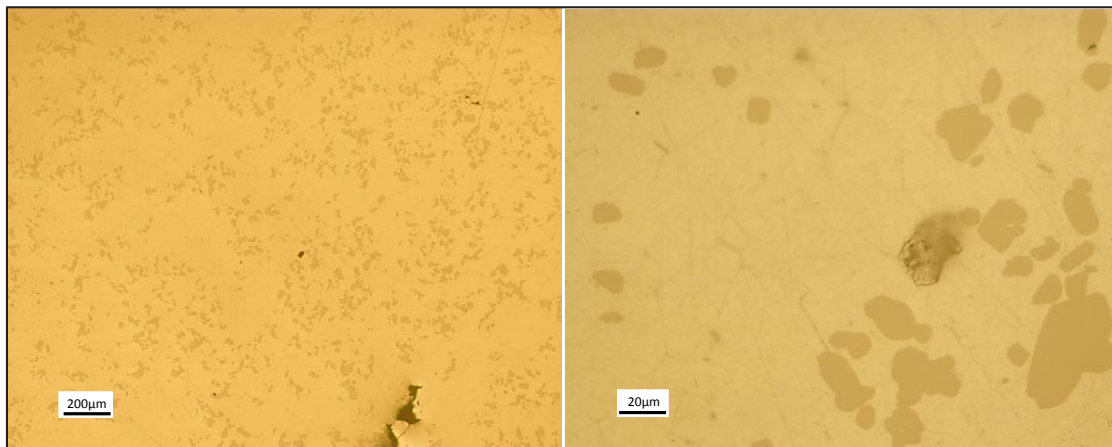
Figure 78. Microstructure of Al-5.65Ti masteralloy

The consumed gas composition is:

Table 10. Composition of consumed gases

Gas	Ar (vol pct.)	O_2 (ppm)	H_2O (ppm)	Hydrocarbons (ppm)
Argon Grade 5	99.999	2	3	0.50
Methane CP grade	99.00	300	300	balance
Methane Research grade	99.999	1	2	balance

Figure 79 helps in describing the procedure. Note that the melt and the furnace (thermocouple at refractory lining) do not follow the same heating and cooling curves. First, the furnace is slowly heated up to 1100°C and held at this temperature for 1 hour in order to allow the melt to reach 1050°C and provide sufficient time for the Al_3Ti intermetallics (see Figure 78) that are present in the master alloy to completely dissolve in the aluminum. The melt then cools down to the set-up time (in Figure 79 it is 1050°C) and the experiment proceeds. After the experiment is complete, the furnace is cooled down with a controlled rate and solidification takes place.
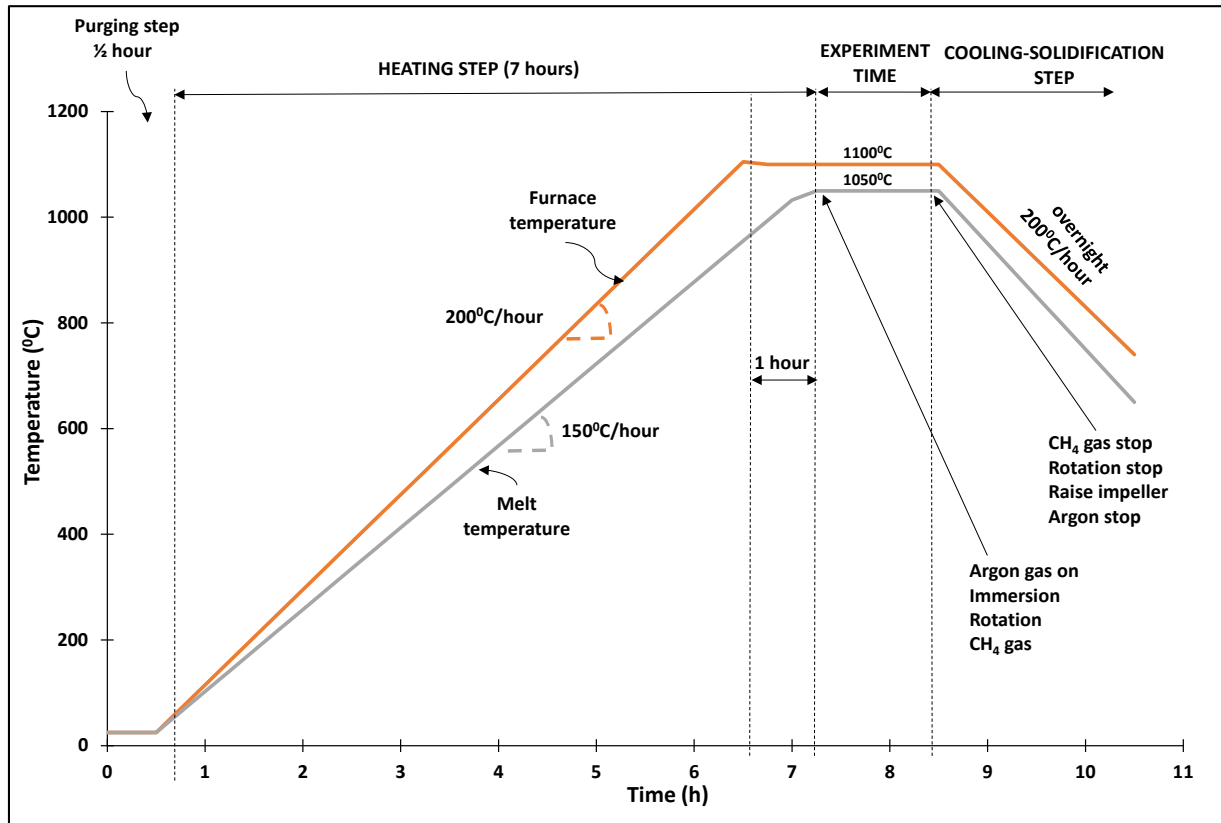
Figure 79. Schematic representation of the procedure used in a typical experiment.

The ingot material is demoulded from the crucible and then cut longitudinally in two halves; one half is macro-etched for macrostructure characterization. A circular section is cut in the other half and samples are taken from three different locations along the ingot height as shown in Fig. 80 for microstructure and nanostructure characterization.
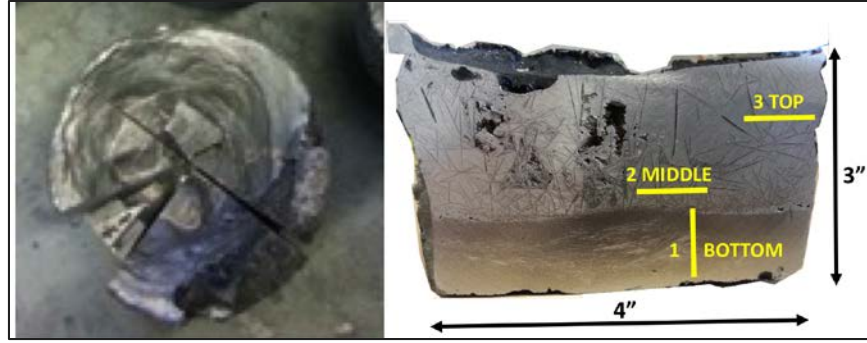
Figure 80. Half of the cut ingot showing locations where samples are taken for characterization.

Sample preparation follows the procedures shown in Table 11 and Table 12. For cleaning purposes distilled water and ethanol are used only.

Table 11. Procedure for macro-characterization of the ingots.

Cutting	Extec Labcut 350F
Mounting	No mounting
Grinding	SiC with grit sizes 240, 320, 400
Polishing	Manual diamond polishing 3µm and 1µm
Etching	NaOH 10wt pct. solution at 70°C for 2-3 minutes followed by rinsing in 50wt pct. HNO_3 and water
Microscopy	No microscopy, visual examination

Table 12. Procedure for micro and nano-characterization

Cutting	Extec Labcut 350F + Allied Diamond Wafering Saw
Mounting	Diallyl Phthalate (glass reinforced) mounting powder
Grinding	SiC with grit sizes 320, 400
Polishing	Struers Tergramin 20 Diamond polishing 3µm 25N, 7:30min, and 1µm 20N, 4:30min
Etching	None for microanalysis. For nanoanalysis NaOH 10wt.% solution for 10s followed by generous rinsing in hot water
Optical microscopy	EPHIPOT 200
SEM-EDS	JEOL 7000F
EDS	X-MaxN Silicon Drift Detector SDD; 80mm2
XRD	GE-XRD-5. Scanning rate 1-2deg/min

XRD analysis is performed in the vertical and the radial orientations as described in Figure 81.
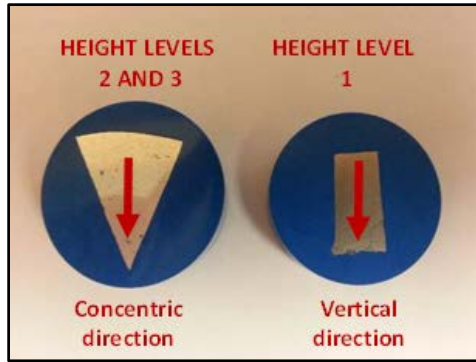
Figure 81. Concentric and vertical orientations for XRD analysis.

3.3. Results and discussion

3.3.1. Microcomposites by the soot route in Exps.1-4

<u>Macrostructure</u>

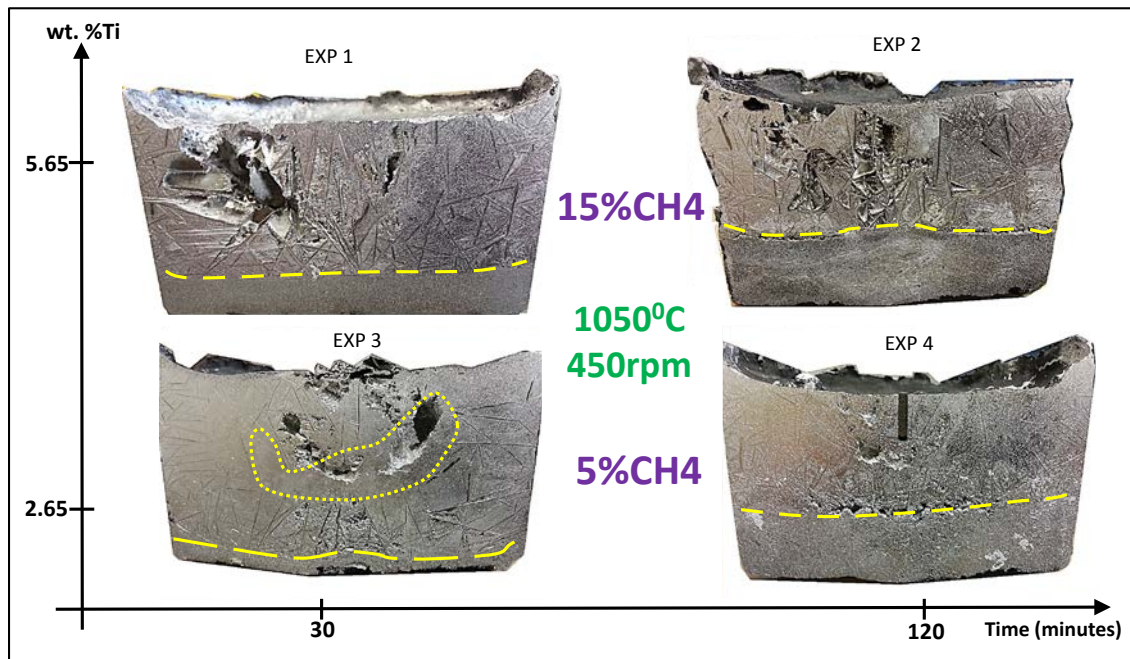Macrostructures from ingots made according to Exps. 1-4 in Figure 82.

Figure 82. Macrostructures of etched material made according to Exps. 1-4.

In Exps. 1-4, the ingots have a bottom domain (limited by a dashed line in Figure 82) full of small particles that increases its height with the experiment time. In Exps. 1 and 2, the concentration of particles in the bottom domain is denser than in Exps. 3, 4. The top domain of the ingot is full of pores and it has needles (presumably Al_3Ti)

104

surrounded by an α-Al matrix. In between the top and the bottom regions (i.e., near the center of the ingot) there is some shrinkage porosity. Exps. 3 also has an equiaxed region that is essentially free of needles (limited by a dotted line in Figure 82).

X-ray diffraction

XRD spectra of material made according to Exp. 2 is shown in Figure 83. X-ray diffraction is a qualitative technique that reliably identifies compounds with a composition above 5wt pct. XRD data has been taken at the three locations specified with the orientation of Figure 81. The presence of TiC is confirmed, but only in the bottom part of the ingot whereas Al_3Ti is present in the whole ingot. Also $AlTi_2C$ ($AlTi_zC_{1-x}$ in more general form) and AlFe and/or $AlFe_2V$ likely exist. Fe and V are impurities in the masteralloy (Table 9). TiH_2 is a byproduct in which the H_2 comes from the methane decomposition into soot. Al_4C_3 existence is a possibility, not fully confirmed by the XRD. Remaining peaks are α-Al_2O_3 aluminum oxides and other impurities. Figure 84 shows the XRD spectra of material taken from the bottom of ingots made according to Exps. 1-4. Exps. 1 and 2 clearly present a higher concentration of Al_3Ti than Exps. 3 and 4. There is no clear trend regarding the amount of Ti_2AlC and TiC. The existence of Al_4C_3 cannot be fully confirmed.
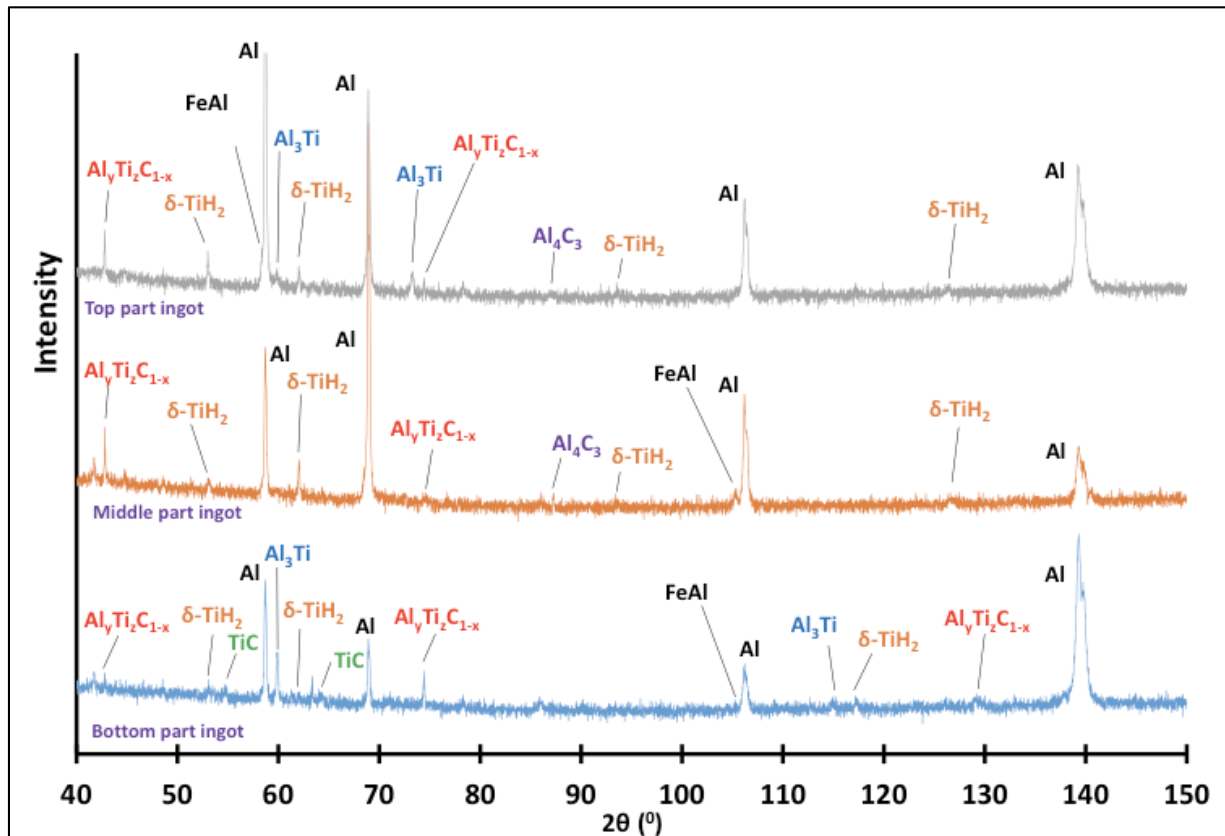
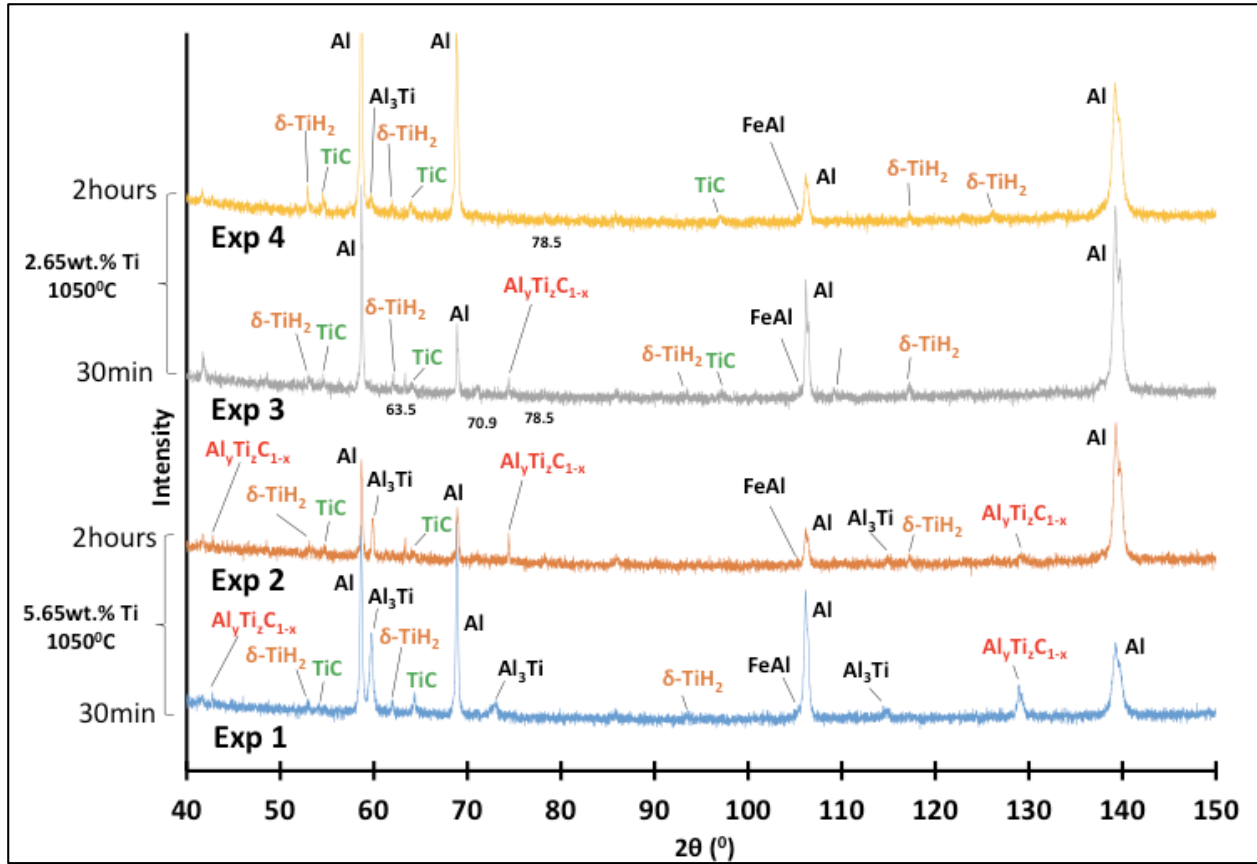Figure 83. XRD spectra (Cr lamp) of samples from Exp. 2.

Figure 84. XRD spectra (Cr lamp) at the ingot bottom location for Exps. 1-4.

In [11] a diffusion couple as the one shown in Figure 85 is used to explain formation of Ti_2AlC and Al_4C_3 as intermediate phases during the production of TiC.
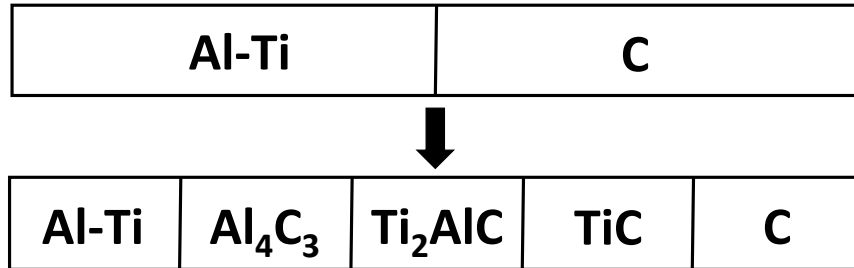

Figure 85. Al-Ti-C diffusion couple

Microstructure

The bottom part of the ingots was characterized with an optical microscope (LOM) and the images are shown in Figure 86.
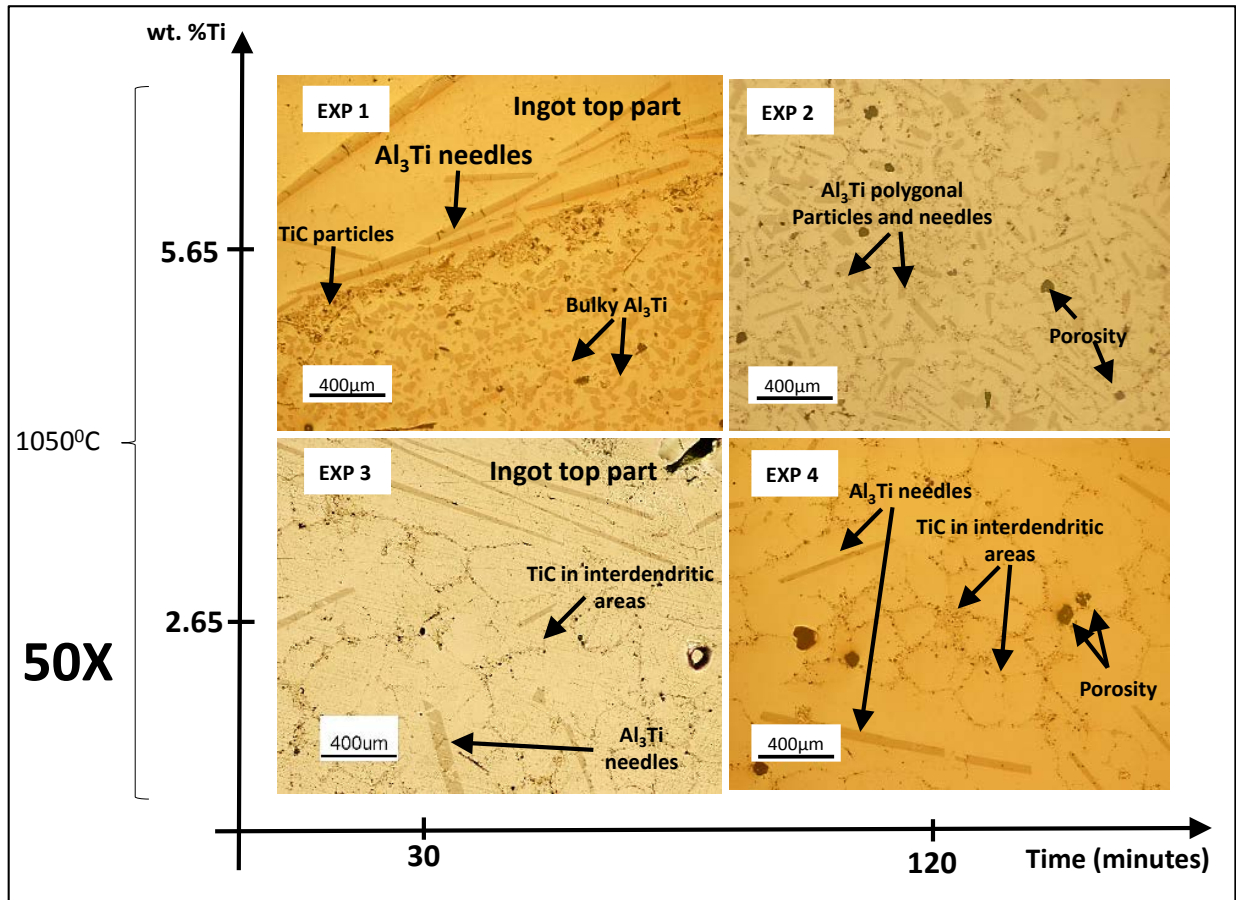
Figure 86. LOM images (50X). Material from the bottom of ingots in Exps. 1-4.

The material from Exp. 1 shows polygonal particles (presumably Al_3Ti) with a thin layer of fine particles (presumably TiC and/or $AlTi_2C$) at the interface with the ingot's top part. The material from Exp. 2 has a bottom that is populated by both polygonal particles and short needles surrounded by fine microparticles segregated within the interdendritic space. The material from Exps. 3, 4 show no polygonal Al_3Ti particles and a low concentration of short needles surrounded by fine particles. An explanation to this observation follows. Exps. 1 and 2 are located in the mushy zone at 1050°C (see Figure 77), which is the maximum furnace temperature so all the Al_3Ti polygonal particles present in the initial master alloy cannot be melted. At the end of Exp. 1, the polygonal Al_3Ti particles settle faster than the fine TiC microparticles that stay in the top. In Exp. 2, the high amounts of TiC that is produced and the consumed polygonal Al_3Ti particles make both the polygonal Al_3Ti and the TiC particles to be mixed in the ingot bottom with a few Al_3Ti short needles. Exps. 3 and 4 are located at the liquidus line in Figure 77. All the polygonal Al_3Ti particles from the original master all oy have melted and only some Al_3Ti needles that are produced during the experiment are left, with surrounding TiC particles. Figure 87 zooms into the TiC-

AlTi$_2$C particles in the interdendritic space at 1000X. An array of fine TiC particles (mostly <5-10μm) are interconnected in between coarse dark particles in Figure 87. The coarse dark particles could be aluminum oxides as detected in the XRD. This will be confirmed with SEM-EDS.
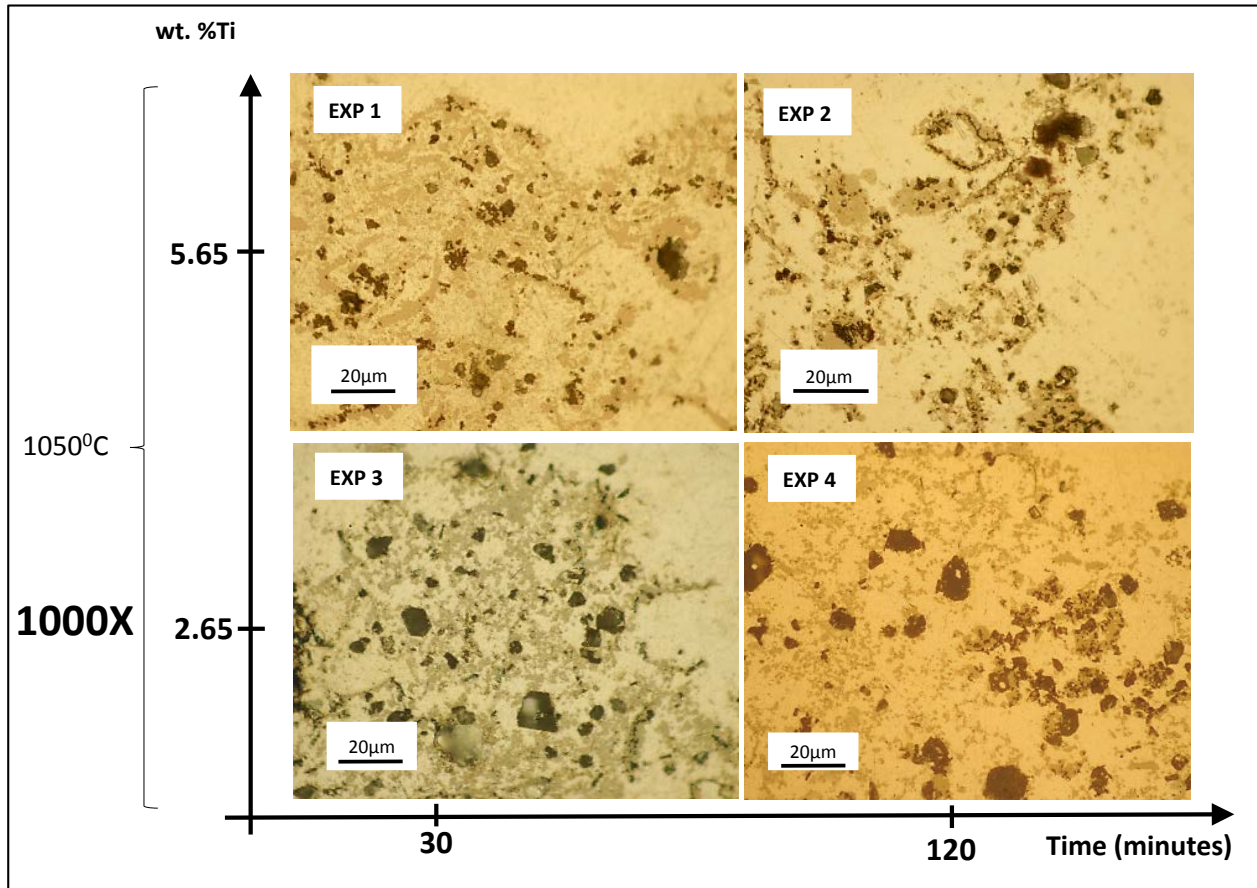

Figure 87. LOM picture at 1000X from the ingot bottom for Exps. 1-4 and 7.

Nanostructure

Figure 88 shows a low magnification BSE-EDS map of the bottom of an ingot produced according to Exp. 2. The composition of the polygonal particles and needles is confirmed to be Al$_3$Ti whereas the interdendritic domain has Al, Ti, O and C as suggested in Figure 87.
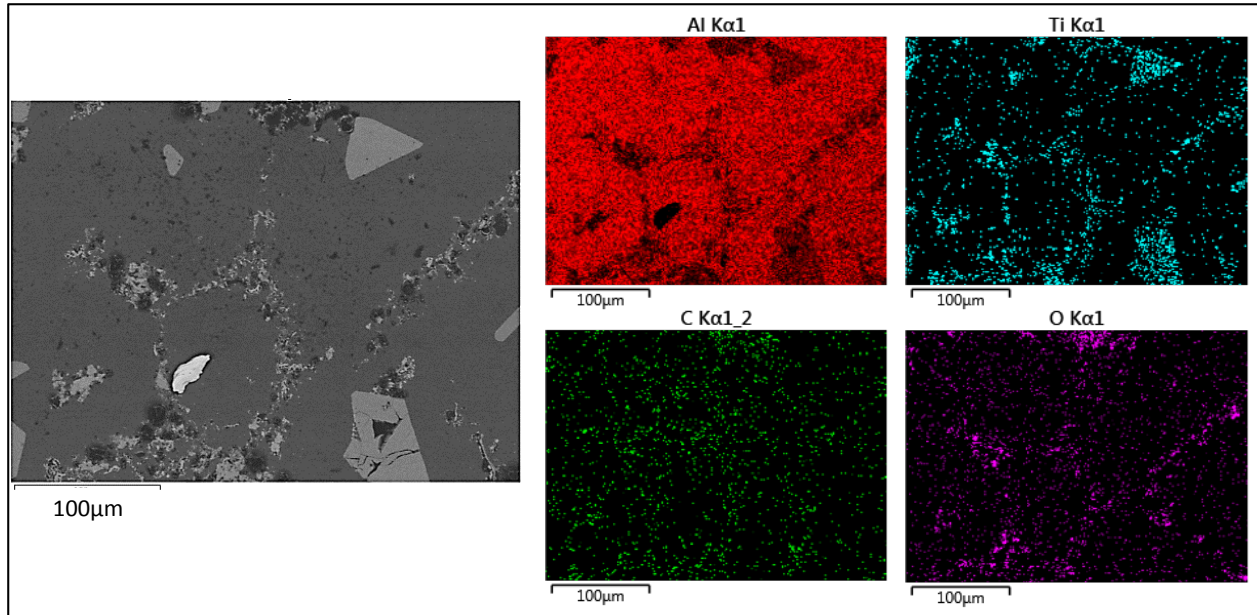
Figure 88. Low magnification BSE-EDS map of the bottom of the ingot produced according to Exp. 2.

Figure 89 shows the interdendritic regions in SEM-EDS mode at 10,000X. The complexity in morphologies and size distribution is obvious. A size distribution that ranges from less than 100nm up to 5µm and morphologies with very irregular shapes and different aspect ratios is observed. 2-3µm aluminum oxide particles are also observed, that have been previously detected in the XRD and show in Figure 86 and Figure 87 as dark particles.
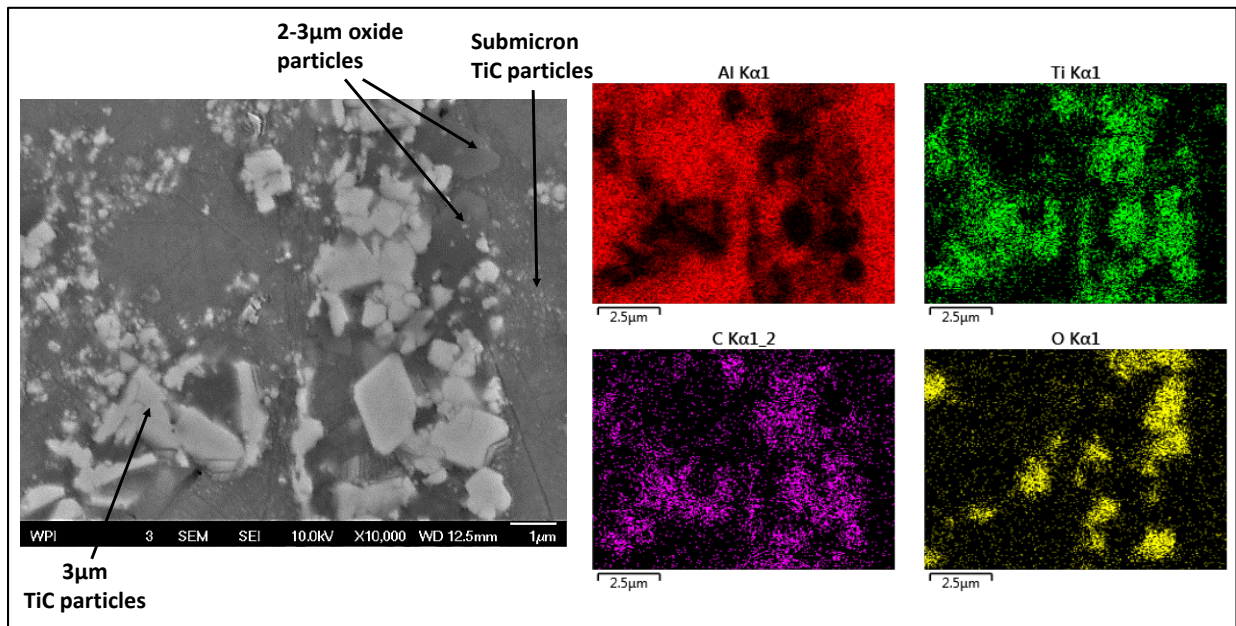
Figure 89. SEI-EDS of the interdendritic area in material produced according to Exp. 2.

The large amount of microparticles suggest that the TiC formation follows the soot route (Figure 9). Figure 90 and Figure 91 show two examples of thick soot particles (d_p>50µm) that are being consumed by the titanium solid diffusion from the melt and TiC formation. The particles have an Al-Ti-C phase in contact with the molten metal that is presumably $AlTi_2C$ (Figure 83 and Figure 85). A closer look of the soot particle in Figure 91 reveals that the TiC region is crumbling into smaller fragments of 1µm in size in Figure 92. It seems reasonable to state that strain incompatibility is causing the crumbling as there is a 17 pct. difference between the $AlTi_2C$ and TiC specific volumes [25].
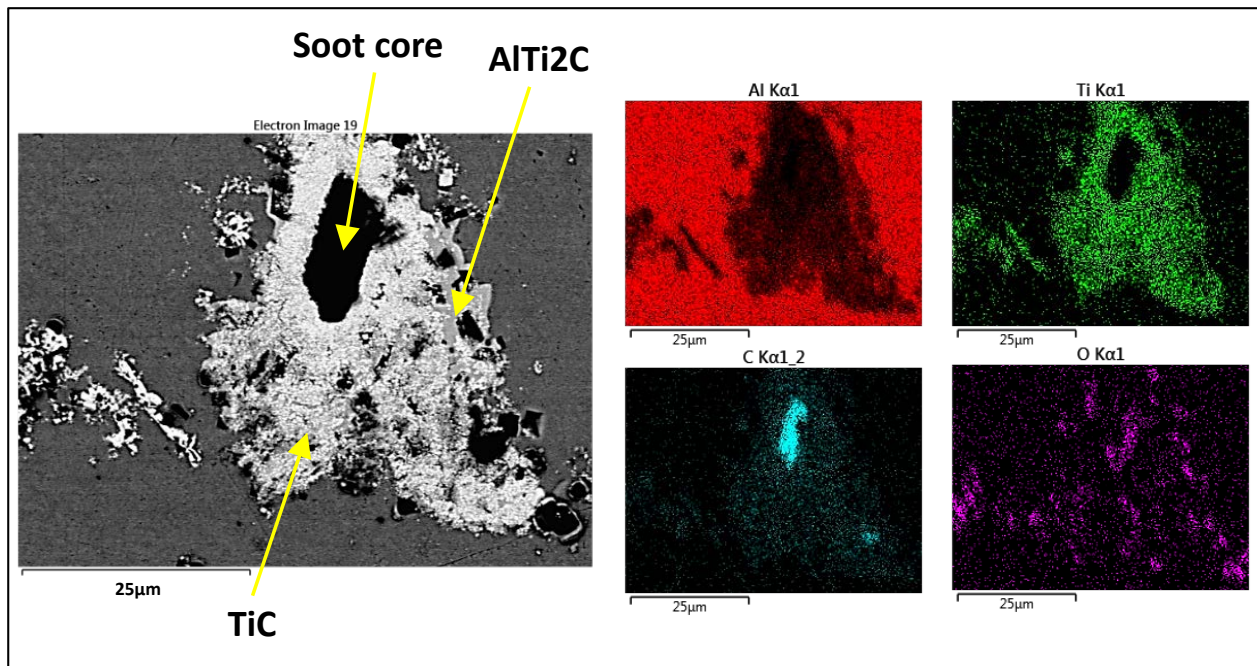
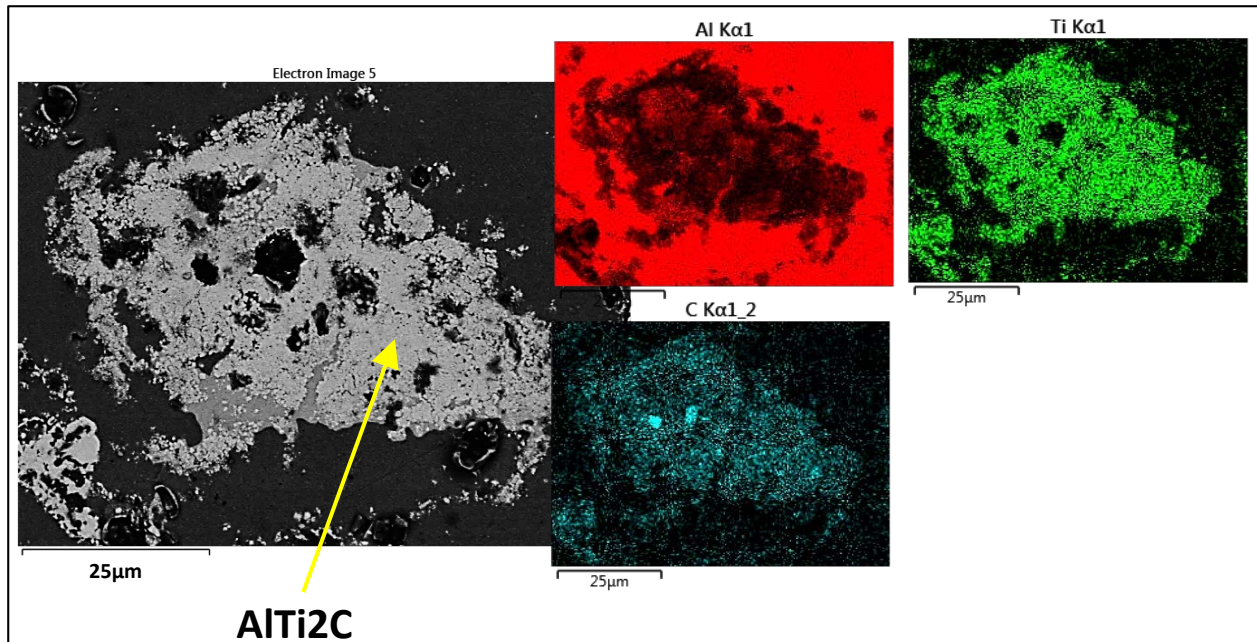Figure 90. SEM-BSE + EDS example of soot particle consumed into crumbling $AlTi_2C$-TiC.

Figure 91. Another SEM-BSE +EDS soot particle (almost consumed) into crumbling TiC in Exp. 2.

The large number of existing submicron particles in the proximity of the particle but in the aluminum matrix (Figure 89) suggests a combined route of soot formation and methane chemisorption for TiC formation (Figure 9).
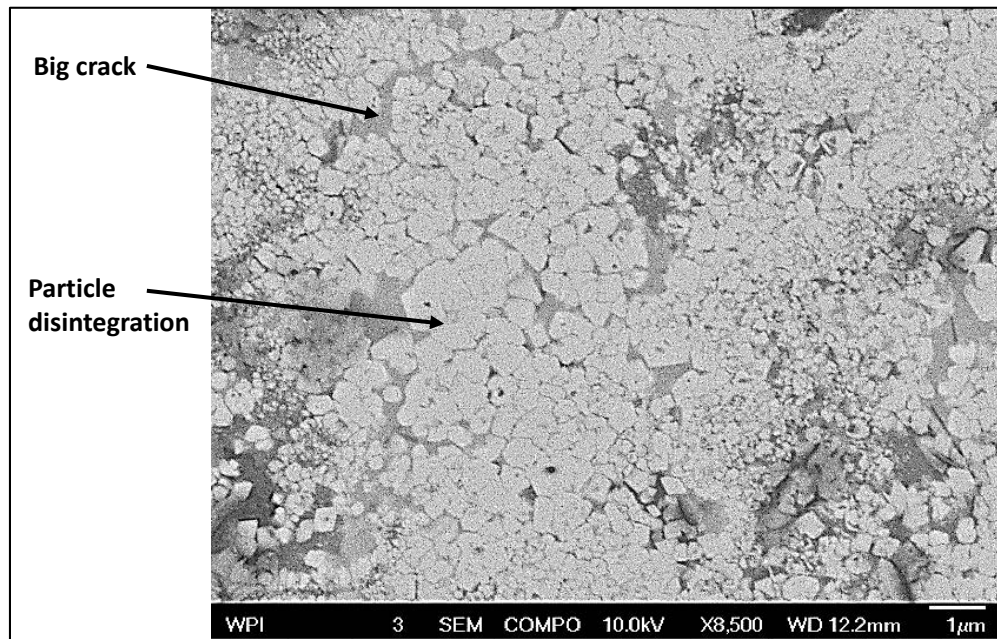

Figure 92. Zoom in of particle in Figure 91 The particle is clearly disintegrating.

However, Figure 93 (left side) confirms that submicron particles are also formed by TiC microparticles crumbling due to carbon diffusion into the aluminum so that the particle stechiometry TiC_x varies.
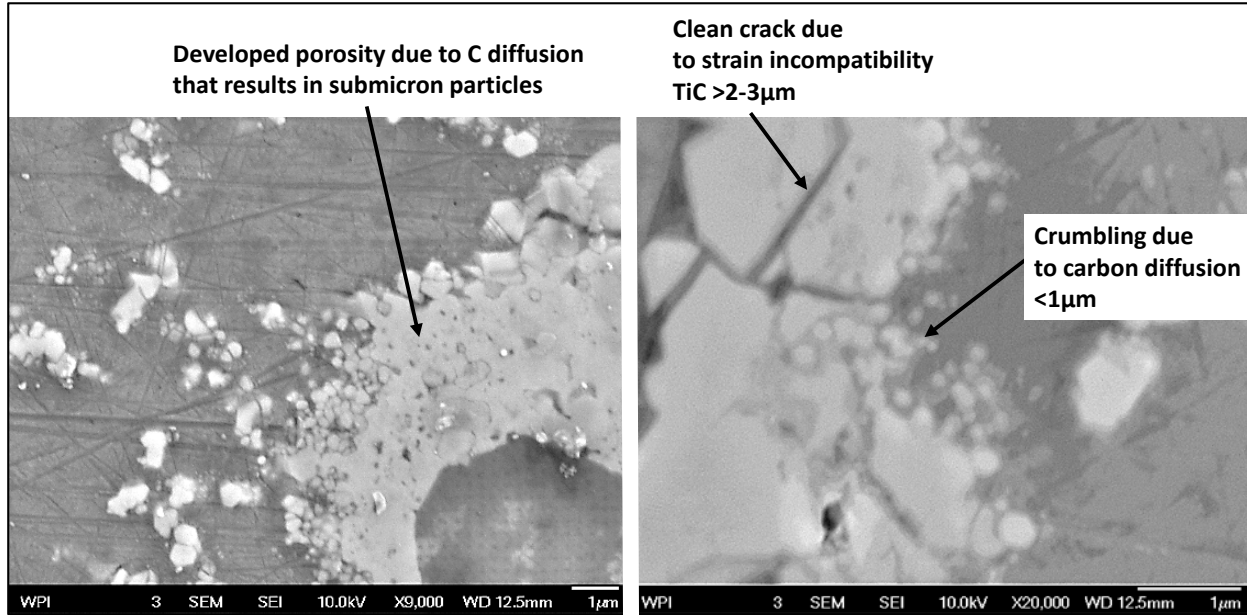

Figure 93. SEM-SEI TiC crumbling by carbon diffusion (left) and incompatibility stresses (right).

Many researchers [8, 25-28] have studied the carbon-Al-Ti reaction and later stability of TiC wet by molten aluminum and concluded carbon diffusion exists. Lin et al [74] observed reactive wetting between a $TiC_{0.7}$ substrate and a molten drop of AlTi1wt pct. The molten drop wetting angle varies with time and stabilizes once the TiC substrate develops micropores and its composition moves into equilibrium with the liquid as illustrated in Figure 94. Strain incompatibility creates clean straight cracks into microparticles ($d_p > 1\mu m$) whereas carbon diffusion results in small TiC submicron particles in the sourrounding of the original particle. A mechanism is hence proposed that works as a crumbling cascade in which 50µm particles break apart into particles<10µm by stress cracking, that crumble into 2-3µm size by a combined mechanism of stress cracking and carbon diffusion (cracks develop into secondary cracks due to existing porosity from carbon diffusion) that finally break into submicron particles by pure carbon diffusion crumbling that cause generalize porosity and particle disintegration. It is also expected that for higher temperature the carbon diffusion mechanism enhances and the dispersion gets finer. The crumbling cascade mechanism is illustrated in Figure 95.
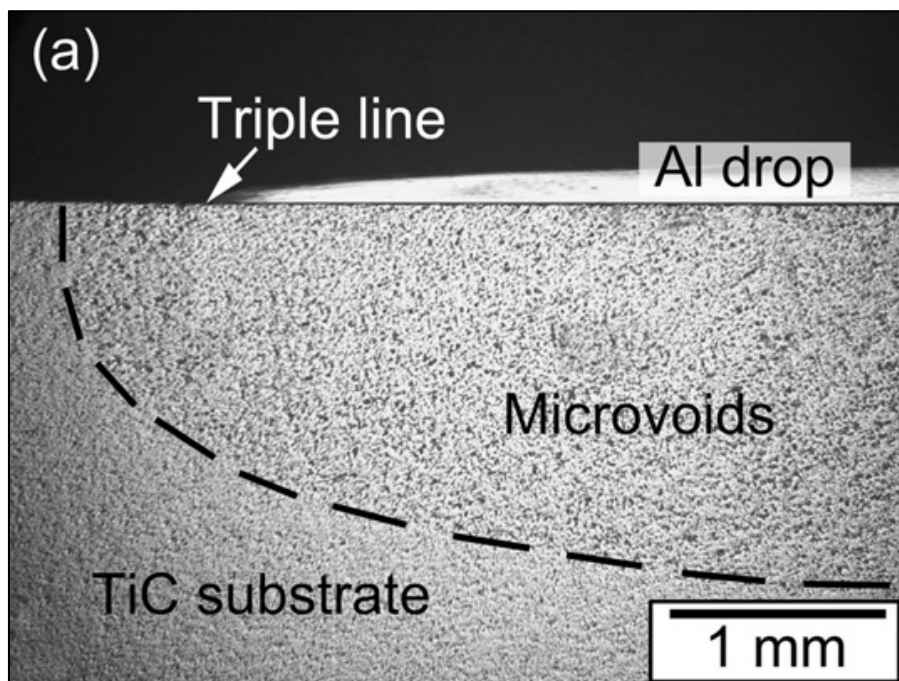
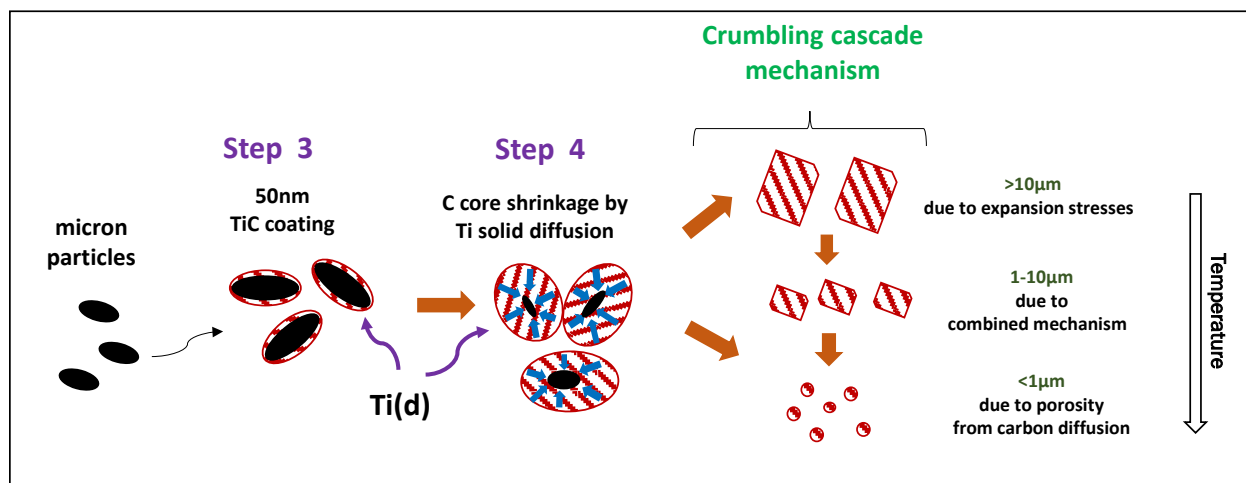Figure 94. Porosity in a TiC$_{0.7}$ substrate in contact with AlTi1 molten drop [74].

Figure 95. Crumbling cascade mechanism.

Therefore, it can be concluded that no evidence can be established of nanoparticles produced by the chemisorption route (Figure 9) in Exps 1-4 and that the chemistry system 'Al-Ti-methane' is oxygen sensitive. With this in mind, our strategy for producing nanoparticles involves encouraging methane chemisorption with an oxygen getter (Figure 25) whereas simultaneously suppressing the soot decomposition along the hollow shaft of the apparatus (Figure 2). In next section, experiments 5-7 have been carried out to study the effect of the furnace temperature

on the soot formation. From Figure 73 we know that less than 5vol pct.CH_4 transforms into soot at 1050^0C. It is reasonable to believe that by decreasing the temperature up to 800-900°C the soot may be completely eliminated. After the soot is eliminated lithium is introduced as an oxygen getter in experiments 8-10 (see Table 8).

3.3.2. Soot avoidance by decreasing the temperature in Exps. 5-7

<u>Macrostructure</u>

Macrostructures from ingots made according to Exps. 5-7 are shown in Figure 96. In experiment 5, the ingot has a nascent bottom domain (limited by a dashed line in Figure 96) full of small particles that will be analyzed with XRD, LOM and SEM. Experiment 6 produces a homogeneous dendritic microstructure containing porosity that is free of needles in the whole ingot body.
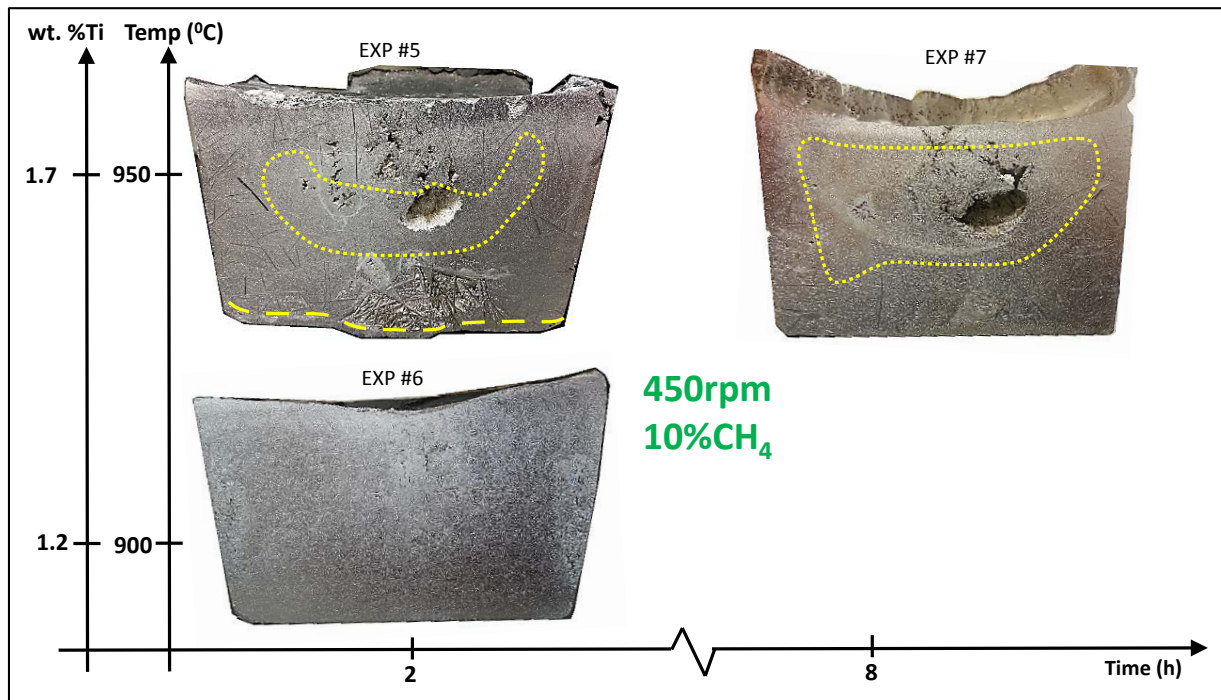

Figure 96. Macrostructures of etched material made according to Exps. 5-7.

<u>X-ray diffraction</u>

Figure 97 shows the XRD spectra of material taken from the bottom of ingots. Incipient TiC formation is detected in the material made according to Exp. 5 but no TiC formation is detected in the material made according to Exps. 6-7. This is in agreement with Figure 96. The three experiments form Ti_2AlC and the presence of Al_4C_3 is a possibility.

Microstructure

Figure 98 and Figure 99 show the optical microscope analysis of the ingot bottom at 50X and 1000X respectively. Experiment 5 presents interdendritic TiC microparticles and settled Al₃Ti needles produced during the experiment. Experiment 6, has a hypoperitectic composition (see Figure 77), and it is a clean matrix with no TiC or Al₃Ti needles evidence. The detected Al-Fe-Ni intermetallics are likely produced from the thermocouple in contact with the molten aluminum. Experiment 7 has been run for eight hours and there is no TiC formation. The Al₃Ti needles in the bottom are also formed during the experiment in molten state.

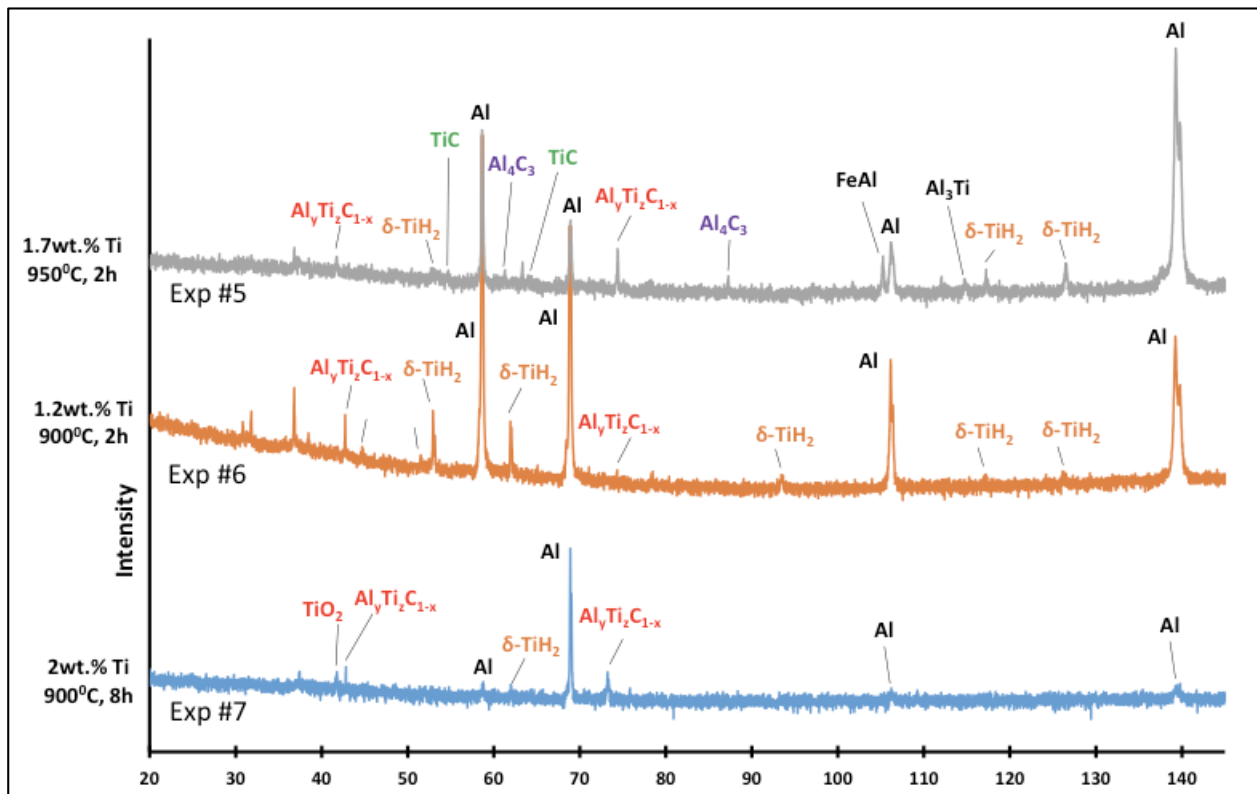
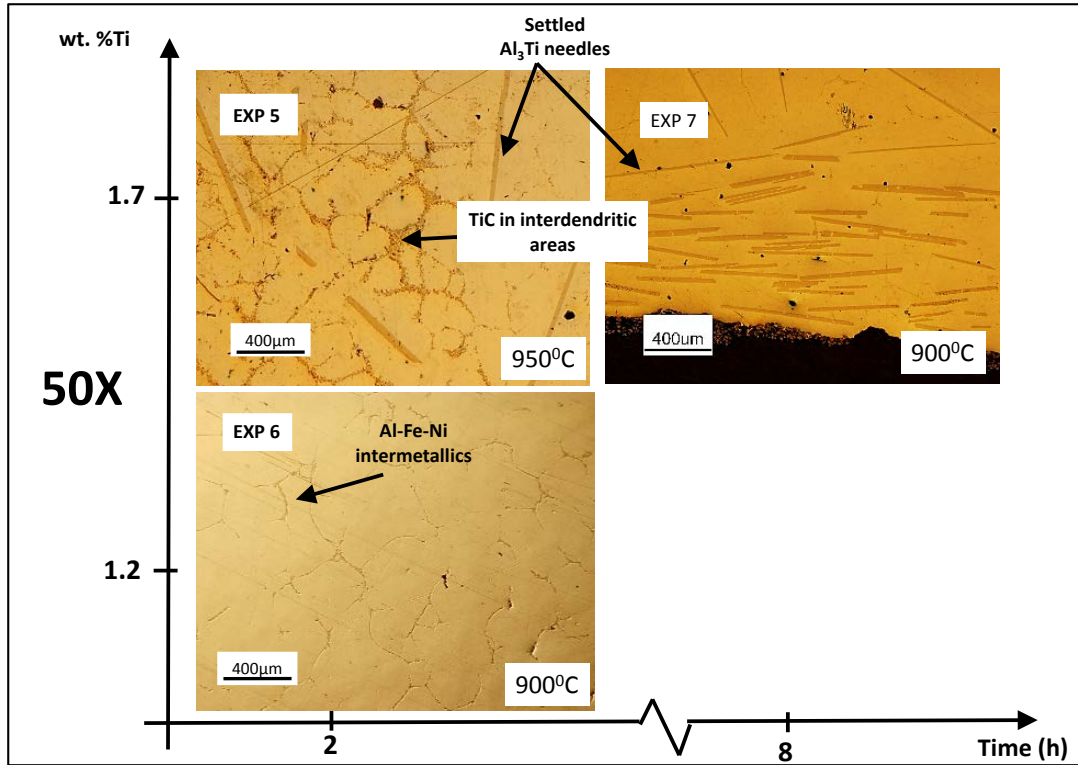Figure 97. XRD spectra (Cr lamp) at the ingot bottom location for Exps. 5-7.
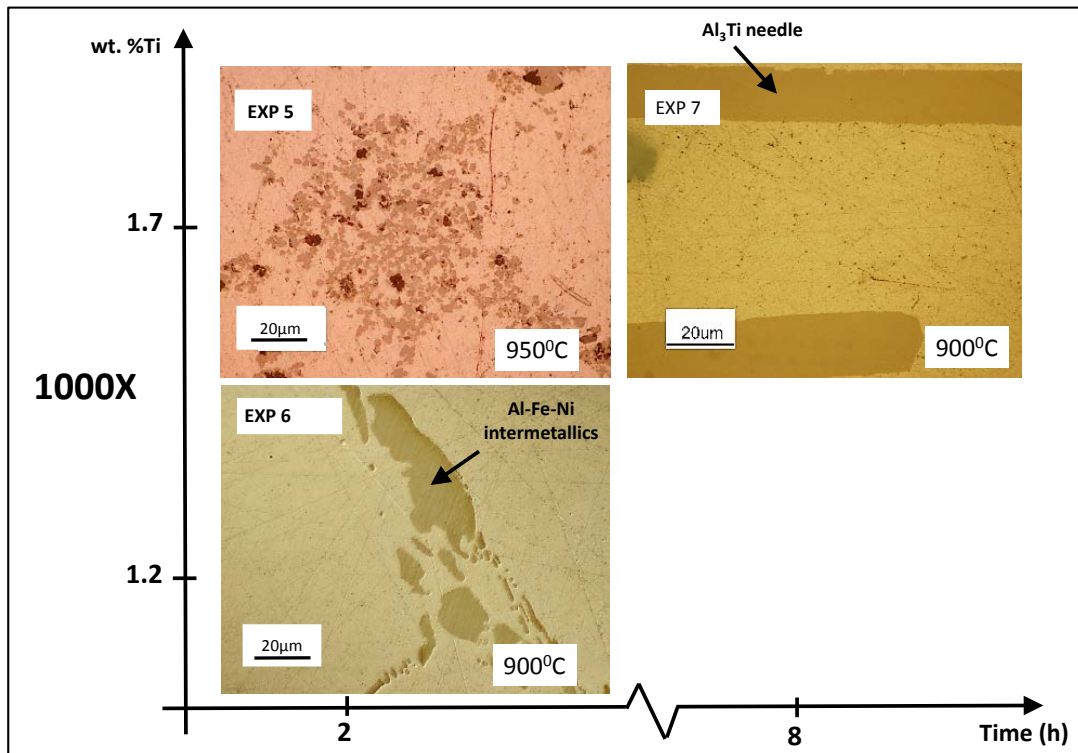
Figure 98. LOM pictures at 50X of Exps. 5-7.

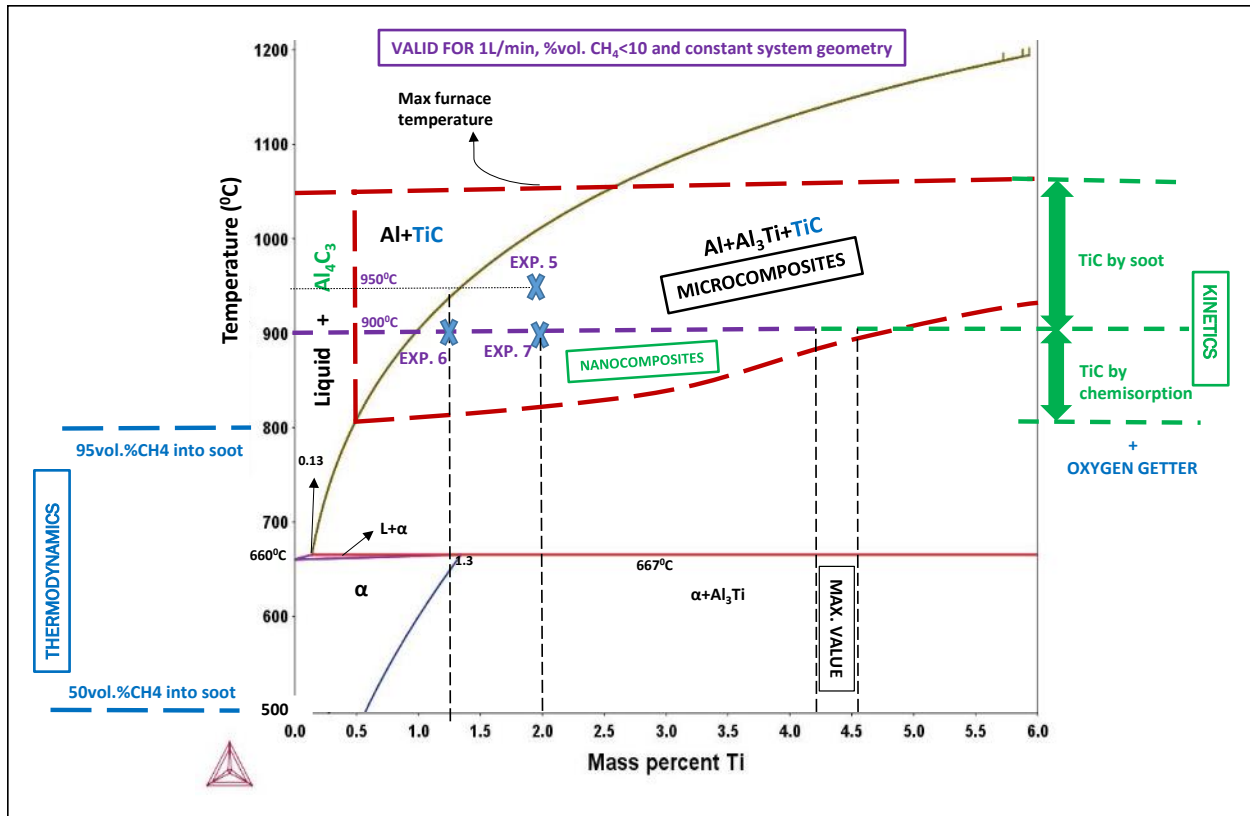Figure 99.LOM pictures at 1000X of Exps. 5-7.

Figure 100. Operation window partitioning into two regions for micro and nanocomposites synthesis.

Experiment 7 allows to draw an isothermal line at 900°C that divides the thermodynamic operation window in two kinetic regions (Figure 100). Above 900°C microcomposites are produced by the soot route and below 900°C no soot is formed and no TiC form. The introduction of an oxygen getter could enable the formation of TiC nanoparticles by any of the mechanisms indicated in Figure 25.

Scaling effects on the operation window for TiC nanocomposites synthesis

Caution is required with the 900°C temperature frontier when scaling up the process as it is determined by the gas decomposition kinetics, i.e. it depends on both system geometry, size, applied gas flow (1L/min) and composition (10vol pct.CH$_4$ in argon). To illustrate the effect of system size, geometry, gas flow and composition on the temperature threshold in Figure 100, another two systems from literature are taken for qualitative comparison.

(1) Shah et al. [107] allocated the methane decomposition to soot at a temperature above 850°C for a space velocity (SV) of 4 ml/(cm³·min). The SV is a measure of how fast the gas goes through the reactor tube, i.e. the inverse of the residence time. High SV values correspond to short residence times and vice versa as shown in the following equation.

117

$$SV = \frac{q[L/min]}{V_{reactor}[cm^3]} = \frac{v[L/min] \cdot vol\%CH_4}{V_{reactor}[cm^3]} \tag{92}$$

(2) In our system, the internal diameter of the hollow shaft is 7mm and it is active for soot formation in its last 10inches below the metal shield where the temperature is high (see Figure 72) plus 4-5inches of molten metal. In this case, for a gas flow rate of 1L/min and vol pct.CH_4=10, the space velocity is 150 ml/(cm³·min) (or 1.5s of residence time) an order of magnitude larger than the SV of Shah et al. [107], which is initially advantageous.

(3) In the case of Sahoo, Khatri and Kozack work [11, 14], 70gr of aluminum (20 times less than 1400gr-3lbs in our system) have been molten in a non-stirred crucible at 1300⁰C. The crucible is supposed to be very compact in size, proportional to the 70gr of aluminum capacity, and the residence time of the methane inside the furnace very short (or high SV values). Assuming inverse proportionality between furnace size and its SV value, SV is 20 times larger than in our case, being its value around 2500 and the residence time some few hundredths of seconds. Such a short time for decomposition receives the name of 'flash decomposition' and it explains the small graphite flakes (50nm in size) produced in [11, 14]. The soot nuclei are synthesized but do not have time to agglomerate and coarsen (Figure 13).

With the help of the two external articles [14, 107] and our Exps 5-7 a qualitative T-t diagram has been sketched in which the different TiC formation kinetic routes are located. The black dashed line between the soot formation and chemisorption areas corresponds with the threshold temperature that separates both TiC formation routes and it depends on the system size and gas composition (see 92). Note that it equals 900⁰C for experiments 5-7 as experimentally concluded in Figure 100 and also equals 850⁰C for the SV of Sha et al [107]. We have no experimental value for the cut of the dashed line at the Y axis, so the 800⁰C is an approximate value.
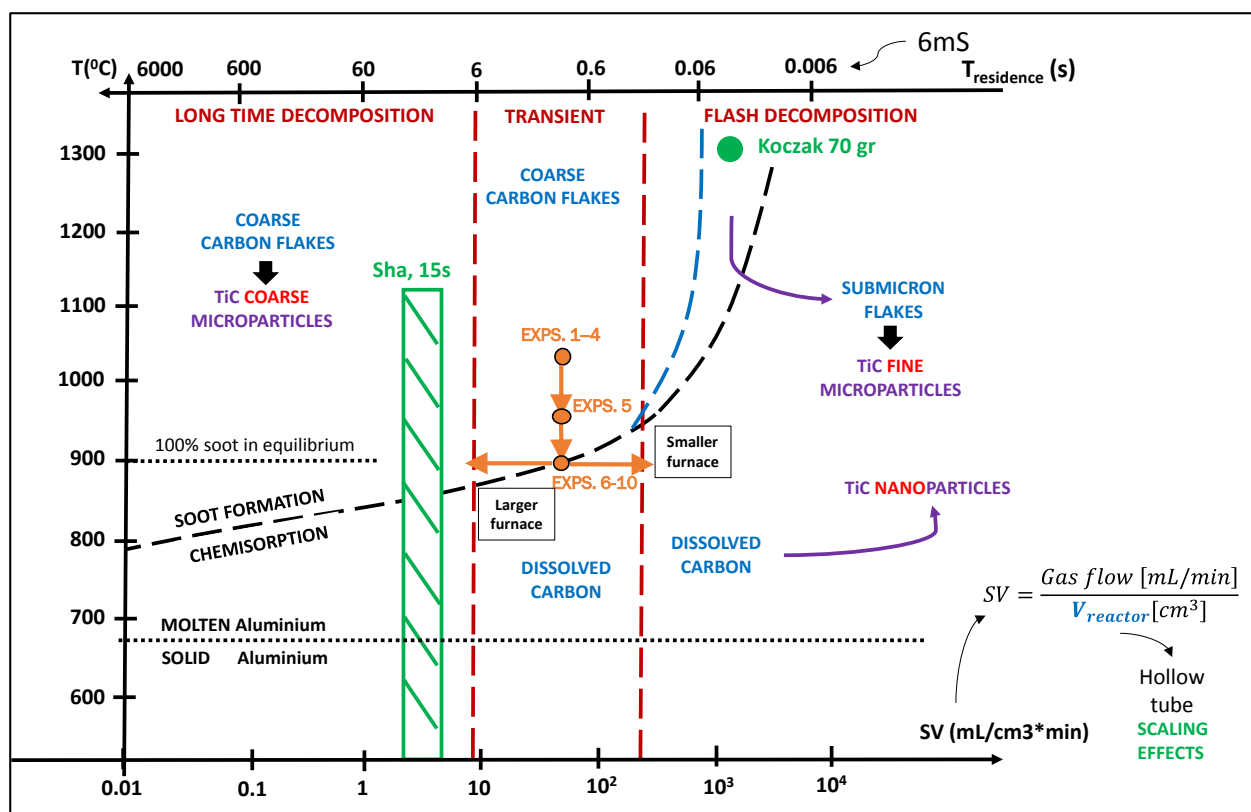
Figure 101. Scaling effects (qualitative) on the kinetic TiC routes regions and soot coarsening.

The previous analysis allows the formulation of a unifying theory that accounts for both our experimental results and the disparing results from Koczak's group [11, 14]. They observed that only submicron soot particles are formed and they do not crumble when converted into TiC, like in our case, but coarsen up to 2-3μm. Their observations were our initial proposal in Figure 9. An explanation to this disagreement needs to consider their specific experiment conditions and scaling effects associated. They bubble 1L/min of gas into stagnant 60gr of molten metal at 1350⁰C. Two observations are made:

(1) Short residence time of the bubble in the melt and high temperature imply strong soot formation in the flash decomposition region (Figure 101). The soot particles do not have time to agglomerate and remain under 100nm.

(2) The small quantity of molten aluminum is easily saturated in dissolved carbon so crumbling due to carbon flux from the particle to the melt is canceled.

The TiC small particles grow and coarsen stably as observed by Koczak's group. In our case we work with 3lbs of material and 1L/min of gas flow at 1050⁰C and both soot agglomeration and no carbon melt saturation are expected. In [108, 109] the rich corner of an Al-Ti-C triangular diagram at 1027⁰C is shown (Figure 102) in which

both carbon saturated molten metal and titanium saturated molten metal and the TiC$_x$ chemistries in equilibrium with them are visualized. Locations for TiCx are not drawn to scale.
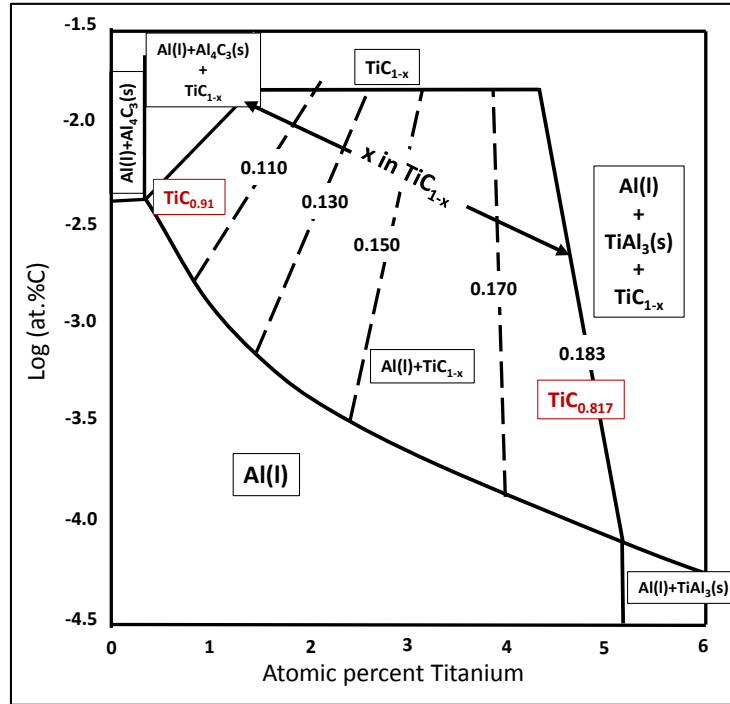

Figure 102. Aluminum rich corner of the Al-Ti-C diagram [109].

In Figure 103 a unified theory for TiC synthesis by the soot route is illustrated.
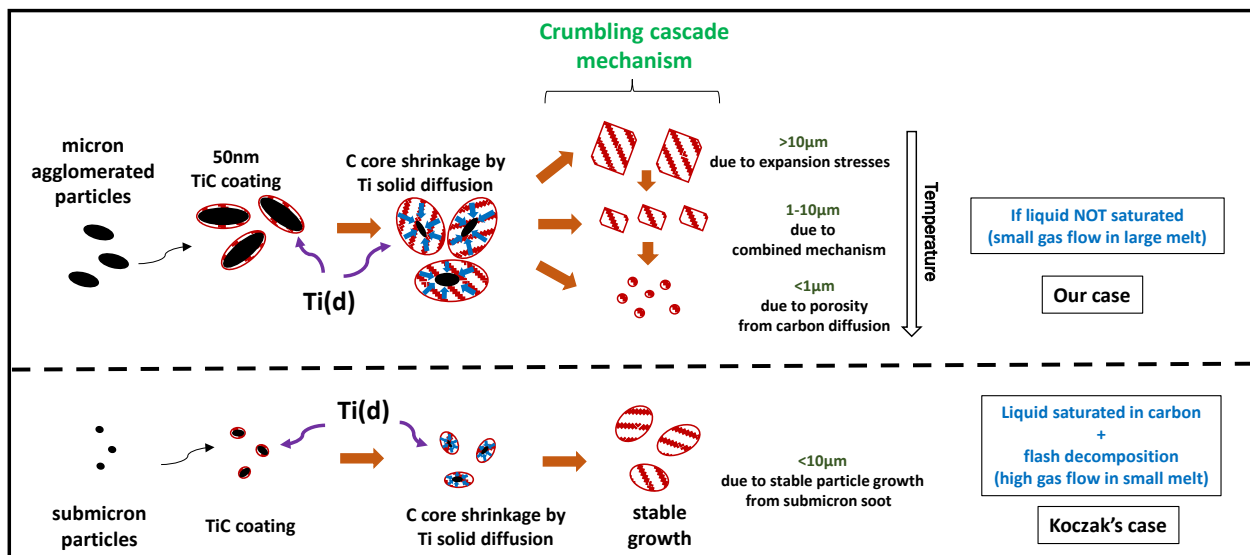

Figure 103. Scaling effects on TiC microparticles mechanism synthesis in the soot formation.

3.3. Nanocomposites formation

Lithium is the selected oxygen getter. An AlLi2.5-Ti diagram is shown in Figure 104 with both the operation window and experiments 8-10 superimposed. Main change in the diagram when compared with the Al-Ti diagram is the shift of the peritectic point from wt pct.Ti=1.3 up to wt pct.Ti=0.61.
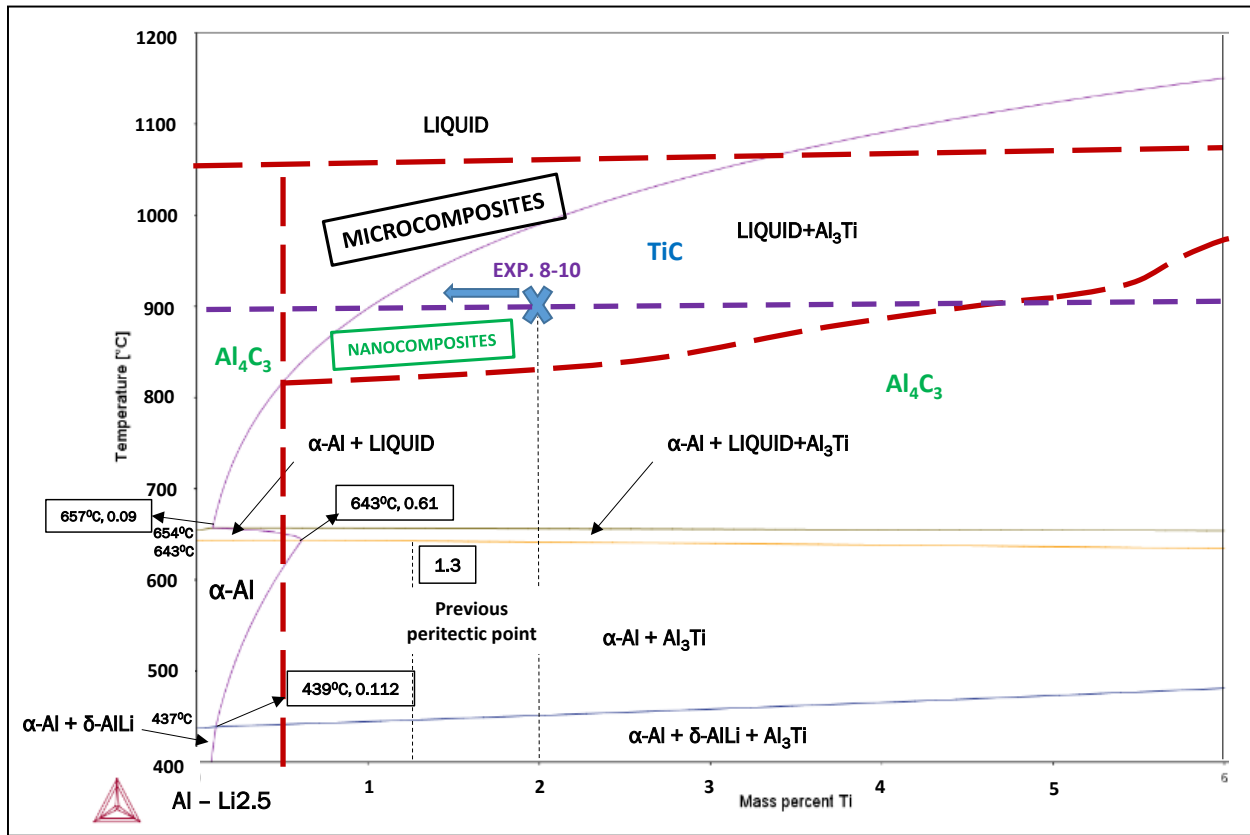

Figure 104. AlLi2.5-Ti diagram and operation window allocation.

<u>Macrostructure</u>

Experiments 8-10 macrostructures are shown in Figure 105. All experiments have a bottom domain with segregated constituents. There are few thin needles in all the experiments distributed across the ingots body. Experiment 9 has a very good defined top vortex region whereas in Exp. 8 it is less defined and in Exp.10 there is no vortex or top formation due to the use of a baffled crucible. The existence of a good defined vortex after solidification implies rheology change, imparted by non-settling nanoparticles. Probably particle segregation occurs, that follows the pattern in Figure 60. The existence of Al_3Ti needles leads to the assumption that the TiC concentration is small.
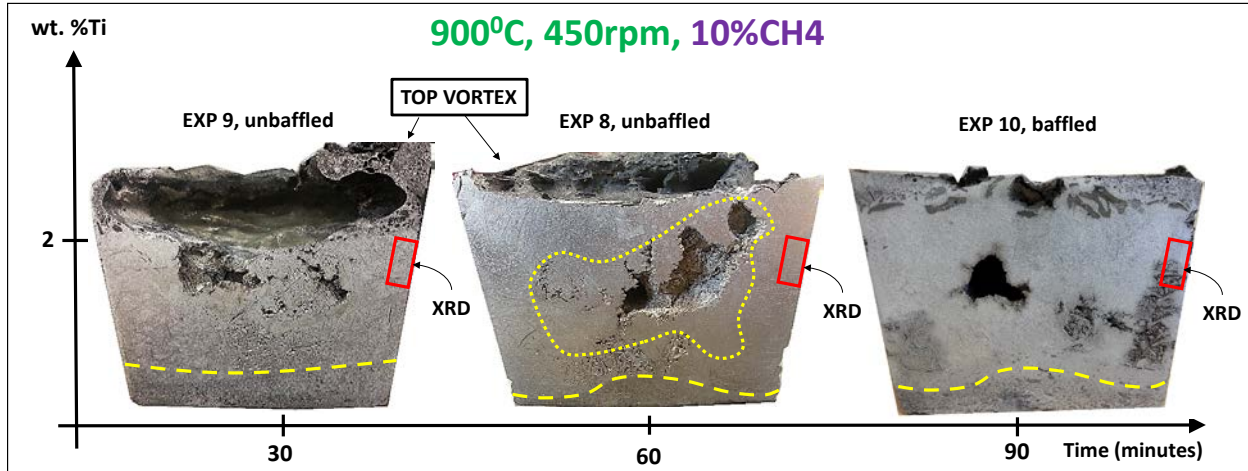
Figure 105. Macrostructures of etched material made according to Exps. 8-10.

X-ray diffraction

The XRD analysis of the experiments 8-10 is done at the peripheral location indicated in Figure 105, in which the TiC concentration is thought to be maximum, after Figure 60. Figure 106 shows some TiC peaks in Exps.9-10 and no peaks in Exp.8. XRD is a cumulative technique and the detection of minor phases (<5vol pct.) is cumbersome. The small TiC peaks in the XRD imply very diluted concentration of TiC. The existence of SiO_2 is explained in later in Figure 118. Some TiO_2 particles have been also observed with a size range of 100-500nm. Regarding the lithium oxide compounds, Scholz and Greil [20] plot an isothermal equilibrium phase diagram at 1000^0C (Figure 107), in which the final product composition that results from contacting 2.3w pct.Li doped aluminum melt with a static nitrogen atmosphere with variable O_2 content is calculated. The $\gamma - LiAlO_2$ is produced from the contact of the melt with the protective atmosphere (pO2<0.1vol pct.) whereas the Li_2O is produced from the contact of the melt with the bubbles (pO2<10^{-6}ppm).
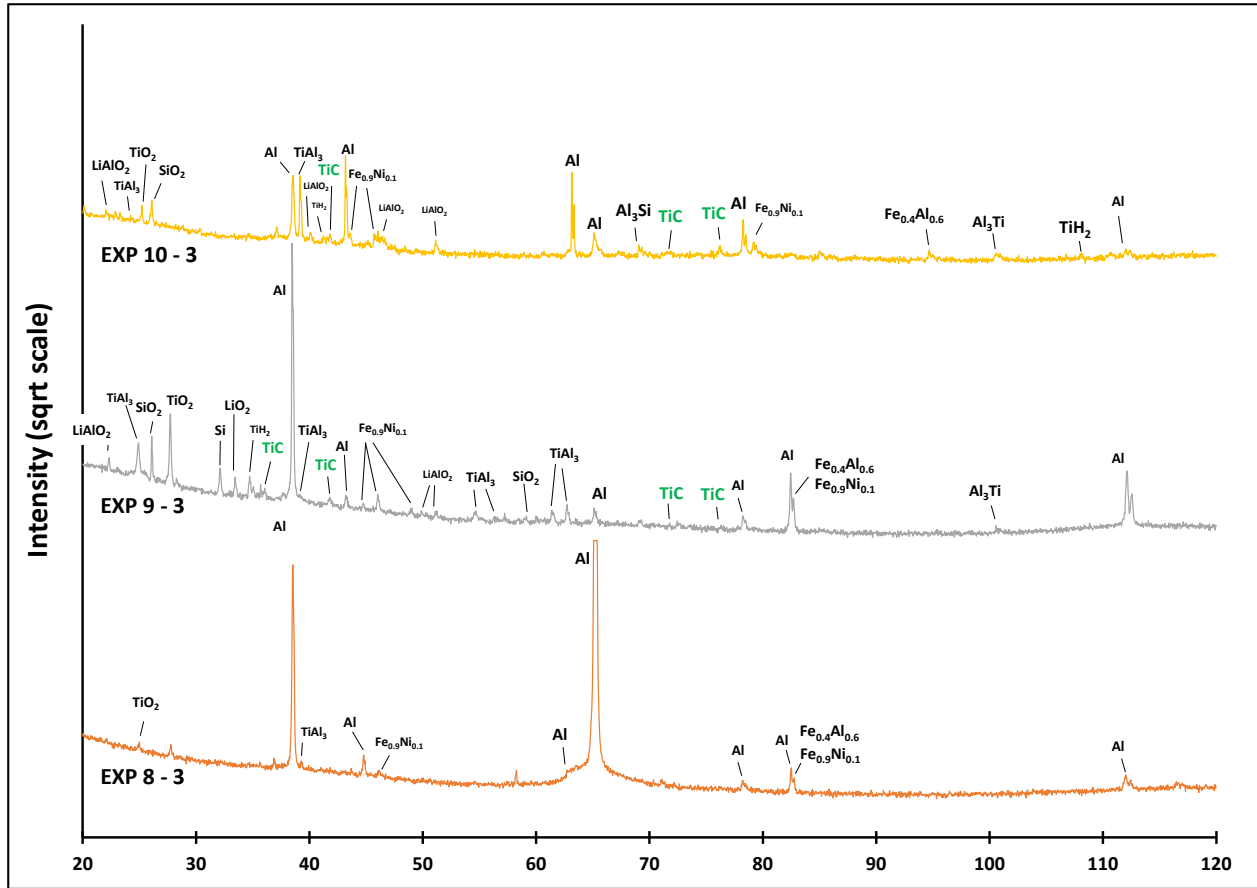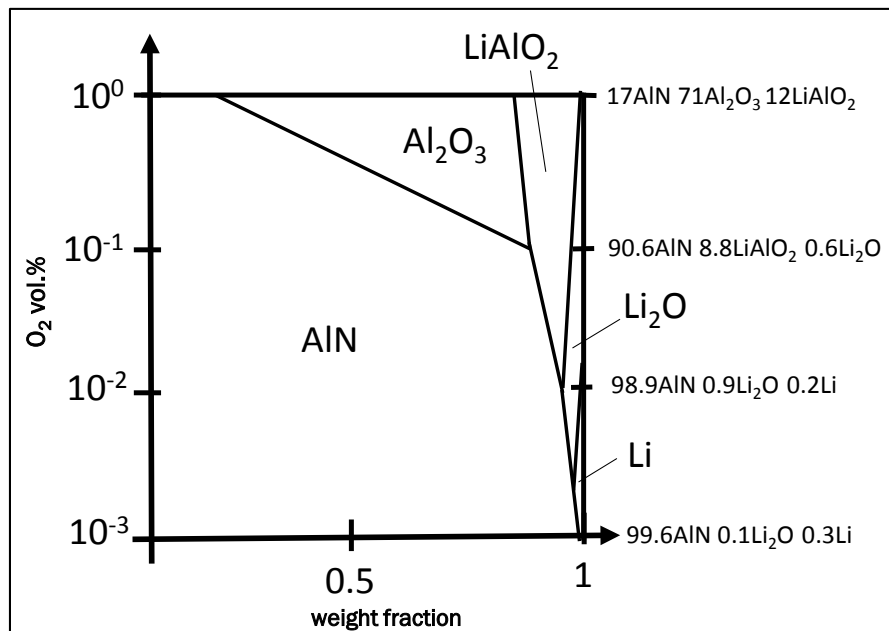
Figure 106. XRD spectra for EXPS. 8-10 (Cu tube).

Figure 107. Isothermal phase diagram of a 2.3wt pct.Li doped Al alloy at 1000^0C in a static N_2 atmosphere with variable O_2 content [20].

Microstructure

LOM pictures of the ingot bottom at 50X and 1000X are presented in Figure 108.
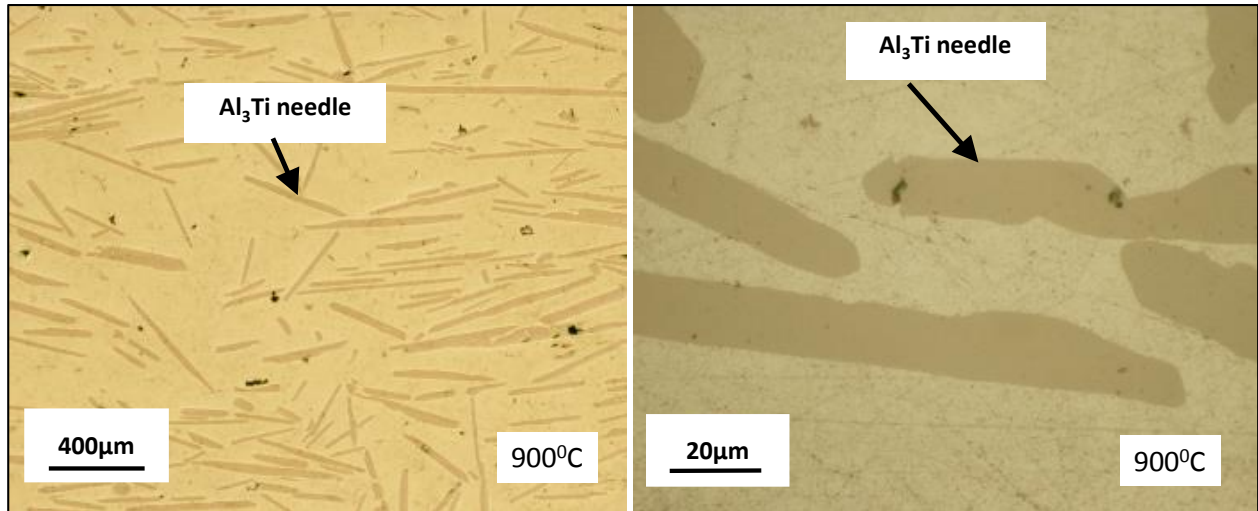
Figure 108. LOM pictures of ingot bottom in Exp. 8 at 50X.

The bottom part of experiments 8-10 have short and thin Al₃Ti needles. They were, as in Exp. 7, presumably precipitated during the experiment time in the liquid-solid region of the AlLi2.5Ti phase diagram (see Figure 104) and sedimented once stirring ceases. TiC microcomposites are not detected in any of the two experiments.

Nanostructure

The as polished matrix surface of the ingot at the peripheral location in Figure 105 is shown in Figure 109. It does not show nanoparticles.

Figure 109. Surface of sample from Exp.10, SEI mode. No nanoparticles are present.

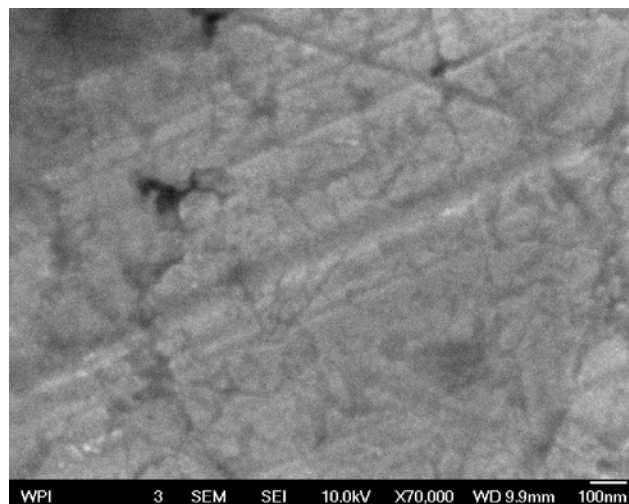In Exps.9-10 if the surface is carefully etched with a 10wt pct.NaOH solution for 10s. The solution uncovers bright spots of 20-30nm in size (Figure 110 left). TiC is inert to NaOH solution [110]. It is hypothesized that during the polishing step tiny small nanoparticles are covered by the aluminum matrix. The sodium hydroxide removes the covering aluminum layer. The TiC particles do not conduct electrons but get charged and bright. Exp.8 shows no bright spots (in Figure 110 right) in coherence with the absence of TiC peaks in Figure 106.
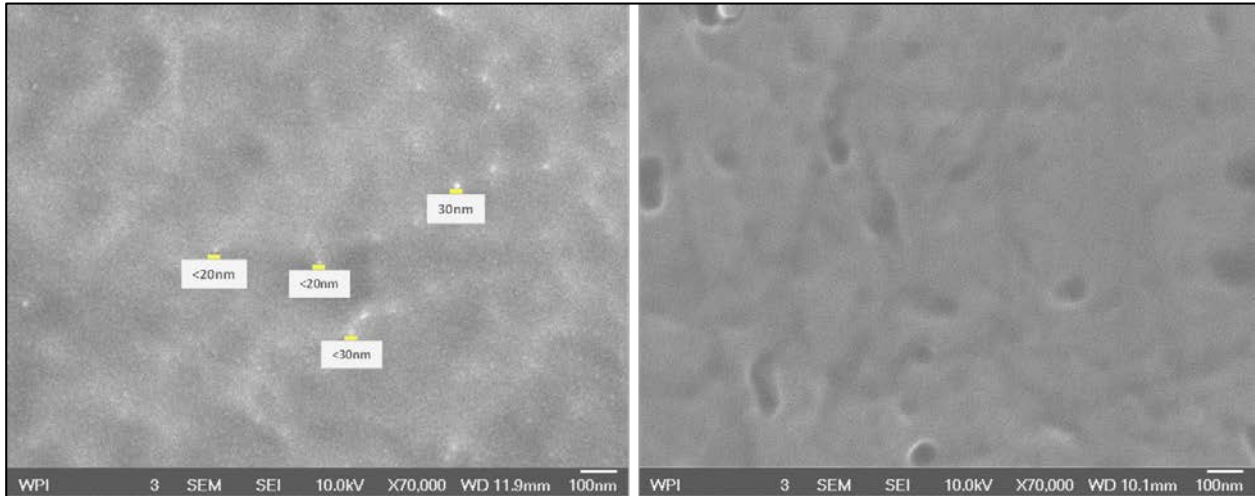

Figure 110. Experiment 10 (left) and Experiment 8 (right) after NaOH 10wt pct. etching for 10s.

The nanoparticles however, are not detected by the SEM-BSE detector in Figure 111. The cause of no BSE signal in the nanoparticles might be the resolution limitation of the BSE detector.
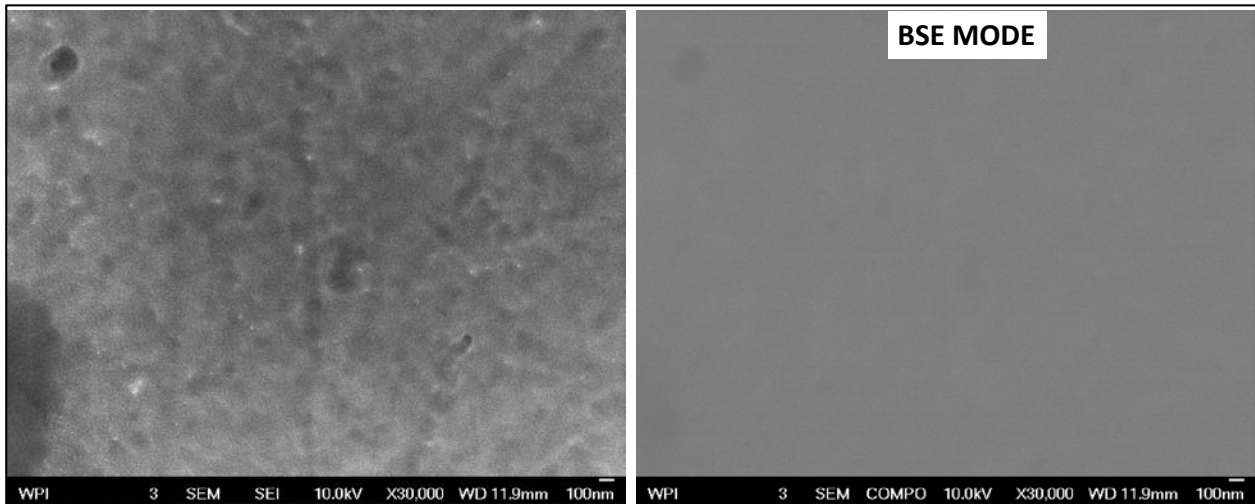

Figure 111. Etched SEI surface (left) and BSE signal (right) in Exp.10.

Figure 112 and Figure 113 show two examples of the BSE detector limitation in some residual TiC crumbling particles in Exps.8 and 10 in which the particles under 100nm, and especially under 50nm pointed with an arrow are not detected in BSE mode.
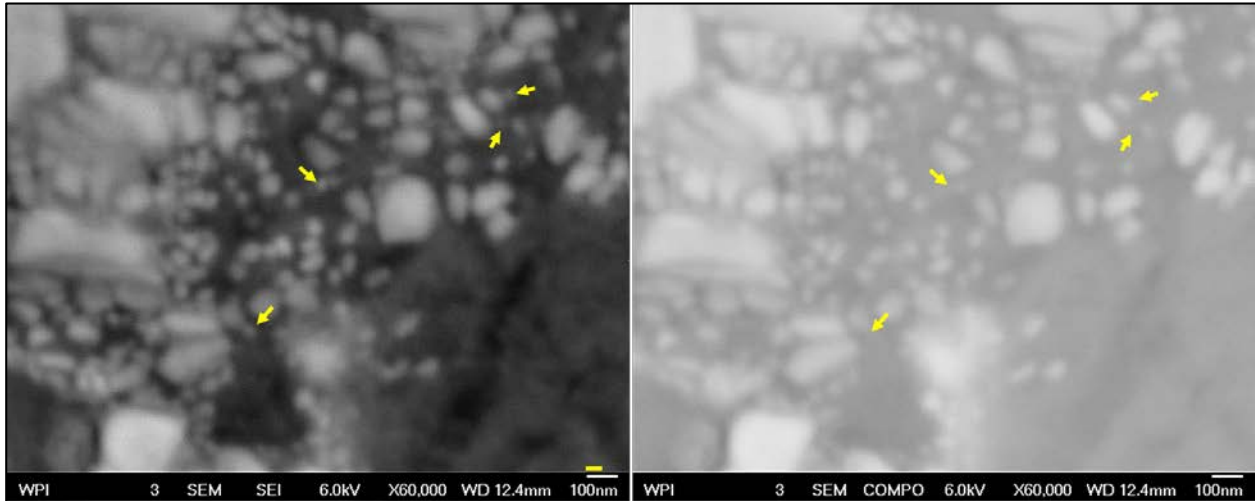
Figure 112. BSE limitation for nanoparticles detection (arrows) in residual crumbling TiC in Exp. 9.
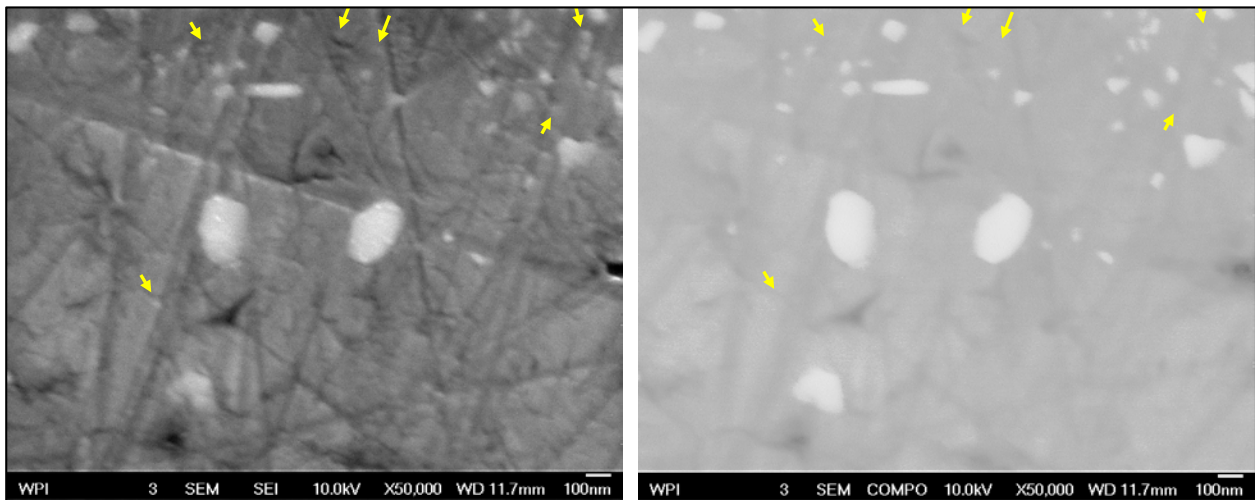
Figure 113. BSE limitation for nanoparticles detection (arrows) in residual crumbling TiC in Exp.8.

SEM-EDS is used to analyze the particles composition in Figure 114, Exp.9 with voltage 8KVs and intensity 1nA as operation parameters. A tiny Ti peak appears for each particle. The EDS analysis of the matrix showing no Ti peak confirms that the Ti peak at the bright spots belongs to the particles. It is so small because the resolution of EDS at 8KVs in aluminum is in the range of 1-1.5µm [111]. Smaller voltage gives better resolution but it is not strong enough to excite the Ti atoms. The

intensity is relatively strong to get enough counts of Ti signal but without losing a lot of resolution. The carbon peak is so big because of environmental hydrocarbons contamination.
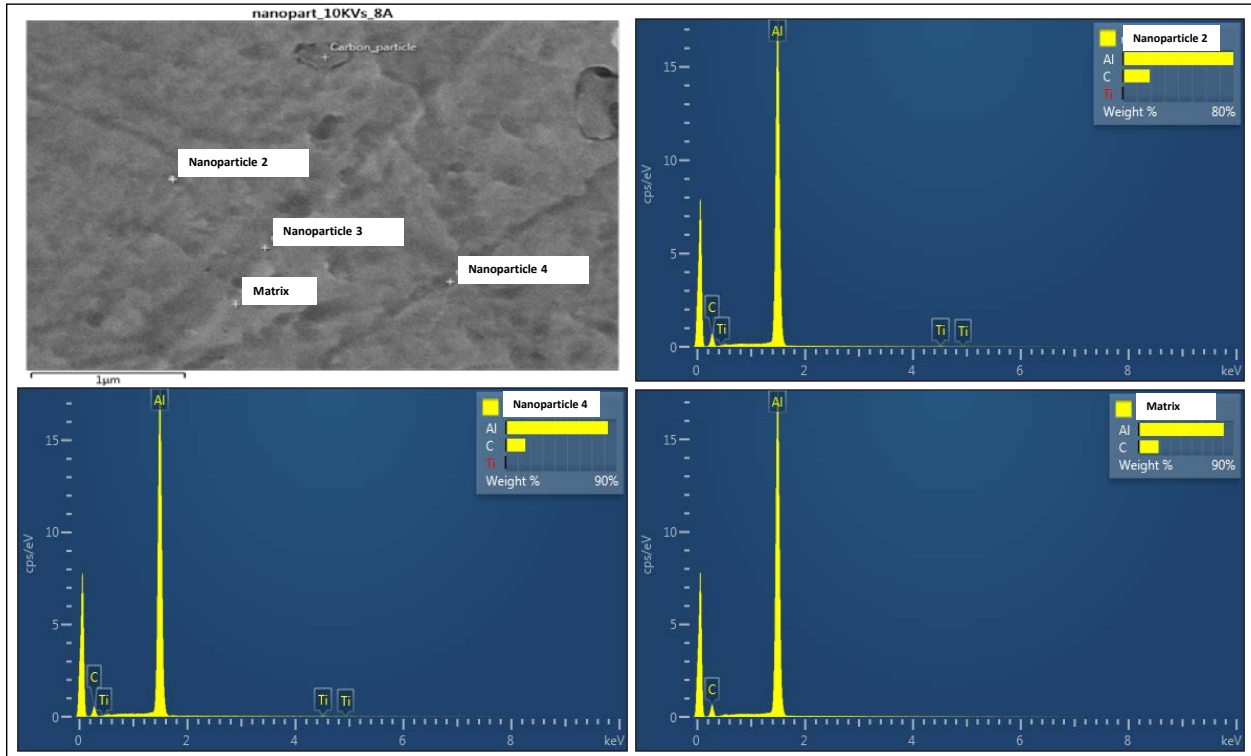
Figure 114. EDS composition of interaction volume embracing the nanoparticles in Exp.9, 8KV,1nA.

It is concluded that, in the absence of TEM confirmation, the charging white spots are TiC$_x$ nanoparticles. Figure 115 shows the variation of both particle concentration and particle size dependent on the ingot location. Five pictures have been taken at each location so the vol pct. and the particle size have been calculated for both Exps.9-10. Both experiments have particles size in the range 15-30nm and loading <1vol pct. but Exp. 9 shows also strong segregation in the ingot top part. This is in coherence with Figure 60. Two pictures of the interdendritic space and the matrix in the top of Exp.9 are shown in Figure 116 in SEM-BSE mode. The big coarse particles segregated in the ingot top part during the experiment are pushed by the solidification front into the interdendritic area whereas submicron nanoparticles stay in the matrix. In Experiment 10 a baffled crucible is used to avoid the vortex formation and vertical segregation. Crucible baffling brakes the circumferential flow pattern and enhances the vertical flow circulation.

127
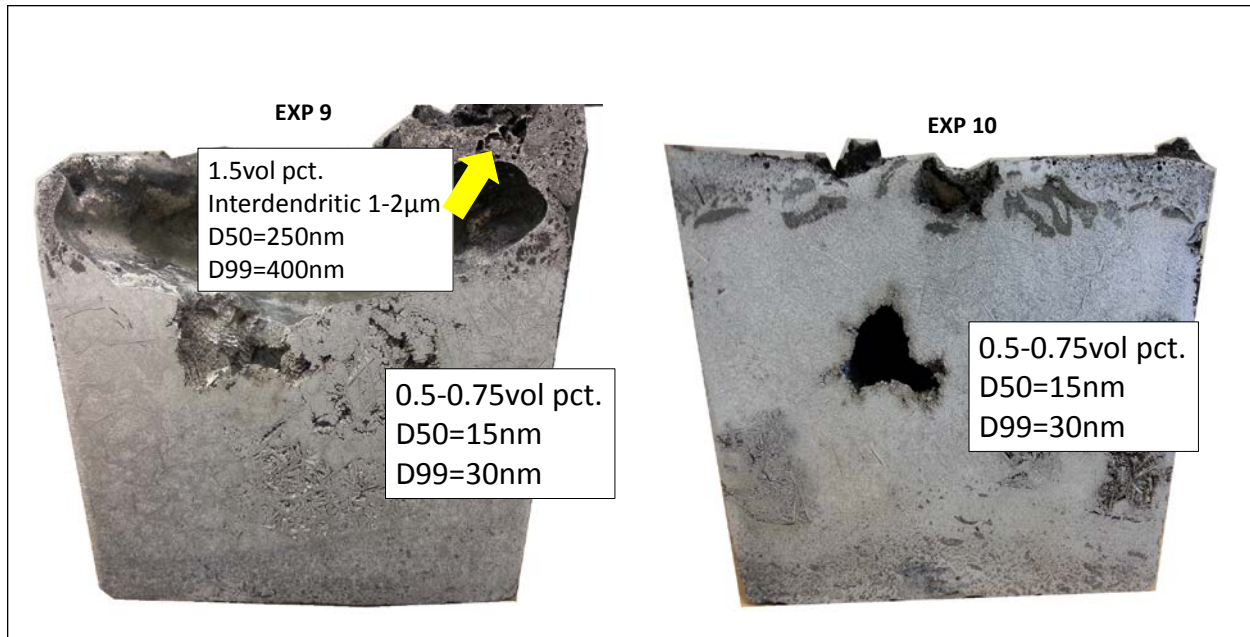
Figure 115. Nanoparticles concentration and particle size map in EXP. 9-10.
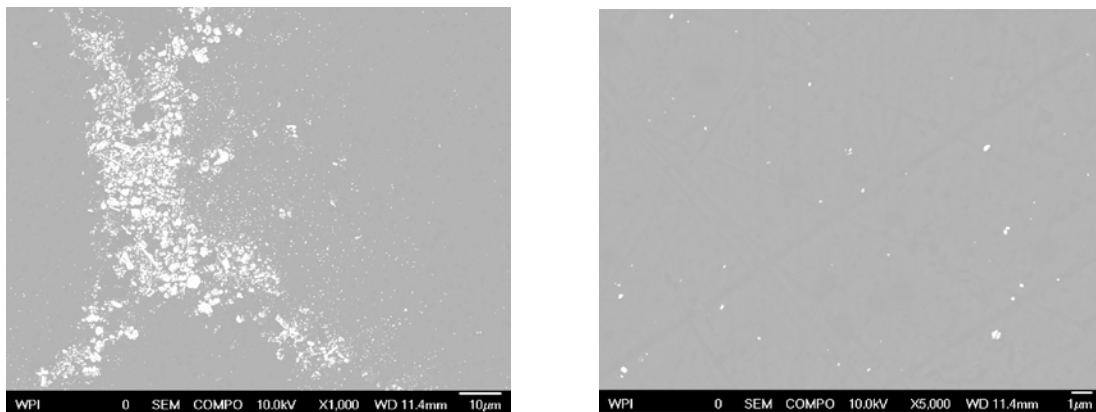
Figure 116. Interdendritic space and matrix particles in SEM-BSE mode in the ingot top part.

The lithium content varies from 1wt pct. to 2.5wt pct. in experiments 8 and 9-10, respectively. Under the conditions of experiments 8-10 there is a lithium content threshold above which the chemisorption happens and nanoparticles are produced. Figure 25 and Figure 29 illustrate the dynamics dependent on the lithium content and oxygen impurity content. Below the given threshold, the incubation time for the methane chemisorption is longer than the bubble lifetime and no chemisorption occurs. Above the lithium content threshold the incubation period decreases so methane chemisorption happens during the bubble lifetime. Allocation of experiments 8-10 in Figure 29 is done in Figure 117.
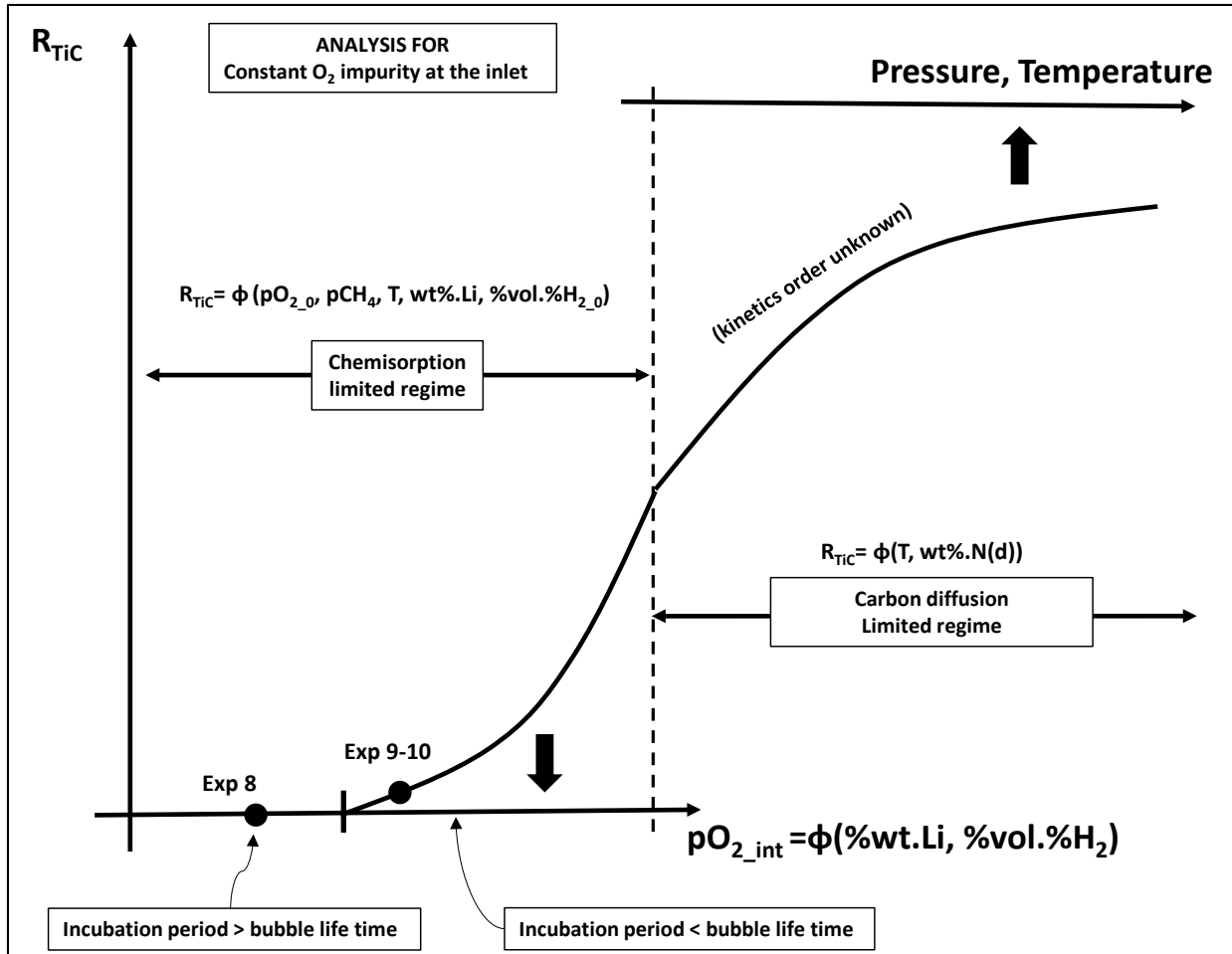
Figure 117. Allocation of Exps 8-10 in the reaction map in Figure 29.

Rheology and particle loading

The melt mixing regime is observed through the eyehole of the furnace in intervals of 10minutes (Figure 2). In experiment 8 no apparent issues occur. In experiments 9 and 10 the impeller breaks after 30minutes (fragments are seen floating). The impellers failure modes at the end of the experiments are shown in Figure 118. Both experiments 9 and 10 have been repeated six times with same result, i.e. impeller or shaft breaks. There is no doubt that due to nanoparticles production a sudden viscosity increase provokes the impeller or shaft failure. In experiment 9 the stagnant vortex formation in Figure 105 was observed to occur progressing from the peripheral to the interior region in the first 15minutes. Increasing melt stagnancy is observed until eventually the impeller breaks.
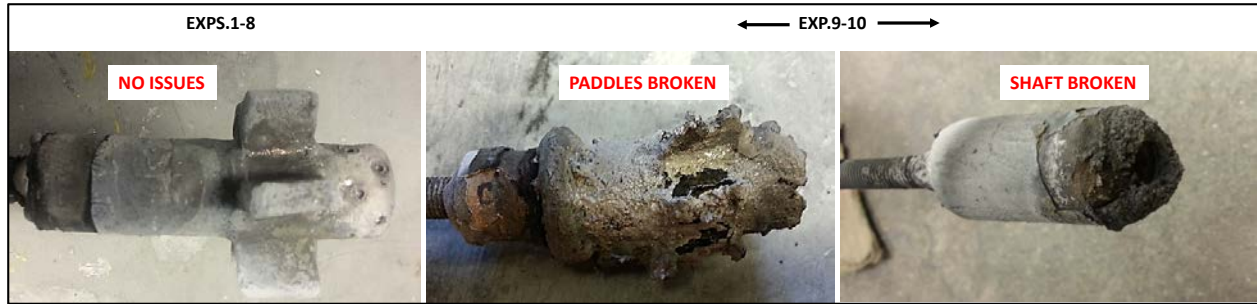
Figure 118. Comparison of impellers after use in Exps. 1-10.

The melt in Exps.9-10 is compared to the melt in Experiment 14 in the work of Makhlouf and Borgonovo for the chemistry Al-AlN [1]. In the Al-AlN chemistry particle size is 60nm (measured at 30.000X) and the loading goes up to 5vol pct. before experiencing rheology problems whereas in the Al-TiC chemistry the same problems are observed at less than 1vol pct. Main two differences between experiments are:

(1) Lower temperature (900°C) of the Al-TiC chemistry vs. 1050°C in the Al-AlN chemistry.

(2) A semi-solid mushy composition for the Al-TiC chemistry in the Al-Ti phase diagram vs. a pure liquid in the Al-AlN chemistry.

Due to the combined effect of those two differences the initial viscosity of the Al-Ti melt is likely to be one or two orders of magnitude higher (1-10cPo vs. 0.1cPo) than the initial viscosity of the AlLi2.5 melt at 1050°C for the Al-AlN chemistry. Both melts are allocated in the viscosity spectrum in Figure 119. The viscosity frontier above which the turbine technology is inefficient is 10cPo. This explains the low loading of the Al-TiC chemistry before rheology problems occur.

Figure 119. Allocation of Al-AlN Exp.14 [1] and our Exps 9-10 in the viscosity spectrum.

130

It is obvious that a more robust mechanical design is required. Increasing the shaft internal wall thickness and the impeller blade fillets will eventually solve the shaft-impeller mechanical failure. However, we still do not know at which experiment time the turbulence-laminar transition regime (in Figure 66) occurs so micropar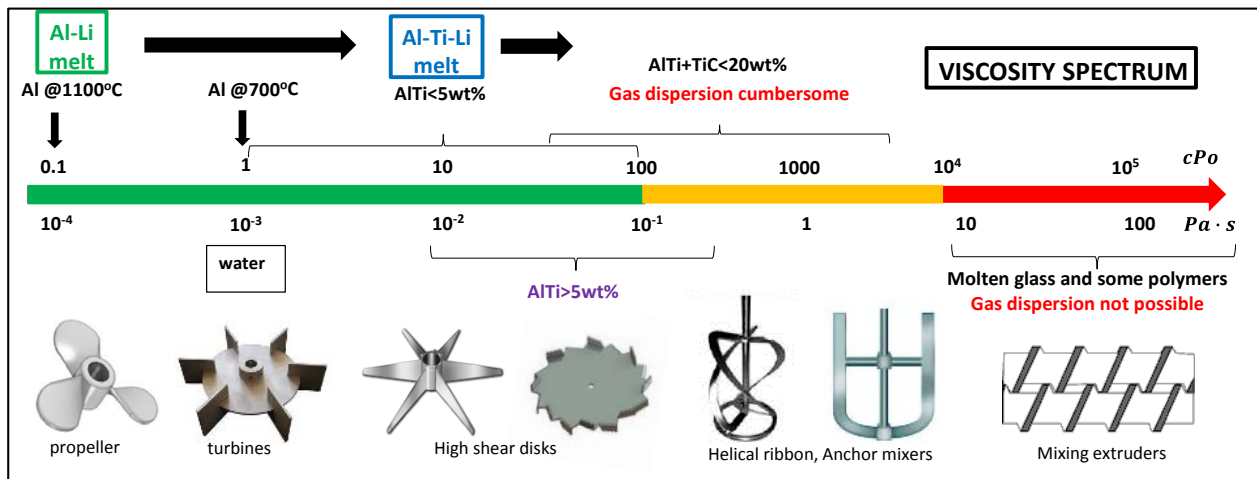ticles can be avoided. Zlokarnik [37] successfully studied the gas dispersion in stirred tanks with no Newtonian melts and increasing rheology. A new number, Galileo number (Ga) is introduced:

$$Ga = \frac{Re}{Fr^{1/2}} = \left(\frac{D^3 \cdot g \cdot \rho^2}{\mu_{eff}^2} \right)^{1/2}$$

The pi-set of the system was introduced in equation 61, and it is, for constant geometry written below:

$$\Pi \equiv \{Ne, Re, Fr, Q\} \equiv \{Ne, Ga, Fr, Q\}$$

The advantage of using Ga number vs. Re number is that Ga is only function of the viscosity whereas Re number is also function of the rotation speed. In the pi-set $\Pi \equiv \{Ne, Ga, Fr, Q\}$, correlations like $Ne = \varphi(Fr, Q, Ga^{-1})$ were experimentally calculated by Zlokarnik in Figure 120 for a melt with increasing rheology. *Fr, Q, Ga^{-1}* depend respectively on the rotation speed, gas flow and liquid viscosity, i.e. each dimensionless number depends on one process variable and the analysis simplifies. The turbulent-laminar transition regime in Figure 120 occurs in the period $Ga_1^{-1} - Ga_2^{-1}$ (or μ_{eff_1}-μ_{eff_2}). In this interval the gas cavities in the impeller (Figure 46-Figure 48) get partially flooded so the bubbles dispersion worsens, the impeller power (Ne number) decreases and most importantly microparticles are produced. Once in the laminar regime the impeller is flooded and there is no gas dispersion. **So the detection of the instability point 'μ_{eff_1}' is a very important piece of information because it indicates the maximum nanoparticles loading above which microparticles are produced.** The instability point or maximum loading can be maximized by following the next two strategies illustrated in Figure 120:

(1) For a given impeller diameter (constant *D*), increasing the *Fr* number (or rotation speed *N*) and decreasing the flow number (or gas flow *q*) shifts the curves upwards and increases the instability point**.**

(2) For constant rotation speed, using a bigger impeller (scale up) will also increase the instability point given that the introduced power increases.

Hypothetical quantitative points are included in Figure 120 to illustrate the two proposed strategies. A direct correspondence between $Ga^{-1} \propto \mu_{eff} \propto time$ is expected what opens the door to the experimental determination of the instability point as a

specific time value along the experiment time. The Newton number follows the formula shown below (see Table 1):

$$Ne = \frac{P}{N^3 \cdot D^5 \cdot \rho_{melt}} \quad \text{with} \quad P = V \cdot I = M \cdot \omega$$

So the pairs *I-time* and *M-time* will follow an analogous experiment evolution to the *Ne-Ga⁻¹* pair in Figure 120.
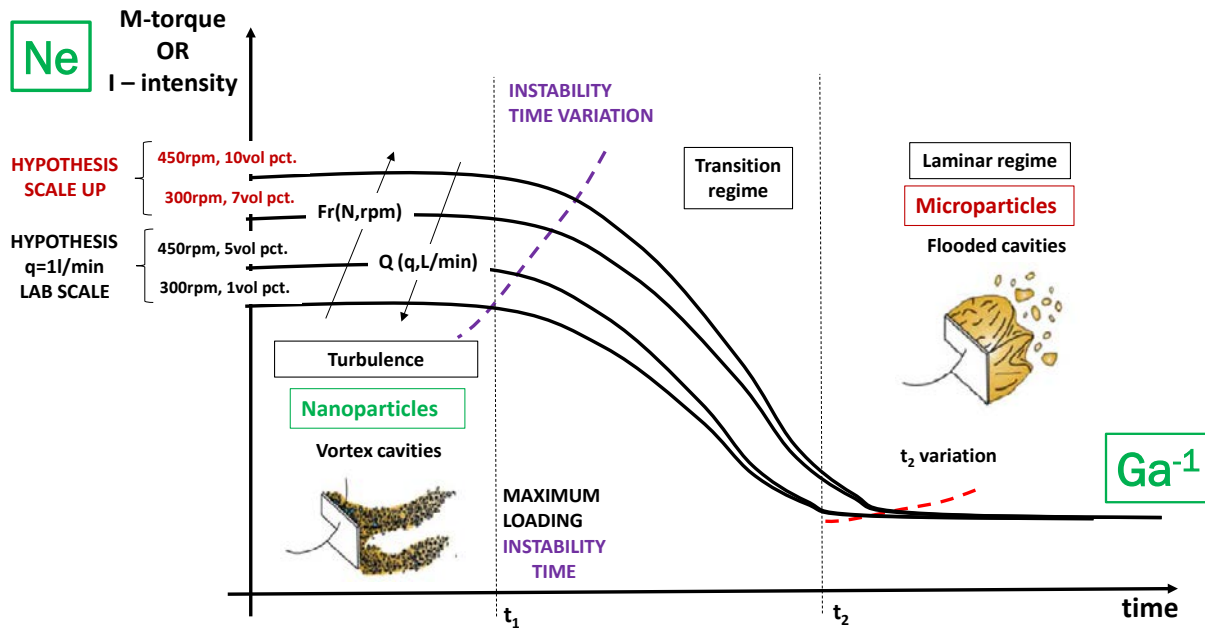
Figure 120. Mixing-gas dispersion regimes with a Newtonian liquid and increasing rheology.

In summary, two options arise to experimentally determine the instability point or maximum loading:

(1) Shaft torque measurement with a wireless strain gauge. Both the instability point and the real liquid viscosity evolution can be measured since the torque reading allows to calculate the exact amount of power that is introduced into the melt.

(2) Intensity consumption of the motor. The instability point can be determined but the real absolute viscosity evolution cannot because the measured power consumption includes the motor mechanical and electrical losses that are not transmitted into the liquid.

3.4. Towards a Marketable Product

Exps. 1-10 represent a valuable set of data to find out trends on the quantity and size distribution of both Al_3Ti needles, TiC microparticles and nanoparticles dispersion vs. process parameters.

3.4.1. Al_3Ti needles formation and control in Exps. 1-6

The Al_3Ti particles that appear in the macrostructure of the ingots are deleterious. They can affect mechanical properties of the A356 reinforced alloy, and they deactivate the nucleation ability of the TiC particles. An understanding of the macrostructure changes as function of titanium content of the melt, temperature, and time follows. The thickness of the Al_3Ti needles of the medium and top parts of the ingots has also been studied. Figure 121 shows the Al_3Ti needles. They have large interspacing (up to millimeters) and their thickness changes along their length.
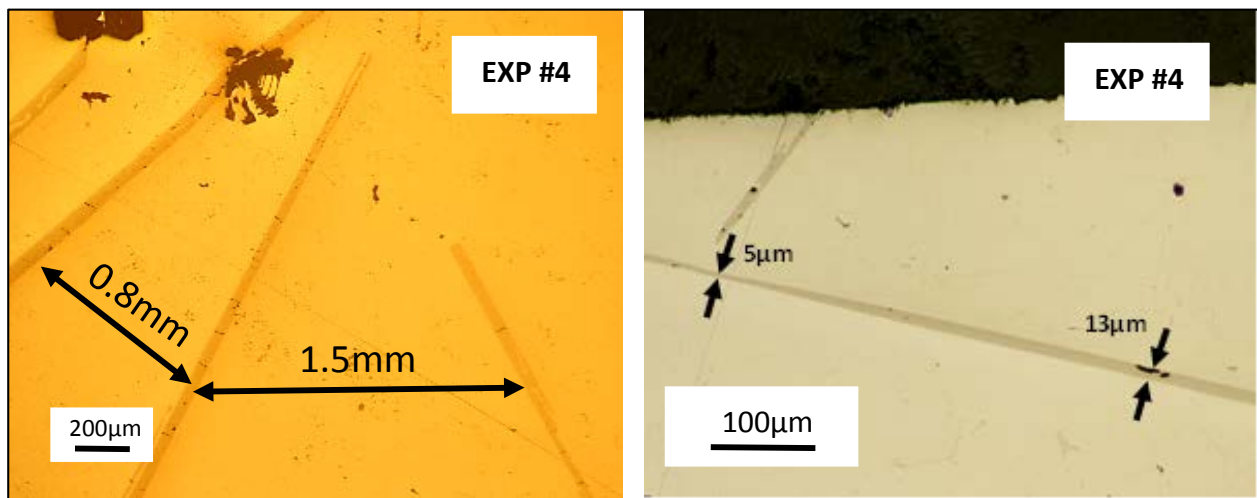

Figure 121. LOM image showing needle interspacing and needle thinning in Exp. 4.

Figure 122 shows semi-quantitatively shows the variation in the average thickness of the Al_3Ti needles (measured at 200X) with the Ti content of the melt.
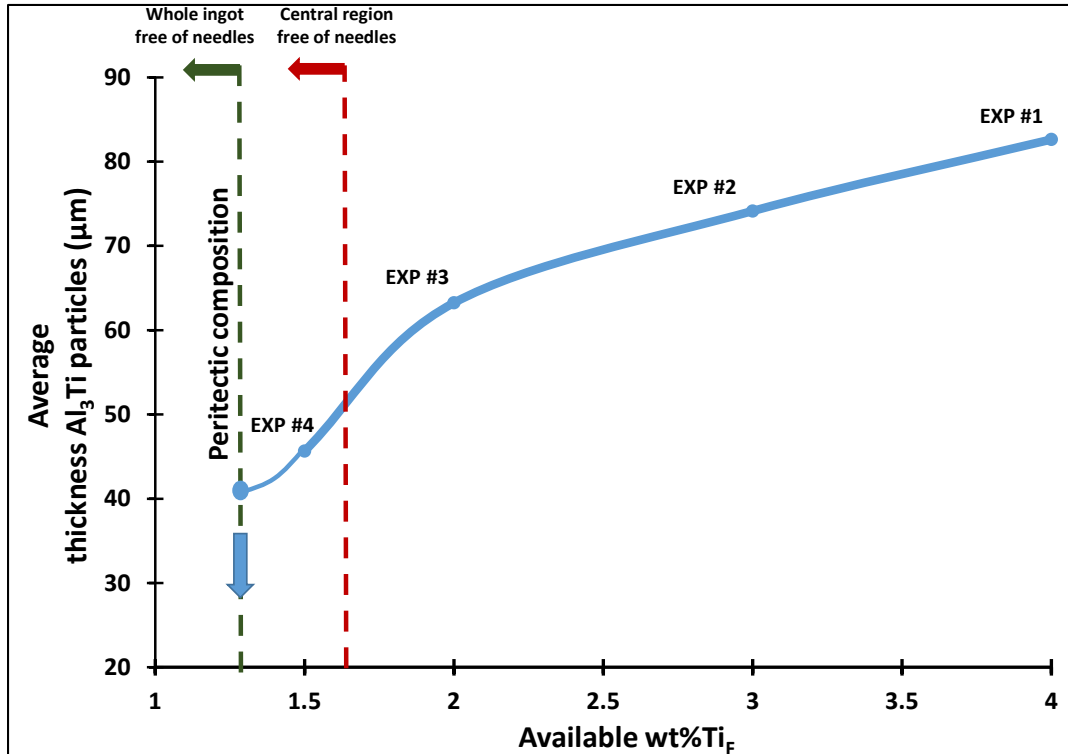
Figure 122. Needles thickness with wt.% Ti evolution.

It can be inferred from Figure 122 that a closer Ti content to the peritectic composition reduces the thickness of the Al$_3$Ti needles. The medium and top parts of the ingots made according to Exps. 1-4 and Exp. 7 have not yet been studied in depth. Even though the XRD indicates no TiC formation in the middle and top regions of the ingots, it confirms the existence of an important quantity of AlTi$_2$C (see Exp. 1 in Figure 82). The same goes for the whole ingot made according to Exps. 5-6 (see Fig. 12). To help understand these macrostructural changes, Figure 123 is constructed based on Figure 82 and Figure 96.

Figure 123 clearly shows the following:

(1) The amount of TiC that forms increases with wt pct. Ti and temperature.

(2) The size of region at the center of the ingot which contains equiaxed free needles can be controlled. It probably depends on temperature, time and the initial wt pct. Ti.

A 5 steps cooling-solidification mechanism that results in the observed ingot macrostructure is proposed in Figure 124. Note that step 1 begins just after the impeller is raised at the end of the experiment. In step 1, TiC particles and Al$_3$Ti polygonal particles are in suspension in the melt. They sink (Step 2) due to their higher density and then solidification begins.

Figure 123. Macrostructural change in the seven experiments.

Figure 124. Proposed ingot solidification mechanism.

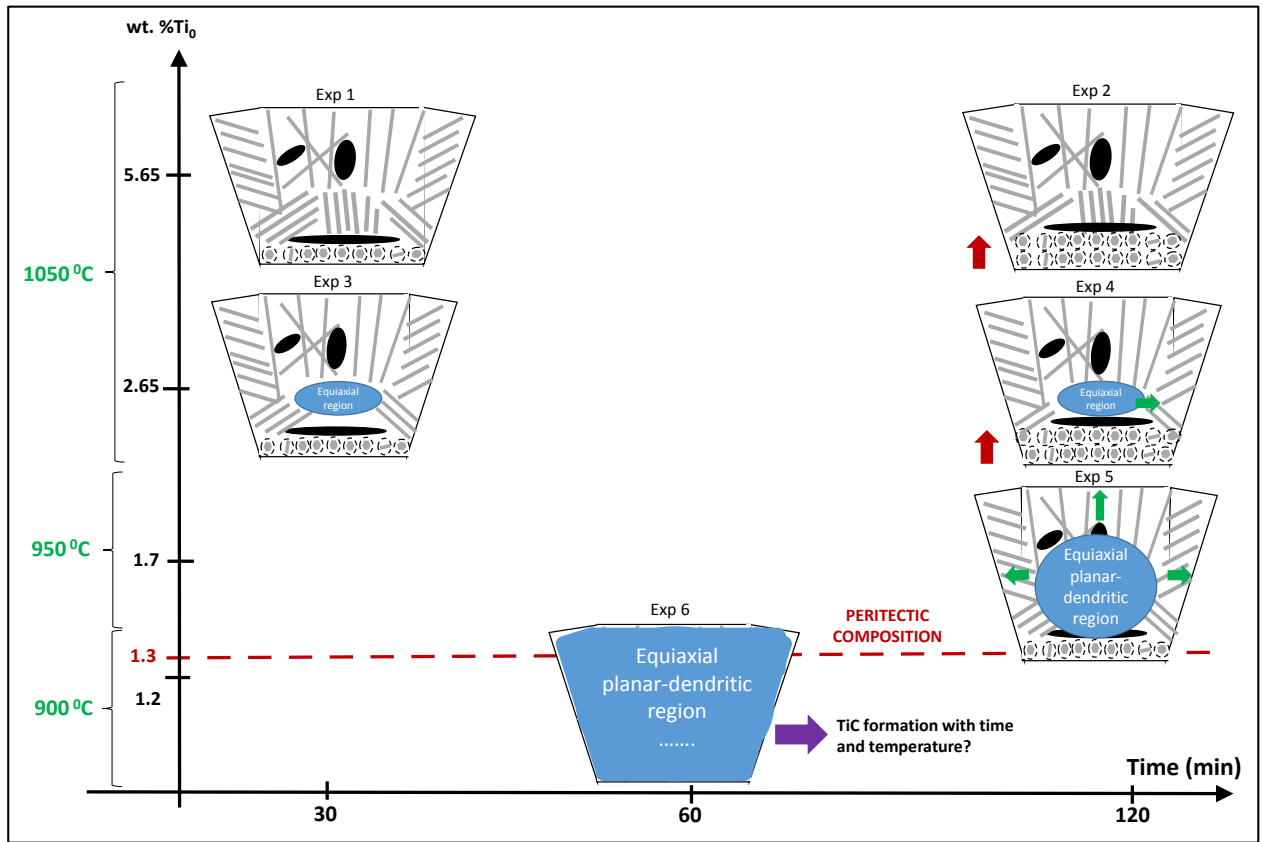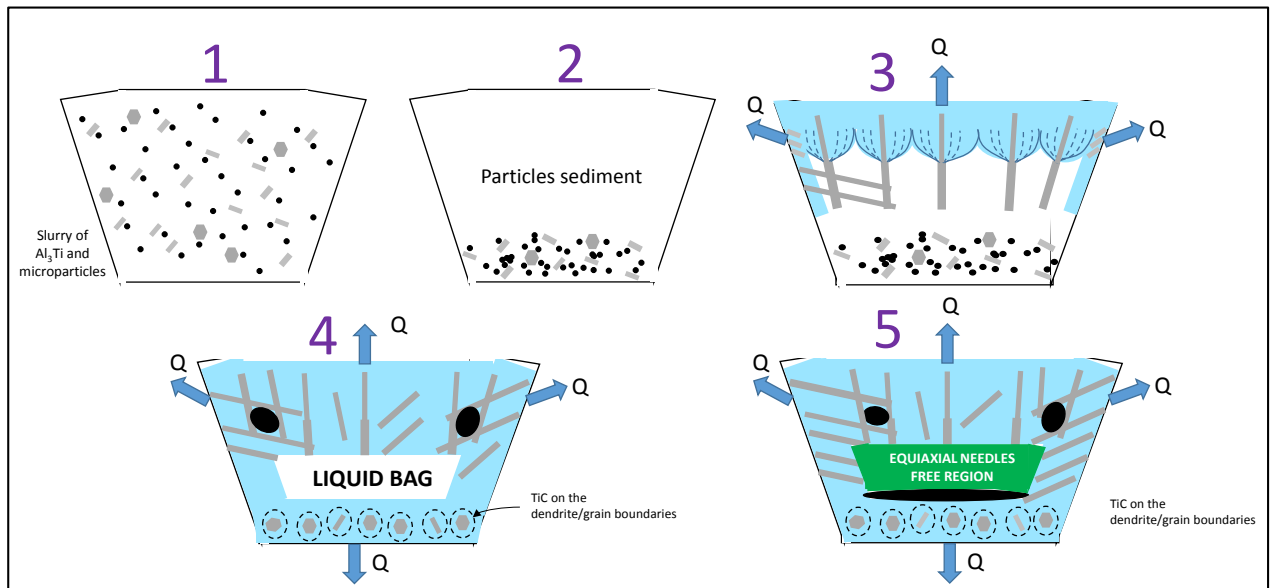In Step 3, a peritectic solidification reaction occurs in which the Al$_3$Ti nuclei grow in a faceted fashion by diffusional growth in the [001] direction resulting in elongated needles that grow parallel to the direction of heat extraction [23]. It is assumed that heat is initially extracted from the top of the apparatus. When the temperature reaches the peritectic point, α-Al nucleates along the Al$_3$Ti needles that become thinner due to the peritectic reaction (93).

$$Al_3Ti(s) + Al(l) \leftrightarrow \alpha\text{-}Al(s) \qquad \text{peritectic reaction} \qquad (93)$$

As solidification progresses, the temperature gradient becomes two-dimensional and a complex network of needles appears and traps liquid in its interior. Solidification progresses into the bottom part of the ingot. This is Step 4 and it is characterized by two sub-steps:

(1) Heat extraction from the bottom is not negligible anymore and the Al$_3$Ti polygonal particles and/or needles that have settled in the bottom of the ingot nucleate the peritectic reaction segregating the TiC/AlTi$_2$C particles in the interdendritic space. An internal liquid *'bag'* remains in the center of the ingot.

(2) The precipitation of Al$_3$Ti needles depletes titanium in the liquid. Upon complete solidification, the mushy zone follows the liquidus line in Figure 125. However, solidification is so slow and the Al$_3$Ti spacing is so large that the mushy liquid doesn't become trapped and efficient mixing with the bulk liquid occurs due to liquid convection and solute diffusion. This results in titanium solute macrosegregation as the bulk liquid also follows the liquidus line in Figure 125.

Finally, Step 5 begins wherein the internal liquid bag, depleted of titanium, solidifies free of needles. The whole process is sketched in Figure 125. It can be concluded that an initial wt pct. Ti in the proximity of the peritectic composition at low enough temperature and/or long enough time enables the final liquid bag to be in hypoperitectic state and to solidify free of needles. Eventually, if the overall final ingot composition is hypo-peritectic, the whole ingot can solidify free of needles.
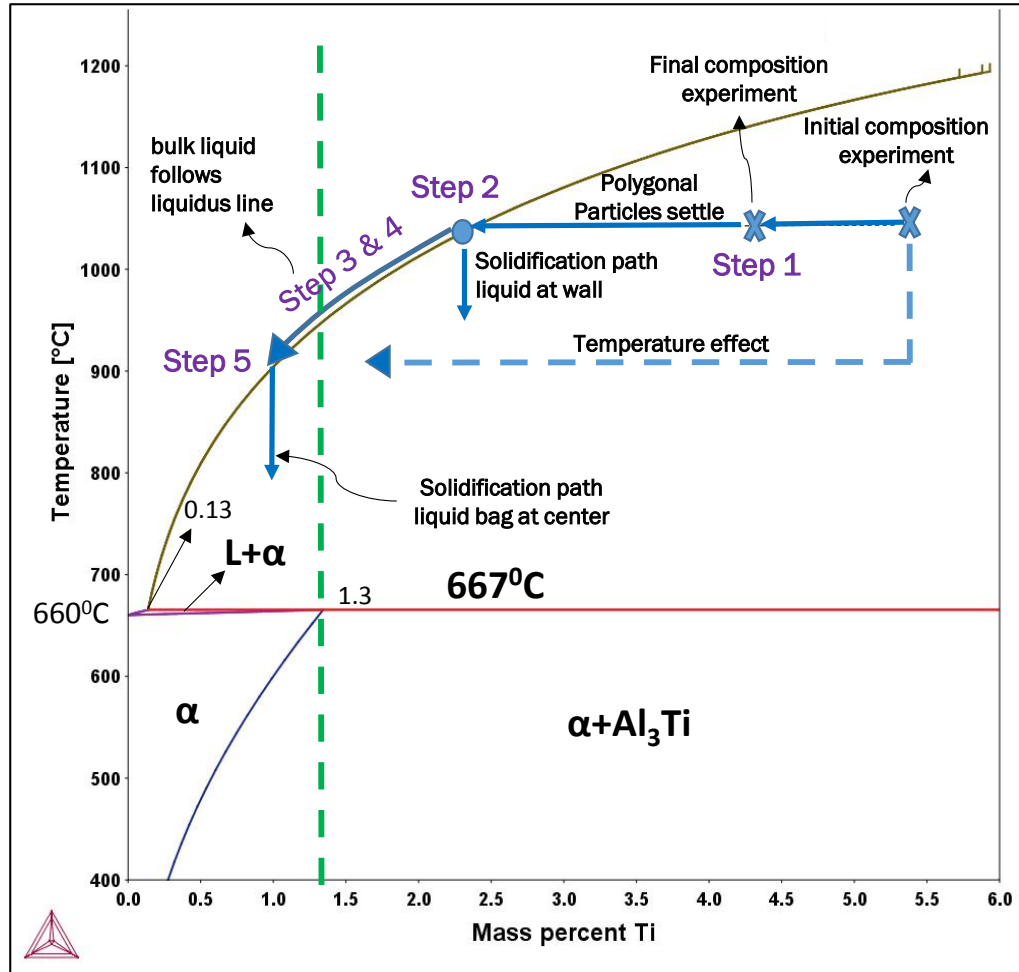
Figure 125. Propose ingot solidification mechanism and titanium macrosegregation.

3.4.2. Economical microcomposites under 2µm particle size

Despite not being adequate for structural applications, microcomposites still find several applications in system parts that require thermal stability and wear resistance. This parts are forged or extruded into the final geometry from an initial slab or billet. Several products exist in the market with SiC or Al_2O_3 particles <5µm and a loading ranging from 15 to 50vol pct. The state of the art for microcomposites billet production implies an ex-situ solid state route in which aluminum powder gets high energy milled with SiC powder and the resulting billet is consolidated by HIP. Our process could compete against the route described above as no initial expensive powder is required and HIP may be alleviated (or even bypassed) by applying pressure during solidification. An initial material target is Al-TiC with 10vol pct. loading and particle size<1-2µm. The TiC dispersion, initially segregated in the interdendritic regions will be homogeneized by the later billet extrusion.

Image analysis has been performed in the ingot bottom of the first five experiments. The TiC vol pct. has been calculated at 200X in three different locations. The particle size distribution of microparticles has been calculated at 1500X and the particle size distribution of submicron particles has been measured at 5000X. Higher magnification would be required to analyze the particles below 100nm. Figure 126 shows the TiC particle size distribution. Some trends and conclusions are observed:

(1) Experiments 3-4 present a much finer TiC dispersion than Exps.1-2. Main factor is believed to be the vol pct.CH_4 change from 15 to 5vol pct. that affects the size and amount of soot coarse particle.

(2) The fraction <3µm in Experiment 4 (2h time) is 20vol pct. larger than in Experiment 3 dispersion (30min time). That means that in Figure 103 crumbling flux is faster than soot flux. The soot formation is the limiting step. This is accordance with Wu and Reddy [16] for SiC dispersions synthesis.

(3) Experiment 5 (950^0C) has a higher fraction of 3-15µm than Experiment 4 (1050^0C). Carbon diffusion crumbling weakens at lower temperature so impact of crumbling due to stress cracking increases and the TiC dispersion coarsens.

Figure 127 shows the loading and titanium conversion in the first five experiments.

(1) The loading is apparently very low from a visual inspection of the ingot bottom (Figure 82 and Figure 96) but it is in agreement with a closer look at 50X in the LOM (Figure 86 and Figure 98). The TiC dispersion is in the interdendritic areas and the matrix is empty.

(2) The most aggressive experiment for soot formation (the limiting step), Experiment 2, has a maximum Ti consumption rate of 0.35wt pct. Ti/hour. It is not surprising since CH_4 was selected to minimize soot (see Figure 73). If the target is a micro-composite with TiC vol pct=10-50 the above consumption rate is not economical. Another gas like acetylene or propane (Figure 73) is required to enhance the soot formation and enhance the Ti consumption rate at least an order of magnitude.
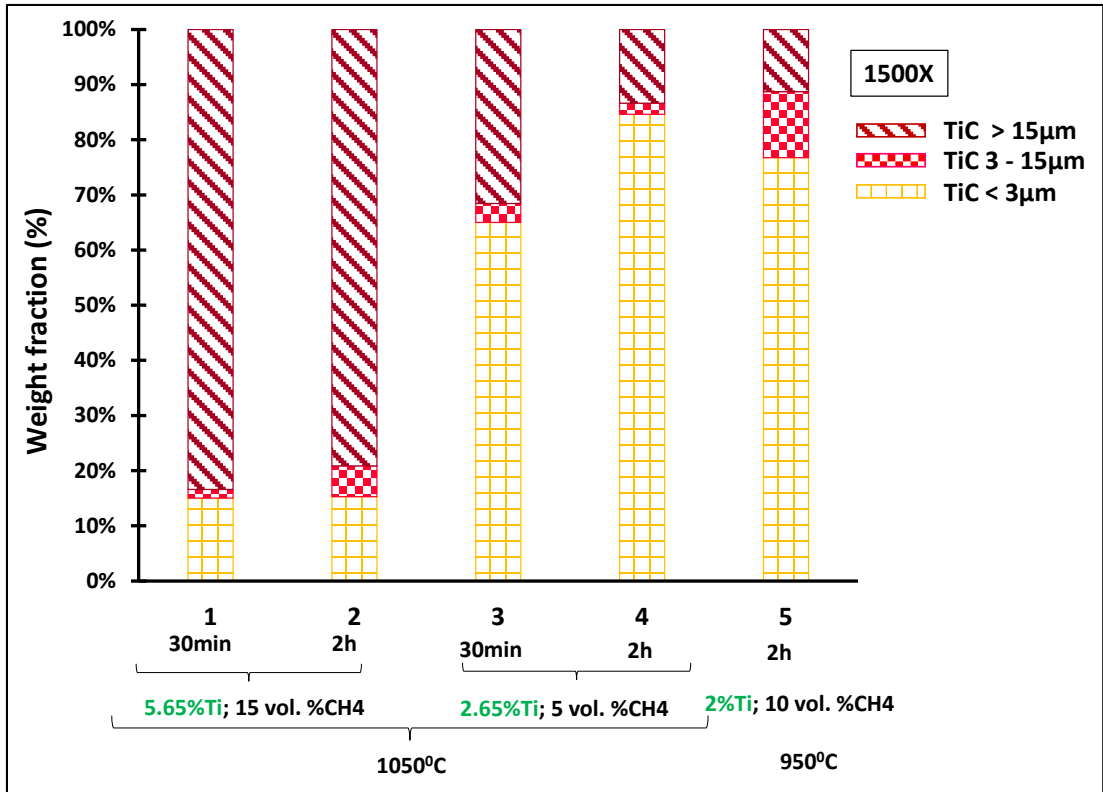
Figure 126. TiC particle size distribution for Exps. 1-5.
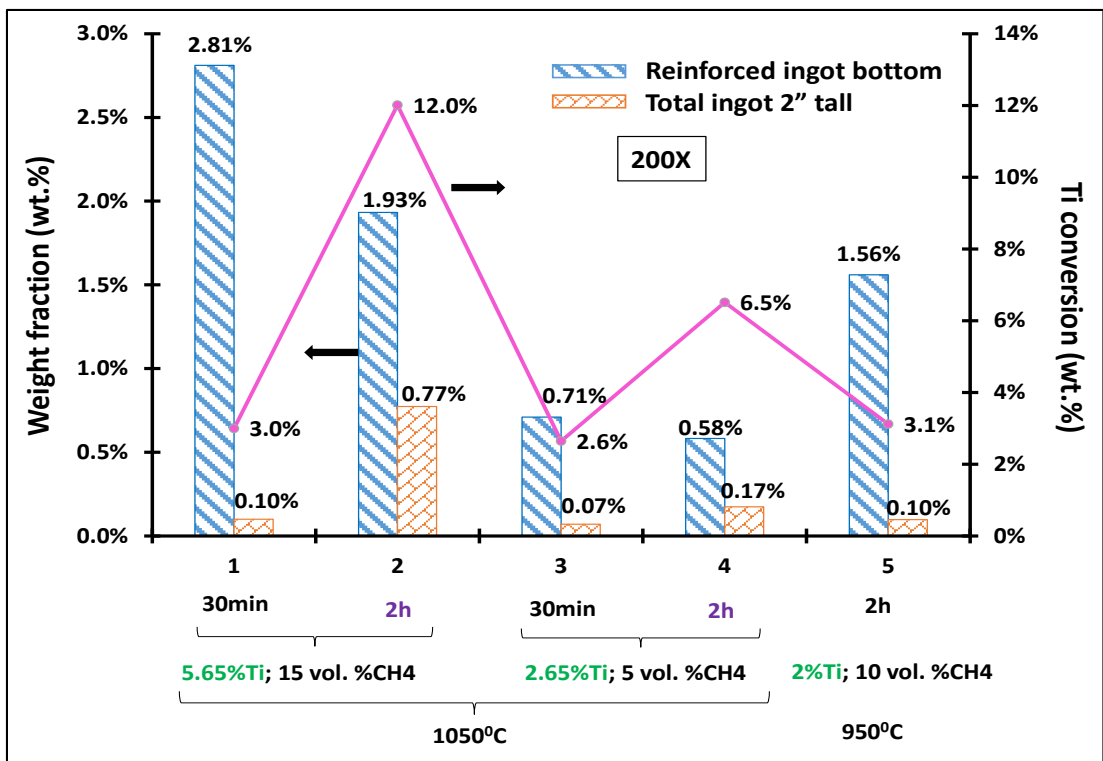
Figure 127. Particle loading of the ingot and Ti conversion for Exps. 1-5.

Experiment 5 is the experiment with finest and narrowest TiC particle size distribution. Above 70pct. of the TiC particles are below 2-3µm. Figure 128 shows a typical TiC dispersion in Experiment 5. It consists of a fine distribution of TiC<2.5µm mixed together with some coarse TiC particle around 10µm in size that result from stress cracking from 20-50µm TiC particles. Figure 129 shows the particle size distribution for TiC particles<2.5µm in Experiment 5. It is a bimodal distribution with two peaks, at 300nm and 1.75 µm. We related each of the peaks with the carbon diffusion crumbling and a mixed mechanism of both strain incompatibility and carbon diffusion crumbling, respectively. A full mass balance is shown in Figure 130.
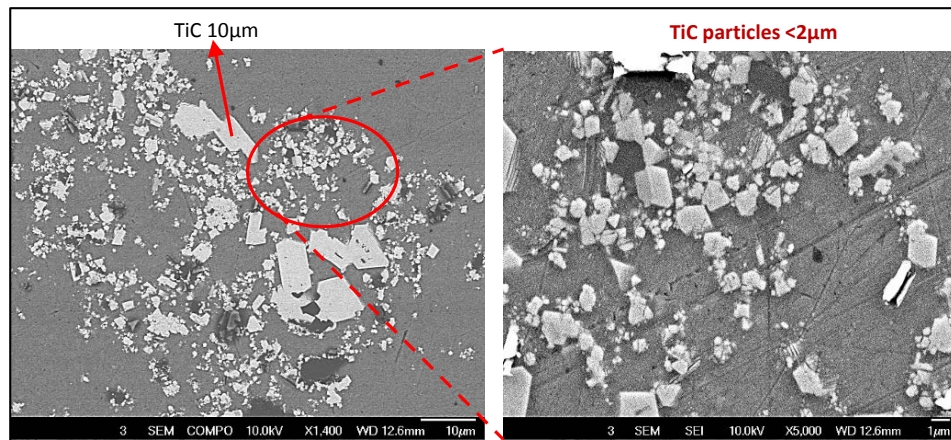
Figure 128. TiC particle size distribution in Exp. 5.
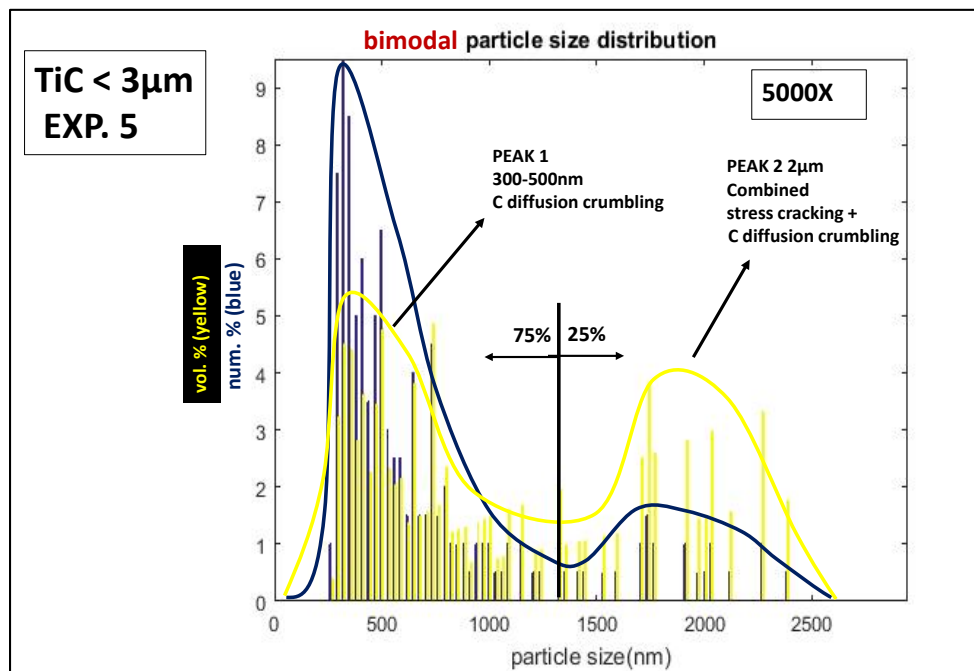
Figure 129. Particle size distribution of TiC dispersion for dp<3µm in Exp. 5.
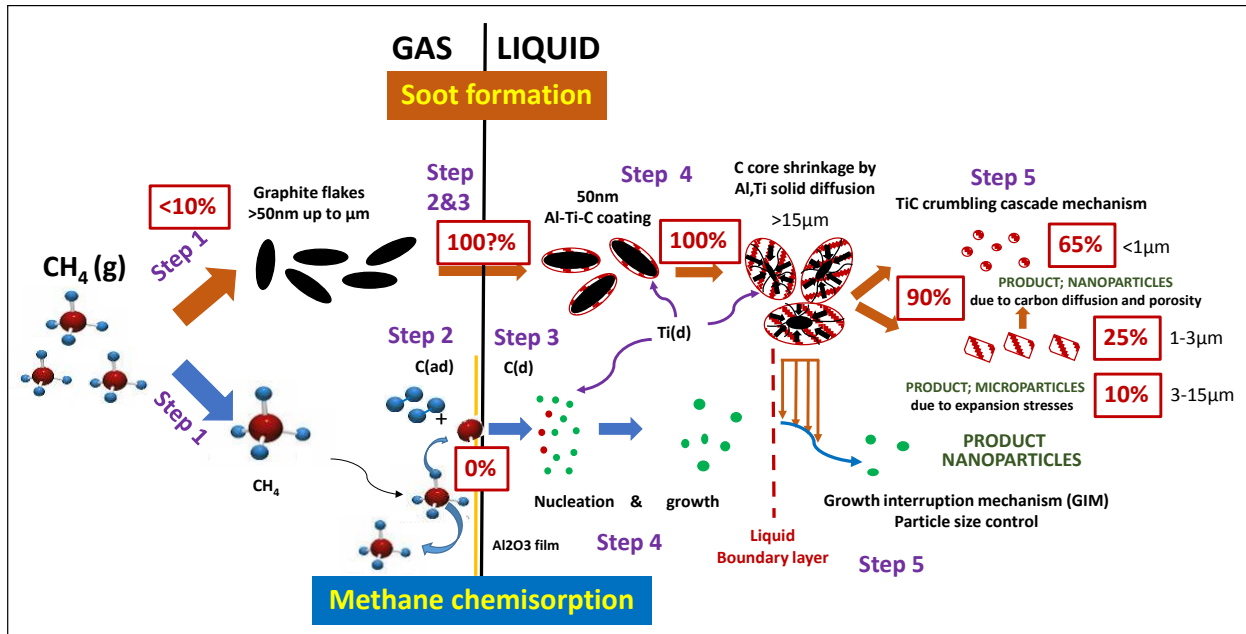
Figure 130. Mass balance for Exp. 5.

With the previous analysis in mind some recommendations are made to obtain a highly loaded TiC microcomposite with fine TiC dispersion (<2μm):

(1) Maximize the soot formation rate. For that (1) operate at high temperature, use a gas with high sooting tendency, increase the gas flow so the interface area 'a' increases.

(2) Stop the carbonaceous gas flow and let the material crumble for long period of time. Enhance carbon diffusion crumbling so particle size gets finer.

In summary, a possible two steps experiment would be, for 3bls of AlTi6 at 1050⁰C: (1) a first step with 2L/min propane:argon 15:85 mixture rotating at 400rpm for 6 hours plus (2) a second step for TiC crumbling during 2 hours with no gas flow, just 400rpm rotation. 400rpm is the rotation speed calculated in Figure 67 for microparticles flotation and 2L/min gas dispersion. Acetylene gas instead of propane can also be used but the instrumentation and safety standards are cumbersome. For the final billet production, our billet has plenty of oxides and porosity. The lab plant should be upgraded so it can operate under both vacuum and pressure. An experiment schedule is proposed in Figure 131 so the experiment is run under vacuum (no oxides) and the solidification happens under pressure (porosity alleviates). The amount of pressure will be related to the pressure drop of the liquid across the interdendritic porosity [112]. The viscosity increase from the TiC particles might be relevant but not huge as the slurry is made from microparticles and not nanoparticles (see Figure 66).
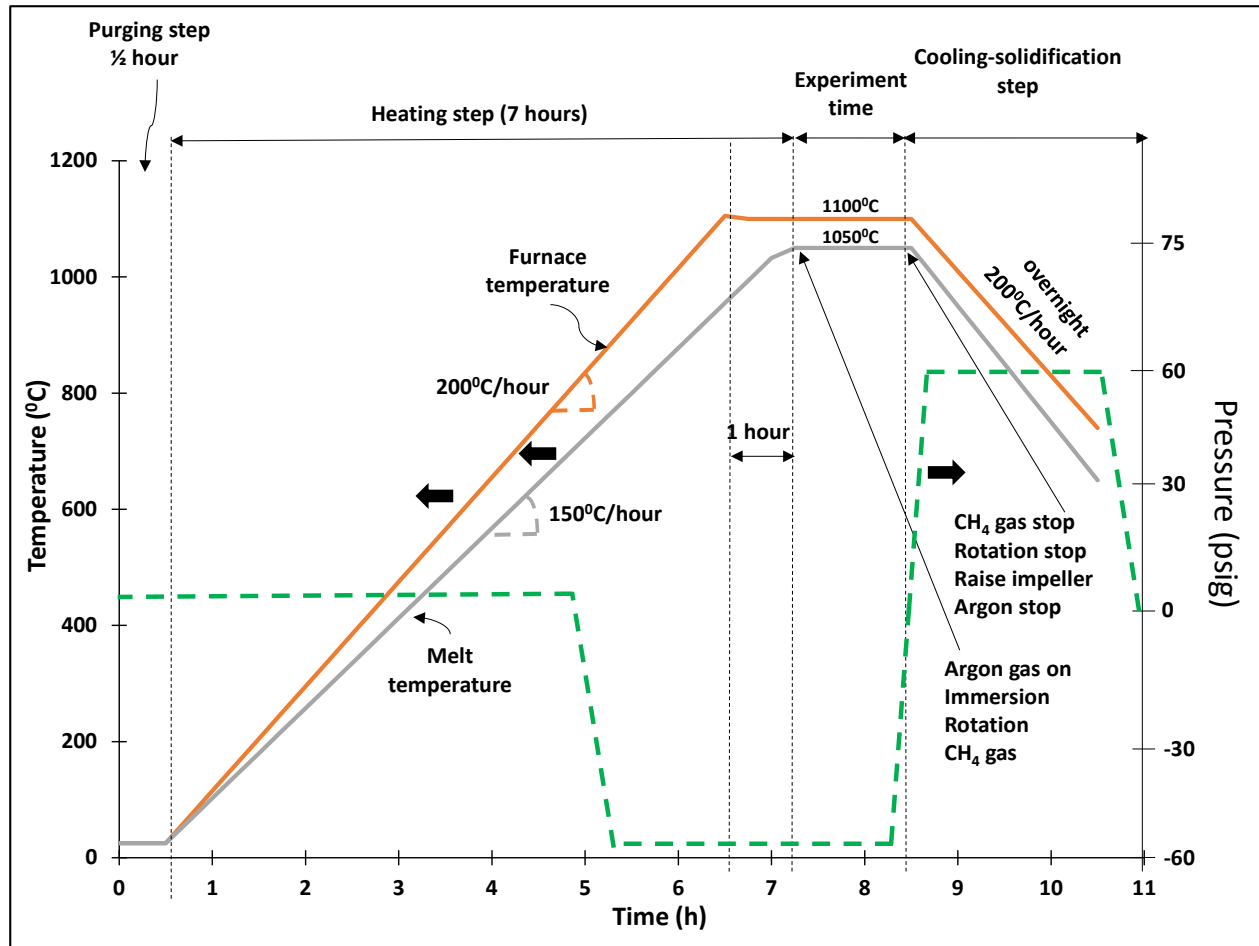
Figure 131. Proposed experiment schedule to avoid oxides and porosity in the final billet.

3.4.3. Nanocomposites with higher loading

The high rheology of the melt and the early instability point in Exps 9-10 has been identified in Figure 119 and Figure 120 as the main barrier to overcome for obtaining a melt with higher loading (5-20vol pct.) of TiC nanoparticles (<100nm). Three avenues are proposed that could potentially solve the rheology issue:

    (1) Increase shear rate and mixing flow in the melt.

    (2) Expand the region free of soot: H_2 addition and residence time reduction

    (3) Zn addition to the melt to decrease its melting and boiling point

    (4) Include molten metal vacuum distillation [113] after gas-liquid in-situ loading.

Shear rate and circulation flow increase

From Chapter 2, the increase of the shear stress will decrease the apparent viscosity and maintain turbulence for longer time (see Figure 61) in a shear thinning liquid. An increase of the rotation speed up to 600rpm and baffling the crucible will definitely

also enhance the turbulence. However, regardless the rotation speed, the turbine technology limit is set to be 10cPo in Figure 119. In the 10-100cPo range the shear disk still creates shear but no flow so stagnation will still happen in the furthest top regions from the impeller. A combination of both shear disk and Rushton turbine in a baffled crucible (optional) is recommended in the 10-100cPo interval.
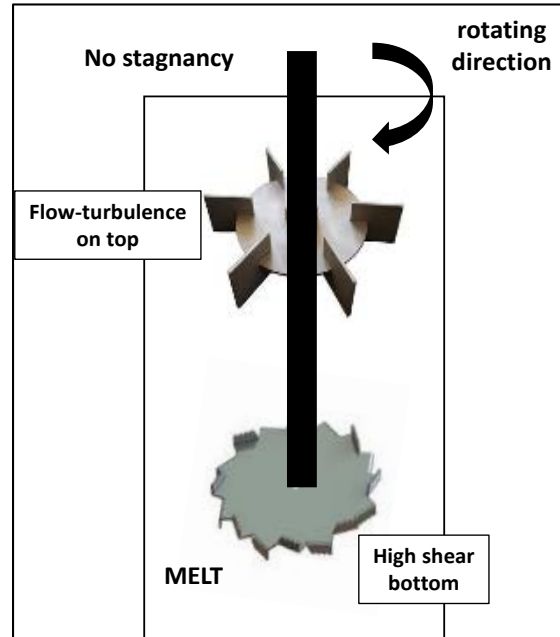
Figure 132. Two impellers arrangement to work in the 10-100cPo region.

Expansion of the region free of soot

Figure 133 conceptually illustrates the impact of increasing the region free of soot.

Two options are proposed:

(1) Reduction of gas residence time in the tube-melt. In terms of gas reaction kinetics (time and temperature), the reduction of the gas residence time inside the furnace by introducing the gas through the crucible bottom (Figure 134) makes sense. However, the overall residence time is reduced from 1.5s up to maximum 0.5s and the threshold temperature increase is not expected to be high in Figure 133. It nevertheless becomes a mandatory design action for the process scale-up so the threshold temperature at 900⁰C does not increase (the residence time increases, see Figure 101).

(2) H_2 introduction into the system, it was calculated in Figure 74 a soot reduction up to 50wt pct. For a 1vol pct.H_2 introduction so its influence on the threshold temperature in Figure 133 will be important.
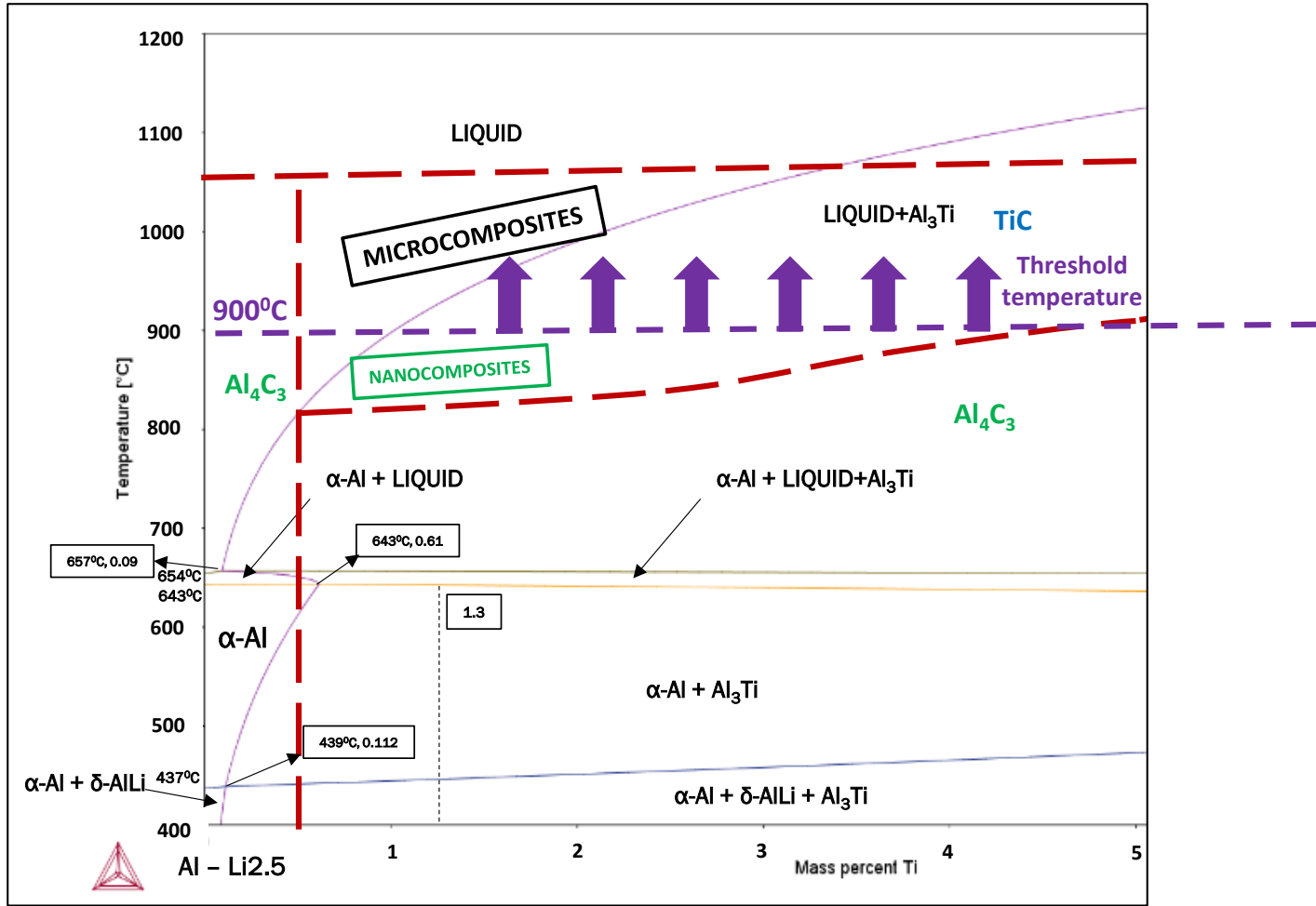
Figure 133. Expansion of the region free of soot in the Al-Ti diagram.
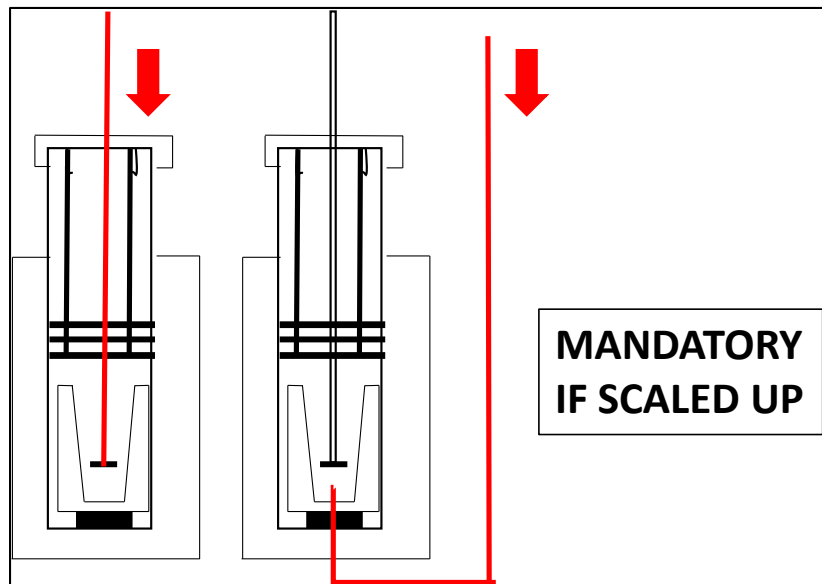
Figure 134. Gas introduced from the top (rotating hollow shaft) or from the bottom.

Zn addition to the melt to decrease its melting and boiling point

Decreasing the melting point of the melt will decrease its viscosity. Additions of zinc could be explored. A substitution of lithium with magnesium as the oxygen getter makes the composition system Al-Mg-Zn-Ti very suitable as a master alloy containing nanoparticles for both aluminum and magnesium based casting and wrought alloys. The Al-Zn phase diagram is included for reference.
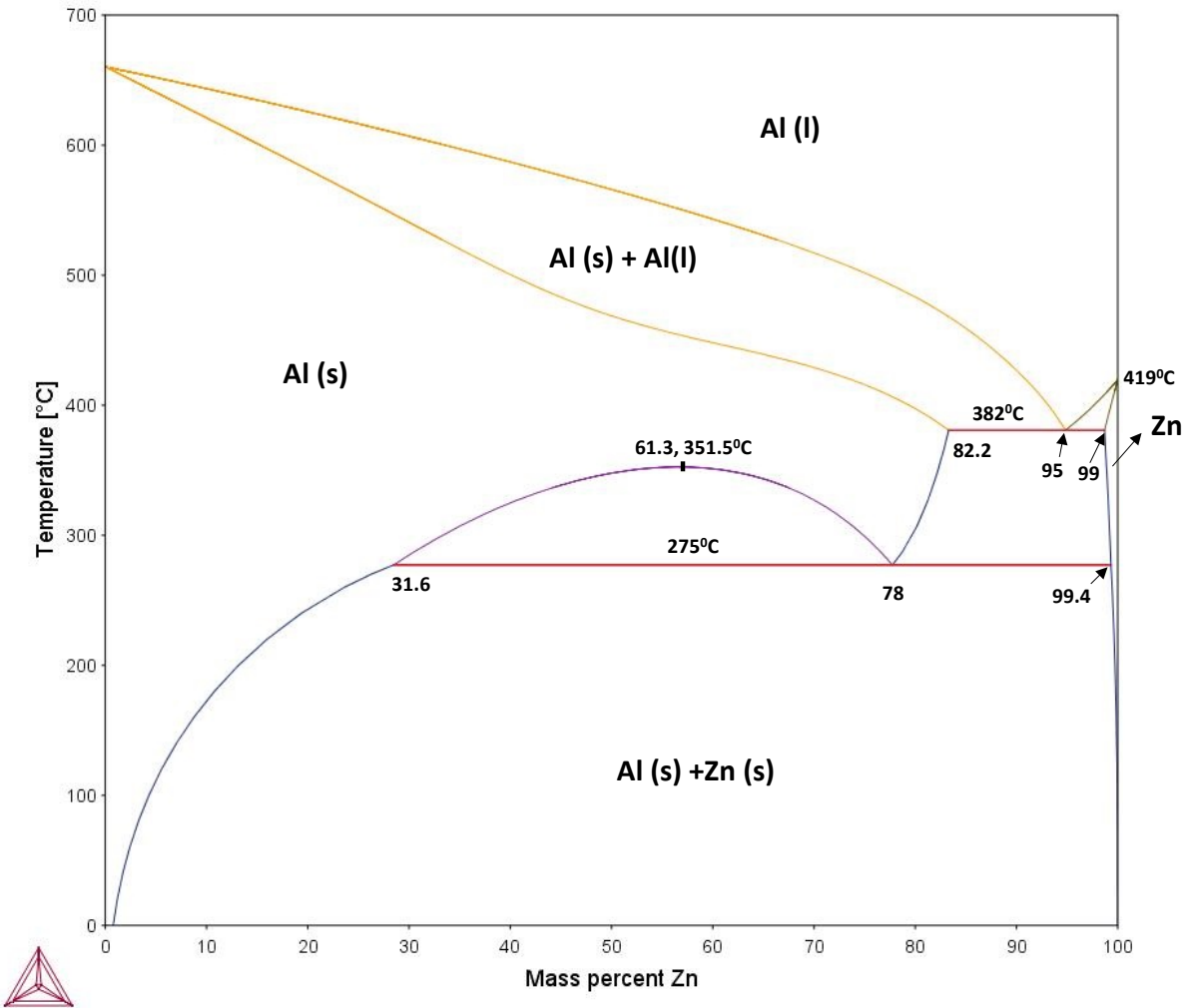
Figure 135. Al-Zn phase diagram

Include molten metal vacuum distillation after gas-liquid in-situ loading

In [113] a MgZn6 melt reinforced with 1vol pct. Of SiC nanoparticles added ex-situ and ultrasonically dispersed is concentrated up to 14vol pct. With no agglomeration by vacuum distillation. The scale is very small. 20gr of melt are reduced by evaporation up to 1gr of melt.

3.5. Summary

An apparatus for the production of Al-TiC nanocomposites has been designed and constructed. It has 3lbs capacity and it is at least ten times larger (10X, one order of magnitude) than any former lab plant designed by other relevant research groups. Ten experiments have been performed, and the milestones are summarize below:

From a mechanistic and technology understanding point of view:

(1) The different processing windows in which each of the TiC synthesis routes (chemisorption and soot formation) operates has been defined and the scaling effects have been considered.

(2) The different steps of the soot route have been completely elucidated. The different crumbling mechanisms have been quantitatively described and a single theory has been proposed that integrates previous divergent experimental results from other research groups and also includes scaling effects.

(3) The oxygen getter assisted chemisorption theory for nanoparticles synthesis has been experimentally confirmed. A minimum amount of lithium has been quantitatively determined for the reaction to proceed.

(4) The Al-Ti ingot peritectic solidification mechanism is described and a strategy for Al_3Ti needles minimization or elimination is presented.

From a point of view for product development and know-how transfer to industry:

(5) An ideal set of processing parameters is proposed for the synthesis of microcomposites billets above 10vol pct. loading and particle size<2µm. It is not a final recipe but a very good starting point for an Al-TiC microcomposites development project. The complete elimination of porosity and oxides requires plant upgrading.

(6) An ingot containing less than 1vol pct. TiC in the form of well dispersed nanoparticles with a size under 30nm and no vertical segregations has been produced in Exp 10.

(7) The melt rheology has been detected as the obstacle for increasing the melt loading above 1vol pct. A set of recommendations to overcome the rheology related problems has been proposed.

References

[1]   C. Borgonovo and M. M. Makhlouf, "Synthesis of Aluminum–Aluminum Nitride Nanocomposites by a Gas–Liquid Reaction II. Microstructure and Mechanical Properties," *Metallurgical and Materials Transactions A,* pp. 1-10.

[2]   C. Borgonovo and M. M. Makhlouf, "Synthesis of Aluminum-Aluminum Nitride Nanocomposites by Gas-Liquid Reactions I. Thermodynamic and Kinetic Considerations," *Metallurgical and Materials Transactions A,* pp. 1-11.

[3]   C. Borgonovo, D. Apelian, and M. M. Makhlouf, "Aluminum nanocomposites for elevated temperature applications," *JOM,* vol. 63, pp. 57-64, 2011.

[4]   C. Borgonovo and M. M. Makhlouf, "In Situ Manufacturing of Nano-Particle Reinforced Metal Matrix Composites (12-067)," *AFS Transactions-American Foundry Society,* vol. 120, p. 133, 2012.

[5]   C. Borgonovo, (2013). Synthesis of Aluminum-Aluminum Nitride Nanocomposites by Gas-Liquid Reactions (Doctoral Dissertation), Mechanical Engineering, Worcester Polytechnic Institute, https://www.wpi.edu/Pubs/ETD/Available/etd042913143643/unrestricted/PHDTHESIS_merged.pdf., 2013.

[6]   C. Borgonovo, "Synthesis of Aluminum-Aluminum Nitride Nanocomposites by Gas-Liquid Reactions (Doctoral Dissertation)," PhD Materials Science, Mechanical Engineering, Worcester Polytechnic Institute, Worcester, Massachusetts, USA, 2013.

[7]   C. Borgonovo, "Production of aluminum-aluminum nitride nano-composites by a gas-liquid reaction," 2014.

[8]   A. Banerji and W. Reif, "Development of Al-Ti-C grain refiners containing TiC," *Metallurgical Transactions A,* vol. 17, pp. 2127-2137, 1986.

[9]   R. A. Rapp and X. Zheng, "Thermodynamic consideration of grain refinement of aluminum alloys by titanium and carbon," *Metallurgical and Materials Transactions A,* vol. 22, pp. 3071-3075, 1991.

[10]   Q. Hou, R. Mutharasan, and M. Koczak, "Feasibility of aluminium nitride formation in aluminum alloys," *Materials Science and Engineering: A,* vol. 195, pp. 121-129, 1995.

[11]   S. Khatri and M. Koczak, "Formation of TiC in in situ processed composites via solid-gas, solid-liquid and liquid-gas reaction in molten Al-Ti," *Materials Science and Engineering: A,* vol. 162, pp. 153-162, 1993.

[12]   M. J. Koczak and K. S. Kumar, "In situ process for producing a composite containing refractory material," ed: Google Patents, 1989.

[13]   M. J. Koczak and M. K. Premkumar, "Emerging technologies for the in-situ production of MMCs," *Jom,* vol. 45, pp. 44-48, 1993.

[14]   P. Sahoo and M. J. Koczak, "Analysis of in situ formation of titanium carbide in aluminum alloys," *Materials Science and Engineering: A,* vol. 144, pp. 37-44, 1991.

[15]   R. G. Reddy and B. Wu, "Production of metal/refractory composites by bubbling gas through a melt," ed: Google Patents, 2002.

[16] B. Wu and R. G. Reddy, "In-situ formation of SiC-reinforced Al-Si alloy composites using methane gas mixtures," *Metallurgical and Materials Transactions B,* vol. 33, pp. 543-550, 2002.

[17] Q. Zheng, B. Wu, and R. G. Reddy, "In-Situ Processing of Al Alloy Composites," *Advanced Engineering Materials,* vol. 5, pp. 167-172, 2003.

[18] Q. Zheng and R. G. Reddy, "Kinetics of In-situ formation of AlN in Al alloy melts by bubbling ammonia gas," *Metallurgical and Materials Transactions B,* vol. 34, pp. 793-804, 2003.

[19] Q. Zheng and R. G. Reddy, "Mechanism of in situ formation of AlN in Al melt using nitrogen gas," *Journal of materials science,* vol. 39, pp. 141-149, 2004.

[20] H. Scholz and P. Greil, "Synthesis of high purity AlN by nitridation of Li-doped Al-melt," *Journal of the European Ceramic Society,* vol. 6, pp. 237-242, 1990.

[21] H. Scholz and P. Greil, "Nitridation reactions of molten Al-(Mg, Si) alloys," *Journal of materials science,* vol. 26, pp. 669-677, 1991.

[22] M. K. Premkumar and M. G. Chu, "Synthesis of TiC particulates and their segregation during solidification in In Situ processed AI-TiC composites," *Metallurgical and Materials Transactions A,* vol. 24, pp. 2358-2362, 1993.

[23] M. K. Premkumar and M. G. Chu, "Al-TiC particulate composite produced by a liquid state in situ process," *Materials Science and Engineering: A,* vol. 202, pp. 172-178, 1995.

[24] Y.-H. Cho, J.-M. Lee, and S.-H. Kim, "Al-TiC Composites Fabricated by a Thermally Activated Reaction Process in an Al Melt Using Al-Ti-C-CuO Powder Mixtures. Part I: Microstructural Evolution and Reaction Mechanism," *Metallurgical and Materials Transactions A,* vol. 45, pp. 5667-5678, 2014.

[25] X. C. Tong and H. S. Fang, "Al-TiC composites In Situ-processed by ingot metallurgy and rapid solidification technology: Part I. Microstructural evolution," *Metallurgical and Materials Transactions A,* vol. 29, pp. 875-891, 1998.

[26] A. M. Kanury, "A kinetic model for metal+ nonmetal reactions," *Metallurgical Transactions A,* vol. 23, pp. 2349-2356, 1992.

[27] A. Jarfors and H. Fredriksson, "On the behaviour of TiC particles in the Al-rich corner of the Al− Ti− C phase diagram," *Microgravity, science and technology,* vol. 3, pp. 216-221, 1991.

[28] A. Jarfors, H. Fredriksson, and L. Froyen, "On the thermodynamics and kinetics of carbides in the aluminium-rich corner of the Al-Ti-C phase diagram," *Materials Science and Engineering: A,* vol. 135, pp. 119-123, 1991.

[29] I. Anza and M. M. Mahklouf, "Synthesis of Al-TiC Nanocomposites by an In-Situ Gas-Liquid Method," *Light Metals 2016,* pp. 245-254, 2016.

[30] M. S. Newkirk and S. F. Dizio, "Novel ceramic materials and methods for making same," ed: Google Patents, 1987.

[31] B. S. S. Daniel and V. S. R. Murthy, "Directed melt oxidation and nitridation of aluminium alloys: a comparison," *Materials & Design,* vol. 16, pp. 155-161, 1995.

[32] B. S. S. Daniel, V. S. R. Murthy, and G. S. Murty, "Metal-ceramic composites via in-situ methods," *Journal of Materials Processing Technology,* vol. 68, pp. 132-155, 1997.

[33] A. Dobi, D. S. Leonard, C. Hall, L. J. Kaufman, T. Langford, S. Slutsky*, et al.,* "Study of a zirconium getter for purification of xenon gas," *Nuclear Instruments and Methods in Physics Research Section A: Accelerators, Spectrometers, Detectors and Associated Equipment,* vol. 620, pp. 594-598, 2010.

[34] N. Masoumi, N. Sohrabi, and A. Behzadmehr, "A new model for calculating the effective viscosity of nanofluids," *Journal of Physics D: Applied Physics,* vol. 42 055501, 2009.

[35] J. Koo and C. Kleinstreuer, "A new thermal conductivity model for nanofluids," *Journal of Nanoparticle Research,* vol. 6, pp. 577-588, 2004.

[36] M. Corcione, "Empirical correlating equations for predicting the effective thermal conductivity and dynamic viscosity of nanofluids," *Energy Conversion and Management,* vol. 52, pp. 789-793, 2011.

[37] M. Zlokarnik, *Stirring: Theory and practice*: John Wiley & Sons, 2008.

[38] H. S. Fogler, "Elements of chemical reaction engineering," 1999.

[39] G. B. Tatterson, *Fluid mixing and gas dispersion in agitated tanks*: McGraw-Hill Companies, 1991.

[40] D. Borin and S. Odenbach, "Viscosity of liquid metal suspensions—experimental approaches and open issues," *The European Physical Journal Special Topics,* vol. 220, pp. 101-110, 2013.

[41] P. Terzieff, "The viscosity of liquid alloys," *Journal of Alloys and Compounds,* vol. 453, pp. 233-240, 2008.

[42] Z. Zhijing, "Viscosity measurement of aluminum alloy containing SiC particulates," 1999, pp. 543-50.

[43] A. W. Nienow, M. F. Edwards, and N. Harnby, *Mixing in the process industries*: Butterworth-Heinemann, 1997.

[44] R. U. Khan, "Pyrolysis of Acetylene for Vacuum Carburizing of Steel: Modeling with Detailed Kinetics," *International journal of chemical reactor engineering,* vol. 7, pp. 23-23, 2009.

[45] A. Holmen, O. Olsvik, and O. A. Rokstad, "Pyrolysis of natural gas: chemistry and process concepts," *Fuel Processing Technology,* vol. 42, pp. 249-267, 1995.

[46] A. Violi, G. A. Voth, and A. F. Sarofim, "A time-scale problem for the formation of soot precursors in premixed flames," *Prepr. Pap.-Am. Chem. Soc., Div. Fuel Chem,* vol. 48, p. 545, 2003.

[47] G. Blanquart and H. Pitsch, "Parameter free aggregation model for soot formation," 2007.

[48] K. A. Jensen, J. M. Suo-Anttila, and L. G. Blevins, "Characterization of soot properties in two-meter JP-8 pool fires," *Sandia National Laboratories Report, SAND2005-0337,* 2005.

[49] J. Ma, *Soot formation during coal pyrolysis*, 1996.

[50] S. R. Shatynski, "The thermochemistry of transition metal carbides," *Oxidation of Metals,* vol. 13, pp. 105-118, 1979.

[51] A. A. Chaudry, "Formation and reactivity of some metal borides and carbides," 1973.

[52] D. R. Gaskell, *Introduction to the thermodynamics of materials* vol. 5th. New York: Taylor & Francis, 2008.

[53] R. C. Dorward, "Discussion of "comments on the solubility of carbon in molten aluminum"," *Metallurgical Transactions A,* vol. 21, pp. 255-257, 1990.

[54] M. Sacchi, D. J. Wales, and S. J. Jenkins, "Mode-specific chemisorption of CH4 on Pt {110}-(1× 2) explored by first-principles molecular dynamics," *The Journal of Physical Chemistry C,* vol. 115, pp. 21832-21842, 2011.

[55] S. Nave, A. K. Tiwari, and B. Jackson, "Dissociative Chemisorption of methane on Ni and Pt Surfaces: mode-specific chemistry and the effects of lattice motion," *The Journal of Physical Chemistry A,* vol. 118, pp. 9615-9631, 2014.

[56] F. Nattino, H. Ueta, H. Chadwick, M. E. van Reijzen, R. D. Beck, B. Jackson*, et al.*, "Ab initio molecular dynamics calculations versus quantum-state-resolved experiments on CHD3+ Pt (111): new insights into a prototypical gas–surface reaction," *The journal of physical chemistry letters,* vol. 5, pp. 1294-1299, 2014.

[57] A. Schweighofer and S. Kudela, "High-Pressure Nitriding of Al-Mg Alloys," *Kovove Materialy,* vol. 15, pp. 257-268, 1977.

[58] E. W. R. Steacie and E. M. Elkin, "A Comparison of the Catalytic Activity of Liquid and Solid Surfaces. The Decomposition of Methanol on Solid and Liquid Zinc," *Proceedings of the Royal Society of London. Series A, Containing Papers of a Mathematical and Physical Character,* vol. 142, pp. 457-465, 1933.

[59] M. Plevan, T. Geißler, A. Abánades, K. Mehravaran, R. K. Rathnam, C. Rubbia*, et al.*, "Thermal cracking of methane in a liquid metal bubble column reactor: Experiments and kinetic analysis," *International Journal of Hydrogen Energy,* vol. 40, pp. 8020-8033, 2015.

[60] R. Datta, A. Singh, I. Halasz, and M. Serban, "Supported molten-metal catalysts," ed: Google Patents, 2001.

[61] S. M. M. B. Burghartz and R. A. H. Edwards, "Gas-phase chemical reactions using a molten metal catalyst," ed: Google Patents, 2004.

[62] S. Swaminathan, B. S. Rao, and V. Jayaram, "The influence of oxygen impurities on the formation of AlN–Al composites by infiltration of molten Al–Mg," *Materials Science and Engineering: A,* vol. 337, pp. 134-139, 2002.

[63] Y. Huashun, J. D. Kim, and S. B. Kang, "The formation of AlN and TiN particles during nitrogen bearing gas injection into Al–Mg–Ti melt," *Materials Science and Engineering: A,* vol. 386, pp. 318-325, 2004.

[64] M. Dyzia and J. Śleziona, "Aluminium matrix composites reinforced with AlN particles formed by in situ reaction," *Archives of Materials Science and Engineering,* vol. 31, pp. 17-20, 2008.

[65] J. Śleziona and M. Dyzia, "Determining the applicability of liquid alloy nitriding in fabrication of Al-AlN particle composites," *Archives of Foundry Engineering,* vol. 8, pp. 134-138, 2008.

[66] T. Y. Kosolapova, *Carbides: properties, production, and applications*: Springer Science & Business Media, 2012.

[67] O. Levenspiel, "Chemical reaction engineering," *Industrial & engineering chemistry research,* vol. 38, pp. 4140-4143, 1999.

[68] M. Zlokarnik, *Scale-up in chemical engineering*: John Wiley & Sons, 2006.

[69] D. J. Tritton, *Physical fluid dynamics*: Springer Science & Business Media, 2012.

[70] W. P. M. Van Swaaij and G. F. Versteeg, "Mass transfer accompanied with complex reversible chemical reactions in gas—liquid systems: an overview," *Chemical Engineering Science,* vol. 47, pp. 3181-3195, 1992.

[71] J. A. Hogendoorn, R. D. V. Bhat, J. A. M. Kuipers, W. P. M. Van Swaaij, and G. F. Versteeg, "Approximation for the enhancement factor applicable to reversible reactions of finite rate in chemically loaded solutions," *Chemical engineering science,* vol. 52, pp. 4547-4559, 1997.

[72] D. A. Porter, K. E. Easterling, and M. Sherif, *Phase Transformations in Metals and Alloys, (Revised Reprint)*: CRC press, 2009.

[73] F. Delannay, L. Froyen, and A. Deruyttere, "The wetting of solids by molten metals and its relation to the preparation of metal-matrix composites composites," *Journal of materials science,* vol. 22, pp. 1-16, 1987.

[74] Q. Lin, P. Shen, L. Yang, S. Jin, and Q. Jiang, "Wetting of TiC by molten Al at 1123–1323K," *Acta materialia,* vol. 59, pp. 1898-1911, 2011.

[75] S. K. Rhee, "Wetting of ceramics by liquid aluminum," *Journal of the American Ceramic Society,* vol. 53, pp. 386-389, 1970.

[76] W. A. Zisman, "Relation of the equilibrium contact angle to liquid and solid constitution," ed, 1964.

[77] T. Hayashi, K. Matsuura, and M. Ohno, "TiC coating on titanium by carbonization reaction using spark plasma sintering," *Materials Transactions,* vol. 54, pp. 2098-2101, 2013.

[78] A. N. Kolmogorov, "The local structure of turbulence in incompressible viscous fluid for very large Reynolds numbers," pp. 301-305.

[79] A. N. Kolmogorov, "On the breakage of drops in a turbulent flow," pp. 825-828.

[80] J. O. Hinze, "Fundamentals of the hydrodynamic mechanism of splitting in dispersion processes," *AIChE Journal,* vol. 1, pp. 289-295, 1955.

[81] C.-H. Song, B.-U. Bae, and D.-J. Euh, "Modeling of bubble coalescence and break-up considering turbulent suppression phenomena in bubbly two-phase flow," *International Journal of Multiphase Flow,* vol. 54, pp. 31-42, 2013.

[82] J. B. Gray and V. W. Uhl, "Mixing Theory and Practice, Vol. 2," ed: Academic Press, 1987.

[83] D. K. Nambiar, R. Kumar, and K. S. Gandhi, "Breakage and coalescence of drops in turbulent stirred dispersions," *Sadhana,* vol. 15, pp. 73-103, 1990.

[84] B. Kristiansen, J. Linden, and M. Mattey, *Citric acid biotechnology*: CRC Press, 2002.

[85] J. A. Asenjo, *Bioreactor system design*: CRC Press, 1994.

[86] N. Willenbacher and K. Georgieva, "Rheology of Disperse Systems," in *Product Design and Engineering*, ed: Wiley-VCH Verlag GmbH & Co. KGaA, 2013, pp. 7-49.

[87] N. H. Sagert and M. J. Quinn, "The coalescence of gas bubbles in dilute aqueous solutions," *Chemical Engineering Science,* vol. 33, pp. 1087-1095, 1978.

[88] V. V. Yaminsky, S. Ohnishi, E. A. Vogler, and R. G. Horn, "Stability of aqueous films between bubbles. Part 1. The effect of speed on bubble coalescence in purified water and simple electrolyte solutions," *Langmuir,* vol. 26, pp. 8061-8074, 2010.

[89] W. Bujalski, M. Konno, and A. W. Nienow, "Scale-up of 45 pitch blade agitators for gas dispersion and solid suspension," pp. 389-398.

[90] V. B. Rewatkar and J. B. Joshi, "Role of sparger design in mechanically agitated gas-liquid reactors. Part I: Power consumption," *Chemical engineering & technology,* vol. 14, pp. 333-347, 1991.

[91] V. B. Rewatkar and J. B. Joshi, "Role of sparger design in mechanically agitated gas-liquid reactors. Part II: Liquid phase mixing," *Chemical engineering & technology,* vol. 14, pp. 386-393, 1991.

[92] Y. Okamoto, M. Nishikawa, and K. Hashimoto, "Energy dissipation rate distribution in mixing vessels and its effects on liquid-liquid dispersion and solid-liquid mass transfer," *Int. Chem. Eng,* vol. 21, pp. 88-91, 1981.

[93] J. M. Smith, "Simple performance correlations for agitated vessels," in *Fluid Mechanics of Mixing*, ed: Springer, 1992, pp. 55-63.

[94] E. Kadic and T. J. Heindel, "Mixing Considerations in Stirred Tank Bioreactors When Using Fluid Property Altering Microorganisms," pp. 859-870.

[95] U. Bröckel, W. Meier, and G. Wagner, *Product design and engineering: formulation of gels and pastes*: John Wiley & Sons, 2013.

[96] A. B. Metzner, R. H. Feehs, H. L. Ramos, R. E. Otto, and J. D. Tuthill, "Agitation of viscous Newtonian and non-Newtonian fluids," *AIChE Journal,* vol. 7, pp. 3-9, 1961.

[97] J. Szekely, *Fluid flow phenomena in metals processing*: Elsevier, 2012.

[98] K. Wichterle and O. Wein, "Threshold of mixing of non-Newtonian liquids," *Int. Chem. Eng,* vol. 21, pp. 116-120, 1981.

[99] A. B. Metzner and R. E. Otto, "Agitation of non-Newtonian fluids," *AIChE Journal,* vol. 3, pp. 3-10, 1957.

[100] M. Hee-Kyung, "Rheological Behavior and Microstructure of/_--Ceramic Particulate/Aluminum Alloy Composites," 1990.

[101] M. H. Jorris, "Study of the dispersion of gases in viscous liquids with application to radioactive krypton and xenon disposal. Part I," Oak Ridge National Lab., TN (USA)1969.

[102] E. L. Cussler, *Diffusion: mass transfer in fluid systems*: Cambridge university press, 2009.

[103] J. H. Spurk and N. Aksel, "Fluid mechanics. 2008," ed: Springer.

[104] Y. G. Dragunov, V. P. Smetannikov, B. A. Gabaraev, M. S. Belyakov, and P. V. Kobzev, "On the choice of correlations for calculating the heat transfer

coefficient in binary gas mixtures," *Journal of Engineering Thermophysics,* vol. 22, pp. 30-42, 2013.

[105] M. G. Zabetakis, "Flammability characteristics of combustible gases and vapors," DTIC Document1965.

[106] F. Zhao, "Experimental measurements and modeling prediction of flammability limits of binary hydrocarbon mixtures," 2008.

[107] N. Shah, D. Panjala, and G. P. Huffman, "Hydrogen production by catalytic decomposition of methane," *Energy & Fuels,* vol. 15, pp. 1528-1534, 2001.

[108] N. Frage, M. Polak, M. P. Dariel, N. Frumin, and L. Levin, "High-temperature phase equilibria in the Al-rich corner of the Al-Ti-C system," *Metallurgical and Materials Transactions A,* vol. 29, pp. 1341-1345, 1998.

[109] V. Raghavan, "Al-C-Ti (Aluminum-Carbon-Titanium)," *Journal of Phase Equilibria and Diffusion,* vol. 27, p. 148, 2006.

[110] W. H. Philipp, "Chemical reactions of carbides, nitrides, and diborides of titanium and zirconium and chemical bonding in these compounds," 1966.

[111] Y. Leng, *Materials characterization: introduction to microscopic and spectroscopic methods*: John Wiley & Sons, 2009.

[112] J. Campbell, *Castings*: Butterworth-Heinemann, 2003.

[113] L.-Y. Chen, J.-Q. Xu, H. Choi, M. Pozuelo, X. Ma, S. Bhowmick*, et al.*, "Processing and properties of magnesium containing a dense uniform dispersion of nanoparticles," *Nature,* vol. 528, pp. 539-543, 2015.